Behaviour of Sandy Soils with Varying Fines Content and Saturation Under Monotonic and Cyclic Triaxial Loading: Experimental Study and Model Validation

Jotheeshwar Velayudham

A thesis submitted in fulfil the requirements for the degree of

Doctor of Philosophy

Supervisors

Prof. David Airey &

Prof. Abbas El-Zein

School of Civil Engineering

Faculty of Engineering

The University of Sydney

31 March 2025

Statement of Originality

This is to certify that to the best of my knowledge; the content of this thesis is my own work. This has not been submitted for any degree or other purposes. I certify that the intellectual content of this thesis is the product of my own work and that all the assistance received in preparing this thesis and sources have been acknowledged.

In line with this declaration, I acknowledge that ChatGPT and Grammarly were used during the preparation of this thesis to assist with language enhancement, including sentence structuring, and paraphrasing. Additionally, ChatGPT was used to support code debugging and development in both Python and MATLAB, particularly for plotting, data processing, and visualisation purposes. All content generated or suggested by these tools was critically reviewed, verified, and modified as needed. I take full responsibility for the content and confirm that the use of generative AI complied with the University of Sydney's guidelines for the responsible use of generative AI in research.

Jotheeshwar Velayudham
31 March 2025

Abstract

The behaviour of sandy soils under varying loading and saturation conditions is of fundamental importance in geotechnical engineering, particularly for the safe and resilient design of infrastructure foundations, embankments, and earth structures. While fully saturated soil behaviour is relatively well understood, the mechanical response of partially saturated soils, especially under cyclic loading remains a topic of active research due to its complexity and significant influence on infrastructure performance. This study investigates the influence of fines content and degree of saturation on the monotonic and cyclic behaviour of sandy soils and attempts to validates a constitutive model capable of simulating these responses using a critical state soil mechanics (CSSM) framework.

The research begins with an experimental investigation involving triaxial testing of sandy soils mixed with varying proportions of non-plastic feldspar fines, conducted under both saturated and partially saturated conditions. The tests include monotonic and cyclic loading scenarios to capture key behavioural characteristics. Special attention is given to the effects of fines content, which can significantly alter soil structure, and contractive/dilative tendencies, as well as the degree of saturation, which controls suction and effective stress distribution in unsaturated conditions.

Experimental results revealed that both fines content and degree of saturation significantly impact the soil's response under monotonic and cyclic loading. Low fines content (<20%) maintained sand-like behaviour with high dilatancy and strength, whereas high fines content (>30%) led to a fines-dominated response with increased compressibility and contractiveness. Similarly, partially saturated soils exhibited enhanced cyclic resistance due to matric suction, though extremely low degrees of saturation introduced brittleness and strain localisation. These observations underscore the need for models that can capture these transitions in behaviour.

To simulate these behaviours, a modified version of the SANISAND-based constitutive model developed by Ghorbani and Airey (2021) was adopted. The model, rooted in the Critical State Soil Mechanics (CSSM) framework, was calibrated using the monotonic test results and considers suction effects, stiffness degradation, and cyclic loading mechanisms. While the model successfully captured the monotonic response across varying fines contents and saturation levels, its performance under cyclic loading remains at a preliminary assessment stage. Due to limitations in the experimental dataset, full calibration of the model's cyclic features such as memory surface and strain accumulation mechanisms, was not feasible. As a result, simulations of cyclic loading in both saturated and unsaturated conditions provided only indicative insights, and accurate prediction of cyclic behaviour is yet to be achieved.

This study demonstrates the potential of critical state-based model to simulate complex soil responses under different saturation and fines conditions, while also highlighting the limitations in current modelling approaches for cyclic behaviour. The findings underscore the importance of targeted experimental data for model calibration and point to the need for further model development, particularly in simulating cyclic degradation, suction hysteresis, and strain accumulation with improved computational efficiency.

Acknowledgement

I would like to express my deepest gratitude to Prof. David Airey for his encouragement, guidance, and patience throughout the supervision of this project. I am profoundly thankful for the numerous opportunities he has provided me to grow as a researcher, professional, and individual. His constant support during the challenging times of the pandemic, enabling me to continue my studies from India, has been instrumental. Prof. Airey's encouragement during my moments of mental strain and his role as a mentor and local guardian have made a lasting impact on my journey, for which I will be forever grateful.

I am also grateful to Prof. Abbas El-Zein for his guidance, particularly in discussions on the constitutive model and the behaviour of unsaturated soils.

My thanks go to Mr. Ross Barker for his technical expertise and support in setting up the testing apparatus. His practical solutions and willingness to answer my questions saved me significant time. I also thank Mr. Garry Towell and Mr. Paul Burrel, who, along with Mr. Ross, contributed to fabricating my sample former.

I extend my appreciation to Prof. Itai Einav, Dr. Benjy Marks, and Dr. François Guillard for including me in SciGEM's group meetings. These meetings greatly improved my public speaking and presentation skills, allowing me to present my research progress regularly.

I extend my appreciation to Prof. Itai Einav and Dr. Ali Hadigheh, my PEM panel members, for their valuable comments during each session, which significantly shaped this research.
Special thanks to Dr. Ganesh Kumar from CSIR-CBRI for providing lab facilities in India to start my experiments and for his unwavering support. I am also grateful to my friends there, SK Jeeva, MD Godson, Ram Kumar, and Aman Kumar.

To my friends and lab mates, Mukesh Singh Bisht, Jiale Zhu, Sepideh Tehari, Hamad Faizi, and Honey Sajan Thomas, thank you for the discussions, support, and shared laughter. A special mention to Mukesh, my roommate, for his companionship.

I would also like to thank all my teachers and professors from the past who recognized my passion for teaching and research and encouraged me to pursue a PhD.

To my friend Sathish Kumar. K, thank you for being my mental pillar and helping me make key decisions throughout my candidature.

I owe special thanks to my parents, Mr. R. Velayudham and Mrs. V. Kavitha, my sister V. Hemaroobini and my unofficial parents cum guardians, Mr. S. Shanmugam (Late) and Mrs. S. Veliyammal, without whom I wouldn't be where I am today. My achievements are dedicated to you.

Finally, to my wife Preetha, I am deeply grateful for your unwavering support and for always encouraging me to strive for my best.

This research reported in this thesis was supported by the award of a Faculty of Engineering Research Scholarship from the University of Sydney, which I gratefully acknowledge.

Table of Contents

List of Figures

List of Tables

Chapter 1
Introduction

1.1 Background

Soil behaviour under different loading conditions is a fundamental aspect of geotechnical engineering, particularly in the context of infrastructure stability and foundation performance (Terzaghi, 1943; Das, 2013). Sandy soils, widely found in natural deposits and used in engineering applications, exhibit complex mechanical responses influenced by fines content, degree of saturation, and cyclic loading conditions (Ishihara, 1993; Mitchell & Soga, 2005). The presence of fines significantly alters shear strength, stiffness, and compressibility, while the degree of saturation affects pore water pressure evolution and effective stress distribution (Thevanayagam et al., 2002; Tsukamoto et al., 2014). Understanding these effects is critical for predicting soil response under monotonic and cyclic loading, particularly for earthquake engineering, embankments, and foundation stability (Seed & Idriss, 1971; Bray & Sancio, 2006).

Partially saturated soil constitutes the upper layer of the earth's land surface and plays a crucial role in geotechnical engineering applications. These soils can be found beneath critical infrastructures, including roads, railways, airports and buried utilities, water supply and sewage systems, power and telecommunications cables, subways, and tunnels. They are often compacted as fill materials for a wide range of global water, sanitation, energy, and transportation systems (Ghayoomi et al., 2013). Furthermore, compacted partially saturated soils are utilized to construct critical infrastructure such as dams, embankments, abutments, and land reclamation activities (Tsukamoto et al., 2014). Hence, the study of partially saturated soils has gained significant interest among researchers over several decades as it is crucial for the safe and efficient design of these structures. The study has reached a state of maturity with the availability of extensive textbooks (Fredlund & Rahardjo, 1993; Lu & Likos, 2004; Murray & Sivakumar, 2010).

Despite significant advancements in understanding partially saturated soils, many aspects of their behaviour remain unresolved. One of the fundamental challenges is capturing the complex relationship between matric suction, effective stress, and deformation, which varies under different environmental conditions and loading scenarios (Zhang & Lytton, 2009). Key uncertainties persist in areas such as volume change behaviour, shear strength evolution, permeability variations, and long-term settlement, particularly for infrastructure exposed to seasonal moisture fluctuations and fluctuating groundwater levels (Rahardjo et al., 2012). A crucial component in unsaturated soil mechanics is the Soil-Water Characteristic Curve (SWCC), which defines the relationship between matric suction and water content. Although various models have been proposed from empirical approaches (Van Genuchten, 1980; Fredlund & Xing, 1994) to advanced hysteretic and temperature-dependent models (Pham et al., 2005; Pedrotti et al., 2020) accurately integrating SWCC into constitutive frameworks remains a challenge, particularly for predicting soil response under transient conditions.

Among the many unresolved aspects, cyclic behaviour of partially saturated soils has gained increasing research attention due to its critical role in seismic engineering, and traffic-induced loading, (Ishihara et al., 2004; Unno et al., 2008; Kimoto et al., 2011). Understanding how cyclic loading influences the stiffness, strength, and degradation mechanisms in partially saturated soils is essential for improving geotechnical design and infrastructure resilience.

The mechanical behaviour of sandy soils is commonly assessed using triaxial tests, which provide key information about soil strength, deformation, and volumetric response under controlled stress conditions (Bishop & Henkel, 1962; Lade, 2016). However, triaxial test results alone may not fully capture the intricate behaviour of sandy soils under cyclic and unsaturated conditions, as factors such as strain accumulation, excess pore water pressure generation, and stiffness degradation significantly influence soil response (Ishihara & Yoshimine, 1992; Unno et al., 2008; Kimoto et al., 2011). To enhance the interpretation of

these test results, this research employs the Critical State Soil Mechanics (CSSM) framework, which provides a unified approach to understanding soil behaviour at different stress states (Schofield & Wroth, 1968; Wood, 1990; Gens & Alonso, 1992). The critical state concept allows for a more comprehensive characterization of shear strength, dilatancy, and strain accumulation, which are essential for evaluating soil stability under varying fines content and saturation levels (Coop & Atkinson, 1993; Been & Jefferies, 1985).

A key challenge in geotechnical engineering is the development and validation of constitutive models capable of accurately predicting soil behaviour under realistic field conditions (Gens & Potts, 1988; Yu, 2006). While several constitutive models exist for sandy soils, their applicability to different fines content and saturation levels under cyclic loading remains uncertain (Ghorbani & Airey, 2021; Tang et al., 2018). Initially, this research aimed to focus extensively on unsaturated soil behaviour, considering the importance of partial saturation in geotechnical structures. However, due to time constraints and the nature of experimental results, the study was broadened to include a wider scope, addressing unsaturated soil behaviour as a part of the investigation rather than the primary focus. The selected constitutive model is capable of simulating unsaturated soil behaviour, allowing for a comparative assessment of soil response across different saturation levels. Preliminary attempts were also made to simulate cyclic behaviour of saturated samples, though accurate calibration was limited by the available dataset.

1.2 Aim

This study aims to bridge existing research gaps by validating a constitutive model using an extensive set of experimental data. The calibration of model parameters is performed using results from triaxial tests (saturated monotonic, saturated cyclic, unsaturated monotonic, and unsaturated cyclic). The model's predictive capabilities are then evaluated by comparing

numerical simulations against experimental findings (Zienkiewicz et al., 1999; Wheeler et al., 2003).

1.3 Research Objectives

To translate the overall aim of this thesis into actionable steps, the research was broken down into a series of interlinked objectives. Each objective addresses a different aspect of the broader goal, from fundamental soil behaviour, through laboratory testing, to numerical model validation. Together, these objectives create a logical workflow: first, to understand how fines content and saturation affect soil behaviour, then to generate meaningful experimental data, and finally to calibrate and test a constitutive model capable of reproducing those behaviours. This breakdown ensures that the thesis moves systematically from observation to interpretation to simulation, providing both practical insight for engineers and a foundation for future research. The specific research objectives are as follows:

i. Conduct a comprehensive program of laboratory testing.

- Perform drained and undrained triaxial tests on samples with different gradations and degrees of saturation.
- Evaluate the peak and residual strength trends, pore water pressure generation and dissipation, volumetric strain evolution, stiffness degradation and softening patterns, cyclic resistance and post cyclic responses.

ii. Investigate the influence of fines content and saturation on soil behaviour.

- Examine how variations in fines content (from clean sand to fines-dominated mixtures) influence the overall soil response under triaxial loading (Ishihara et al., 2004; Tsukamoto et al., 2014).
- Assess how degrees of saturation (fully saturated and partially saturated) affect the soil's mechanical behaviour (Been & Jefferies, 1985; Coop & Atkinson, 1993).

- Evaluate the resulting changes in stress–strain response, including peak and residual behaviour.
- Investigate variations in stiffness and how they evolve with different fines contents and saturation levels.
- Analyse the influence on dilatancy and the transition between contractive and dilative tendencies.
- Determine the overall strength characteristics and how these parameters interact under monotonic and cyclic triaxial loading conditions.

iii. To characterise the critical state behaviour and establish Critical State Lines (CSLs) for various sand–fines mixtures

- Define and interpret the CSL for each gradation under saturated and partially saturated conditions.
- Investigate whether transitional fines content soils follow a unique CSL or exhibit bifurcation based on fabric and initial density.

iv. To validate and calibrate an advanced SANISAND-based constitutive model for sandy soils under monotonic and preliminary cyclic loading

- Use experimental data to calibrate stiffness, dilatancy, peak strength, and state-dependent parameters of the Ghorbani & Airey (2021) model, including recent enhancements by Chen et al. (2024).
- Assess the model's ability to simulate the behaviour of soils with different fines contents and degrees of saturation under various loading paths.

v. To evaluate the potential of the constitutive model in simulating unsaturated soil behaviour

- Test the capability of the selected model to incorporate suction effects through coupling with the Soil-Water Characteristic Curve (SWCC).

- Conduct preliminary simulations of unsaturated cyclic behaviour and identify limitations due to partial calibration.

vi. To identify key research gaps and propose future directions for model improvement and experimental extension

- Highlight challenges encountered in testing and modelling partially saturated soils, particularly under cyclic loading.
- Recommend additional tests, parameter refinement, and numerical strategies for improving the robustness of the model in practical geotechnical applications.

1.4 Limitations of the Research

While the study advances current understanding in several areas, the following limitations are acknowledged:

- **Cyclic Model Calibration under Unsaturated Conditions**: Comprehensive calibration of the model for unsaturated cyclic loading could not be achieved due to the limited number of cyclic tests. As a result, cyclic parameters were estimated using values from published studies, which may not fully capture the behaviour of the sands tested in this study.
- **Limited Experimental Cyclic Testing**: Due to the time-intensive nature of cyclic triaxial testing and equipment constraints, the number of cyclic tests conducted, particularly under partial saturation was limited. A more extensive testing program is needed to fully quantify cyclic degradation mechanisms and enable robust model calibration for various degrees of saturation and fines content.
- **Numerical Complexity and Computational Demand**: Accurate simulation of cyclic loading in partially saturated soils presents significant numerical challenges. Capturing the combined effects of suction, strain accumulation, and stress-path dependency requires advanced constitutive formulations with numerous parameters. The

implementation of such models is computationally demanding, particularly when simulating extended cyclic histories, limiting the practicality of repeated model runs and parameter optimisation. These computational constraints, along with insufficient data on suction-dependent cyclic behaviour, restricted full-scale numerical validation.

- **Simplified Boundary Conditions and Test Configurations**: Laboratory element testing is conducted under idealised, axisymmetric conditions, which do not fully reflect complex boundary conditions encountered in real geotechnical problems. While essential for fundamental insight and model development, the findings may not directly translate to full-scale field applications without further boundary value modelling.
- **Exclusion of Plastic Fines and Field-Scale Simulations**: The focus on non-plastic fines ensures clarity in interpreting mechanical responses but limits direct applicability to natural soils with high plasticity. Likewise, this study does not include finite element simulations of practical problems such as embankment or foundation performance, which would require further model development and validation.

Despite these limitations, the study generates an extensive experimental dataset and offers critical insights into the behaviour of sandy soils across a range of conditions. It also provides a foundational step toward improved constitutive modelling of partially saturated cyclic soil behaviour.

1.5 Layout of Thesis

This thesis is structured to present the development, calibration, and validation of a constitutive model for sandy and well-graded soils under monotonic and cyclic triaxial loading. Chapter 2 introduces the constitutive model, outlining its governing equations and theoretical framework. It also specifies the key experiments required for model calibration, ensuring that the model can simulate soil behaviour under different loading conditions. Chapter 3 provides a detailed description of the materials used in this study, including their physical and mechanical

properties, and presents the experimental methodologies employed. This chapter outlines the laboratory tests conducted, including triaxial tests for stress-strain behaviour, one-dimensional (1-D) compression tests for compressibility assessment, and the HYPROP test for determining the Soil-Water Characteristic Curve (SWCC), which is crucial for understanding the hydro-mechanical behaviour of unsaturated soils. Additionally, this chapter describes the apparatus configurations and testing protocols used to ensure reliable experimental results.

Chapter 4 presents the experimental results obtained from the triaxial tests, analysing soil behaviour under varying fines content and saturation conditions. This chapter discusses key aspects such as stress-strain response, stiffness degradation, cyclic resistance, and volumetric changes, providing insights into the fundamental mechanisms governing soil response. Chapter 5 focuses on the calibration and validation of the constitutive model using experimental data. The calibration process is carried out either directly from experiments or by fitting the model parameters to replicate the experimental behaviour observed in the laboratory tests. The model's performance is evaluated through numerical simulations of four types of triaxial tests conducted on all soil types: saturated monotonic, saturated cyclic, unsaturated monotonic, and unsaturated cyclic tests. While the model is assessed in detail under monotonic loading conditions, only preliminary attempts were made to capture cyclic behaviour of saturated samples, as mentioned earlier, due to limited experimental data for full calibration.

Finally, Chapter 6 summarizes the key findings of the study and provides recommendations for future research, including potential refinements to the model and further experimental investigations.

Chapter 2
Literature Review

2.1 Behaviour of Sandy Soils with Varying Fines Content and Saturation

The mechanical behaviour of sandy soils is influenced by several interdependent factors, including particle size distribution, fines content, degree of saturation, and stress history. These factors affect key soil properties such as shear strength, stiffness, dilatancy, permeability, and compressibility, which play a critical role in determining soil response under monotonic and cyclic loading conditions (Mitchell & Soga, 2005; Thevanayagam et al., 2002; Tsukamoto et al., 2014). The addition of fines (silt and clay fractions) can significantly alter the soil's structural arrangement and mechanical response by affecting grain contacts, interparticle friction, and drainage characteristics (Polito & Martin, 2001; Monkul & Ozden, 2007). Similarly, saturation levels impact the effective stress, suction, and pore pressure response, leading to variations in liquefaction susceptibility, strength degradation, and stiffness evolution (Fredlund & Rahardjo, 1993; Lu & Likos, 2004; Tsukamoto et al., 2014). A comprehensive understanding of these influences is essential for improving the predictive capabilities of constitutive models and geotechnical design methodologies, particularly for applications in earthquake engineering, embankment stability, and foundation performance (Seed & Idriss, 1971; Ishihara, 1993; Bray & Sancio, 2006).

2.1.1 Influence of Fines Content on Sandy Soil Behaviour

Fines content in sandy soils generally refers to the proportion of particles smaller than 0.075 mm, including silt and clay fractions. The inclusion of fines alters particle packing, contact mechanics, and permeability, thereby influencing the soil's overall response under different loading conditions (Mitchell & Soga, 2005; Thevanayagam et al., 2002). The effect of fines content on soil behaviour can be categorised into three regimes:

1. **Fines as Non-Plastic Fillers** (Low Fines Content, <10%)

- At low fines content, fines primarily occupy void spaces between sand grains without significantly altering the grain structure (Thevanayagam, 1998; Polito & Martin, 2001).
- The sand matrix dominates the mechanical response, resulting in high permeability and a dilatant response under shearing (Zlatović & Ishihara, 1995).

2. **Transition Behaviour** (Moderate Fines Content, 10–30%)
   - At moderate fines content, particle contacts are modified, leading to a reduction in permeability and dilatancy (Carraro et al., 2009).
   - Depending on fines plasticity, this transition phase may result in either increased or decreased liquefaction resistance and strength (Polito & Martin, 2001; Thevanayagam et al., 2002).
3. **Fines-Dominated Behaviour** (High Fines Content, >30%)
   - At high fines content, the soil structure transitions to a fines-dominated matrix, leading to higher compressibility and lower permeability (Monkul & Ozden, 2007).
   - The behaviour begins to resemble that of silt or clay, with increased contractiveness and a greater tendency for strain accumulation (Juneja & Mohammed-Aslam, 2017).

A key parameter in understanding the influence of fines content is the threshold fines content (TFC), beyond which the soil structure shifts from sand-dominated to fines-dominated. The TFC varies depending on factors such as grain shape, particle gradation, and compaction energy (Thevanayagam, 1998; Carraro et al., 2009).

Building on the concept of threshold fines content, several researchers have proposed approaches to incorporate fines effects into constitutive modelling through a single evolving parameter rather than recalibrating entire models for each fine's percentage. For example, Rahman and Lo (2008, 2009) introduced the concept of an equivalent granular void ratio (e^*) and state parameter (ψ^*), which adjusts the soil state to account for fines content implicitly. Rahman et al. (2011) showed that by linking e^* and ψ^* to fines content, sand–fines mixtures

could be described using parameter sets derived for clean sand, avoiding discrete recalibrations for each mixture. Similarly, Ghafarian et al. (2020) embedded fines content into the hardening modulus and other critical state parameters as smooth functions, enabling the constitutive model to transition between sand-dominant and fines-dominant behaviour. These approaches provide a promising framework for future work, where fines content could be treated as a continuous variable within state-parameter-based models like SANISAND, improving both efficiency and predictive power.

While many natural soils contain plastic fines (e.g., clays), this study employs non-plastic feldspar fines to isolate the mechanical effects of fines content and saturation without the confounding influence of plasticity or swelling. This approach provides a clearer understanding of the role of fines in modifying the stiffness, pore pressure generation, and cyclic resistance of sandy soils. By removing the complexity of swell-shrink behaviour, the experimental design ensures that observed trends are more directly attributable to fines content and degree of saturation.

Although feldspar fines may not be as commonly encountered as clay in typical field conditions, non-plastic fines are not uncommon in specific geological contexts such as:

- Weathered igneous or metamorphic terrains, where feldspar minerals break down into silt-sized non-plastic particles,
- Engineered fills or manufactured sands, where non-plastic fines may be deliberately used to improve drainage or reduce swell potential, and
- Desert or arid environments, where clay content is minimal and fine fractions are often non-plastic.

Therefore, while the findings may not directly represent highly plastic soils, they are applicable to geotechnical scenarios involving non-plastic fines, and they form a valuable reference for understanding fundamental trends in partially saturated soils. Moreover, the insights from this

controlled study lay the groundwork for future investigations involving plastic fines, where coupled effects such as suction, time dependency, and mineralogy can be superimposed on the current findings

2.1.2 Influence of Saturation on Sandy Soil Behaviour

Saturation level directly influences soil pore pressure response, effective stress, and strength characteristics. The behaviour of sandy soils under different saturation conditions can be categorised into three distinct states:

1. **Fully Saturated Sands**
    - In fully saturated conditions, the response is governed by pore water pressure buildup and dissipation (Seed & Idriss, 1971; Ishihara, 1993).
    - Under undrained cyclic loading, excess pore pressure can lead to liquefaction and loss of strength, particularly in loose sands (Bray & Sancio, 2006; Tsukamoto et al., 2014).

2. **Partially Saturated Sands**
    - Partially saturated sands contain both air and water, generating matric suction, which increases apparent cohesion and enhances soil strength (Vanapalli et al., 1996; Lu & Likos, 2004).
    - The behaviour is nonlinear and influenced by moisture content and stress history (Fredlund & Xing, 1994; Pedrotti et al., 2020).

3. **Dry Sands**
    - Dry sands exhibit higher peak strength and dilative behaviour due to the absence of pore water pressure effects (Lade, 1993).
    - The response is primarily controlled by interparticle friction and fabric arrangement (Been & Jefferies, 1985).

While dry sands have distinct behavioural characteristics, this study focuses exclusively on fully saturated and partially saturated conditions in triaxial testing. The decision to exclude dry sands is based on practical considerations and research relevance. In natural and engineered environments, sandy soils are rarely completely dry, as infiltration, groundwater fluctuations, and environmental moisture often maintain a certain level of saturation (Fredlund & Rahardjo, 1993). Moreover, in geotechnical applications such as earthquake engineering, embankments, and buried infrastructure, partially saturated and saturated states are the most critical for stability assessment and cyclic performance analysis (Tsukamoto et al., 2014; Rahardjo et al., 2012).

Furthermore, triaxial testing of dry sands presents additional experimental challenges, including sample preparation difficulties, uniformity concerns, and excessive dilation effects, which can complicate data interpretation (Lade, 1993). By focusing on saturated and partially saturated conditions, this study provides insights into the influence of matric suction, excess pore pressure generation, and cyclic resistance, which are key factors in practical geotechnical applications.

2.1.3 Combined Influence of Fines Content and Saturation

The combined effect of fines content and saturation leads to a highly variable response depending on factors such as particle arrangement, drainage conditions, and suction effects. Some key observations from past research include:

- At low fines content, increasing saturation leads to reduced shear strength and increased liquefaction susceptibility (Ishihara et al., 2004; Tsukamoto et al., 2014).
- At high fines content, the role of matric suction becomes more dominant, contributing to apparent cohesion and increased strength in partially saturated conditions (Rahardjo et al., 2012).

- Transitional fines content soils exhibit highly variable behaviour, where saturation effects depend on fabric, density, and stress history (Thevanayagam et al., 2002).

The critical state framework provides a valuable approach for analysing the interaction between fines content and saturation. Studies have shown that partially saturated sands can exhibit a unique critical state line (CSL), dependent on suction and saturation levels (Gens & Alonso, 1992; Wheeler et al., 2003). However, more recent research indicates that transitional materials particularly those with intermediate fines content or mixed fabric—may not exhibit a unique CSL. Kwa and Airey (2016) showed that samples with 40% fines content failed along different and parallel CSLs depending on their initial density, suggesting bifurcation of the critical state surface. Similarly, Shipton and Coop (2012) observed that changes in soil fabric during reconstitution can lead to multiple CSLs for the same material. Yin and Chang (2009) also demonstrated that stress path dependency (compression vs. extension) can result in non-unique CSLs, further challenging the universality of the critical state concept in transitional or structured soils. These findings suggest caution when applying a single critical state framework to soils with variable fines content, fabric, or loading histories.

2.1.4 Implications for Practical Engineering Applications

Understanding the influence of fines content and saturation is critical for improving geotechnical design methodologies, particularly in:

- Liquefaction mitigation through controlling fines content and degree of saturation (Bray & Sancio, 2006).
- Foundation stability assessment in partially saturated soils, where matric suction effects must be considered (Vanapalli et al., 1996).
- Slope stability and embankment design, where moisture variations impact long-term performance (Rahardjo et al., 2012).

- Design of compacted fills, particularly for transportation infrastructure, retaining structures, and land reclamation projects (Ghayoomi et al., 2013; Tsukamoto et al., 2014).
- Seismic engineering, where understanding cyclic behaviour in partially saturated soils is essential to ensure stability (Ishihara et al., 2004; Kimoto et al., 2011).

A thorough understanding of sandy soil behaviour with varying fines content and saturation requires extensive laboratory experimentation to assess stress-strain response, stiffness degradation, and strength evolution. The next section reviews experimental studies from past research, highlighting key methodologies, findings, and their relevance to this study.

2.2 Experimental Studies on Monotonic Behaviour of Sandy Soils

Monotonic loading tests are essential for understanding the fundamental stress-strain behaviour, strength, and volumetric response of sandy soils. These tests, commonly performed using triaxial compression, direct shear, or simple shear apparatuses, provide insights into peak and residual shear strength, dilation, contractiveness, and failure modes (Bishop & Henkel, 1962; Lade, 2016). Researchers have extensively studied the influence of fines content and degree of saturation on the monotonic response of sandy soils to establish critical state parameters and stress-strain characteristics under different conditions (Been & Jefferies, 1985; Thevanayagam et al., 2002).

2.2.1 Influence of Fines Content on Monotonic Behaviour

The effect of fines content on soil strength and deformation has been widely investigated using triaxial tests under drained and undrained conditions. Zlatović & Ishihara (1995) conducted a series of triaxial tests on Toyoura sand with varying amounts of fines and found that when fines content was below 20%, the soil retained its sand-like structure, exhibiting dilatancy and high peak strength. However, when fines exceeded 30%, the behaviour transitioned to contractive, with reduced peak strength and increased volumetric strain. Similarly, Thevanayagam et al.

(2002) observed that low-plasticity silty sands (fines content < 25%) exhibit increased stiffness and peak strength, whereas high-fines content sands (>30%) behave more like fine-grained soils, experiencing pore pressure buildup and strength loss in undrained conditions.

Triaxial compression tests conducted by Carraro et al. (2009) on silica sand mixed with non-plastic fines revealed that fines content up to 10% increases shear strength and dilatancy due to improved particle interlocking as shown in Figure 2.1. However, beyond this threshold, fines start to dominate the behaviour, reducing strength and increasing compressibility. Their undrained tests showed that the peak deviatoric stress decreased with increasing the fines content by 40%, indicating a significant strength reduction with increasing fines content which confirms the previous research.

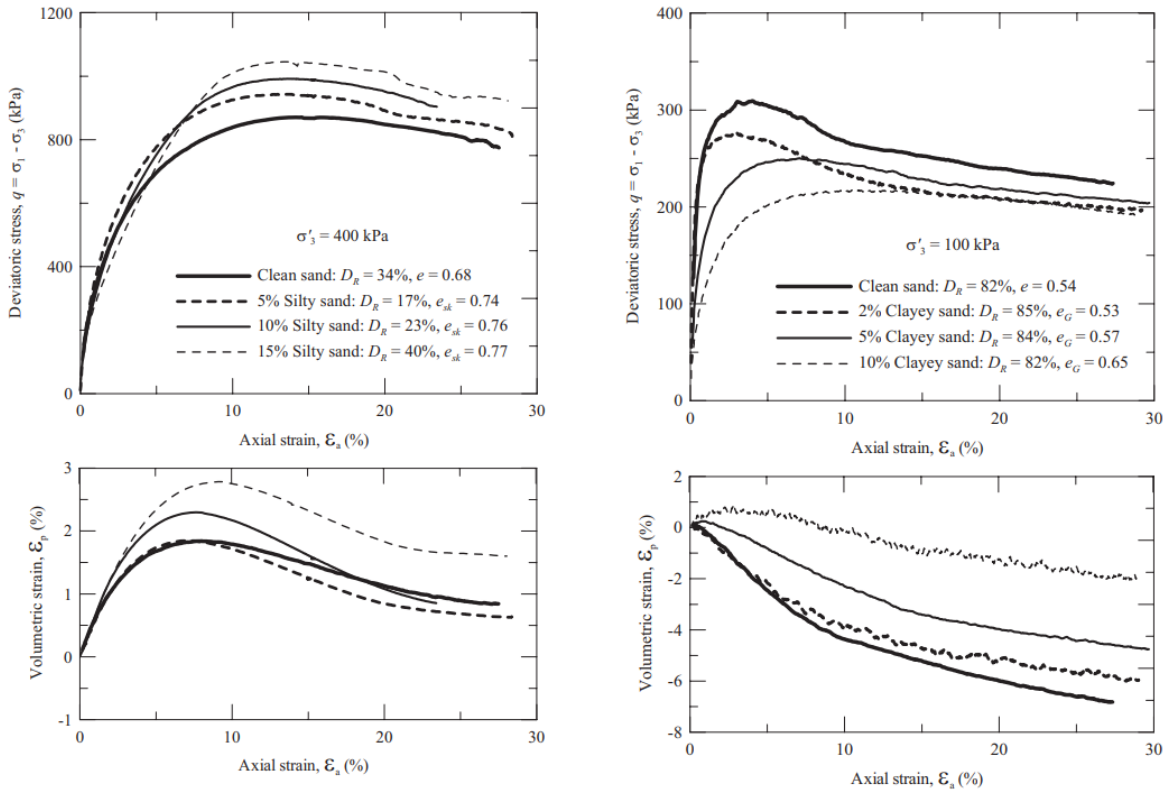

Figure 2.1: Stress-Strain-Volumetric response of loose and dense sand with varying fines (after Carraro et al, 2009)

2.2.2 Influence of Saturation on Monotonic Behaviour

The degree of saturation has a profound effect on shear strength, stiffness, and volumetric strain accumulation in sandy soils. Fully saturated sands exhibit contractive behaviour and excess pore pressure buildup, often leading to strain softening under undrained loading conditions (Seed & Idriss, 1971; Tsukamoto et al., 2014; Tsukamoto & Ishihara, 2022). Been & Jefferies (1985) demonstrated that loose saturated sands under undrained conditions reach critical state shear strength at much lower strains compared to partially saturated sands, due to the rapid development of excess pore pressure.

This behaviour is well illustrated in Figure 2.2, which presents a schematic overview of undrained triaxial test responses for sandy soils with varying initial densities and drainage conditions. The figure shows the evolution of stress paths (q–p′), void ratio changes, and axial strain behaviour under undrained loading. Loose specimens (e.g., paths A to B"C″) exhibit contractive behaviour, generating pore pressure and leading to flow-type failure. Dense specimens (e.g., paths A to B, C) show dilative behaviour, often reaching a peak before stabilising on the steady state line. Intermediate states (paths A' to B' and C′) demonstrate limited flow and post-peak strain softening. This framework helps contextualise how saturation levels influence contractive versus dilative tendencies during monotonic undrained loading.

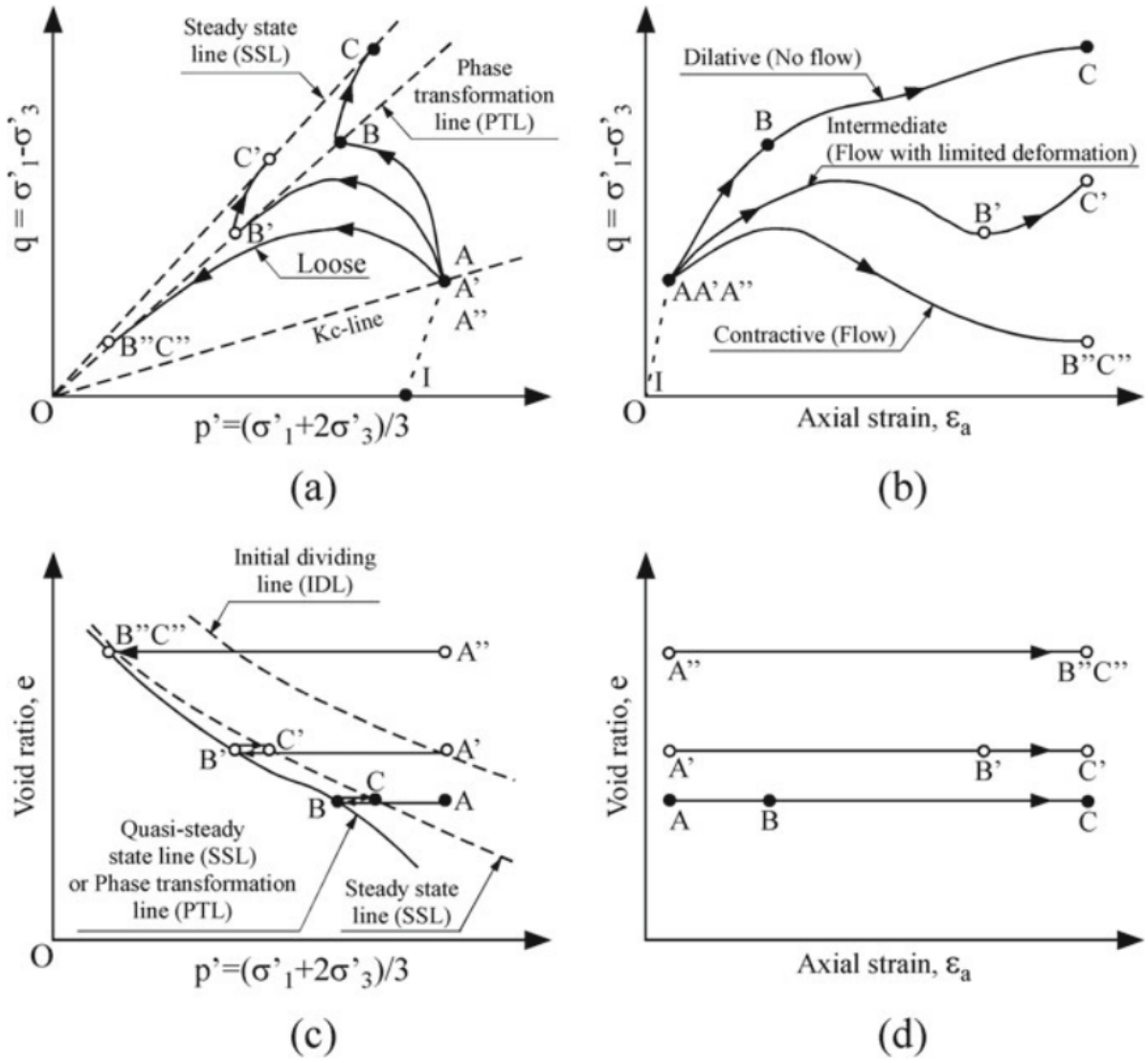

Figure 2.2: Schematic diagram showing typical behaviour undrained tests (after Tsukamoto & Ishihara, 2022)

In contrast, partially saturated sands develop matric suction, increasing their apparent cohesion and stiffness. Studies by Vanapalli et al. (1996) showed that at a degree of saturation of 80%, unsaturated sands exhibited 25-50% higher shear strength than their saturated counterparts due to the contribution of suction to the effective stress. Similarly, Lu & Likos (2004) observed that partially saturated sand specimens with a suction of 10-30 kPa displayed significantly lower compressibility and higher peak strength than fully saturated specimens.

Experimental results from Fredlund & Rahardjo (1993) indicated that for sands with degrees of saturation between 60% and 90%, matric suction effects contribute to shear strength

increases of 10–35%. However, at very low saturations (below 30%), the soil becomes more brittle, leading to sudden strength loss and strain localisation upon failure (Lu & Likos, 2004). This suggests that the influence of partial saturation is highly nonlinear and dependent on suction control, requiring precise laboratory techniques such as the axis translation method or suction-controlled triaxial testing for accurate assessment.

2.2.3 Influence of Fines content on Cyclic behaviour

The role of fines content in cyclic soil behaviour has been a subject of extensive research. Many of the monotonic loading studies conducted by researchers have been extended to cyclic loading conditions, aiming to evaluate how soil properties evolve under repeated stress cycles. Thevanayagam (1998) found that silica sand containing 15-20% non-plastic fines exhibits increased cyclic resistance compared to clean sand, as the fines fill voids and improve packing density. However, at fines content exceeding 30%, cyclic strength deteriorates due to increased contractiveness and pore pressure buildup. Their cyclic triaxial tests on loose silty sands at 100 kPa confining pressure showed that cyclic resistance ratio (CRR) reduced from 0.18 for clean sand to 0.12 at 40% fines content, indicating a significant reduction in resistance to liquefaction.

Studies by Polito & Martin (2001) on Nevada sand mixed with low-plasticity fines confirmed that at low fines content (<20%), cyclic resistance improved. However, at higher fines content, the number of cycles to liquefaction significantly decreased due to increased pore pressure generation and strain accumulation. Similarly, Zlatović & Ishihara (1995) observed that sands with 10% fines showed 30% higher liquefaction resistance than clean sand, but beyond 25% fines content, liquefaction resistance reduced drastically. Kwa and Airey (2017) conducted cyclic triaxial tests on sand-fines mixtures under varying fines content. Their results showed that cyclic resistance increases up to an optimum fines content (20-30%) before decreasing due to increased contractiveness and pore pressure buildup as shown in Figure 2.3. These findings

align with previous studies, highlighting the importance of fines content in assessing cyclic soil behaviour.

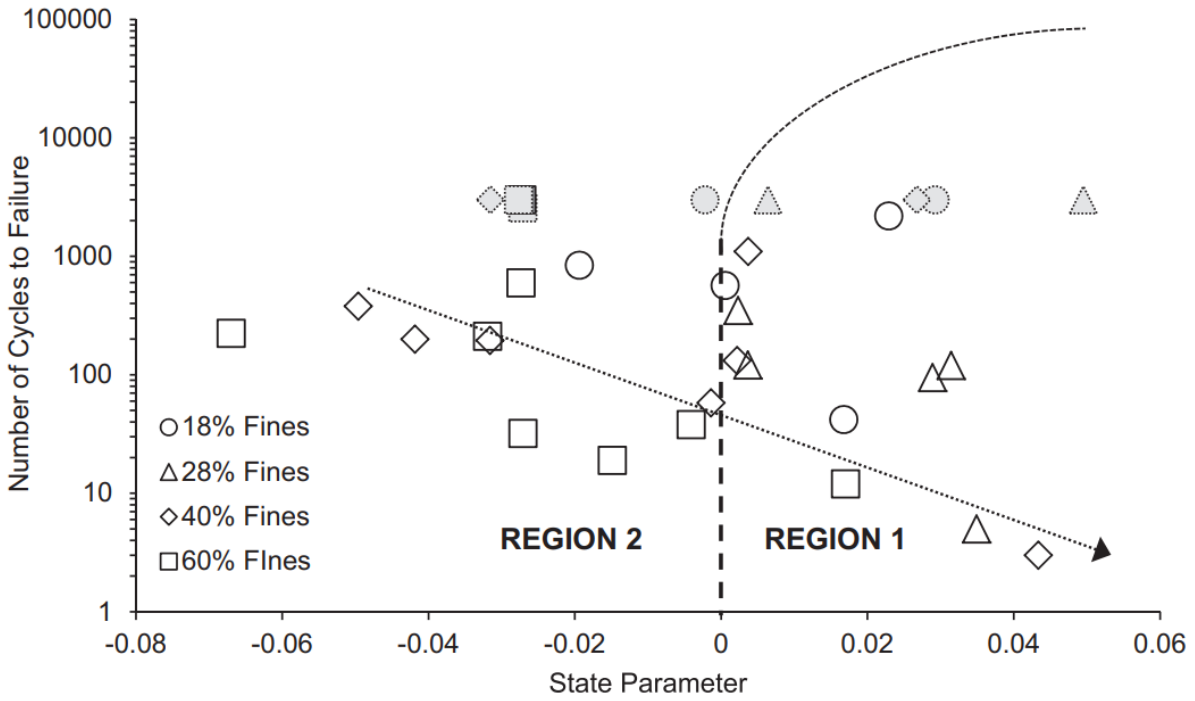

Figure 2.3: Cyclic Resistance of Sand with varying fines - State Parameter (Kwa, 2019)

2.3 Studies on Unsaturated Soil Behaviour

Partially saturated soils exhibit distinct mechanical responses when subjected to cyclic loading, which refers to the repeated application of stress or strain over time. These loading conditions commonly occur in structures affected by seismic activity, traffic loads, wave-induced forces, and industrial vibrations. Unlike fully saturated soils, which are more prone to pore pressure buildup and liquefaction, partially saturated soils benefit from matric suction, leading to enhanced stiffness and resistance to cyclic degradation (Chaney, 1978; Ng & Menzies, 2007). However, this resistance is highly dependent on particle size distribution, grading, and compressibility (Tsukamoto et al., 2014).

Cyclic behaviour of partially saturated soils plays a critical role in infrastructure stability, particularly in regions prone to earthquakes, flooding, and seasonal moisture variations. The failure of foundations, embankments, and slopes due to cyclic softening and instability has

been widely reported. Table 2.1 shows catastrophic failures, including the 2023 Turkey-Syria Earthquake, the 2011 Christchurch Earthquake, and the 2008 Wenchuan Earthquake, where cyclic loading-induced liquefaction and loss of strength in unsaturated soils led to severe economic losses and human casualties. Similarly, repeated wetting-drying cycles and traffic-induced stress have caused long-term pavement and railway subgrade failures, resulting in billions in maintenance costs (FHWA, 2016; Dixon et al., 2006).

A fundamental aspect of unsaturated soil mechanics is the Soil-Water Characteristic Curve (SWCC), which describes the relationship between matric suction and moisture content (Fredlund & Rahardjo, 1993). Experimental research has demonstrated that matric suction enhances soil strength and stiffness, making it a critical factor in assessing partially saturated soil stability (Lu & Likos, 2004; Pedrotti et al., 2020). Several experimental techniques have been developed to determine the SWCC, including axis translation, filter paper methods, and HYPROP testing (Fredlund & Rahardjo, 1993; Pham et al., 2005). The SWCC is known to exhibit hysteretic behaviour, meaning that wetting and drying paths differ, which poses challenges for constitutive modelling of unsaturated soils (Van Genuchten, 1980; Gens & Alonso, 1992). The role of saturation changes in shear strength and deformation characteristics remains a crucial focus in experimental geomechanics, as discussed in greater detail in the later section on Soil-Water Characteristic Curve (SWCC).

Numerous experimental studies have been conducted to investigate the cyclic behaviour of both saturated and unsaturated soils, providing understanding into their mechanical response under repeated loading. While research on saturated soils has been more extensive, particularly in the context of liquefaction and cyclic mobility, studies on unsaturated soils have focused on how matric suction and partial saturation influence cyclic resistance. Laboratory investigations have explored various factors affecting cyclic response, including the degree of saturation, fines content, and soil grading, to better understand their role in shear strength, volumetric

behaviour, and energy dissipation. To better understand these factors and their effect on cyclic behaviour, researchers have used different laboratory tests to study soil response under controlled conditions, which are explained in the following section.

Table 2.1 Notable Geotechnical Failures Associated with Unsaturated Soils

Event	Cause	Description	Damage Estimate	Lives Lost	Citation
2023 Turkey-Syria Earthquake	Seismic-induced liquefaction and ground settlement	Liquefaction and ground failure due to cyclic loading in unsaturated sandy and silty deposits, leading to building collapses and infrastructure damage.	AU$34 billion	59,000+	World Bank, 2023;
2018 Hokkaido Earthquake (Japan)	Earthquake-induced landslides	Landslides occurred in volcanic ash deposits with unsaturated soil behaviour.	AU$2.28 - 4.65 billion	41	Yamagishi & Yamazaki, 2018
2013 Uttarakhand Landslides (India)	Rainfall-induced landslides	Slope instability due to rainfall altering matric suction.	AU$3.04 billion	5700+	NDMA, 2013
2010-2011 Christchurch Earthquakes (New Zealand)	Seismic-induced settlement and liquefaction	Cyclic softening and settlement in unsaturated sandy soils.	AU$30 billion	-	Cubrinovski et al., 2011
2011 Brisbane Floods (Australia)	Flood-induced weakening of embankments	Water infiltration reduced soil strength, leading to embankment failure.	AU$2.38 billion	-	Queensland Reconstruction Authority, 2012

2009 Black Saturday Bushfires (Australia)	Bushfire-induced soil erosion and weakening	Fire-induced hydrophobicity altered infiltration and erosion rates.	AU$4.4 billion	-	Teague et al., 2010
2008 Wenchuan Earthquake (China)	Earthquake-triggered liquefaction and landslides	Liquefaction and slope failures in partially saturated soils.	AU$228.0 billion	87,000	Wang et al., 2011
2005 La Conchita Landslide (USA)	Rainfall-triggered slope failure	Infiltration led to increased pore pressure and slope instability.	AU$46 million	10	Jibson, 2005
Western Australia Seasonal Soil Movements	Swelling/shrinkage cycles in clayey soils	Expansive soils underwent significant volume changes under seasonal moisture variations.	AU$3 billion	-	Main Roads WA, 2015
2000 UK Railway Embankment Failure	Wetting-drying cycles affecting railway embankments	Cyclic swelling/shrinkage weakened the soil, causing infrastructure settlement.	AU$200.0 million	-	Dixon et al., 2006
US Road Pavement Failures	Traffic-induced cyclic loading leading to settlement and rutting	Repeated traffic loading exacerbated compaction and settlement in unsaturated subgrades.	AU$7.6 billion	-	FHWA, 2016

2.4 Experimental Studies on Partially Saturated Soils

Understanding the cyclic response of soils requires controlled laboratory experiments that replicate in situ stress conditions. Soil element tests provide direct measurements of stress-strain relationships, pore pressure evolution, and failure mechanisms, making them fundamental in developing and validating constitutive models. Several types of tests have been conducted in the literature to examine the cyclic behaviour of soils, including triaxial tests, simple shear tests, resonant column tests, cyclic direct shear tests, and cyclic hollow cylinder tests. Cyclic triaxial tests have been the most widely employed, as they provide control over confining stress, drainage conditions, and loading frequency, making them suitable for studying strain accumulation, stiffness degradation, and failure mechanisms under repeated loading. Simple shear tests allow for the direct application of cyclic loading under constant volume or drained conditions, making them valuable for analysing shear strain evolution and pore pressure buildup. Resonant column tests focus on the dynamic properties of soils, such as shear modulus and damping ratio, which are critical for understanding seismic response. Cyclic direct shear tests have been used to study interface behaviour and shear strength degradation, while hollow cylinder tests allow for complex stress path applications, particularly in anisotropic conditions.

2.4.1 Influence of Degree of Saturation

The degree of saturation has a critical impact on the cyclic behaviour of soils, influencing their stiffness, shear strength, and resistance to liquefaction. Experimental studies consistently show that decreasing the degree of saturation enhances cyclic resistance due to matric suction, which stabilizes the soil and delays pore pressure generation. However, at very low saturations, brittleness and strain localisation may occur, especially in dense sands.

Research by Ishihara et al. (2004), Unno et al. (2008), and Kimoto et al. (2011) demonstrated that partially saturated sands exhibit improved cyclic resistance compared to fully saturated ones. These studies used B-value adjustments and suction-controlled triaxial tests to confirm the benefits of suction. Nonetheless, air entrapment at very low saturations can reduce uniformity and increase brittleness.

A range of suction control techniques have been employed, including axis translation, filter paper methods, and humidity control chambers. Each method has its strengths: axis translation offers precise suction control, while humidity chambers simulate field-like moisture cycles. These tools are critical for testing and understanding saturation effects in cyclic behaviour.

2.4.2 Influence of Soil Grading and Compressibility

Soil grading and compressibility are key factors in determining cyclic soil response. Well-graded soils exhibit improved cyclic resistance due to enhanced interlocking and reduced pore pressure generation, while highly compressible soils tend to accumulate strain and undergo strength degradation under cyclic loading.

Studies on silty sands, such as those by Whang et al. (2004), Chin et al. (2010), and Kim et al. (2019), highlight the interplay of fines content, drainage conditions, and suction. Excessive fines lead to higher compressibility and reduced resistance to cyclic degradation. Conversely, well-graded sands with moderate fines content can benefit from improved stiffness and cyclic stability.

In road-base and sub-base materials, findings by Ohiduzzaman et al. (2012) and Ishikawa et al. (2014) confirm that fines content and water content significantly affect deformation behaviour. Optimal fines content (typically around 10–15%) supports dilative response, whereas higher contents increase compressibility.

Overall, maintaining proper grading and managing compressibility are essential for ensuring long-term performance of soils subjected to repeated loading, particularly in transportation and seismic applications.

2.4.3 Triaxial Testing

Triaxial testing is a core method for evaluating the mechanical behaviour of soils under controlled stress conditions. It allows precise simulation of field-relevant stress paths and is particularly suited for analysing shear strength, stiffness degradation, and pore pressure response under monotonic and cyclic loading.

Depending on drainage and consolidation conditions, triaxial tests are classified into Consolidated Drained (CD), Consolidated Undrained (CU), and Unconsolidated Undrained (UU) types. For cyclic loading, triaxial tests measure critical parameters such as Cyclic Resistance Ratio (CRR), excess pore pressure, and post-cyclic volumetric strain.

Partially saturated tests require suction control, which is achieved using techniques like axis translation or humidity regulation. These tools enable the evaluation of the effects of matric suction on soil behaviour, which is essential in simulating in situ conditions. Triaxial testing is thus a key experimental tool in this research, supporting model calibration and providing robust data for constitutive model validation.

2.5 Critical State Soil Mechanics

The critical state framework provides a fundamental approach to analysing soil behaviour under cyclic loading. This framework defines soil behaviour in terms of state parameters, stress paths, and the ultimate strength condition, offering a means to evaluate how soils transition between elastic, plastic, and failure states during cyclic loading. The concept of critical state soil mechanics (CSSM) has been widely applied to saturated and unsaturated soils, allowing for a unified representation of soil response under monotonic and cyclic loading.

The Critical State Line (CSL) is central to CSSM, representing conditions under which soil can deform continuously without experiencing additional volume change or strength increase. Understanding this concept is key in evaluating the transition between dilatant and contractive responses, which plays an important role in assessing liquefaction risks, foundation stability, and cyclic degradation (Ishihara, 1993; Jefferies & Been, 2006). The critical state condition in triaxial space is generally defined by:

$$q = M\,p' \qquad 1$$

$$v = \Gamma - \lambda\,ln\,p' \qquad 2$$

where: $q = \sigma_1' - \sigma_3'$ is the deviatoric stress, $p' = (\sigma_1' + 2\sigma_3')/3$ is the mean effective stress, v is the specific volume, M is the slope of the Critical State Line (CSL) in stress space, Γ is the intercept of the CSL in semi-log space, λ is the slope of the CSL in semi-log space, representing the compression index under critical state conditions.

These expressions describe how, at critical state, the relationship between mean effective stress, deviatoric stress, and specific volume remains uniquely defined, enabling effective predictions for soil response in drained and undrained conditions.

Within this framework, soil behaviour is characterised by state parameters such as mean effective stress, void ratio, and shear stress, which dictate whether a soil is contracting or dilating under cyclic loads. Studies have shown that unsaturated soils follow different critical state lines depending on their initial saturation and suction levels. This is particularly relevant in triaxial testing, where critical state parameters help define yielding, failure states, and post-cyclic settlement.

Since unsaturated soil response is affected by matric suction as this influences the apparent effective stress, which controls shear strength, stiffness, and deformation, it is essential to

analyse the Soil-Water Characteristic Curve (SWCC). The next section delves into SWCC principles, experimental determination, and its significance in controlling soil behaviour under different saturation levels.

2.6 SWCC and Stress State in Unsaturated Soils

The Soil-Water Characteristic Curve (SWCC) describes the relationship between matric suction and the soil's water retention properties, including degree of saturation, volumetric water content, and gravimetric water content. This function is fundamental in unsaturated soil mechanics as it defines the soil's ability to retain water under different suction conditions, influencing shear strength, compressibility, permeability, and overall mechanical behaviour (Fredlund & Rahardjo, 1993; Lu & Likos, 2004).

Several mathematical models have been developed to represent the SWCC, with two of the most commonly used being the Van Genuchten (1980) equation and the Fredlund & Xing (1994) equation. The Van Genuchten equation expresses the volumetric water content as a function of matric suction and is widely used for coarse-grained soils, whereas the Fredlund & Xing model is particularly useful for capturing the behaviour of both coarse- and fine-grained soils, incorporating an additional correction factor to improve accuracy at low suction levels. The Fredlund & Xing (1994) equation is given by:

$$\theta = \theta_s \left[\frac{1}{\ln\left(e + (\psi/\,\mathrm{a})^n\right)}\right]^m \qquad 3$$

θ is the volumetric water content, θ_s is the saturated volumetric water content, ψ is the matric suction, a, n, m are curve-fitting parameters that define the shape of the SWCC, e is the natural exponential constant.

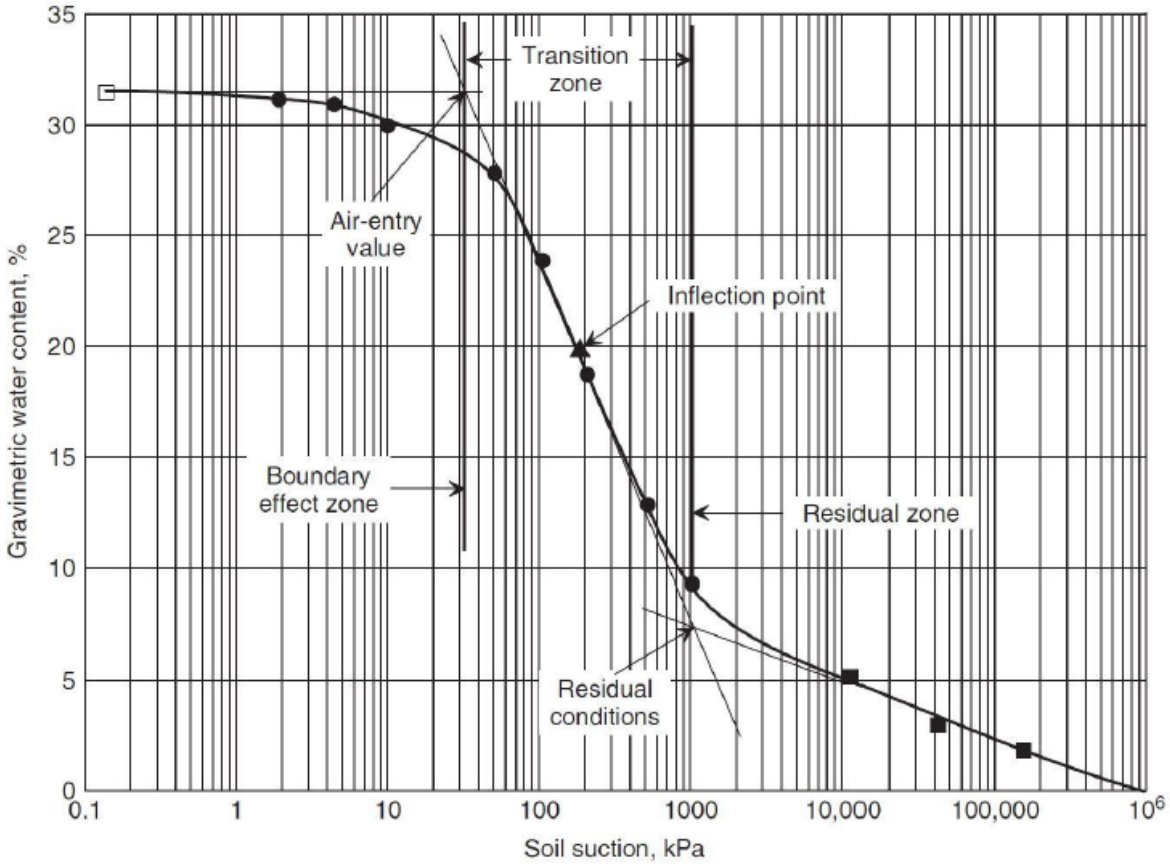

Figure 2.4: Components of SWCC (after Fredlund and Rahardjo, 1993)

The shape of the SWCC is divided into three main regions. At low matric suction, the soil remains fully saturated, meaning all pore spaces are filled with water. As suction increases, air begins to enter larger pores, leading to a gradual decrease in water content in what is known as the transition zone. At very high suction levels, only thin films of water remain, and further increases in suction result in minimal changes in water content, defining the residual zone as shown in Figure 2.4. The slope of the SWCC provides insight into how quickly a soil desaturates, with well-graded soils exhibiting a more gradual transition and uniformly graded sands showing sharper desaturation curves (Pham et al., 2005; Pedrotti et al., 2020).

2.6.1 Stress State in Unsaturated Soils

The behaviour of unsaturated soils is governed by complex interactions between pore water, pore air, and soil particles, requiring an extension of traditional effective stress principles.

Unlike saturated soils, where the effective stress equation depends solely on total stress and pore water pressure, unsaturated soils involve an additional stress component due to matric suction. This suction enhances shear strength and cyclic resistance, making it a crucial factor in the analysis of soil stability under changing moisture conditions.

One of the earliest and most widely accepted approaches for incorporating suction into the effective stress equation in unsaturated soil mechanics was proposed by Bishop (1959). The Bishop's effective stress equation introduces a material-dependent parameter, χ, which defines the extent to which suction contributes to strength. The modified effective stress equation is given by:

$$\boldsymbol{\sigma' = \sigma - u_a + \chi(u_a - u_w)} \qquad 4$$

Where σ' is the effective stress, σ is the total stress, u_a is the pore air pressure, u_w is the pore water pressure, and χ is the material-dependent parameter that defines the extent to which suction contributes to strength.

Various studies have investigated how χ-values change under different degrees of saturation and stress paths, revealing that unsaturated soils do not always follow a linear relationship between suction and strength. The nonlinearity of the SWCC and hysteretic effects in cyclic loading further complicate predictions of unsaturated soil response. Triaxial tests incorporating suction control techniques provide essential data for refining χ-based formulations and improving constitutive models that account for effective stress variations in unsaturated conditions.

By integrating unsaturated soil mechanics into cyclic triaxial test analysis, this study aims to enhance the predictive capability of constitutive models and improve the understanding of cyclic behaviour in unsaturated sands along with their saturated counterparts.

2.7 Numerical Modelling of Partially Saturated Soils

Numerical modelling plays a crucial role in predicting the cyclic behaviour of partially saturated soils, enabling simulations of complex loading conditions that are difficult to replicate in laboratory experiments. Experimental studies provide data that enables the development of predictive numerical models, which can then be used for engineering design and risk assessment. Various numerical approaches, primarily based on the finite element method (FEM), have been proposed to describe the behaviour of unsaturated soils as a multiphase system consisting of air, water, and solid phases (Lewis & Schrefler, 1982; Khalili et al., 2008; Shahbodagh-Khan et al., 2015; Ghorbani et al., 2016; Ghorbani et al., 2018a). These approaches typically rely on the effective stress concept and incorporate different assumptions and simplifications to manage computational complexity. However, to simulate cyclic behaviour accurately, these numerical methods must be coupled with an appropriate constitutive model that captures the stress-strain response, stiffness degradation, and accumulation of plastic strains in partially saturated soils. Developing an accurate constitutive model for cyclic loading remains a challenge, even for well-studied saturated soils. The incorporation of suction effects into various elastoplastic constitutive models for saturated soils has been the foundation for most unsaturated cyclic models (Khalili et al., 2008; Bian & Shahrour, 2009; Liu & Muraleetharan, 2012; Ghorbani et al., 2018a). Several constitutive models for unsaturated soils have been integrated into commercial software, including the Barcelona Basic Model (BBM) in PLAXIS, the UBC (University of British Columbia) Sand Model in FLAC, the SANISAND Model in ABAQUS and FLAC, and the Modified Cam-Clay model adapted for unsaturated conditions. While these models offer a framework for simulating suction effects and stress-dependent behaviour, they exhibit notable limitations when applied to cyclic loading. The BBM model, for instance, effectively captures suction-induced hardening but struggles to simulate cyclic degradation and energy dissipation mechanisms.

Similarly, the UBC Sand Model is widely used for seismic liquefaction analysis but is primarily designed for fully saturated conditions, making it less effective for partially saturated soils without further modifications.

The SANISAND model, a state-dependent critical-state-based formulation, has been extensively applied to cyclic loading problems due to its ability to capture strain accumulation, cyclic mobility, and stiffness degradation. While SANISAND effectively replicates liquefaction triggering and post-liquefaction behaviour, its standard formulation does not explicitly account for suction effects in unsaturated soils. Some researchers have extended SANISAND by incorporating suction-dependent yield surfaces and stress invariants, but its application to partially saturated soils remain an area of ongoing research. Despite these theoretical advancements, only limited applications of these numerical approaches to boundary value problems have been reported. Many studies simplify complex soil behaviour by neglecting the hysteretic nature of the soil-water characteristic curve (SWCC) or assuming passive air pressure, which reduces the accuracy of cyclic response predictions (Bian et al., 2017; Khoei & Mohammadnejad, 2011; Zienkiewicz et al., 1999). These limitations stem from the challenges associated with implementing these models, the large number of input parameters required, and the additional computational complexities involved in cyclic analyses. Overcoming these challenges and improving the performance of finite element solutions for modelling the cyclic response of partially saturated soils is a key focus of this research.

Constitutive models used in geotechnical engineering can be categorised into two main types. Simple models have relatively few parameters and are often limited in their ability to capture complex soil behaviours. These models are appealing due to their ease of implementation and low computational cost, making them useful for preliminary design applications. However, they often rely on simplified assumptions, such as constant stiffness or linear stress-strain

relationships, which do not fully account for hysteretic behaviour, strain accumulation, and suction effects. On the other hand, more advanced models incorporate a greater number of parameters and provide a more accurate representation of cyclic soil behaviour. These models can capture nonlinear stress-strain responses, suction-dependent stiffness evolution, and cyclic degradation mechanisms, but they require extensive calibration using experimental data and can be computationally demanding. The trade-off between simplicity and accuracy is an important consideration in numerical modelling, particularly when selecting a model for practical applications. However, the increased number of parameters introduces significant challenges in model calibration, as experimental data for these parameters are often limited or difficult to obtain. Many advanced models require extensive laboratory testing to determine key parameters such as suction-dependent stiffness, critical state parameters, and cyclic strain accumulation factors. Since experimental studies on partially saturated soils remain relatively scarce, the lack of sufficient data often restricts the applicability of these models and affects their predictive accuracy.

To overcome these challenges, this study aims to validate a modified and improved version of the SANISAND model, specifically the Ghorbani and Airey (2021) model through laboratory experiments. By conducting triaxial tests under controlled suction conditions, this research provides experimental data to calibrate and refine the constitutive model. The triaxial testing setup allows for systematic control of stress paths, pore pressure conditions, and cyclic loading parameters, ensuring that the experimental results can be directly compared with numerical predictions. This approach enhances the reliability and accuracy of the model in simulating the cyclic behaviour of partially saturated soils, addressing one of the key limitations in existing constitutive models.

However, it is acknowledged that the calibration of the constitutive model under cyclic loading remains at a preliminary stage due to the limited availability of comprehensive experimental

data, particularly under varied fines content and saturation conditions. Given this limitation, the primary contribution of this research lies in the detailed experimental investigation and numerical modelling of monotonic behaviour, and in establishing a robust framework for partial model calibration and validation under cyclic loading.

Future work will focus on extending the model's applicability to cyclic loading by: (i) conducting additional cyclic triaxial tests under varied fines content and saturation conditions to enhance the dataset; (ii) incorporating suction-dependent hysteresis and strain accumulation functions into the SANISAND framework; and (iii) evaluating the model performance in boundary value problems using finite element simulations. These strategies will help progressively improve the model's capacity to simulate cyclic degradation and energy dissipation mechanisms in partially saturated soils.

2.8 Research Gaps and Addressed Challenges

- Limited experimental studies have examined the combined effects of fines content and partial saturation under cyclic loading conditions. This study addressed this gap by testing soils across a range of gradations and saturation levels using both Sydney Sand and Well-Graded Sand mixtures.
- The transition from sand-like to fines-dominated behaviour, especially in partially saturated states, is not yet fully understood. This work investigated this transition in detail using monotonic and cyclic triaxial testing.
- There is a lack of critical state-based data for partially saturated soils, particularly for transitional fines contents. This research established Critical State Lines (CSLs) for eight gradations and analysed the impact of fines and saturation on key CSL parameters.
- Existing constitutive models often fail to accurately capture suction effects, strain accumulation, and cyclic degradation. This study implemented and calibrated a

SANISAND-based model for monotonic behaviour and initiated its extension to cyclic behaviour under both saturated and unsaturated conditions.

- Dual CSL behaviour has been reported in soils with intermediate fines content and varying densities. This study minimised such effects through controlled sample preparation and confirmed CSL convergence across all tested mixtures.
- The role of suction in cyclic behaviour is still experimentally challenging to capture. While this study included preliminary unsaturated cyclic simulations, full calibration of suction-related cyclic parameters remains a task for future work.
- Most modelling efforts focus on a single soil type. This study uniquely incorporated both uniformly graded and well-graded sands, allowing for assessment of model performance across diverse soil structures.
- Existing test datasets rarely cover the full range of conditions required for advanced model calibration. This study generated new high-quality data under drained and undrained, saturated and unsaturated, monotonic and cyclic loading conditions to support future modelling advancements.

Chapter 3
Description of Constitutive Model

3.1 Introduction

This chapter focuses on the constitutive modelling framework adopted for the experimental validation of triaxial tests for capturing the monotonic, cyclic behaviour of sands under both saturated and unsaturated condition. The model used in this thesis builds upon the fundamental work by Ghorbani and Airey (2021), who developed a constitutive model specifically designed to capture the hydro-mechanical behaviour of unsaturated sands, The Ghorbani and Airey, (2021) model is an evolution of SANISAND model, which is widely recognised in geotechnical engineering for its ability to simulate the stress-strain behaviour of granular soil under various loading conditions.

The original model (referred to the model by Ghorbani and Airey, 2021 in this thesis) effectively integrates both isotropic and kinematic hardening laws to capture the anisotropic behaviour of sands. It accounts for the effects of stress-induced anisotropy, non-linear compressibility, and transitions between saturated and unsaturated states, making it a robust tool for modelling complex soil behaviour. However, certain challenges remained unresolved, particularly in capturing the behaviour of partially saturated soils under cyclic loading, where issues such as stress overshooting, memory effects, and hardening behaviours need further refinement.

To address these challenges, Liuxin Chen introduced several key developments to the original model. Chen's modifications include the incorporation of stress overshooting mechanisms (Chen et al., 2022a; 2022b), the introduction of memory surfaces (Chen et al., 2024a; 2024b), and the modelling of volumetric and cyclic hardening in unsaturated soils (Chen et al., 2021; Chen et al., 2024c). These enhancements enable the model to more accurately simulate the cyclic behaviour of sands under various degrees of saturation, improving its predictive capabilities in geotechnical applications.

Compared to other available constitutive models, the SANISAND-based framework was selected in this study due to its strong critical state foundation, adaptability to state-dependent formulations, and capability to incorporate both saturation and fabric effects. Models such as the BBM (Alonso et al., 1990), Modified Cam-Clay (Roscoe & Burland, 1968), and Extended Drucker-Prager are commonly used for unsaturated soils but are primarily suited to cohesive materials and may not capture the state-dependent behaviour typical of sandy soils under large deformations. The UBC Sand model (Byrne, 1991) is widely used for saturated cyclic liquefaction analysis but lacks generality in modelling unsaturated conditions. In contrast, SANISAND and its extensions, including those by Ghorbani and Airey (2021) and Chen et al. (2024) provide a unified approach applicable to both monotonic and cyclic loading of sands across varying saturation levels.

Although this study primarily focuses on monotonic loading and only preliminarily explores cyclic response, the adoption of this extended SANISAND framework is intended to support future research in cyclic modelling of unsaturated granular soils, building on a theoretically sound and extensible platform.

The primary aim of this chapter is to elaborate on the structure and capabilities of the enhanced model. A calibration process is described in chapter 5 to determine the model parameters, ensuring that the predicted hydro-mechanical responses align closely with experimental data.

3.2 General Equations and Assumptions

3.2.1 Basic equations

In the triaxial stress space, the mean effective stress is denoted as $p' = (1/3)(\sigma'_1 + 2\sigma'_3)$ and the deviatoric stress as $q = \sigma'_1 - \sigma'_3$, deviatoric strain $\epsilon_q = (2/3)(\epsilon_1 - \epsilon_3)$ and volumetric strain $\epsilon_v = \epsilon_1 + 2\epsilon_2$. The total strain can be described as the sum of elastic strain and plastic strain components as in equation 5.

$$d\epsilon = d\epsilon^e + d\epsilon^p \quad (5)$$

This model adopts the elastoplastic framework where the stress ratio $\eta = q/p'$ is introduced and the incremental stress-strain relation of elastic strain, $d\epsilon^e$ and plastic strain rate, $d\epsilon^p$ can be further divided into deviatoric and volumetric components as shown in the equations 6, 7 and 8.

$$d\epsilon_q^e = \frac{dq}{3G} \quad (6)$$

$$d\epsilon_v^e = \frac{dp'}{K} \quad (7)$$

$$d\epsilon_q^p = \frac{d\eta}{H} \quad (8)$$

Where G is incremental shear moduli and K is incremental bulk moduli, both of which are the functions of mean effective stress p' and void ratio e, and H is plastic Hardening modulus.

3.2.2 Yield Surface

Constitutive models that adopt an elastoplastic framework use a yield surface which encompasses a purely elastic zone. This model employs bounding surface plasticity and assumes that plastic strains accompany all the deformations even at low strain levels. The yield surface within this bounding surface is given by:

$$F = |\eta - \alpha_k| - m_{iso}\sqrt{1 - \left(\frac{p'}{\alpha_{iso}}\right)^{n_{iso}}} \quad (9)$$

Where, α_k is kinematic hardening parameter and the bisector of the surface as shown in Figure 3.1 (a); α_{iso} controls the size of the bounding surface, and can be obtained from a Limiting Compression Curve (LCC) at high stress levels as shown in Figure 3.1 (b); m_{iso} is a material parameter that controls the wedge aperture of the bounding surface; n_{iso} is a material parameter that controls the shape of the bounding surface near the cap.

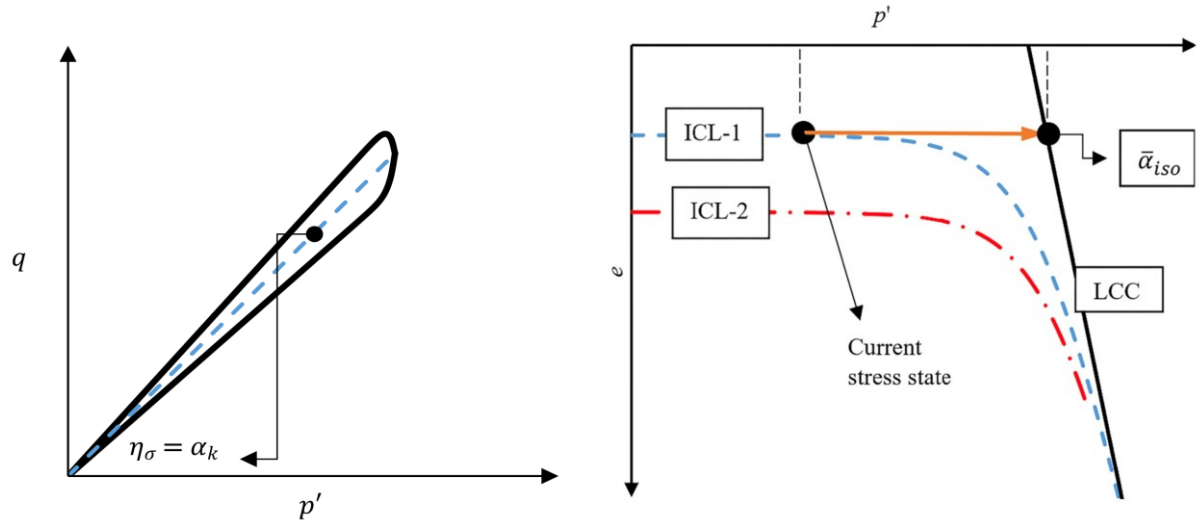

Figure 3.1: (a) Graphical representation of bounding surface; (b) Graphical representation of α_{iso} in LCC; (Ghorbani and Airey, 2020)

3.2.3 Elastic Moduli

The elastic moduli of the soil, specifically the shear modulus G and bulk modulus K, are crucial in describing the soil's response to stress changes within the elastic range. The moduli are functions of mean effective stress and void ratio that following the hypoelastic laws. The shear modulus G can be defined as:

$$G = G_0 p_a \left(\frac{p'}{p_a}\right)^{\frac{1}{2}} \frac{(2.97 - e)^2}{1 + e} \qquad 10$$

Where, G_0 is a dimensionless material constant related to the small-strain shear modulus, and p_a is atmospheric pressure.

$$K = K_0 p_a \left(\frac{p'}{p_a}\right)^{\frac{1}{2}} \left(\frac{1 + e}{e}\right)^{\frac{2}{3}} \qquad 11$$

Here, K_0 is a dimensionless material parameter that controls the shape of isotropic swelling line. Both moduli are influenced by the soil's void ratio, with changes in void ratio affecting the stiffness of the soil. These relationships highlight the dependency of soil stiffness on its stress state and void structure, which are essential for accurate predictions of soil behaviour under varying loading conditions.

3.2.4 Isotropic Hardening Law

The isotropic hardening law describes how the yield surface expands or contracts uniformly with changes in stress state, particularly in response to isotropic compression or unloading. The Isotropic Compression Line (ICL) of loose soils or soils with low initial confining stress tend to be asymptotic at high stress state to an LCC. At these high stress levels, particle crushing is almost certain which influences the compressibility of the soil and the shape of Critical State Line (CSL).

The ICL of fully saturated soil assured to converge into the LCC at high stress states and the LCC can be generalised into a straight line in log-log space of void ratio and mean effective stress.

$$ln\, e = ln\, N_l - \lambda\, ln\, p' \qquad 12$$

Where N_l denotes the value of void ratio on the LCC when p' is 1 kPa which is also a material parameter, and λ is the slope of the LCC in a ln e – ln p' plot. Considering the LCC as the upper limit for volume changes, the rate of volume change along the ICL can be obtained by interpolation.

$$d\epsilon_v = \frac{e}{(1+e)}\lambda\frac{dp'}{p'}\left(1-\delta_p^{\theta}\right) + \frac{dp'}{K}\delta_p^{\theta} \qquad 13$$

The first term $\frac{e}{(1+e)}\lambda\frac{dp\prime}{p\prime}$, represents the increment of volumetric strain derived from the LCC, while the second term $\frac{dp\prime}{K}$, is the increment of elastic volumetric strain, θ is a material parameter controlling the transition of ICL to LCC, and δ_p is an interpolation term that adjusts the rate of volumetric change.

An additional component called a bonding variable, ξ, which represents the suction or degree of saturation, is introduced to define the LCC for the unsaturated soils to capture the collapse phenomenon. The bonding variable is defined as:

$$\xi = (1 - S_w) g(\tilde{p}_c) \quad 14$$

Where, S_w is degree of saturation, and $g(\tilde{p}_c) = 1 + \frac{\tilde{p}_c}{10.7+2.4\tilde{p}_c}$, represents the intergranular force exerted between two soil grains represented in two identical spheres (Bojra, 2004). $\tilde{p}_c$ is suction with respect to atmospheric pressure. The void ratio in the unsaturated state can be related by the ξ component from the saturated equivalent by relation as follows:

$$e = e_s f(\xi) \quad 15$$

Where, e_s is the void ratio on the saturated LCC for the current p' and f(ξ) is given by:

$$f(\xi) = 1 - b_1(1 - exp\,(b_2 \xi)) \quad 16$$

Where, b_1 and b_2 are fitting parameters. So, eventually the LCC for unsaturated conditions, incorporating the bonding variable, is given by:

$$ln\, e = ln\, N_l - \lambda\, ln\, p' + ln\, f(\xi) \quad 17$$

This formulation captures the effects of partial saturation on soil compressibility, enabling the model to simulate the collapse phenomena observed in unsaturated soils.

3.2.5 Critical State Line

The Critical State Line (CSL) in soil mechanics represents the condition where soil reaches a steady state of deformation under continuous shearing, with no further changes in volume or stress. As the bi-logarithmic space of void ratio and mean effective stress is advantageous in avoiding unrealistic negative values of void ratio at high stress state, the CSL equation is also represented in this space. The CSL in the saturated condition is given by:

$$ln\, e = ln\, N_c - \lambda\, ln(p' + \alpha_{csl}) \quad 18$$

Here, N_c is material parameter denoting the value of void ratio on the CSL when $p' + \alpha_{csl} = 1$. The parameter α_{csl} influences the curvature of the CSL in the same space, allowing for a

more accurate representation of soil behaviour at different stress levels. For unsaturated conditions, the CSL is extended to account for the bonding variable ξ:

$$ln\, e = ln\, N_c - \lambda\, ln(p' + \alpha_{csl}) + ln\, f(\xi) \quad 19$$

This extension enables the model to capture the effects of partial saturation on the critical state behaviour, that it assumes the CSL shifts due to suction.

3.2.6 Kinematic Hardening

The Kinetic hardening law controls the hardening and softening of the soil before it reaches the critical state which also accounts for the history of loading and unloading cycles. This translation is crucial for modelling the cyclic behaviour of soils, where repeated loading can lead to changes in the material's response. The graphical representation of the bounding lines is shown in Figure 3.2. The bounding surface is determined by a relation between the peak stress ratio and state parameter,

$$M^b = M\ exp\ \langle -n^b \psi \rangle \quad 20$$

Where M is critical state stress ratio, n^b is a material parameter influencing stress ratio on M^b space and $\psi = e - e_c$. The MacCaulay bracket carries the condition as follows: If $\langle -n^b \psi \rangle > 0$; the value of $\langle -n^b \psi \rangle$ is $-n^b \psi$; if $\langle -n^b \psi \rangle \leq 0$; then the value of $\langle -n^b \psi \rangle$ is 0. The kinematic hardening evolution is derived from the equation below:

$$\frac{\partial \alpha_k}{\partial \epsilon_q^p} = h(M^b - \eta_\sigma) \quad 21$$

In this equation, ϵ_q^p deviatoric plastic strain, η_σ is stress ratio at reversal of stress and the h is a function of stress and void ratio. The parameter h is defined as:

$$h = h_0 G_0 (1 - c_h e) \left(\frac{p'}{p_a}\right)^{-\frac{1}{2}} \frac{1}{|n_\sigma - \eta_\sigma^{in}|^{\zeta'}} \quad 22$$

Where h_0 and c_h are material parameters, η_σ^{in} is the value of stress ratio at initial reversal and ζ' is responsible for smooth initiation and termination of the kinematic hardening process. This formulation allows the model to capture the effects of loading history on soil behaviour, particularly under cyclic loading conditions.

Before reaching the critical state, the soil exhibits dilatancy, where the volume change is influenced by the stress ratio relative to the dilatancy surface. In a typical sand saturated undrained test, the restriction on the soils tendency to compress results in excess pore water pressure increases but with sufficient deformation this reverses as the soil wants to dilate and the excess water pressure tends to drop until it reaches the CSL. The initial part of the soil behaviour changes (For instance, if the soil is compressing, once the dilatancy surface is reached, the tends to dilate) on the dilatancy surface which is a line with a slope of M^d in q-p' space as shown in Figure 3.2, and the slope of dilatancy surface is described by.

$$M^d = M\,exp(n^d\psi) \tag{23}$$

Where n^d is material parameter influencing the stress ratio on M^d surface and n^d is always greater than or equal to zero. The dilatancy D, can be defined as ratio of plastic volumetric strain and plastic deviatoric strain and is defined by.

$$D = \frac{d\epsilon_v^p}{d\epsilon_q^p} = LA_d(M^d - \eta_\sigma) \tag{24}$$

Where $L = 1$ when $\eta_\sigma - \alpha \geq 0$ and $L = -1$ when $\eta_\sigma - \alpha < 0$, A_d denotes the dilatancy coefficient. During cyclic tests, the fabric of the soil can change after significant volumetric strain. This effect is captured by modifying the dilatancy coefficient.

$$A_d = A_0(1 + zL) \tag{25}$$

Where A_0 is a model parameter, and z is the fabric dilatancy parameter. The evolution of z is described by:

$$dz = A(z)\left(-d\epsilon_v^p\right) = -c_z(-d\epsilon_v^p)(z_{max}L + z) \quad (26)$$

Where c_z and z_{max} are model parameters influencing the reversal loading stress path during cyclic loading.

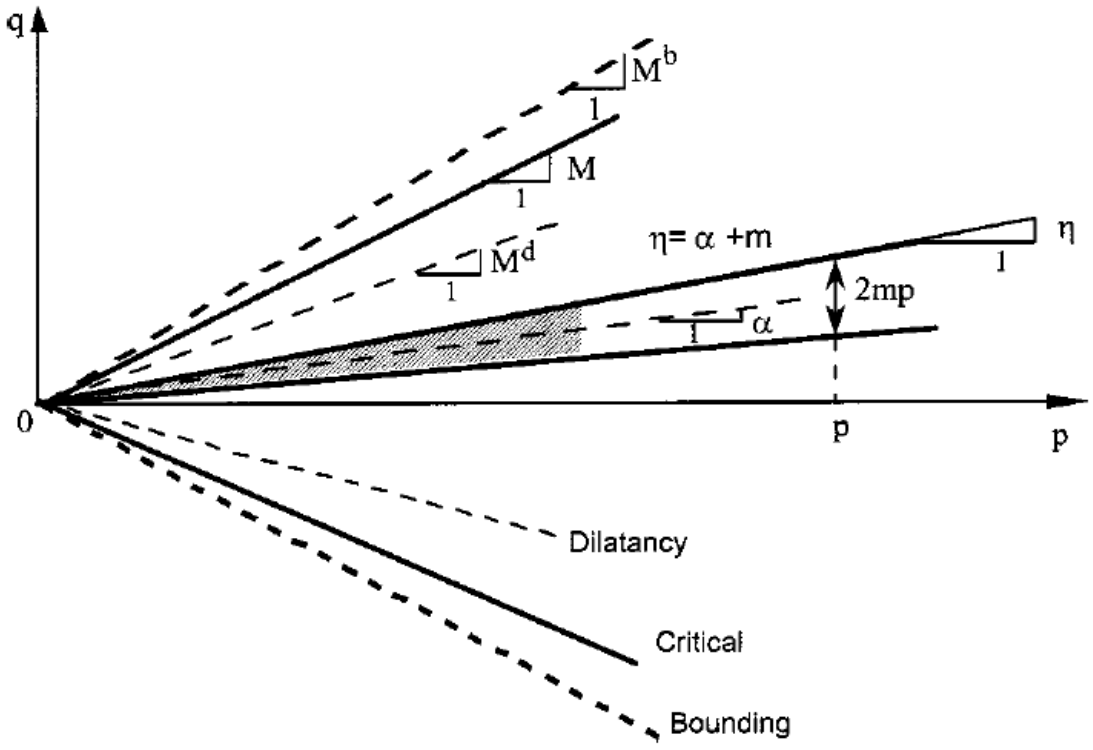

Figure 3.2: Graphical representation of the yield, critical, dilatancy, and bounding lines (Dafalias and Manzari, 2004)

3.2.7 Soil Water Characteristic Curve (SWCC)

The Soil-Water Characteristic Curve (SWCC) is a fundamental concept in unsaturated soil mechanics, describing the characteristic of soil's ability to retain or resist moisture content changes with respect to change in void ratio or suction. It is a function of soil suction and void ratio and mostly hysteretic in cycles of wetting and drying and in cyclic loading. It is important for the model to capture the SWCC behaviour to simulate the cyclic behaviour of unsaturated soils. The scaled suction of the soil, p_c^* is a normalised form of matric suction that can be defined as:

$$p_c^* = e^{\Omega'} p_c \tag{27}$$

Where Ω' material parameter influencing the volume changes in the SWCC equation. According to the SWCC equation, a change of degree of saturation dS_w in response to a change in suction dp_c^* can be expressed as:

$$dS_w = \left(\left(\frac{p_c^*}{p_c^{*\alpha}} \right)^{b_\alpha} \frac{\partial S_w^\alpha}{\partial p_c^*} + Y^{*sc} \right) . dp_c^* \tag{28}$$

Where $p_c^{*\alpha}$ is the normalised suction with respect to atmospheric pressure defined as:

$$p_c^{*\alpha} = S_w^{\alpha-1}(S_w), (\alpha = w, d) \tag{29}$$

And Y^{*sc} is a parameter that controls the smooth transition of wetting and drying hysteresis and is given by:

$$Y^{*sc} = Y^{*r} \left(\frac{p_c^* - p_c^{*\alpha}}{p_c^{*r} - p_c^{*\alpha}} \right)^{b_{sc}} \tag{30}$$

Hence the SWCC equation, following the approach of Manzanal et al. (2011), can be described by:

$$S_w^\alpha = S_{rw} + (1 - S_{rw}) * \left(ln \left[exp(1) + \left(\frac{p_c^*}{P^\alpha} \right)^{n_x^\alpha} \right] \right)^{-m_x^\alpha} \tag{31}$$

Where S_w^α is degree of saturation, superscript α is w for wetting and d for drying, S_{rw} is the residual degree of saturation, and n_x^α and m_x^α are fitting parameters of the Fredlund and Xing model (Fredlund and Xing, 1994). This formulation allows the model to capture the complex interactions between soil suction, moisture content, and volumetric changes, which are essential for predicting the behaviour of unsaturated soils under cyclic loading.

In the model used in this thesis, suction effects are incorporated not only through stiffness adjustments via the SWCC, but also indirectly influence the yield surface through the suction-dependent formulation of the critical state line. Specifically, the shift of the CSL under

unsaturated conditions reflects the impact of suction on strength mobilisation. While explicit hysteresis of the SWCC is not incorporated in this version, the influence of suction on yield behaviour is embedded via the bounding and dilatancy surface modifications. Thus, suction affects both stiffness and yielding response in the current model framework.

3.3 Stress Overshooting

The stress overshooting phenomenon primarily occurs due to abrupt, unrealistic stiffness increases when a stress reversal is misinterpreted as a significant loading event. An approach to managing stress overshooting was introduced in SANISAND-Z0 by Dafalias and Taiebat, (2016). This approach has been integrated in the enhanced constitutive model (Chen at al., 2022). The solution involves updating the back-stress ratio tensor using a weighted combination of past and current states, modified by the equivalent plastic strain. The update rule for back stress ratio, $\alpha_{in}^{(i+1)}$ is given by equation 32. The idea is to use a weighted average of the back-stress tensor from the previous loading step $(i-1)$ and the current step (i) with the weighting coefficient.

$$\alpha_{in}^{(i+1)} = m\alpha_{in}^{(i-1)} + (1-m)\alpha^{(i)} \qquad 32$$

Here, m is the weighting coefficient and it is defined based on the ratio of equivalent plastic strains during the loading step i and a material threshold and the weighting coefficient m is given by:

$$m = \langle 1 - \left(\frac{e_{eq}^{p(i)}}{e_{eq}^{-p}} \right)^{j} \rangle \qquad 33$$

The parameter j controls the sensitivity of the weighting coefficient. The implementation of these equations within the original model leads to more stable and realistic simulations, particularly under complex loading paths.

3.4 Semifluidised state and Memory Surface

The concept of a semi-fluidised state was introduced to improve the model's ability to capture the shearing behaviour of sands by Andres et al., (2020) and led to the development of the SANISAND-Sf model. On the other hand, the concept of a loading memory surface and memory surface hardening was introduced to capture the cyclic behaviour of sand by Di Benedetto et al., (2014) and Corti et al., (2016). This memory surface concept was integrated with SANISAND-Sf by Yang et al., (2023) who proposed the SANISAND-MSf model to address the soil behaviour during ratcheting, shakedown and liquefaction of soils, the concepts of memory surface and semi-fluidised state have been integrated in the enhanced model by Chen et al., (2024).

3.4.1 Memory Surface

The memory surface (MS) concept is introduced to capture the complex behaviour of soils under cyclic loading, especially the transition between hardening and softening phases. The MS evolution is guided by the accumulation of plastic strains, both contractive and dilative. The memory surface helps in modelling the soil stiffness, ensuring that the model can simulate both the increase in stiffness (shakedown) and decrease in stiffness (softening) under different loading conditions. The MS is defined by a factor called the memory surface hardening modulus that controls the hardening and softening behaviour of the material under cyclic loading much like the kinematic hardening.

The general framework of the Memory Surface Hardening (MSH) model, originally formulated by Corti and Diambra (2017) as illustrated in Figure 3.3. In this framework, the memory surface f_M evolves in the multiaxial stress space, capturing the effects of past stress history. The soil exhibits stiffer behaviour when loaded within this surface. The hardening modulus is adjusted

based on the distance between the current stress state and its projections on the memory and bounding surfaces σ_M and σ_B.u

Memory surface expansion occurs due to contractive plastic volumetric strains, as shown in Figure 3.4, indicating that the material is becoming more stable and denser. Conversely, memory surface contraction occurs due to dilative plastic strains, representing fabric degradation and stiffness loss, as illustrated in Figure 3.5.

These schematics demonstrate how the memory surface adjusts dynamically throughout cyclic loading, expanding during contractive cycles and shrinking during dilative cycles. This mechanism enhances the model's capability to simulate phenomena such as shakedown, ratcheting, and cyclic mobility observed in granular soils.

In this framework:

- f_M represents the evolving memory surface function.
- σ_B is the bounding stress surface, equivalent to the historical outer limit of stress state.
- σ_M is the memory surface stress, analogous to the current elastic boundary informed by past stress paths.

In the current model, these are respectively represented or approximated through:

- b^M: a stress-related internal state variable controlling evolution,
- f_e: a scaling function of plastic strain (Equation 35),
- $\mathcal{T}$: a threshold function controlling transition behaviour (Equation 36),
- h_m: the hardening modulus (Equation 34) that embodies the response to previous loading intensity.

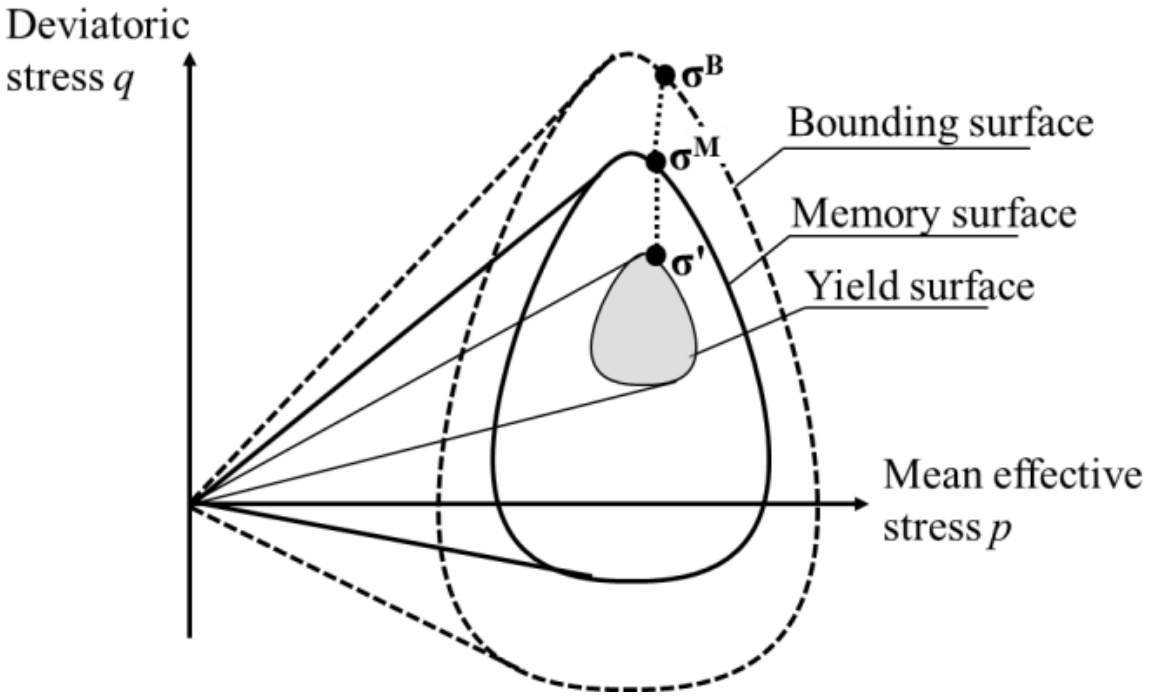

Figure 3.3: Schematic representation of the Memory Surface Hardening Model (Corti and Diambra, 2017)

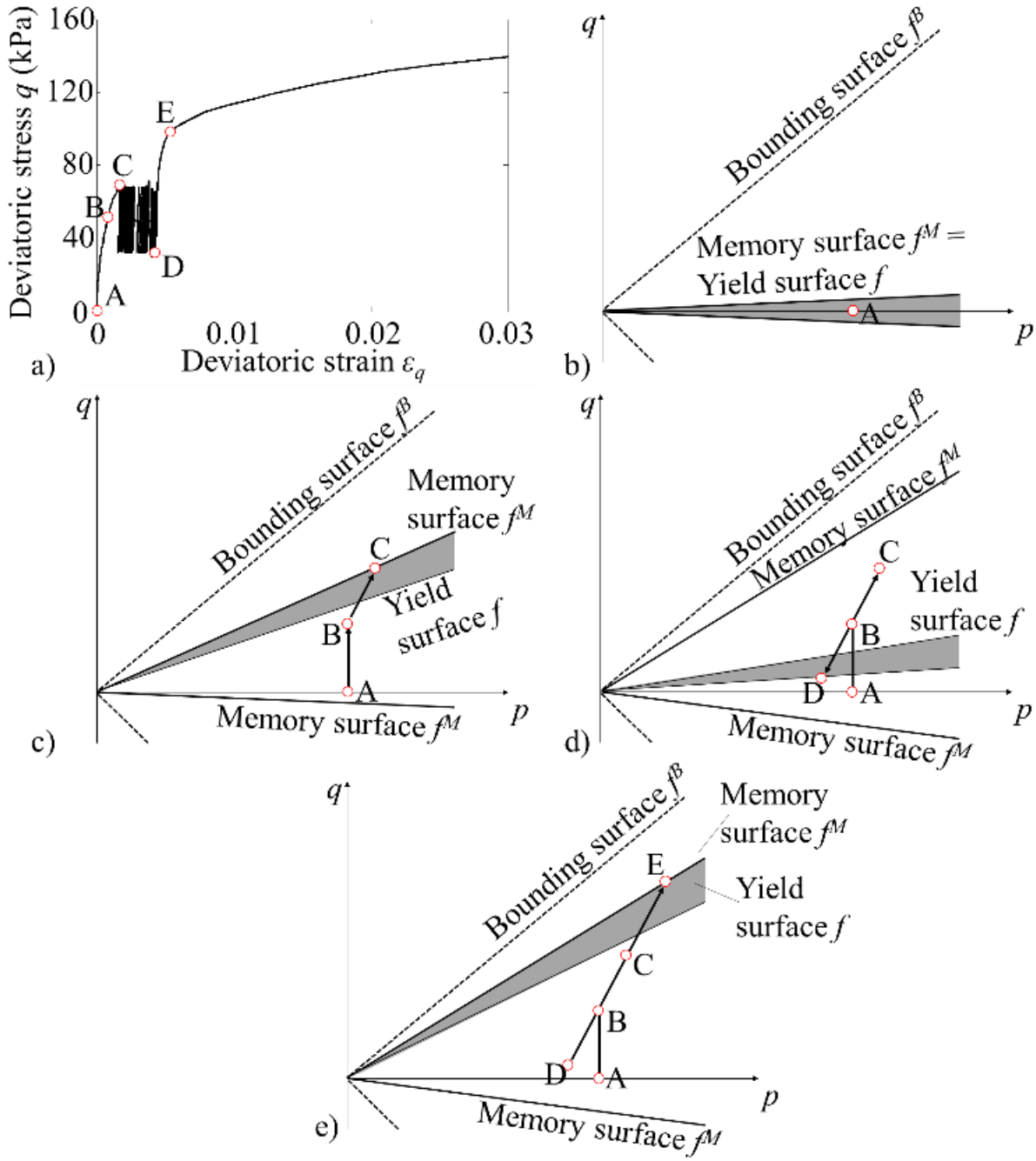

Figure 3.4: Evolution of memory surface during drained cyclic triaxial testing followed by monotonic shearing (After Corti and Diambra, 2017) (a) experimental stress-strain response; (b) initial stress state before loading; c) memory surface expands during initial loading; (d) evolution under cyclic loading; (e) final state during monotonic reloading.

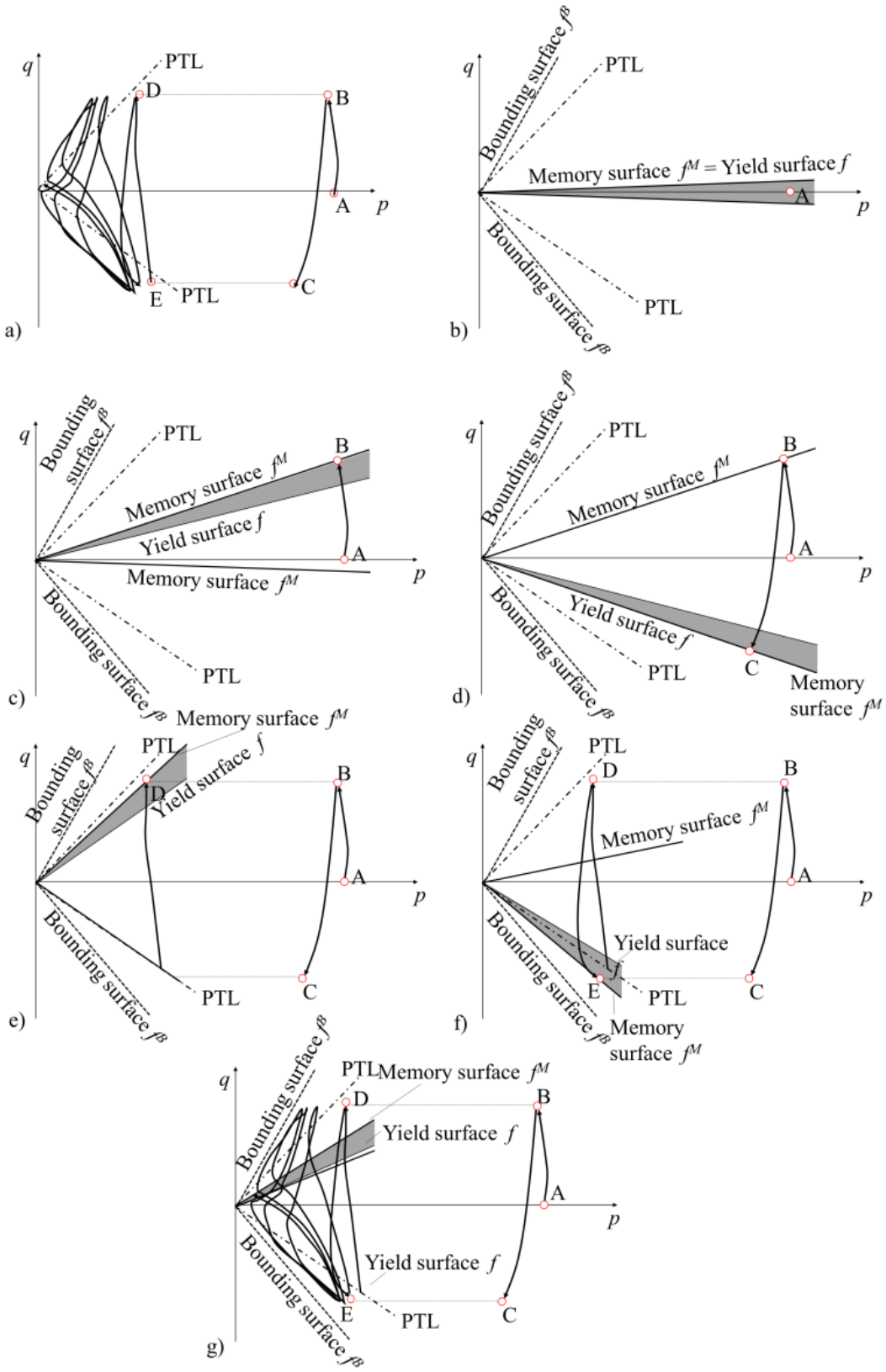

Figure 3.5: Memory surface evolution for dense sand under undrained cyclic loading (After Corti and Diambra, 2017). (a) experimental stress path (Zhang et al., 2011); (b) model response before shearing; (c) first loading path; (d) stress reversal; e) state prior to crossing the Phase Transformation Line (PTL); (f) surface contraction due to dilative strains; (g) configuration under cyclic mobility.

The hardening modulus h_m, is given by:

$$h_m = a_m exp\left(-\left(\frac{b^M}{b_{ref}} f_e + \mu_0\right)^{-h_1}\right) - a_m exp\left(-(\mu_0)^{-h_1}\right) \quad 34$$

Where a_m is a material constant that scales the memory surface hardening modulus, b^M represents a stress-related variable or an internal state variable that influences the hardening modulus with a reference value of b_{ref} which ensures the dimensional consistency. b^M can be related to the magnitude of cyclic stress or strain applied to the material; f_e is a scaling factor that modulates the plastic strain, and it can be described by:

$$f_e = 10^4 \left(tanh\left(\mu_1(\chi^p - \mathcal{T})\right) + 1\right) + 1 \quad 35$$

Here, χ^p is the plastic strain hardening modulus. The *tanh* function is used to smooth the transition as the plastic strain accumulates, ensuring that the scaling effect is gradual. The parameter $\mathcal{T}$ is a threshold that influences the behaviour of the model under cyclic loading.

$$\mathcal{T} = j_0 exp\left(j_1 \left(\frac{|q|^r_{max}}{q_{ref}}\right) + j_2 e - j_3 \left(\frac{p'_{ave,0}}{p_a}\right) + j_4 |M_c - \eta_0^{ave}|\right) \quad 36$$

Where $|q|^r_{max}$ is maximum deviatoric stress, $p'_{ave,0}$ is average mean effective stress, η_0^{ave} is average stress ratio, j_0, j_1, j_2, j_3 and j_4, are model fitting parameters. This threshold helps in determining when the model should transition between different states, such as from shakedown to ratcheting.

3.4.2 Semifluidised State

The semifluidised (Sf) state is a critical concept in the constitutive modelling of sands under cyclic loading, particularly in understanding and predicting soil behaviour during and after liquefaction events. The evolution of this concept has been driven by the need to accurately simulate the transition of soil from a solid-like to a fluid-like behaviour, which occurs when

the mean effective stress in the soil reduces significantly, leading to a loss of intergranular contacts. The semifluidised state factor can be described using semifluidised state factor f^*_{semi} representing the degree to which the soil has transitioned into the semifluidised state. It quantifies the reduction in soil stiffness and resistance to deformation as the soil approaches a fluid-like behaviour. It is given by:

$$f^*_{semi} = (1 - \langle 1 - p_r \rangle)^{x\mathcal{L}\sqrt{l_{semi}}} \quad 37$$

Where p_r is a pressure ratio defined as $p_r = \frac{p}{p_{th}}$ and p_{th} is threshold pressure that can be physically interpreted as the stress level at which the soil structure is no longer able to maintain its solid framework due to insufficient interparticle contact forces. x is a material parameter that controls the rate of evolution of the Sf state. l_{semi} is semifluidisation state variable based on loading history; $\mathcal{L}$ is the loading index and is given by:

$$\mathcal{L} = g(\theta, c)^{n_g(1-l_{semi})} \quad 38$$

Here $g(\theta, c)$ represents the stress state, where $\mathcal{L}$, is a measure of the deviatoric stress and c represents a material specific fitting constant. n_g is a material parameter that controls the nonlinearity of the loading index's dependence on the semifluidisation state variable, l_{semi}. The differential change in the semifluidisation state variable can be given by:

$$dl_{semi} = \langle d\lambda \rangle [c_l \langle 1 - p_r \rangle (1 - l_{semi})^{n_l}] - c_r l_{semi} |d\varepsilon_v| \quad 39$$

Where $d\lambda$ is a measure of plastic loading increment, c_l is a material constant that scales the rate of evolution of Sf state during plastic loading, and n_l is a parameter that controls the nonlinearity of the evolution of the Sf state.

3.5 Numerical Implementation of the Model

The model is constructed with a stress integration scheme that employs the bounding surface plasticity framework. For predictions of monotonic tests paths the model uses a loading surface

construction which enables the plastic modulus, hardening laws and loading directions to be determined. For the prediction of tests with cyclic loading, the memory surface and Sf state concepts are employed along with the kinematic hardening laws mentioned in the above sections. To ensure the accuracy of the integration, the method includes an error control mechanism that adjusts the step size during the integration process. If the error exceeds a specified tolerance, the step size is reduced, and the integration is retried. The integration scheme includes mechanisms to ensure smooth transitions between different states, such as switching between isotropic and kinematic hardening. An activation function is used to manage these transitions, preventing abrupt changes that could destabilize the numerical simulation. For the sake of efficiency, the monotonic tests (both saturated and unsaturated) are simulated with the original model (Ghorbani and Airey, 2021) and the cyclic tests are simulated with the enhanced model (Chen et al, 2024) which is has been modified to capture the complex cyclic responses of soil.

3.6 Experiments for Calibration

In the original model, a total of 36 input parameters are utilized, comprising 18 material parameters, 8 initial test values, and 10 error control parameters that remain largely constant across all tests. The revised model introduces an additional 11 material parameters for stress overshooting, memory surface, and semifluidised state modules, bringing the total to 49 parameters. Of these, 34 are material parameters, as shown in Table 3.1. Among these material parameters, 11 are directly derived from experimental results, 21 parameters are determined through curve fitting with their corresponding equations and compared with simulation results, 2 are established using a trial-and-error method within a fixed range.

To calibrate the model, a series of experiments must be conducted. The yield surface and isotropic hardening parameters can be calibrated through the Normal Compression Line (NCL), which is plotted from 1-D compression tests at high-stress states. The Critical State

Line (CSL) requires multiple triaxial tests at varying void ratios and pre-consolidation stresses, performed under both drained and undrained conditions. Kinematic hardening parameters are calibrated using results from undrained monotonic triaxial tests. Soil-Water Characteristic Curve (SWCC) parameters are obtained by comparing experimental SWCC results, specifically using the Hyprop device in this study. Stress overshooting and memory surface parameters are derived from drained cyclic triaxial tests, focusing on cycles at high-stress states. Semifluidised state parameters are calibrated using undrained cyclic triaxial tests where soil liquefaction has occurred. A detailed explanation of the calibration procedures and techniques using experimental data is provided in Chapter 5.

Table 3.1: Model parameters with associated equations and experiments

Description	Associated formulation	Model Parameters	Experiments required
Elasticity	$G = G_0 p_a \left(\frac{p'}{p_a}\right)^{\frac{1}{2}} \frac{(2.97-e)^2}{1+e}$	G_0	Drained triaxial test
	$K = K_0 p_a \left(\frac{p'}{p_a}\right)^{\frac{1}{2}} \left(\frac{1+e}{e}\right)^{\frac{2}{3}}$		
	$K_0 = -3 \frac{\left(p_2'^{\frac{1}{3}} - p_1'^{\frac{1}{3}}\right)}{p_a^{\frac{1}{3}}(ln\, e_2 - ln\, e_1)}$	K_0	Isotropic compression test
Kinematic Hardening	$M^b = M\ exp\ \langle -n^b \psi \rangle$	n^b	Drained and undrained triaxial tests
	$h = h_0 G_0 (1 - c_h e) \left(\frac{p'}{p_a}\right)^{-\frac{1}{2}} \frac{1}{\lvert n_\sigma - \eta_\sigma^{in} \rvert^{\zeta'}}$	c_h, h_0	Trial and error
Dilatancy	$M^d = M\ exp(n^d \psi)$	n^d	Drained and undrained triaxial tests
	$D = \frac{d\epsilon_v^p}{d\epsilon_q^p} = L A_d (M^d - \eta_\sigma)$	A_d	Drained triaxial test
	$A(z)\left(-d\epsilon_v^p\right) = -c_z(-d\epsilon_v^p)(z_{max} L + z)$	c_z, z_{max}	Unloading stage of triaxial test or cyclic triaxial test
	$ln\, e = ln\, N_l - \lambda\, ln\, p'$	N_l, λ	Compression tests at high stress levels
Critical State	$ln\, e = ln\, N_c - \lambda\, ln(p_c{}' + \alpha_{csl})$	N_c, λ, α_{csl}	A series of drained and undrained triaxial tests
	$M = \frac{6 \sin \phi'_{cs}}{3 - \sin \phi'_{cs}}$; $c = \frac{M_c}{M_e}$	M, c	A series of drained and undrained triaxial tests

	$h_m = a_m exp\left(-\left(\frac{b^M}{b_{ref}} f_e + \mu_0\right)^{-h_1}\right) - a_m exp\left(-(\mu_0)^{-h_1}\right)$	$\mu_0, h_1, a_0, a_1, a_2$	A series of drained cyclic tests at different void ratios
Memory Surface	$\mathcal{T} = j_0 exp\left(j_1\left(\frac{\lvert q\rvert^r_{max}}{q_{ref}}\right) + j_2 e - j_3\left(\frac{p'_{ave,0}}{p_a}\right) + j_4\lvert M_c - \eta_0^{ave}\rvert\right)$	j_0, j_1, j_2, j_3, j_4	A series of drained cyclic tests at different void ratios
Semifluidised state	$f^*_{semi} = (1 - \langle 1 - p_r\rangle)^{x\mathcal{L}\sqrt{l_{semi}}}$	x	Sensitivity analysis simulating drained cyclic tests
	$\mathcal{L} = g(\theta, c)^{n_g(1-l_{semi})}$	n_g	Undrained cyclic test with data of post-liquefaction
	$dl_{semi} = \langle d\lambda\rangle[c_l\langle 1 - p_r\rangle(1 - l_{semi})^{n_l}] - c_r l_{semi}\lvert d\varepsilon_v\rvert$	n_l, c_l, c_r	Sensitivity analysis simulating drained cyclic tests

The model calibration process involves a comprehensive series of tests across a diverse range of soils, including sand with fines contents varying from 0% to 60% and a well graded gravely sand with fines contents varying from 18% to 60% as detailed in Chapter 3. While Kwa (2019) and Mohammadi (2020) previously conducted tests on some of these soils (SS0F, WGS18F, WGS28F, WGS40F, and WGS60F) during their respective PhD studies, the current research has implemented an extensive set of new tests, complementing and extending the existing data. This comprehensive approach has been designed to produce a robust dataset consisting of monotonic, cyclic, saturated, unsaturated, drained, and undrained tests for model calibration and validation. The subsequent chapter provides an analysis of the experimental results obtained from both calibration and validation tests.

Chapter 4
Experimental setup and apparatus configuration

4.1 Introduction

This chapter presents the materials, apparatus, and methods used to examine sand's mechanical behaviour. It presents the experimental plan, explaining the selection and properties of materials used and the testing procedures for the series of experiments conducted. Attention is given to the reasoning behind the choice of apparatus, highlighting significant adjustments made to the conventional setup to suit the specific requirements of this research. This section presents the experimental plan and its implementation, ensuring that the results are accurate, thus establishing a solid groundwork for the findings presented in subsequent chapters.

As discussed in the previous chapter, the experimental plan includes 1-D compression tests, triaxial tests, and tests to establish the SWCC of the various materials. Tests for general characterisation of the materials were also performed. Sydney Sand with non-plastic fines contents from 0-60% have been tested in the triaxial apparatus under a range of consolidation pressures till large deformations to identify the critical state in both drained and undrained conditions for material characterisation. To explore the versatility of the constitutive model, a Well Graded Soil (WGS) investigated in Kwa (2019) with different grain shapes and particle size distributions has also been tested. Limited tests on WGS were performed to complement the triaxial test results reported by Kwa (2019). For all soil gradings, cyclic tests were conducted during which several cycles were applied before shearing monotonically to failure at large strains. Monotonic and cyclic unsaturated tests were also conducted on all 8 gradations to study the effect of the degree of saturation. Brief statements on calibration, repeatability, and measurement uncertainty are provided at the end of each test methodology to document data reliability.

4.2 Materials

A variety of non-plastic silty sands were studied in this research. These were manufactured by mixing Sydney Sand and feldspar fines in various proportions and by mixing basalt aggregates and feldspar fines to create a range of well graded soils. The natural Sydney sand is classified as SP in the Unified System, which is uniform in grain size and poorly graded. Several researchers have studied Sydney sand, and extensive triaxial data is available (Rahman & Lo, 2007; Kwa, 2019; Mohammadi, 2019). However, due to the natural material being sourced from different locations with slight variations in particle characteristics, parameters such as those describing the position of the critical state line are not consistent. Feldspar fines were added to Sydney Sand at different percentages (i.e., 20, 40, and 60%) to study the influence of fines. The particle size distributions of the various grades are shown in Figure 4.1 and the mixture properties are listed in Table 4.1. The WGS is a reconstituted well graded soil mixture comprised of basalt aggregates and feldspar fines at different percentages (i.e., 18, 28, 40, and 60%). The basalt aggregates are angular with moderate sphericity and particle sizes ranging between 9.5mm to 0.15mm. The grading curves for the WGS mixtures are shown in Figure 4.2 and their properties are listed in Table 4.1. The feldspar fines used in this study comprises of 60% plagioclase-Orthoclase feldspar and 10-30% albite and are of sub-rounded, moderate sphericity.

Soil properties were determined using Australian Standards (AS) or ASTM standards wherever suitable. While determining the minimum and maximum dry density of soils, AS 1289.5.5.1 recommends that the fines content (percentage passing the 0.075 mm sieve) should not exceed 12%, to maintain the validity of the method for cohesionless materials. Similarly, ASTM D7382-20 is applicable primarily to cohesionless soils, and for soils containing more than 15% fines, it suggests using impact compaction methods instead, such as those specified in other ASTM standards (e.g., D698 or D1557). In this study, the proportion of fines in most samples

exceeded these recommended limits. However, the tests were conducted using the standard vibratory or placement methods to provide indicative values of minimum and maximum dry density.

The rationale for using vibratory methods despite exceeding the fines thresholds lies in the consistency and research-oriented purpose of the study. Standards typically limit fines content in vibratory compaction to reduce the risk of fines segregation and ensure uniformity. To mitigate these concerns, samples were carefully placed in multiple layers, and compaction was applied incrementally before placing the dead weight. Particular attention was paid to avoiding segregation during placement, and post-test inspection confirmed that no segregation or layering of fines occurred. This sample preparation procedure was kept consistent across all tests, including triaxial and oedometer samples to ensure reproducibility.

These results were not used for specification compliance but to allow comparison across different gradations and fines contents within a consistent testing framework. The intention was to study trends in relative density and cyclic response with varying fines, rather than to achieve absolute compliance with compaction criteria. Therefore, the use of vibratory methods was considered acceptable for comparative and research purposes, and repeatable outcomes were confirmed through controlled preparation and post-test observations. Because of this reason, the relative density value more than one is possible.

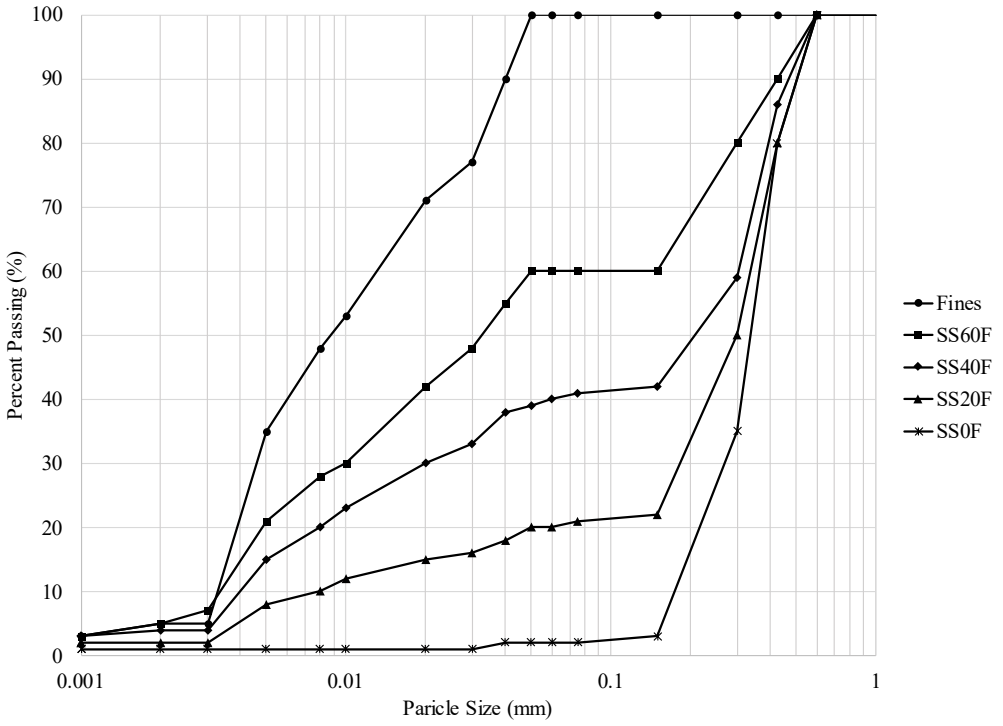

Figure 4.1: Particle Size Distribution of Sydney Sand, Fines and Sydney Sand with Fines

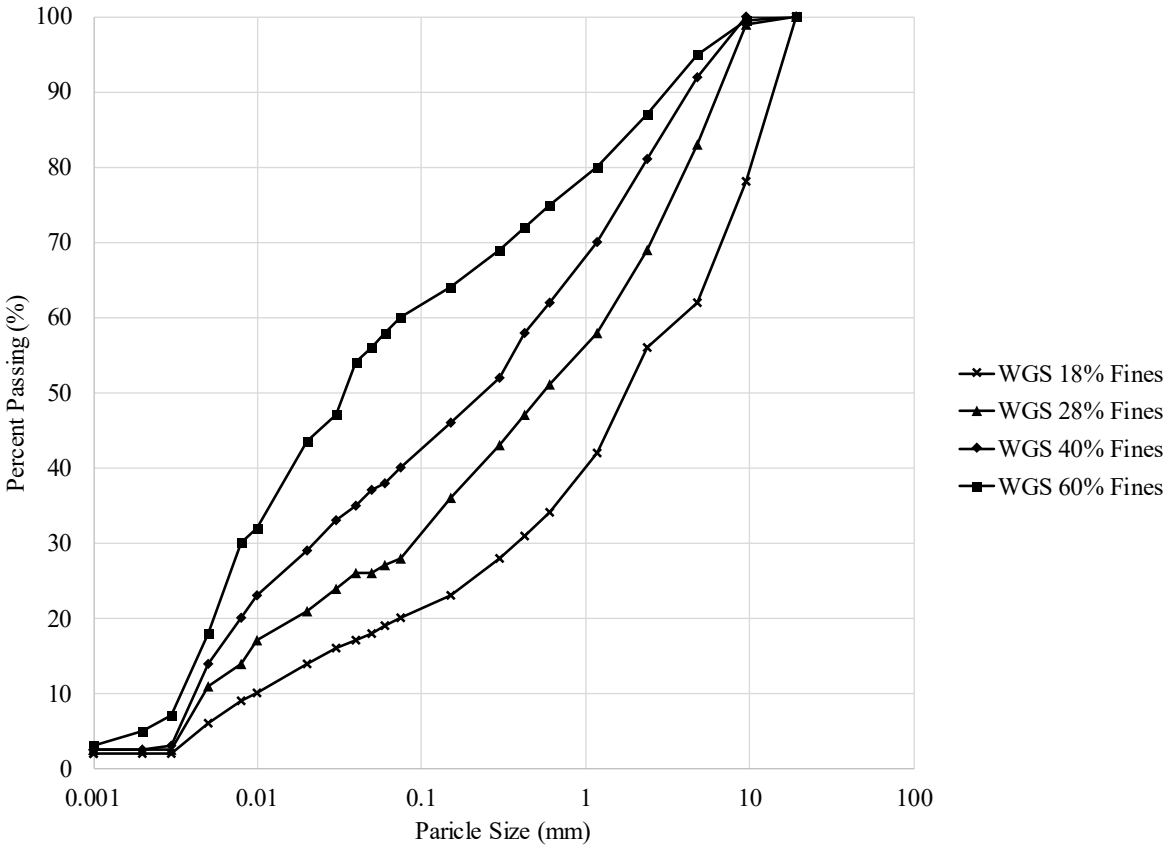

Figure 4.2: Particle Size Distribution of WGS soil with fines.

Table 4.1 General soil characteristics

S.no	Description	SS0F	SS20F	SS40F	SS60F	Felspar Fines	WGS18F	WGS28F	WGS40F	WGS60F
1	Mean grain size, D_{50} (mm)	0.342	0.3	0.221	0.033	0.01	1.837	0.556	0.25	0.034
2	Coefficient of curvature, C_c	1.132	1.772	0.321	0.348	0.470	3.717	1.323	0.231	0.241
3	Coefficient of uniformity, C_u	1.335	13.607	15.232	8.375	2.976	10.313	14.875	22.778	9.375
4	Specific gravity, G_s	2.650	2.633	2.617	2.601	2.57	2.87	2.83	2.8	2.66
5	Minimum void ratio, e_{min}	0.574	0.482	0.66	0.698	1.086	0.350	0.392	0.470	0.570
6	Maximum void ratio, e_{max}	0.85	0.740	0.97	1.14	2.330	0.630	0.748	0.775	0.830

4.3 One-dimensional Compression Tests

The one-dimensional compression tests were conducted to establish the limiting compression curves, which necessitate loading at stress states up to 50 MPa. However, conventional oedometers and lever arm oedometers are limited to a maximum load capacity of 10 kN. Even when using the smallest standard sample size of 38 mm diameter, this corresponds to a maximum theoretical vertical stress of approximately 8.8 MPa. In practical testing conditions, however, due to mechanical and calibration constraints, stress levels are often limited to around 2 MPa to maintain measurement reliability and avoid frame deformation. Therefore, to achieve the required higher stress levels approaching 50 MPa, modifications to the testing apparatus were necessary.

4.3.1 Modified Oedometer

The conventional consolidation cell used in this study was mounted on a Wykeham Farrance Tritech loading frame with a capacity of 100kN, equipped with a designated loading ram. The consolidation cell consists of a stainless-steel confining ring, measuring 10mm in thickness, a top platen, two porous discs, and a steel container base designed to hold water. The schematic diagram of the standard oedometer consolidation cell is shown in Figure 4.4, while the modified apparatus is illustrated in Figure 4.3.

The use of a 50 mm diameter sample allows vertical stresses of up to approximately 50.9 MPa to be achieved under a maximum load of 100 kN, based on the stress equation $\sigma = P/A$. The high-capacity loading frame, in conjunction with a rigid frame design, ensured minimal deformation or compliance during loading.

Prior to testing, calibration was performed to verify system reliability. The 100 kN load cell was checked against reference weights, and the Linear Variable Differential Transformer (LVDT) was calibrated using a micrometer stage to confirm accuracy in displacement

measurements. The frame deflection under maximum load was found to be negligible. Additionally, two tests were repeated for Sydney Sand to confirm the repeatability and consistency of the compression curves, particularly at high stress levels.

4.3.2 Testing Methodology

All tests were conducted on samples with a diameter of 50 mm and an initial height of 34 mm. Although the diameter-to-height ratio does not meet the recommended value of 4 according to ASTM-D2435M-11, the mandatory minimum height and diameter requirements relative to the maximum particle size were satisfied. Regardless of the soil type, the material was oven-dried and placed loosely in the oedometer consolidation ring, with Whatman filter paper (10 μm thickness) and brass porous discs at both the top and bottom of the specimen. A specially designed top platen with a groove for a steel ball was positioned over the sample to align the loading ram with the steel ball. Axial deformation was measured using a Linear Variable Differential Transformer (LVDT). The loading frame operated at a speed of 0.05 mm/min during loading and 0.005 mm/min during unloading. Vertical load and axial deformation data were recorded every 30 seconds using computer software. Load was increased to the maximum of 100 kN, before unloading to zero. Compression curves were then generated, plotting vertical effective stress against void ratio.

While the modified oedometer allowed for the application of vertical stresses up to ~50 MPa, enabling the derivation of the Limiting Compression Curve (LCC), it is important to recognise potential limitations in interpreting results at very high stress levels. At such stress magnitudes, particle crushing becomes inevitable, particularly for the more angular sand grains and those containing weaker mineral constituents. This crushing can artificially increase measured compressibility because the reduction in void ratio reflects both mechanical rearrangement of the soil skeleton and the creation of new fines. These limitations were considered when interpreting the LCC slopes and comparing compressibility parameters between materials.

Load cell and LVDT calibrations were checked before each test series; repeat Sydney Sand runs confirmed curve repeatability at high stress. Across runs, LVDT repeatability was within ±0.002 mm and load within ±0.3% of full scale, giving an estimated uncertainty in e of ±0.005 at peak load.

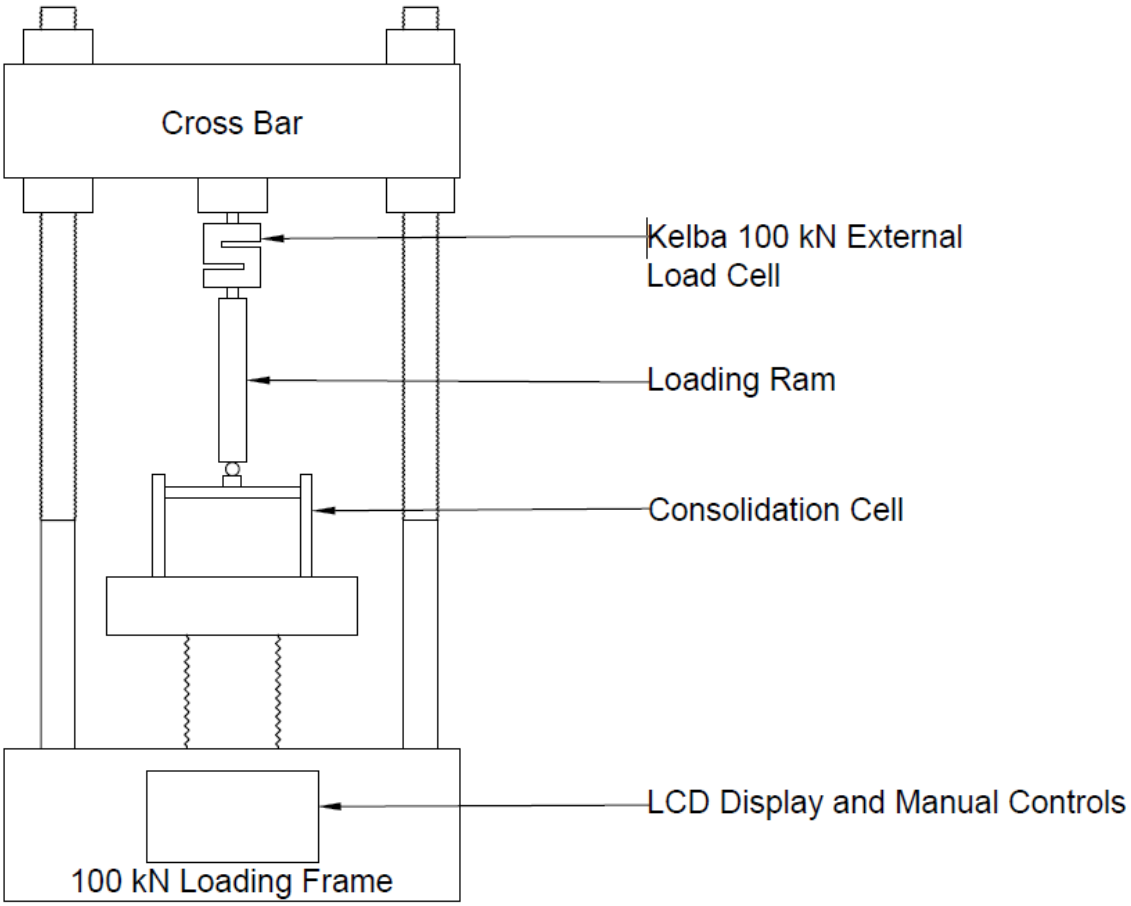

Figure 4.3: Scheme of Modified Oedometer Apparatus

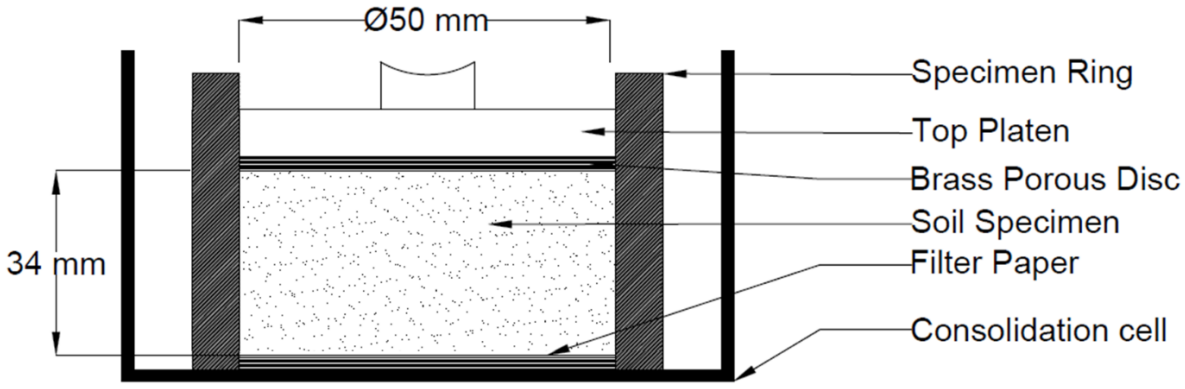

Figure 4.4: Oedometer - Consolidation Cell

4.4 Triaxial Apparatus

4.4.1 Apparatus Assembly

Figure 4.5 shows a schematic diagram of the triaxial apparatus. Tests have been performed on samples with minimum size of 50 mm and 100 mm in triaxial cells of 1.8 MPa cell pressure capacity. The sample is loaded by a ram fitted with a VJ Tech submersible 25kN load cell to measure the deviator load on the sample. The triaxial cell is mounted in a 50kN Wykeham Farrance Tritech loading frame to compress the sample using a bottom drive motor at various speeds per the sample's requirement. The setup is complemented by a Kelba 25kN external load cell attached to the crossbar which is provided in case the internal submersible load cell fails. The water is filled into the cell using a pressure-aided water bottle, and further pressure is maintained using a GDS Digital Pressure Volume Controller with a 2MPa capacity.

All load cells and pressure transducers used in the triaxial system were calibrated prior to testing using standard calibration procedures or reference pressure devices. The VJ Tech 25 kN submersible load cell and the Kelba external load cell were cross validated during trial loading, confirming deviation within ±0.5%. LVDTs were checked against micrometer stages, and all transducers (cell pressure, pore pressure, and volume change) were tested for drift and zero error.

Data reliability was further ensured through real-time monitoring using TRIAX software, which flagged any deviation beyond set thresholds in load or pressure data.

The triaxial base has been modified in-house to accommodate instrumentation and provide space for additional ports for cables. One outlet from the sample base is connected to a Druck 2MPa pore pressure transducer filled with water to measure the pore water pressure inside the sample. Another outlet from the sample base and the sample top plate are connected to a 2MPa GDS Digital Pressure Volume Controller to control the back pressure and measure volume change in the samples. The volume change is measured by the porewater volume displaced out

of the sample. These GDS controllers are filled with distilled water before each test being careful to minimise trapped air and maintained at 21±2℃ to minimise the thermal expansion of the metal containers and the water.

The axial displacement of the soil sample is measured using two external LVDTs. One with a range of about 30mm and accuracy of ±0.001mm, and the other with an extended range of about 100mm and accuracy of 0.01mm to ensure no loss of data at large displacements.

The instrumentation is monitored by a combined data acquisition setup connected to the computer and controlled by a software program called TRIAX. This program was written at the Soil Mechanics laboratory at the University of Sydney and has undergone several user modifications over the years. The software can control the pressure controllers, loading frame, and reading rates at all the test stages. The working of the software and testing procedure are explained in further sections.

4.4.2 Tests Performed and label

Test labels are given to distinguish the tests. The scheme used the first letter to denote whether the test is Monotonic (M) or cyclic (C), the second letter to denote Saturated (S) or unsaturated (U), the third letter to denote the drainage condition (D - Drained & U - Undrained) followed by a two/three letter code for material (SS - Sydney Sand & WGS - Well Graded Soil) separated by an underscore "_", followed by numerical with suffix F for percentage fines mixed in the soil followed by consolidation stress in numbers and finally a letter to denote its initial density (L- Loose, M-Medium, and D-Dense). For instance, MSD_SS0F100L denotes Loose Sydney sand with 0% fines tested in a saturated drained condition under Monotonic loading with consolidation stress of 100kPa.

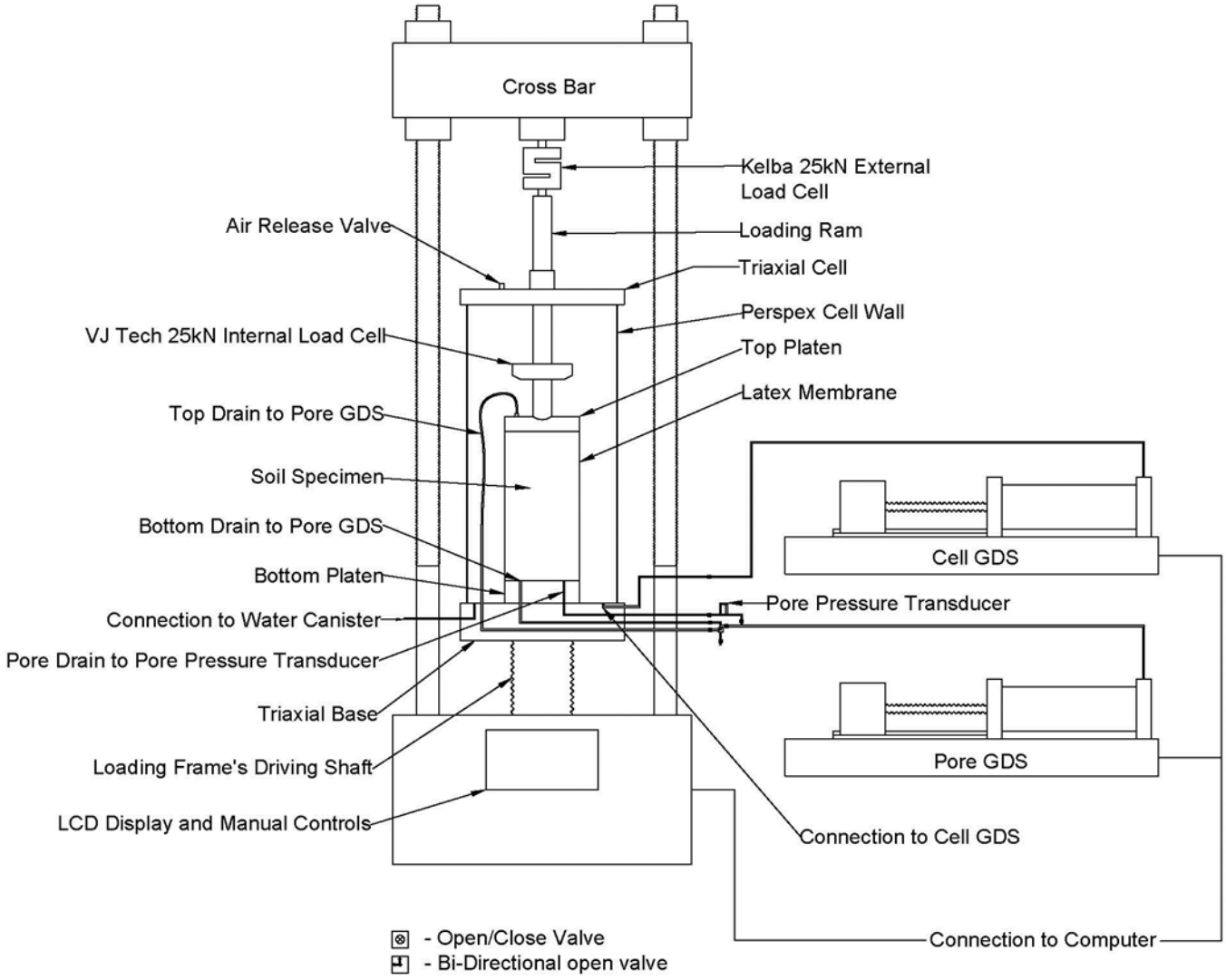

Figure 4.5: Scheme of Triaxial Apparatus used

4.4.3 Sample preparation and Saturation

The saturated tests were conducted with samples of two sizes. The majority of Sydney sand and Sydney sand with various percent of fines were prepared with dimensions of 55mm diameter and 110mm height with a 0.2mm thick latex membrane, whereas all the WGS specimens and some sand specimens were prepared with dimensions of 100mm diameter and 200mm height cylindrical samples with a 0.6mm thick latex membrane. Different sizes have been used because smaller samples are easier to assemble and disassemble and take less time to saturate and consolidate, however, bigger samples are required for WGS because to meet particle size consideration. The maximum diameter of the grains is 9.5mm, and by using a

diameter of 100mm a D/d_{max} of >6 could be achieved satisfying standard requirements (ASTM D4767 and ASTM D5311). Here D is the diameter of the specimen and d_{max} is the diameter of largest particle in the soil. 100mm diameter samples were also used for unsaturated tests as this minimised the volume of water in the cell which reduced errors in volume changes, discussed further below.

The latex membrane is placed over the triaxial base, sealed, and fastened with two O-rings over them. A split mould was placed around the sample and the membrane held to this using a vacuum. After placing a porous disc and a Whatman filter paper of 10 μm, a uniform mixture of soil with 2-5% moisture by weight is filled in 10-12 layers. Each layer is compacted gently using a tamping bar (25mm diameter and 100mm height) for 55mm samples and a compaction hammer (type-D) as in Modified Proctor Fagerberg Test (Dayal, 2017) for the 100 mm samples. The dry density of the sample was controlled by tamping each layer uniformly as per requirement. The soil surface was filled flat and capped with a filter paper, porous disc, and top platen. Then, the membrane was stretched over the top platen and sealed with two O-rings. The top drain is now connected to the top platen, and a maximum suction of 20 kPa was applied to the sample. The split mould was removed and then the soil specimen's dimensions were measured. Even though the soil was filled into an expanded membrane of the same internal diameter as the sample, the measured diameter was always less than this because of the membrane's elasticity and the finite soil stiffness.

Then the cell was assembled, being careful to ensure the specimen alignment. The Cell was filled with water and a cell pressure of 20kPa was applied. Water flush was used to displace air until no further air bubbles were observed meanwhile the sample height was monitored for axial displacement. The sample was saturated by ramping the back pressure to between 500 and 1000 kPa at the rate of 5 kPa per minute to dissolve any trapped air. The sample was held at high pressure until Skempton's B value (Skempton, 1954) of 0.98 or above was achieved.

For initially dense samples the B value didn't increase above 0.95 even after waiting for 12 hours. If the rate of volume change was less than 10mm^3/minute, then the soil was considered to be saturated as also suggested in ASTM D5311. To confirm repeatability, a limited number of duplicate samples were tested under similar initial conditions. The resulting stress-strain and pore pressure responses showed consistent trends, confirming procedural reproducibility in sample preparation and loading.

4.4.4 Consolidation and Shearing

Consolidation and Shearing stages in the TRIAX software are controlled by segments that the user can define. According to the segment values the software can control the Cell pressure, Pore pressure and the loading frame. Before starting the consolidation, the drainage condition, motor speed and save intervals with respect to axial load, axial strain, change in pressure and elapsed time are defined. The principal stresses (σ_1 and σ_3) were simultaneously ramped up to the target mean effective stresses at the rate of maximum 5kPa/minute and the loading frame was set at the speed of 0.05mm/minute. Feedback from the loadcell was used to turn the motor on or off to achieve the intended stress. The sample can be consolidated either isotropically or anisotropically at any stress state up to the maximum cell pressure of 1.8MPa, which is the maximum capacity of the cell. Once the target consolidation stress was reached, the pressures were held until the deformation rate reduced to zero. This usually required a wait of 1 hour for dense samples and 2-3 hours for loose samples.

After consolidation, the segments can be used to shear the sample. Drainage and loading can be chosen at this stage. Both drained and undrained tests have been performed on saturated soils. The top and bottom pore drain taps are closed for undrained tests and left open for drained tests. Shearing by monotonic loading is achieved by driving the triaxial base up at 0.05mm per minute (maximum shearing rate - 0.05% of specimen height per minute as mentioned in ASTM standards D4767-11). For the undrained tests, the speed should be maintained at a maximum

of 2% of specimen height per hour, so there is enough time for the pore pressure to equilibrate throughout the sample. Simultaneously, the pore pressure in the sample is monitored by the pore pressure transducer connected to the base of the sample. For drained tests, the volume change is monitored by the pressure-volume controller during the test. Calculated strains are determined using the inverse calculation method with axial strain, which is explained later in this chapter.

For cyclic tests, regardless of the drainage condition, the TRIAX program is set up to loop through 40 stress states as shown in Figure 4.6 (Segment 2 to 41), which completes a cycle. During cycles, the cell pressure is constant, typically equal to consolidation stress, and the axial stress σ_1, is varied. The target σ_1 for each segment and the required time to achieve the stress are entered into the program. If the target stress is not achieved within the entered time, the software is set to wait until the stress is achieved, up to a specific limit. In each segment, the software commands the loading frame to move up or down to increase or decrease the stress respectively. For most of the cyclic tests, samples were sheared at maximum speed of 0.5mm/minute to ensure that the loading rates were sufficient to achieve the target segment values in the specified time. For the tests on loose specimens, those with void ratios close to e_{max}, this loading rate was too fast to maintain the defined frequency (usually between 0.002 Hz and 0.004 Hz) and led to overshooting and noisy response. For such samples, the loading rate was reduced as slow as 0.1mm/minute to maintain reasonable waveform of the cycle.

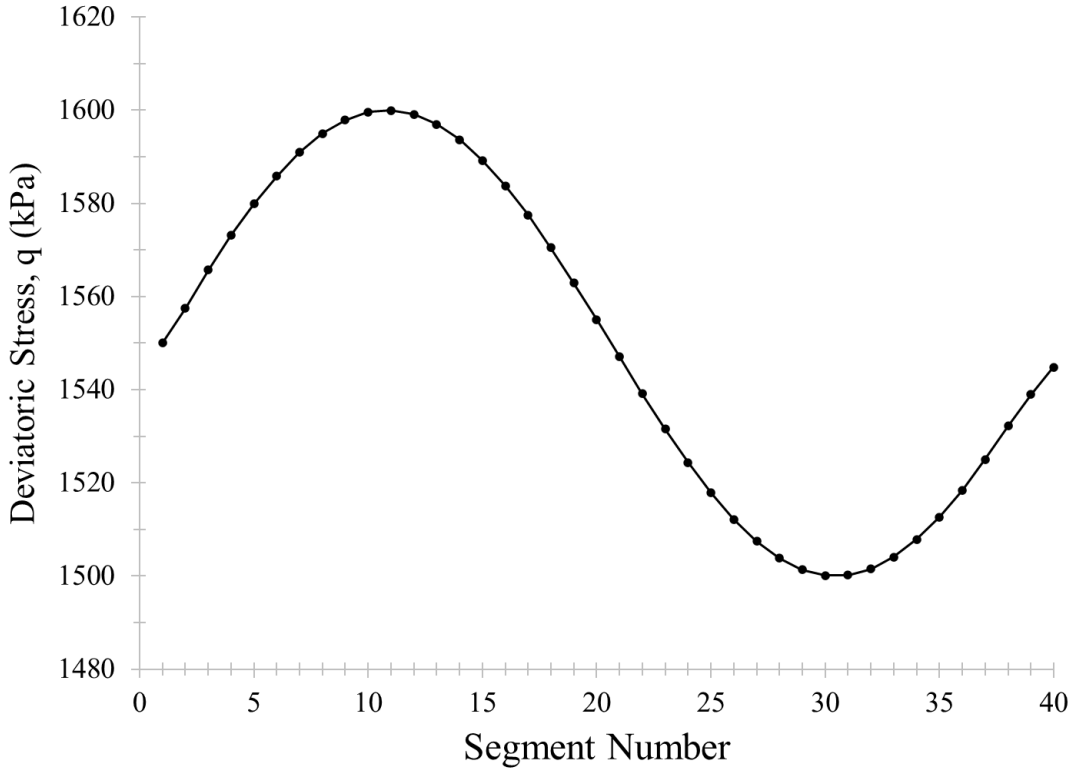

Figure 4.6: Cyclic load - Segment increments for one period.

The cycle loops were ended manually when the axial strain was more than 0.05 for a single cycle. Then, the amplitude was increased for next set of cycles, or the sample was allowed to fail monotonically at a constant strain rate until large strains of more than 20% were reached and the critical state attained. Once the test was completed, the drainage taps were closed until the cell pressure was reduced and the cell was removed. The moisture content of the soil was measured carefully, by securing the entire soil mass from the latex membrane. This moisture content is used to verify the measured volume change during the test.

4.4.5 Calculation of Sample Volume and its Validation

To calculate how the sample volume changed during the test and to verify the moisture content, a step-by-step method was used starting from the end of the test. An estimated value close to the final sample volume was assumed for the last step. From there, the volume at each previous

step was calculated by subtracting the change in pore water volume between steps. This was done using the formula:

(Volume at current step = Volume at next step – (Pore volume change at next step – Pore volume change at current step).

By repeating this calculation backward from the last step to the first, the sample volume was determined for every stage of the test. However, since the initial guess may not be perfect, there can be a constant error (or offset) throughout the values. This offset was corrected by comparing the calculated volume at the first step with the actual initial sample volume, which was determined from the sample's original dimensions. The final volume values were then adjusted to ensure the calculated starting volume matched the real one.

Using the corrected volume and the measured sample height at each step, the sample diameter was calculated. With this information, the void ratio and moisture content were computed using the known specific gravity and dry mass of the soil. Finally, the moisture content calculated at the end of the test was compared with the moisture content obtained from oven-drying the sample. For unsaturated tests, the sample was divided into four equal parts, two from the top half and two from the bottom half, and the moisture content of each part was measured. This approach ensured the uniformity of moisture distribution within the specimen could be checked and further confirmed the accuracy of the calculation.

4.5 Unsaturated Triaxial Apparatus

The conventional triaxial setup was modified to perform unsaturated tests by fitting a high-air-entry porous disc (HAEPD) at the bottom and an additional pore air pressure transducer at the top drain. This assembly is similar to the apparatus described in Fredlund and Rahardjo (1993), except for its inability to measure and regulate the air pressure. The test procedure and measurement of pore pressures are explained in further sections.

4.5.1 HAEPD and Sample Base

The function of HAEPD is to prevent airflow from the sample to the GDS pressure controller (Pore GDS) used to regulate pore water pressure. It is a ceramic disc of small pores that allows only water to pass through under normal testing conditions, and air can only penetrate the disc at pressure exceeding approximately 3000 kPa, provided the disc remains fully saturated (typically achieved with a pore size corresponding to 1.5–2 μm). The 80mm diameter HAEPD is sealed into a 100mm triaxial pedestal with a set of O-rings, as shown in the Figure 4.7. The pedestal has a spiral groove on the top where the HAEPD is placed to better measure the pore water pressure of the sample. As the disc is relatively impermeable, the sample's pore pressure measurement can be affected even with the groove. This potential discrepancy was investigated in detail for the current test setup by Kwa (2019), who found that the measurement error introduced by the HAEPD under the adopted test conditions is typically within 1–2 kPa, which is negligible compared to the applied pore pressures during tests.

Water pressure is regulated at the base of the specimen using a GDS pore pressure controller connected to the base of the pedestal. This controller allows for the application and measurement of pore water pressure during saturated and unsaturated testing. Air pressure is applied and maintained at the top boundary of the sample using a separate GDS air pressure controller. During unsaturated tests, this system allows independent control of matric suction via the axis translation technique. Depending on the test conditions, air pressure may either be maintained constant throughout the test or vented to atmospheric pressure following equilibration. The disc acts as a barrier that ensures air from the top boundary does not enter the water line or the pore pressure measurement system beneath the specimen.

The disc is always fully saturated to avoid air burrowing into the disc. The pedestal with the disc in a beaker of water is kept inside a vacuum chamber at -30kPa for over a week until no further air bubbles are released. Pore water pressure is controlled using the GDS pressure

controller connected to the bottom of the pedestal, and pore pressure is measured by the transducer positioned at the base of the pedestal. Air pressure is controlled on the top boundary of the specimen using a separate GDS air pressure controller, and it is either maintained constant after equilibration or left open to the atmosphere depending on the test requirement.

The disc was reused across all triaxial tests to maintain consistency in pore pressure boundary conditions. However, before each test, it was carefully inspected and re-saturated under vacuum conditions to ensure full saturation. In rare cases where partial desaturation was suspected, such as when unexpectedly large volumetric changes or signs of cavitation occurred during testing, the test results were excluded from analysis. This quality control step was essential to avoid compromising the accuracy of pore pressure regulation and measurement due to air passage through a desaturated disc.

All fluid lines, including the connections from the pedestal to the Pore GDS and pore pressure transducers, were thoroughly flushed and saturated with de-aired distilled water before assembly to eliminate trapped air. The lower pore pressure transducer measured the sample's pore pressure, while a separate port to the Pore GDS allowed both the regulation of pore pressure and monitoring of volume change to track saturation levels.

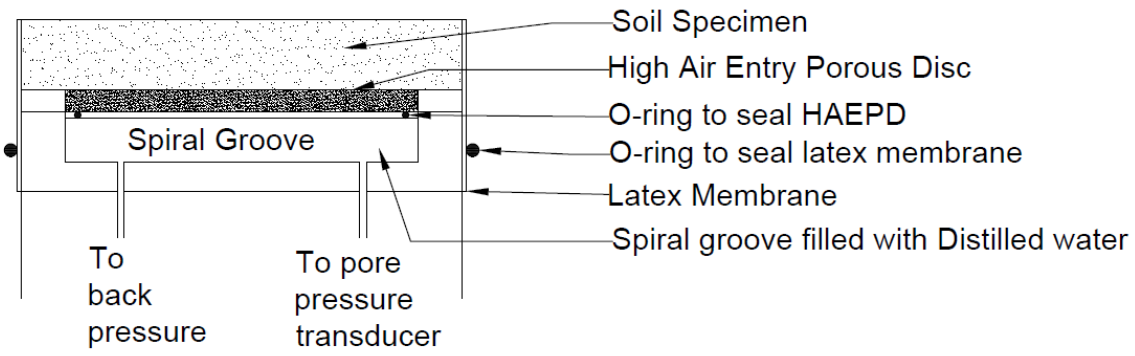

(a)

(b)

Figure 4.7: (a) Bottom Pedestal setup for Unsaturated tests
(b) Spiral groove – HAEPD base (after Lajmiri et al., 2022)

4.5.2 Measurement of Pore Air Pressure

The pore drain from the top of the sample is open to the atmosphere and has a 2MPa Druck air pressure transducer in the line to measure the air pressure if the top drain is closed. This transducer is similar to the pore water pressure transducer, but the diaphragm fluid is air instead of water. A relatively coarse porous disc is used at the top of the sample to minimise water entry into the porous disk. The top line is frequently checked for blockage or traces of water and cleared with pressurised air between tests to keep the line clear.

4.5.3 Measurement of Sample Volume Change

Generally, the volume change measurements in unsaturated triaxial tests are measured either by measuring the axial and radial dimensions of the sample using internal instrumentation or by measuring the change in the cell water volume. Measuring the internal dimension involves challenging instrumental setups and leads to difficulty in interpretation because of non-uniform deformation even when the soil is compressed uniformly, and when shear planes form, and sample bulging occurs. So, in this study, we have adopted the latter method of using the cell volume changes. In this method, the triaxial sample is typically enclosed by a smaller cell to minimise the errors due to cell volume changing with cell pressure, water absorption, thermal expansion, creeping of the cell at constant high pressure, etc (Bishop and Donald, 1961; Cui and Delage, 1996; Ng and Menzies, 2007; Romero et al., 1997). However, these setups usually use smaller samples with a diameter of 50mm or less and a height of 100mm, in which the abovementioned errors are significant for that size. So, all the unsaturated tests in this study were tested on larger samples of 100mm diameter and 200mm height in the cell of similar size instead of using a small inner cell where the cell water volume is significantly reduced. Also, essential corrections for the cell volume errors have been implemented to improve the accuracy of the cell volume measurement. The possible volume errors that have been considered in the correction are: - **i.** Water absorption, **ii.** Creep of the cell at constant cell pressure, **iii.** Displacement of water due to increase in cell pressure, **iv.** Displacement of water to dissolve the trapped air in the cell, **v.** Expansion of the cell, and **vi.** Displacement of water to compensate the volume of loading ram entering the cell. In order to eliminate the errors, the total volume change excluding the volume change due to the sample was measured and calibrated against the measured volume change during the test. The cell is filled with water by placing an incompressible solid metal cylinder (of size 100mm diameter and 200mm height) instead of the actual sample. The cell pressure is ramped up to 1500kPa, and the volume change is

measured while the pressure was increased. This pressure was held overnight to observe any creep effects, which were insignificant compared to the sample volume change. A polynomial relationship has been derived between the volume change and the cell pressure as shown in Figure 4.8. This equation has been used to negate the error in volume measurement. This equation has been used to correct the error in volume measurement. The correction is specifically applied to a saturated drained test, where the volume change is calculated based on both the pore water volume and the cell volume, as illustrated in Figure 4.9.

$$\text{Volume correction} = \underbrace{0.000176\,(CP^3) - 0.5077\,(CP^2) + 535.87\,(CP)}_{\text{Correction for i, ii, iii, iv \& v}} - \underbrace{[(\text{Axial displacement})\,(a_{lr})]}_{\text{Correction for vi}}$$

Figure 4.8: Volume Correction for unsaturated tests:
Where, CP – Cell pressure; a_{lr} – cross sectional area of loading ram

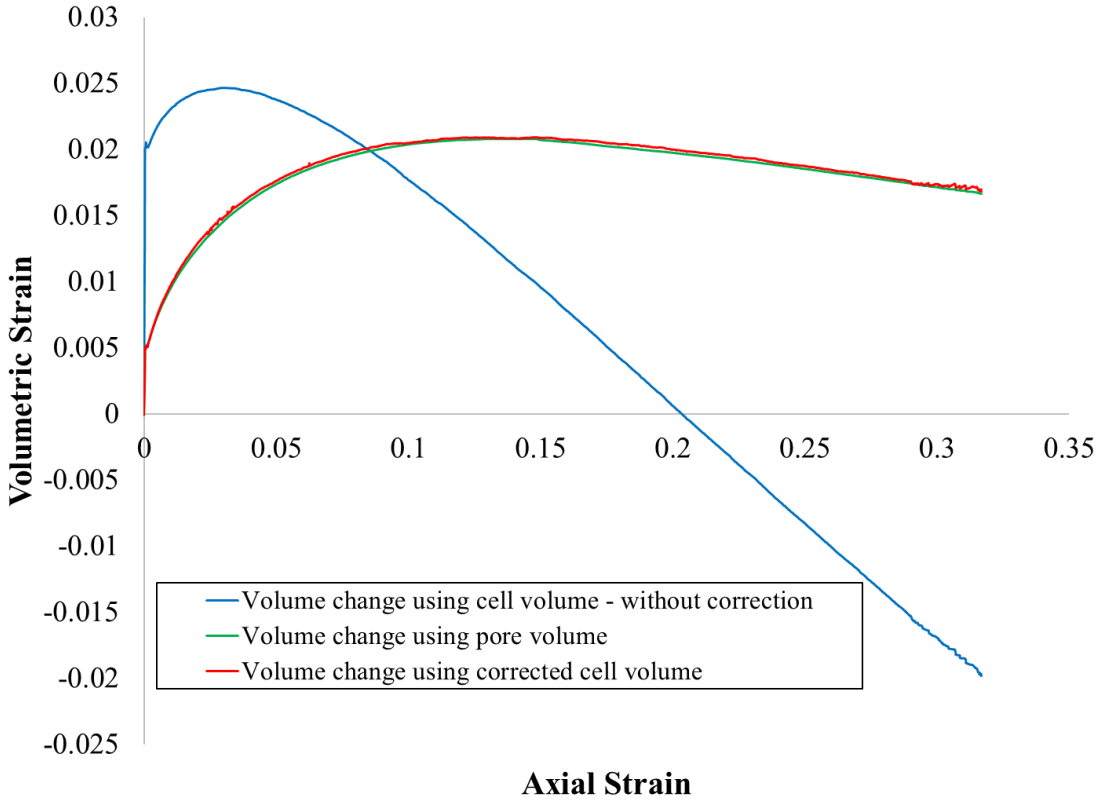

Figure 4.9: Volume correction applied to a saturated drained test

Even after applying this correction, a discrepancy of approximately 2500–3000 mm³ between the corrected and actual volume has been observed in unsaturated tests. It has been studied in detail by Kwa (2019) and found that these variations are due to the displacement of water to dissolve the trapped air while filling the cell, expansion of the cell, and absorption of water into the cell. This variation is relatively small compared to the typical sample volume change, around 60,000-120,000mm^3.

4.5.4 Sample Assembly and Saturation

The sample is assembled on the HAEPD pedestal instead of the normal bottom platen used for saturated samples, but the rest of the preparation procedure is similar to the saturated tests. For Sydney sand, samples are mixed with a gravimetric moisture content of 10-15% beforehand, and further water is pumped in or out of the soil to achieve the target suction of the test. Sydney sand with fines and the WGS soils were mixed with moisture content lower than the air entry value of the mixture (Air entry value as in Soil Water Characteristic Curve). Once the sample was set up, the cell was filled with water and a minimum cell pressure of 15kPa was applied. The top drain was opened to the atmosphere. Then, the suction (0-10 kPa) was applied through Pore GDS, allowing it overnight to attain equilibrium. Once equilibrium was attained, the water displaced was measured, and the degree of saturation was noted. If there were any water droplets trapped in the top drain after equilibrium, it was cleaned to ensure the accuracy of pore air pressure measurement.

4.5.5 Sample Consolidation and Shearing

All the unsaturated soils in this study were tested at a net-consolidation stress of 100kPa at different suctions to focus on the cyclic behaviour of soil at different degrees of saturation. Consolidation of the unsaturated soils was achieved by ramping up the confining stress to the target consolidation stress of 100kPa. Then the pressure was held for 2-3 hours and observed

for any displacement of water from the sample. When the volume change become less than 10mm^3 per hour, then the soil was considered to be consolidated. According to the drainage condition (Undrained - constant moisture content test and Drained - constant suction test) of the test, the top drain was closed or opened to atmosphere. Finally, the shearing of the sample was controlled by the software with the same procedure used in the saturated tests. After the test was completed, wet and dry masses of the soil are recorded to measure the moisture content and to verify the volume change during the test. Matric suction was controlled by axis translation, $s = u_a - u_w$. HAEPD-related measurement error was taken as 1–2 kPa (Kwa, 2019). Druck air and pore-water transducers were calibrated against reference gauges; air lines were inspected/cleared between tests. Overall suction uncertainty is estimated as ±3 kPa (combining air ±2 kPa, water ±2 kPa, and HAEPD effects in quadrature). Volume-change corrections were applied; the residual offset (≈2.5–3.0 cm³) is less than 5% of typical total volume change.

4.6 SWCC

The relationship between soil suction and degree of saturation is characterized by the Soil Water Characteristic Curve (SWCC), which is fundamental in understanding the hydraulic behaviour of unsaturated soils (Fredlund & Xing, 1994). The SWCC serves as a crucial tool for predicting various unsaturated soil properties, including permeability, shear strength, and volume change characteristics (Vanapalli et al., 1999; Lu & Likos, 2004).

For the WGS family, the SWCC was previously determined by Kwa (2019), while Rahman (2007) conducted SWCC tests on Sydney sand. In the present study, the SWCC for Sydney sand with varying fines content has been investigated and integrated with existing data to provide a comprehensive understanding of the material's hydraulic properties.

Although several methods exist for determining the SWCC, such as the pressure plate apparatus (Fredlund & Rahardjo, 1993) and the filter paper method (Bulut & Leong, 2008), this study employs the HYPROP system. The HYPROP (HYdraulic PROPerty analyzer) is a

modern, automated device that utilizes the evaporation method to measure the SWCC and unsaturated hydraulic conductivity simultaneously (Schindler et al., 2010). This method offers advantages in terms of accuracy, speed, and the ability to obtain continuous data points over a wide range of suctions up to 100 kPa (Peters & Durner, 2008).

4.6.1 HYPROP Apparatus

The main components of the apparatus include the HYPROP sensor unit with two precision tensiometers, a 250 cm^3 soil sampling ring, LABROS Balance (accuracy ±0.01g), HYPROP USB adapter for data logging, and LABROS SoilView software for measurement control and data acquisition. The HYPROP sensor unit contains two high-precision tensiometers positioned at different heights within the soil sample to measure soil water tension. The entire assembly is placed on a high-precision balance to continuously monitor sample mass and calculate water content changes as shown in Figure 4.10.

Proper calibration of the HYPROP system is essential for accurate measurements. The LABROS SoilView software automatically checks for offset deviations and prompts for recalibration if necessary (Schindler et al., 2010b). The LABROS Balance is calibrated using its internal calibration weight, a process performed initially, after any change in position, or if inaccurate values are observed. The air entry value of the ceramic tips is periodically verified using a specialized setup with a compressor and pressure gauge by de-airing the system as shown in the Figure 4.11. Additionally, the temperature sensor's accuracy is checked against a calibrated reference thermometer at regular intervals. These calibration procedures ensure the reliability and accuracy of the SWCC measurements throughout the testing program.

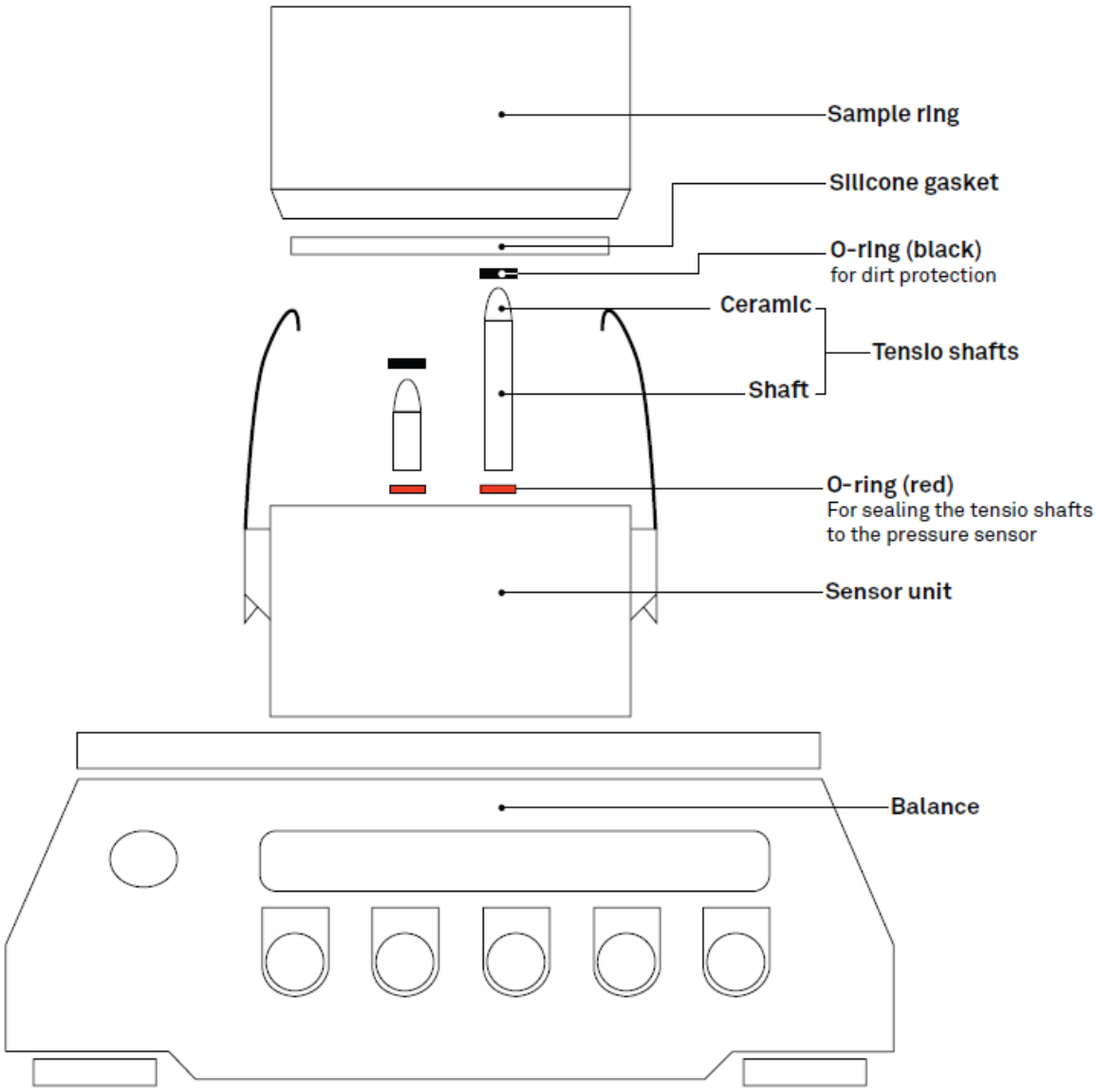

Figure 4.10: Components of HYPROP Apparatus (HYPROP Web Manual)

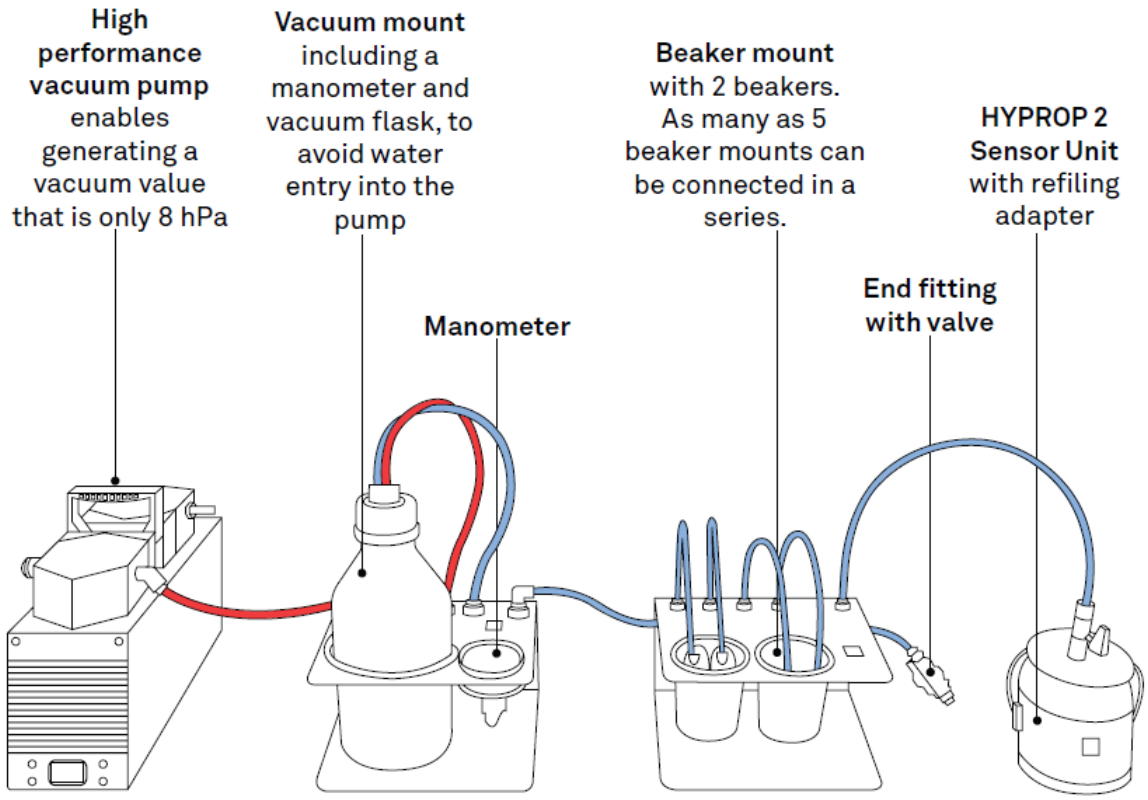

Figure 4.11: HYPROP Apparatus: De-airing System (HYPROP Web Manual)

4.6.2 Testing Methodology

Setting up a sample in the HYPROP system involves several key steps. First, the soil is poured and compacted in 4-6 layers, into the 250 cm^3 stainless steel sampling ring. Then, the sample is saturated from the bottom up by placing it in a beaker of distilled water for 24-48 hours. If the soil is slumpy, the sample is saturated in a slurry consolidation setup with an effective stress of 100 kPa by hanging weights on the top. Then the sample is trimmed off with the sampling ring. The HYPROP sensor unit is then prepared by de-airing and filling the tensiometers with deionized water using either the vacuum pump or syringe method. Two holes are carefully drilled in the saturated soil sample to accommodate the tensiometers, and the HYPROP sensor unit is assembled with the soil sample. The assembled unit is placed on a high-precision balance, connected to the data logging system, and the evaporation measurement is initiated using LABROS SoilView software. The system automatically records sample mass and tension

values at 10-minute intervals as the sample dries via evaporation. The test continues until the tensiometers reach their measurement limit, typically around -85 to -100 kPa or the sample is dry enough to let in air. After measurement, the sample is oven dried at 105°C for 24 hours to determine the dry soil mass. This process allows for the continuous measurement of soil water tension and water content throughout the drying cycle, enabling the construction of detailed soil water characteristic curve.

The HYPROP system is widely used for determining the SWCC in the low suction range (up to ~300 kPa), leveraging tensiometers to provide high-resolution measurements in the near-saturation domain. It is generally accepted that HYPROP is fairly accurate up to the air-entry value, beyond which tensiometer cavitation and measurement unreliability begin to occur (Peters & Durner, 2008; Schindler & Müller, 2006). Therefore, HYPROP performs best in the suction range from 0 to 300 kPa, which corresponds to the wet portion of the SWCC where pore spaces are still largely connected.

Comparative studies have shown that combining HYPROP with other methods enhances the accuracy and completeness of SWCC characterization across the full suction range. For instance, Schindler et al. (2010) and Romero et al. (2000) compare HYPROP with pressure plate extractors and the filter paper method, demonstrating that while HYPROP is highly reliable at low suction, pressure plate techniques extend the measurement range to 1500 kPa and filter paper methods cover an even broader suction domain (up to several MPa), albeit with more variability. These comparisons highlight that no single method covers the full SWCC range with high precision, and a hybrid approach is often necessary for comprehensive characterization. Given that this study focuses exclusively on the lower suction range, the use of HYPROP is considered appropriate, offering sufficient resolution and accuracy for capturing the near-saturation portion of the SWCC relevant to the experimental objectives.

Chapter 5
Soil Behaviour through Experimental Investigation

5.1 Introduction

This chapter describes the experiments conducted to calibrate and validate the model, as well as the soil responses to their respective hydraulic and mechanical loading conditions. The calibration process involves a series of triaxial tests, 1-D compression tests, and tests for soil-water characteristic curves (SWCCs). Most constitutive models are calibrated using a single soil type or soils for which parameters are well established and available. This thesis aims to calibrate the model developed by Ghorbani and Airey (2021), and the latest version (Chen et al., 2024) (referred to as the revised model in subsequent text), using eight varieties of sandy soils. Four of these are composed of Sydney sand with 0%, 20%, 40%, and 60% feldspar fines, while the other four are well-graded manufactured sands (WGS) containing angular basalt aggregates of different sizes, mixed with 18%, 28%, 40%, and 60% feldspar fines. Sydney sand without fines has been studied extensively by several researchers (Lo et al., 1990; Chu, 1991; Cameron & Carter, 2009; Rahman et al., 2009; Mohammadi & Airey, 2019; Duraisamy, 2016). Results from an extensive set of saturated undrained cyclic tests by Mohammadi (2020) were used for model calibration together with additional tests to extend the database. Similarly, Kwa (2019) also performed multiple triaxial tests on silty sand and WGS in both saturated and unsaturated condition to investigate the liquefaction behaviour of shipped metallic ores. Some of the required test results were obtained by repeating certain experiments to ensure the continuity of the study, while others were directly referenced from their PhD theses for calibration and validation purposes. The remaining tests including saturated drained cyclic tests on Sydney Sand and WGS mixtures, as well as unsaturated monotonic and cyclic tests under constant suction conditions were attempted as part of the experimental program. While several unsaturated monotonic tests were conducted, many of them were affected by equipment limitations and data acquisition issues, rendering the results unreliable for interpretation. Consequently, these specific datasets were excluded from the final analysis.

Despite these challenges, a sufficient number of saturated monotonic tests were successfully completed to establish the Critical State Line (CSL) for each soil mixture. Additionally, at least one unsaturated monotonic test was performed on each mixture, aiming to evaluate the shift in critical state behaviour between saturated and unsaturated conditions. Furthermore, one unsaturated cyclic test was conducted for each soil type to assess the model's capability in simulating cyclic response under unsaturated conditions.

Although totally 136 were carried out during the course of this research, a total of 35 saturated monotonic tests, 23 saturated cyclic tests, 11 unsaturated monotonic tests, and 9 unsaturated cyclic tests on both Sydney Sand and WGS mixtures have been selected and presented in this chapter for detailed analysis and model validation.

5.2 Compression Behaviour

This section investigates the compression behaviour of various sand types through a series of one-dimensional (1D) compression tests. The primary objective is to derive the Limiting Compression Curves (LCCs) and their corresponding parameters, N_l and λ, from the test data by plotting void ratio against effective vertical stress in log-log space. The LCC represents the asymptotic response of a soil subjected to high compressive stresses and is governed by the intrinsic compressibility of the soil (Alonso et al., 1990; Romero et al., 1999). The slope component λ is comparable to that of the Critical State Line (CSL) when plotted in the same stress space ($log\ e - log\ p'$), as discussed in Chapter 2. Although conventional 1D compression tests are conducted in terms of effective vertical stress, the slope of the LCC remains the same when plotted against mean effective stress because $K_{0,nc}$ is constant for normally compressed soils (Gens and Alonso, 1992).

The oedometer tests in this study were performed in dry conditions. While traditional oedometer tests are typically conducted under saturated conditions to evaluate time-dependent consolidation behaviour (Head, 1980; Terzaghi, 1943), dry testing was adopted to avoid

complications such as fines migration, particle segregation, and difficulties in preparing loose samples with consistent structure (Tarantino and De Col, 2008; Delage et al., 1996). The aim of these tests was solely to define the LCC, which is independent of initial suction and degree of saturation when the soil is subjected to sufficiently high stress (Romero and Vaunat, 2000; Gallipoli et al., 2003). Furthermore, as the LCC for a given material is unique and does not depend on the initial void ratio (Alonso et al., 1990), variations in initial state between samples do not affect the derived values of N_l and λ. Although samples were prepared using the same compaction energy, differences in fines content resulted in different initial void ratios, making direct comparison of compression curves inappropriate. Nevertheless, LCCs provide a consistent and rational basis for comparing the compressibility of different soil mixtures.

The observed compression curves at stress levels exceeding ~10–15 MPa should be interpreted with caution. Grain crushing progressively contributed to additional void ratio reduction beyond what would occur from rearrangement alone, especially for mixtures containing higher fines contents.

This has two implications for the interpretation of compressibility:

i. the λ values derived from the high-stress segment of the LCC may partially reflect crushing-induced fabric changes rather than purely elastic–plastic compression; and
ii. differences in mineral hardness, particle angularity, and fines content between soil types could mean that some mixtures crush more readily, leading to apparent differences in compressibility that are in fact crushing-driven.

While the tests were designed to isolate the intrinsic compressibility of the soils, these crushing effects represent an upper bound to the stress range over which the derived LCC can be directly applied in practice.

To assess whether saturation condition significantly influenced the derived LCC, tests on clean Sydney Sand were repeated under both saturated and dry conditions. The results showed only

minor changes to the compression curves, with λ and N_I values differing by no more than three decimal places. This confirms that, for clean quartz-rich sands, the impact of saturation on the intrinsic LCC is negligible, reinforcing the interpretation that crushing rather than suction state dominates the compressibility behaviour at the high stress levels tested.

5.2.1 Sydney Sand Family

Compression tests were conducted on a group of soil mixtures referred to as the Sydney Sand family. This included pure Sydney Sand and mixtures with 20%, 40%, and 60% fines content. The tests aimed to determine the LCC for each composition, with all tests conducted under dry conditions to eliminate pore water effects and ensure sample consistency. The compression curves and derived LCCs for each material are presented in Figure 5.1 (a) –(d).

Pure Sydney Sand, classified as a poorly graded sand, displayed the lowest compressibility among the tested materials. This behaviour is attributed to its uniform grain size distribution, which limits the potential for particle rearrangement under applied stress. Similar trends have been observed in previous studies that showed poorly graded sands exhibit lower compressibility due to limited inter-particle adjustment under vertical loading (Cubrinovski and Ishihara, 1999). The absence of finer particles in the matrix reduces the number of inter-particle contacts and void-filling potential, resulting in a flatter compression curve and lower λ value. The granular structure of the material promotes high skeletal stiffness and resistance to compression, which is reflected in the lowest λ of 0.39.

The identification of the Limiting Compression Curve (LCC) for each mixture was carried out by examining the compression trajectories in $\log e$–$\log \sigma'$ space and progressively fitting a straight line to the high-stress segment where curvature visibly reduced. No unloading–reloading cycles were performed; instead, the LCC was empirically derived by extending this fitted line through the final portion of the data where compression response was approaching a constant slope. This method is consistent with previous studies (Delage et al., 1996; Romero

et al., 1999) that accept LCC convergence based on the trajectory trend when stress levels approach the crushing threshold.

Comparison of limiting compression parameters and limiting compression curves are shown in Figure 5.2 and Figure 5.3 respectively. As fines were incrementally added to the Sydney Sand mixtures, the particle size distribution broadened, and a significant change in compression behaviour was observed. The addition of 20% fines caused a noticeable increase in compressibility, with the LCC slope λ increasing to 0.58. Further inclusion of 40% fines led to a slightly higher λ of 0.60, suggesting that the presence of fines improved the packing structure and facilitated particle rearrangement. The finer particles fill the voids between coarse grains, contributing to increased inter-particle contacts and allowing for greater rearrangement during compression. However, when the fines content reached 60%, the λ value slightly decreased to 0.562. This may be attributed to a transition in soil behaviour, where excessive fines begin to govern the mechanical response, reducing the soil's ability to deform under high stress due to cohesive-like behaviour, a phenomenon discussed by Dafalias and Manzari (2004).

Assessing the compression curves visually, the change in curvature and flattening of the compression trajectories are apparent in the mixtures with 20%, 40%, and 60% fines. These materials clearly show a tendency to converge toward a defined limiting slope at high stress levels. However, in the case of the pure Sydney Sand (SS0F), while the curve does not exhibit a fully flattened region due to equipment limitations, there is a visible trend indicating the onset of curvature reduction. The test reached the maximum capacity of the oedometer apparatus at 50 MPa, and beyond this, further compression data could not be acquired. Despite the absence of a fully defined plateau, the shape of the curve at the maximum stress level suggests that the sample is approaching its LCC. Similar interpretations are accepted in the literature where LCC convergence is assumed based on curvature trends, especially in high-stress dry compression tests (Delage et al., 1996; Romero et al., 1999).

These findings highlight the non-linear effect of fines on compression behaviour and suggest that there is an optimal fines range for achieving maximum compressibility in sand-fines mixtures. The progressive increase and subsequent decrease in λ with fines content reflects the competing influences of improved particle packing and increased stiffness from fine-dominated matrix structure, consistent with interpretations by Liu and Carter (2002).

Table 5.1: Comparison of Limiting Compression Curves: Sydney Sand Family

S.No	Type of Soil	N_l	λ
1	Sydney Sand	27.5	0.39
2	Sydney Sand with 20% Fines	97	0.58
3	Sydney Sand with 40% Fines	100	0.6
4	Sydney Sand with 60% Fines	150	0.562

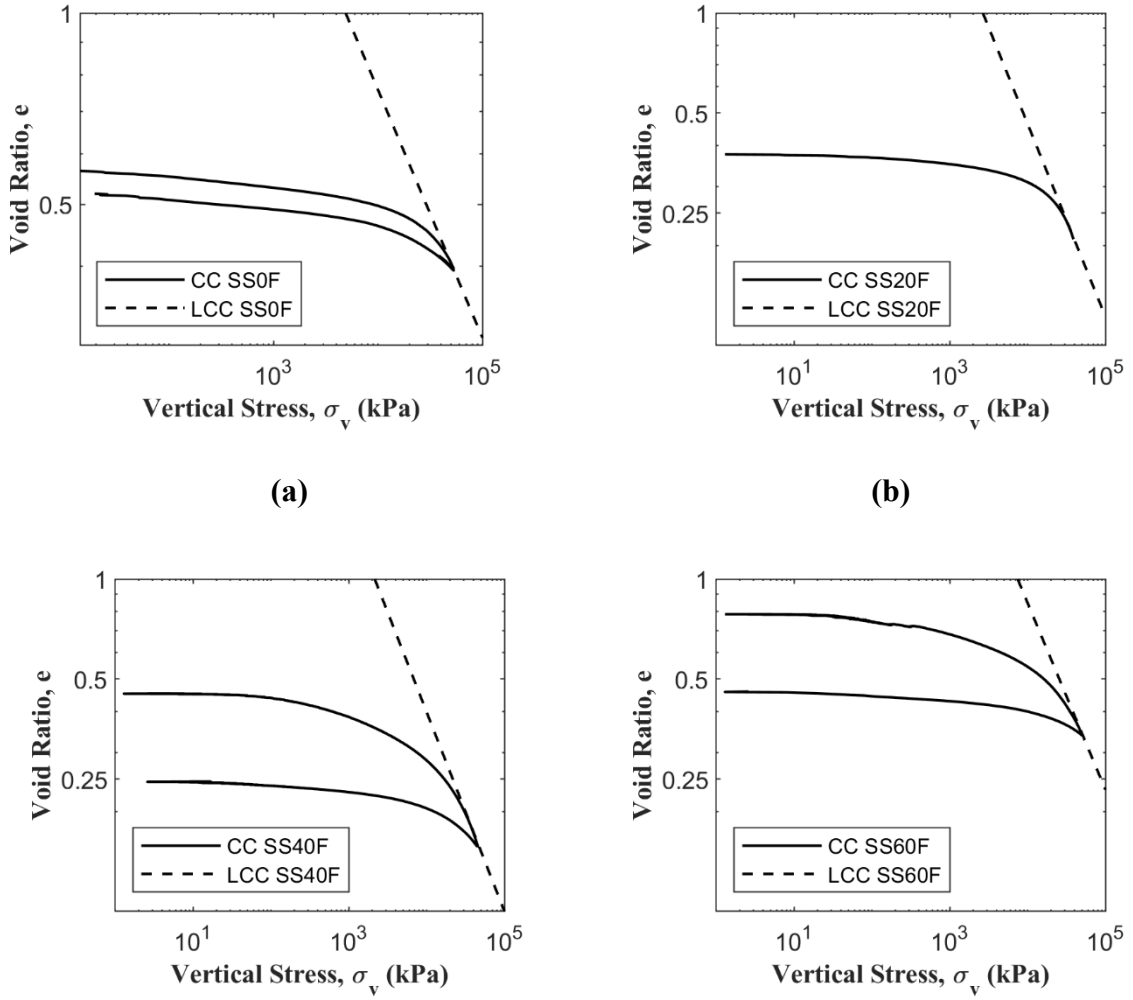

Figure 5.1: Compression Curve (Load-Unload Response) and Limiting Compression Curve (LCC) for (a) Sydney Sand, (b) Sydney sand with 20% fines, (c) Sydney Sand with 40% fines and (d) Sydney sand with 60% fines.

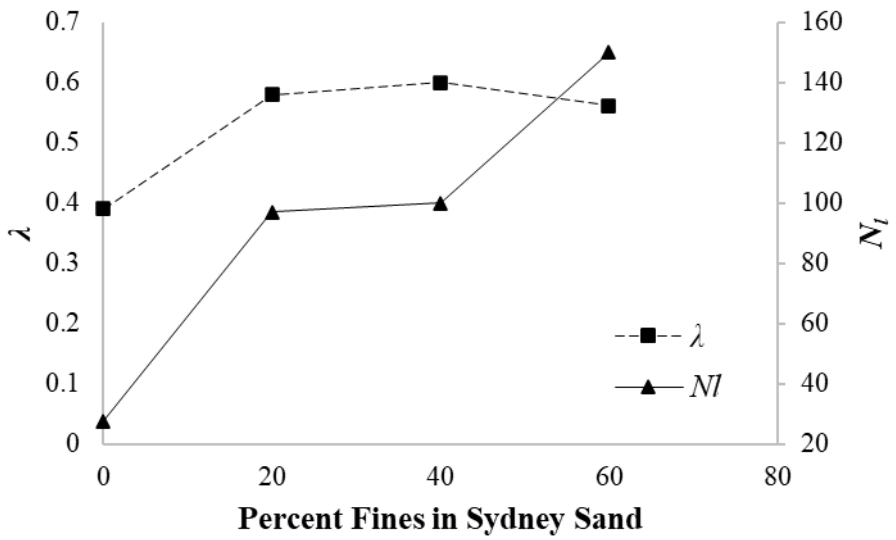

Figure 5.2: Comparison of N_l and λ of Sydney Sand Family

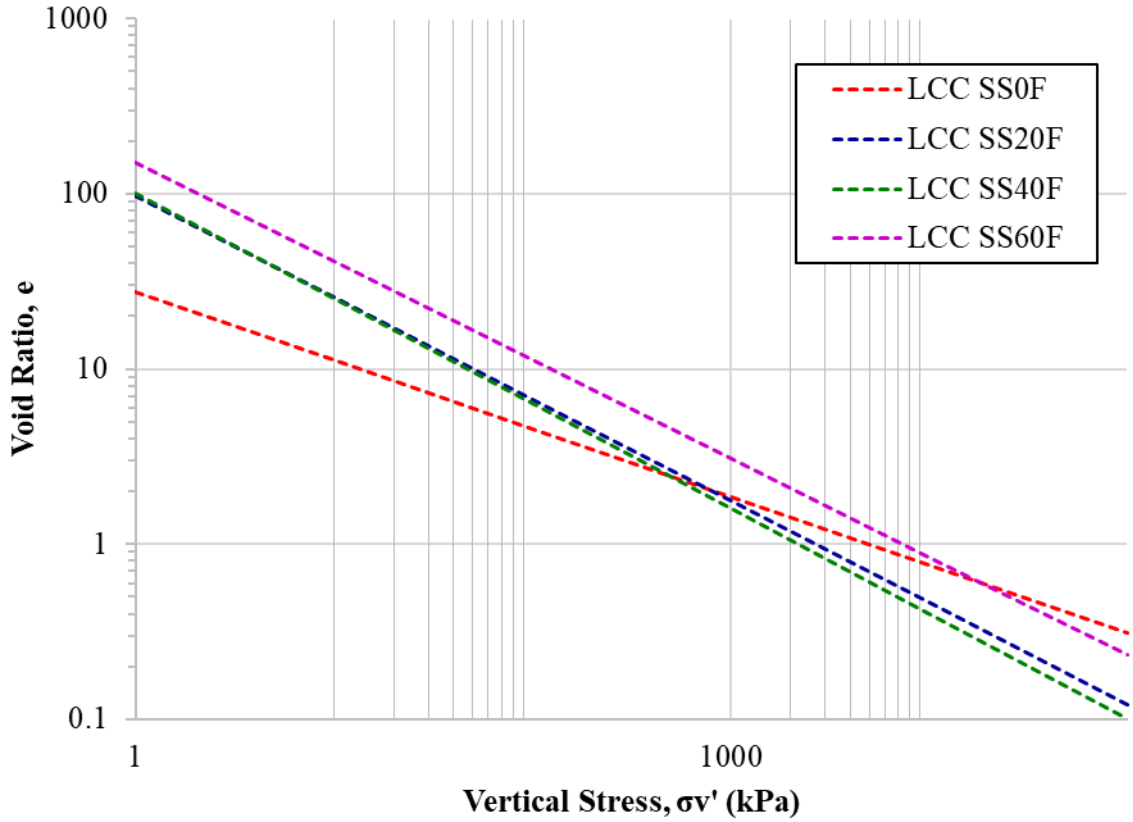

Figure 5.3: Limiting Compression Curves: Sydney Sand Family

5.2.2 WGS Family

The Well-Graded Sand (WGS) family was tested using the same methodology as the Sydney Sand family. The WGS mixtures included 18%, 28%, 40%, and 60% fines content, and the corresponding compression behaviours are illustrated in Figure 5.4 (a) – (d). The base WGS

material, with 18% fines, is inherently well-graded and composed of angular particles. These characteristics result in a dense packing structure with high inter-particle friction and interlocking. The LCC slope λ for this sample was the highest at 0.65, indicating significant compressibility despite its dense nature. Similar behaviour has been reported by Pestana and Whittle (1995), who highlighted that angular particles and well-graded structures can initially promote higher compressibility due to mechanical interlocking that later stabilises under stress. Comparison of limiting compression parameters and limiting compression curves are shown in Figure 5.5 and Figure 5.6, respectively. As fines content increased to 28%, 40%, and 60%, a gradual decrease in λ was observed, with values of 0.58, 0.52, and 0.45 respectively. The addition of fines in an already dense and well-graded material may lead to the filling of inter-particle voids, thereby restricting further rearrangement. This trend is consistent with findings from Xiao et al. (2010), who demonstrated that excessive fines in well-graded soils could reduce compressibility by limiting structural deformation at high stress states. Unlike the Sydney Sand mixtures, which benefited from added fines to improve gradation, the WGS materials already exhibited efficient packing and interlocking at the outset. Thus, further fines reduced available pore space without significantly enhancing rearrangement potential at high stress state of compression curve.

The influence of particle shape and initial gradation is particularly evident in the WGS family. The angularity of the particles contributes to greater resistance to deformation, and the well-graded matrix limits compressibility even as fines content increases. These results demonstrate that for a soil already optimized in terms of structure and interlock, additional fines may reduce rather than enhance its compressibility characteristics. This observation supports the conclusions by Thevanayagam et al. (2002), who noted that the interaction between coarse and fine particles becomes less effective beyond a certain fines content threshold.

Table 5.2: Comparison of Limiting compression Curves: WGS Family

S.No	Type of Soil	N_l	λ
1	Well Graded Sand with 18% Fines	172	0.65
2	Well Graded Sand with 28% Fines	91.5	0.58
3	Well Graded Sand with 40% Fines	49.4	0.52
4	Well Graded Sand with 60% Fines	27.2	0.45

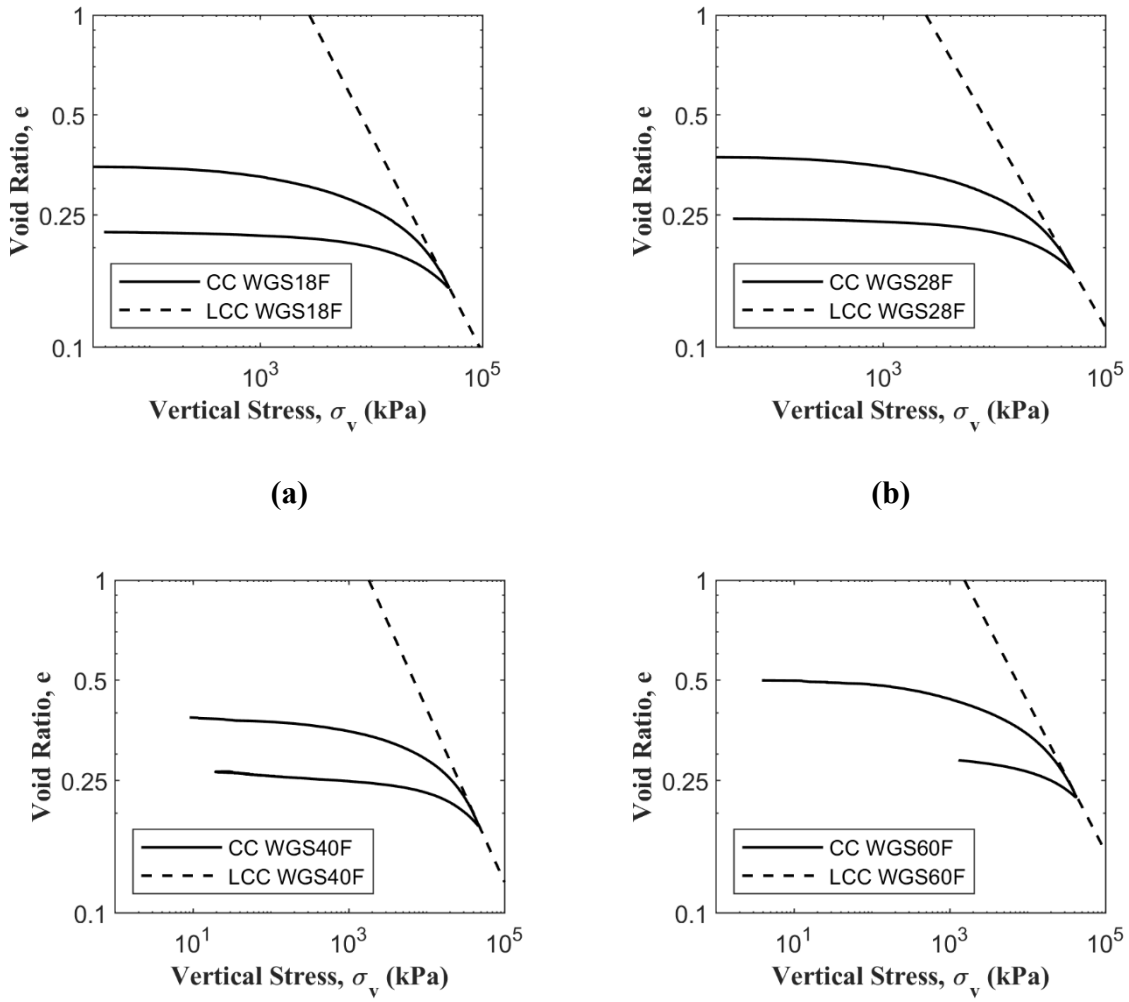

Figure 5.4: Compression Curve (Load-Unload Response) and Limiting Compression Curve (LCC) for (a) WGS with 18% fines, (b) WGS with 28% fines, (c) WGS with 40% fines and (d) WGS with 60% fines.

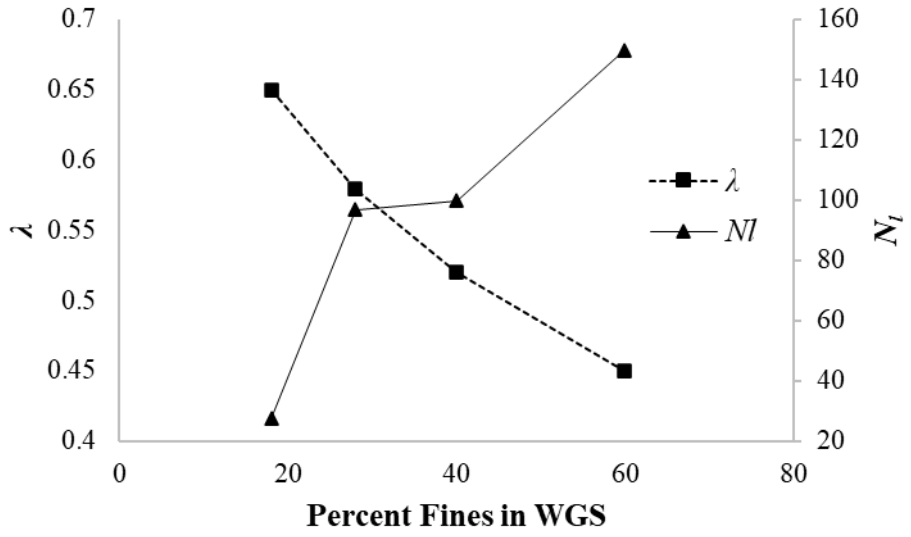

Figure 5.5: Comparison of N_l and λ of WGS Family

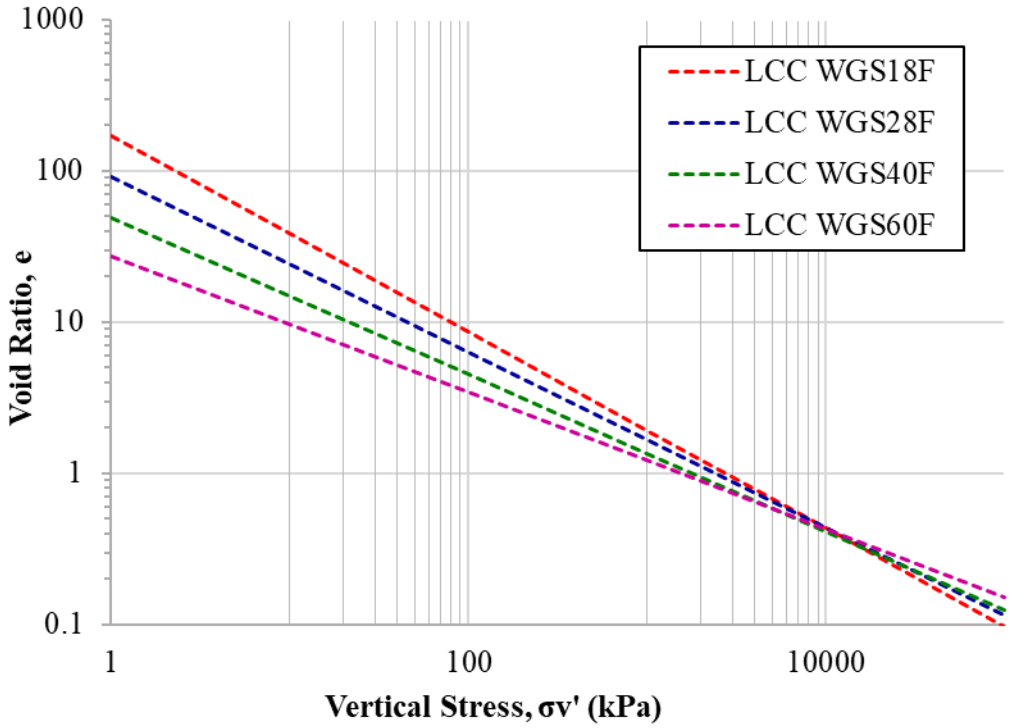

Figure 5.6: Limiting Compression Curves: WGS Family

5.3 Critical State Behaviour

To thoroughly investigate the critical state behaviour of the materials considered in this study, an extensive series of triaxial tests were conducted. The critical state line (CSL) is a unique

characteristic for each soil gradation, necessitating separate determination for each mixture of Sydney sand and WGS with different percentages of fines. To establish a CSL for each material, a minimum of 4 triaxial tests were performed across a range of initial void ratios and confining stresses. The testing program consisted of consolidated drained (CD) and consolidated undrained (CU) triaxial compression tests. For each fines content, samples were prepared at multiple initial void ratios ranging from loose to dense states. Effective confining stresses varied from 50 kPa to 1500 kPa to capture behaviour across low to high stress regimes.

The primary objectives of this comprehensive testing program were to determine the unique CSL for each fines content in both *e-log p′* and *q-p′* spaces, quantify the effects of fines content on the location and slope of the CSL, analyse the influence of fines on the stress-strain and volumetric responses of the soil, evaluate how fines content affects the critical state parameters (M, λ, N_c, and α_{csl}), and provide high-quality experimental data for calibration and validation of constitutive models. By conducting tests across a wide range of initial states, the critical state behaviour of the soil at different void ratios and stress states could be comprehensively addressed. This approach allowed for a thorough examination of how fines content impacts the soil's volumetric and deviatoric responses during shearing to critical states. To ensure consistency of CSL selection across all gradations (Both Sydney Sand and WGS mixtures), CSL points were identified using a common operational criterion: a late-strain stress-ratio plateau where $|d(q/p')/d\varepsilon_1| < 0.02$ per % strain sustained over ≥3–5% axial strain, supplemented in drained tests (where available) by a volumetric stabilisation check ($|d\varepsilon_v/d\varepsilon_1| \rightarrow 0$ following the dilation turning point). Where shear localisation truncated data, the last pre-localisation point was retained and a short-range trend extrapolation (final 3–5% strain) was used, constrained to the mixture's common trend.

5.3.1 Summary of Saturated tests

A series of saturated triaxial tests were conducted on both the Sydney Sand and WGS families to investigate their critical state behaviour. Approximately 20 tests were performed on Sydney Sand to establish its Critical State Line (CSL). Since Sydney Sand with fines and WGS materials had already been extensively studied by Kwa (2019), who plotted their critical state lines, a smaller number of confirmatory tests (minimum of two per material type) were required to verify the CSL position for these materials.

The testing program included both monotonic and cyclic triaxial tests under drained and undrained conditions. For Sydney Sand, the monotonic tests were conducted under confining pressures ranging from 50 kPa to 1500 kPa, while cyclic tests covered pressures between 100 kPa and 1300 kPa. Additionally, tests were performed on Sydney Sand with fines contents of 20%, 40%, and 60%, following similar conditions to evaluate how fines influence critical state behaviour. To further validate the CSL for WGS soil, both monotonic and cyclic tests were carried out on this material as well.

As discussed in Chapter 3, standard methods for determining minimum and maximum void ratios are not applicable to soils with fines content exceeding 15%. Therefore, for soil mixtures containing more than 15% fines, relative density (Dr) is not a reliable index. In such cases, Dr values greater than 1.0 are not physically meaningful but rather indicative of significant compression during sample preparation and the application of confining stress.

This comprehensive testing program provides a robust dataset for analysing the critical state behaviour of these materials, ensuring accurate calibration and validation of constitutive models. Results of the monotonic drained and undrained tests on Sydney Sand are presented in Table 5.3. The tests on Sydney Sand with varying fines content are described in Table 5.4, while Table 5.5 outlines the cyclic drained and undrained tests on Sydney Sand family. Table 5.6, and Table 5.7 summarize the monotonic and cyclic tests on WGS soil, respectively. These

results provide valuable insights into the behaviour of these materials under various loading conditions.

Table 5.3. Summary of Saturated Monotonic Triaxial Tests on Sydney Sand.

Test No	Test Label	p_i'	e_i	e_{cs}	p_{cs}'	q_{cs}	Drainage
M1	MSD_SS0F50L	50	0.8023	0.7973	78.80	99.13	Drained
M2	MSD_SS0F100L	100	0.7632	0.8144	166.54	209.42	Drained
M3	MSD_SS0F100MD	100	0.6718	0.6708	211.63	319.68	Drained
M4	MSD_SS0F150L	150	0.8312	0.8063	241.64	286.39	Drained
M5	MSD_SS0F200MD	200	0.6028	0.6803	330.38	419.10	Drained
M6	MSD_SS0F300MD	300	0.6063	0.7215	525.53	678.95	Drained
M7	MSD_SS0F1500L	1500	0.8015	0.7475	2322.79	2478.74	Drained
M8	MSU_SS0F100Di	100	0.6633	0.6633	1882.37	2372.66	Undrained
M9	MSU_SS0F100Dii	100	0.5842	0.5842	1978.8	2587.92	Undrained
M10	MSU_SS0F100L	100	0.7645	0.7645	37.11	56.38	Undrained
M11	MSU_SS0F200Di	200	0.7268	0.7268	2064.34	2470.26	Undrained
M12	MSU_SS0F200Dii	200	0.6603	0.6603	1511.7	1746.68	Undrained
M13	MSU_SS0F200Li	200	0.7962	0.7962	118.68	154.67	Undrained
M14	MSU_SS0F200Lii	200	0.7080	0.7080	686.30	747.49	Undrained
M15	MSU_SS0F300D	300	0.6358	0.6358	1703.51	1975.37	Undrained
M16	MSU_SS0F300L	300	0.7812	0.7812	88.54	88.93	Undrained
M17	MSU_SS0F1500L	1500	0.7415	0.7415	1741.52	1982.68	Undrained

Table 5.4 Summary of Saturated Monotonic Drained and Undrained Triaxial Tests on Silty Sand

Test No	Test Label	p_i'	e_i	e_{cs}	p_{cs}'	q_{cs}	Drainage
M18	MSD_SS20F100MD	100	0.5948	0.5479	198.18	292.78	Drained
M19*	MSD_SS20F100L	100	0.6095	0.5420	211.31	318.67	Drained
M20	MSU_SS20F100L	100	0.6265	0.6265	11.11	3.43	Undrained
M21	MSU_SS20F300D	300	0.5541	0.5541	364.70	183.23	Drained
M22*	MSD_SS20F300L	300	0.6567	0.5160	555.01	674.16	Drained
M23	MSU_SS20F300MD	300	0.4654	0.4654	479.48	674.52	Drained
M24	MSD_SS20F300MD	300	0.5638	0.5121	568.88	789.85	Drained
M25*	MSD_SS20F500L	500	0.5638	0.5121	568.884	789.84	Drained
M26	MSD_SS20F1000MD	1000	0.5518	0.4934	1699.19	2235.74	Drained
M27	MSD_SS40F100L	100	0.5433	0.4948	276.15	197.2	Drained
M28*	MSD_SS40F300	300	0.5427	0.4512	451.98	351.18	Drained
M29	MSD_SS40F500L	500	0.4665	0.4243	1477.32	984.28	Drained
M30	MSU_SS40F500L	500	0.5409	0.4510	229.68	334.64	Undrained
M31	MSD_SS40F1300	1300	0.4837	0.4156	2279.68	4432.88	Drained
M32	MSU_SS60F100	100	0.5732	0.5897	201.065	147.94	Undrained
M33	MSD_SS60F500	500	0.5898	0.5485	1013.08	1529.57	Drained
M34	MSU_SS60F1300	1500	0.5269	0.5269	2605.67	3903.42	Undrained
M35	MSD_SS60F1300	1500	0.5662	0.5261	2049.57	3374.10	Drained

*Volumetric strain not recorded; projected void ratio is presented in the table.

Table 5.5 Summary of Saturated Cyclic Drained and Undrained Triaxial Tests on Sydney Sand Family

Test No	Test Label	p_i'	e_{cyc}	e_f	q_{amp}	CSR	No of cycles	Drainage
C1	CSD_SS0F100L	100	0.8123	0.8120	50	0.2688	100	Drained
C2	CSD_SS0F300L	300	0.7991	0.7963	120	0.200	100	Drained
C3i	CSD_SS0F500Li	500	0.8128	0.8094	100	0.100	100	Drained
C3ii	CSD_SS0F500Lii	500	0.8094	0.8037	200	0.200	100	Drained
C3iii	CSD_SS0F500Liii	500	0.8037	0.7916	400	0.400	100	Drained
C3iv	CSD_SS0F500Liv	500	0.7916	0.7702	800	0.800	100	Drained
C4	CSD_SS0F1000L	1000	0.8007	0.7491	100	0.050	100	Drained
C5	CSU_SS0F1000L	1000	0.7914	0.7914	100	0.050	100	Undrained
C6*	CSD_SS20F100L	100	0.5785	0.5410	50	0.250	100	Drained
C7*	CSD_SS20F100Lii	100	1.3675	0.5170	100	0.500	10	Drained
C8	CSD_SS20F100Liii	100	0.5854	0.5240	110	0.550	2800	Drained
C9i	CSU_SS20F500Liv	100	0.4723	0.4723	100	0.500	50	Undrained
C9ii	CSU_SS20F500Liv	100	0.4723	0.4723	200	1.00	50	Undrained
C10*	CSD_SS20F500MD	500	0.8067	0.4898	110	0.110	100	Drained
C11	CSU_SS40F100i	100	0.5089	0.5089	110	0.500	670	Undrained
C12	CSU_SS40F100Lii	100	0.4739	0.4739	100	0.500	80	Undrained
C13	CSU_SS40F100Liii	100	0.5683	0.5549	125	0.625	2	Undrained
C14	CSU_SS40F100iv	100	0.4014	0.4014	115	0.575	100	Undrained
C15	CSD_SS40F100	100	0.4563	0.4661	120	0.600	25	Drained
C16	CSD_SS40F500	500	0.5276	0.4060	145	0.145	82	Drained
C17	CSD_SS60F100i	100	0.9880	0.5871	110	0.550	704	Drained
C18	CSD_SS60F100ii	100	0.5606	0.5025	125	0.625	1224	Drained
C19	CSD_SS60F300	300	0.7106	0.6983	120	0.200	50	Drained
C20	CSU_SS60F100i	100	0.5989	0.5989	135	0.320	3	Undrained

C21	CSU_SS60F100ii	100	0.5910	0.5910	20	0.100	100	Undrained
C22	CSU_SS60F100iii	100	0.5721	0.5721	100	0.500	200	Undrained
C23	CSU_SS60F500i	500	0.6067	0.5282	100	0.100	82	Undrained

*Volumetric strain not recorded; projected void ratio is presented in the table.

Table 5.6 Summary of Monotonic Tests on Well Graded Sand

Test NO	Test Label	p_i'	e_i	e_{cs}	p_{cs}'	q_{cs}	Drainage
M36	MSU_WGS18F100	100	0.2668	0.2668	31.14	53.16	Undrained
M37	MSD_WGS18F500	500	0.2619	0.2254	1166.22	1994.56	Drained
M38	MSD_WGS28F500	500	0.4556	0.3851	1098.03	1788.91	Drained
M39	MSU_WGS28F100	100	0.4166	0.3987	7.72	10.32	Undrained
M40	MSD_WGS40F500	500	0.4229	0.4050	1087.19	1753.94	Drained
M41	MSD_WGS40F100	100	0.4741	0.4312	218.79	344.92	Drained
M42	MSD_WGS60F100	100	0.5361	0.5106	183.81	274.48	Drained
M43	MSD_WGS60F500	500	0.6154	0.4851	1119.18	1853.10	Drained

Table 5.7 Summary of Cyclic Triaxial Tests on Well Graded Sand

Test NO	Test Label	p_i'	e_{cyc}	e_f	q_{amp}	CSR	No of cycles	Drainage
C24*	CSD_WGS18F100	100	0.4881	0.2531	115	0.575	100	Drained
C25	CSD_WGS28F500L	500	0.4857	0.3381	100	0.100	28	Drained
C26	CSD_WGS40F500	500	0.3309	0.3100	100	0.100	20	Drained
C27	CSD_WGS60F500	500	0.4893	0.4631	120	0.120	24	Drained
C28	CSD_WGS60F500	500	0.5056	0.4633	125	0.125	60	Drained

*Volumetric strain not recorded; projected void ratio is presented in the table.

5.3.2 Stress–Strain and Critical State Behaviour of Sydney Sand Family

This section presents the interpretation of stress-strain, volumetric, and pore pressure responses of Sydney Sand and its mixtures with 20%, 40%, and 60% fines under both drained and

undrained triaxial loading conditions. To avoid confusion and improve clarity in interpretation, the results for Sydney Sand (drained and undrained), and each fines mixture are presented in separate figures. This approach enables a clearer visual comparison across different fines contents while minimising overlap and clutter. A combined comparison plot is included separately to highlight convergence trends toward the critical state. The results are used to interpret the behaviour across different densities, drainage conditions, and fines contents, as well as to define critical state parameters relevant for further model development.

Drained Triaxial Response of Sydney Sand (0% Fines)

Figure 5.7 shows the stress-strain behaviour of Sydney Sand under drained conditions across different densities. Loose samples (e.g., M1, M2, M4) display a continuous strain hardening response, characterised by a steady increase in deviatoric stress with increasing axial strain, until a plateau is reached. This plateau, occurring beyond 15% axial strain in most cases, indicates the approach to critical state, where the stress no longer changes significantly with further deformation and volumetric strain stabilises.

Dense samples (e.g., M3, M5, M6) initially show a rapid increase in deviatoric stress up to a peak value, after which the stress gradually reduces, indicating strain softening. This behaviour is associated with the development of dilation. As dense samples shear, their structure expands (dilates), resulting in a reduction in mean effective stress, and consequently a drop in deviatoric stress after peak. In some samples like M5, a shear plane formed during the test, leading to a localised stress drop. After this point, accurate volume measurements are no longer reliable due to strain localisation.

To support the identification of critical state conditions, normalised stress plots as in Figure 5.8 were used to illustrate the convergence of all drained tests towards a common critical state line (CSL). These plots provide visual confirmation that samples, regardless of density, trend toward a unique limiting stress ratio. For tests that did not fully reach this convergence due to

equipment limitations or shear localisation, rational extrapolation was performed. This involved extending the stress-strain trend toward the CSL using nearby samples with similar initial conditions that reached critical state. A common CSL was thus derived based on a combination of experimental endpoints and informed extrapolation.

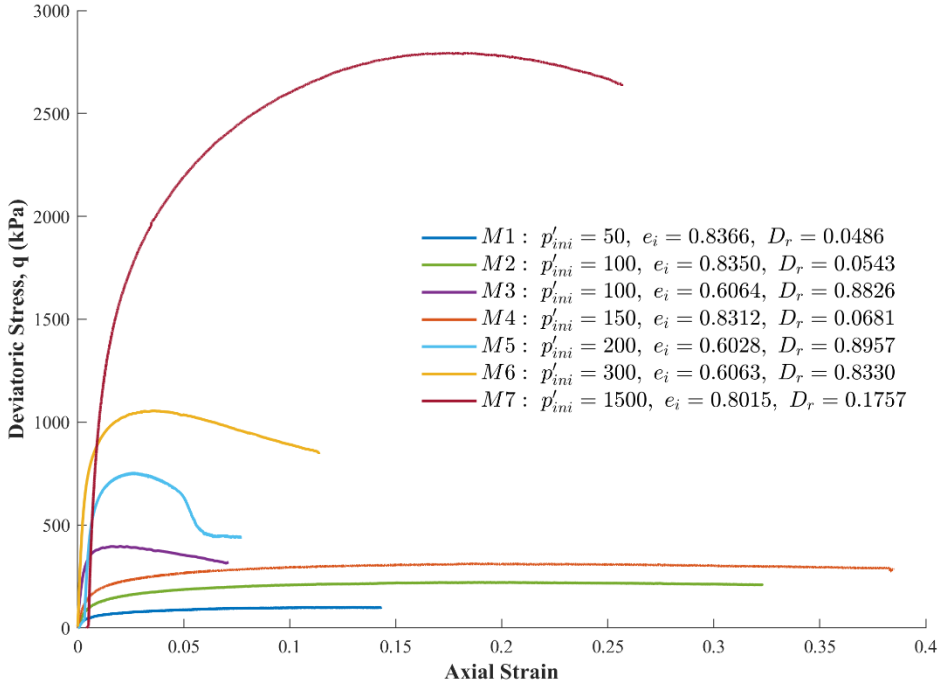

Figure 5.7: Stress Strain response for drained tests - Sydney Sand

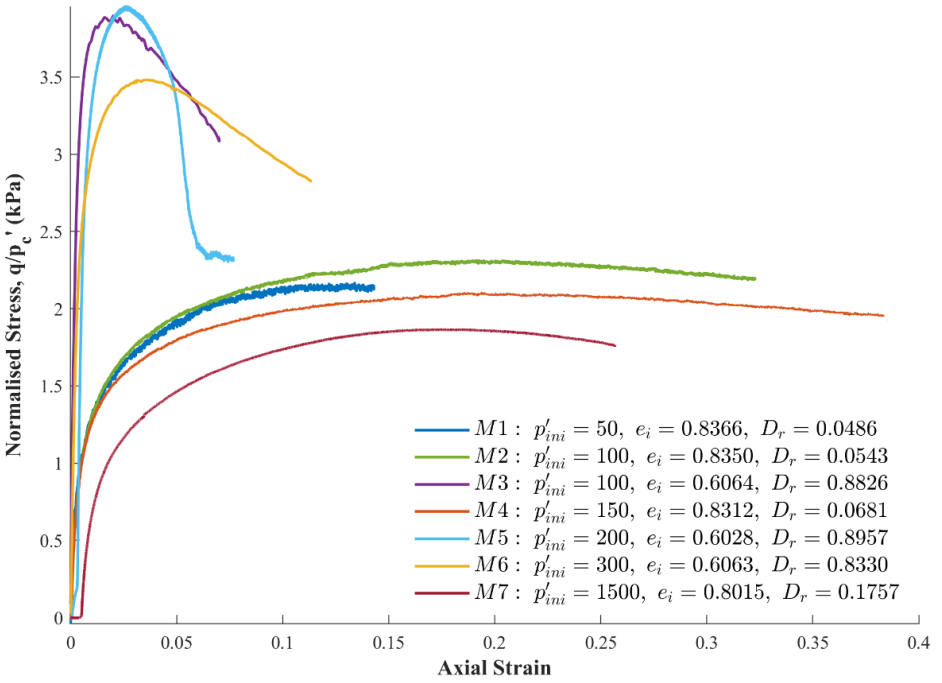

Figure 5.8: Normalised Stress vs Axial Strain: Drained tests - Sydney Sand

Undrained Triaxial Response of Sydney Sand (0% Fines)

The stress-strain behaviour of undrained tests is shown in Figure 5.9, with corresponding normalised plots in Figure 5.10. In undrained conditions, volumetric strain is zero, and excess pore pressure generation governs the effective stress path as shown in Figure 5.11.

Loose samples (e.g., M10, M13, M14) exhibit a contractive response characterised by rapid generation of positive pore pressure during shearing. As axial strain increases, the rise in pore pressure leads to a reduction in effective stress, which causes a reduction in shear strength after the peak, an indicator of strain softening. This behaviour is evident in samples like M10, where static liquefaction is observed.

Dense samples (e.g., M15, M16, M17) initially develop small amounts of positive pore pressure but soon begin to exhibit dilation. Since the volume is constant, this dilative tendency causes pore pressures to reduce, thereby increasing effective stress. As a result, dense samples sustain higher shear stresses and show peak strengths well above those of loose samples. The enhanced stability of dense samples under undrained loading is reflected in their higher peak stress and delayed softening behaviour.

Pore pressure responses are presented in Figures 5.11 and 5.12. These plots, showing pore pressure change versus axial strain, provide insight into the compressive or dilative tendencies of the soil under undrained shearing. Loose samples show a continuous increase in pore pressure, while dense samples show a reversal (drop in pore pressure), corresponding to dilative behaviour.

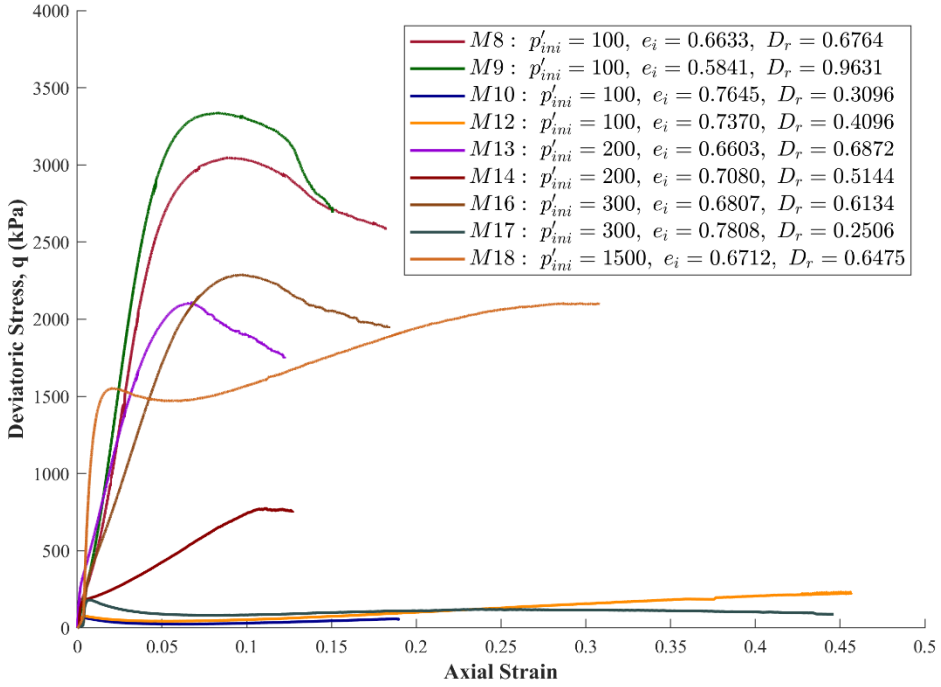

Figure 5.9: Stress Strain response of undrained tests - Sydney Sand

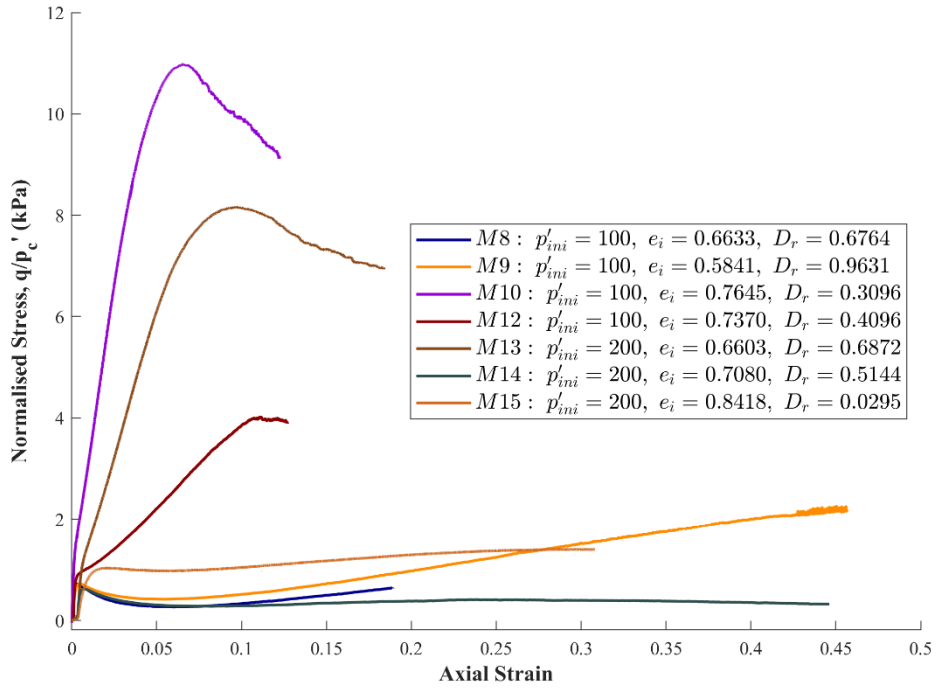

Figure 5.10: Normalised Stress vs Axial Strain - Undrained Tests - Sydney Sand

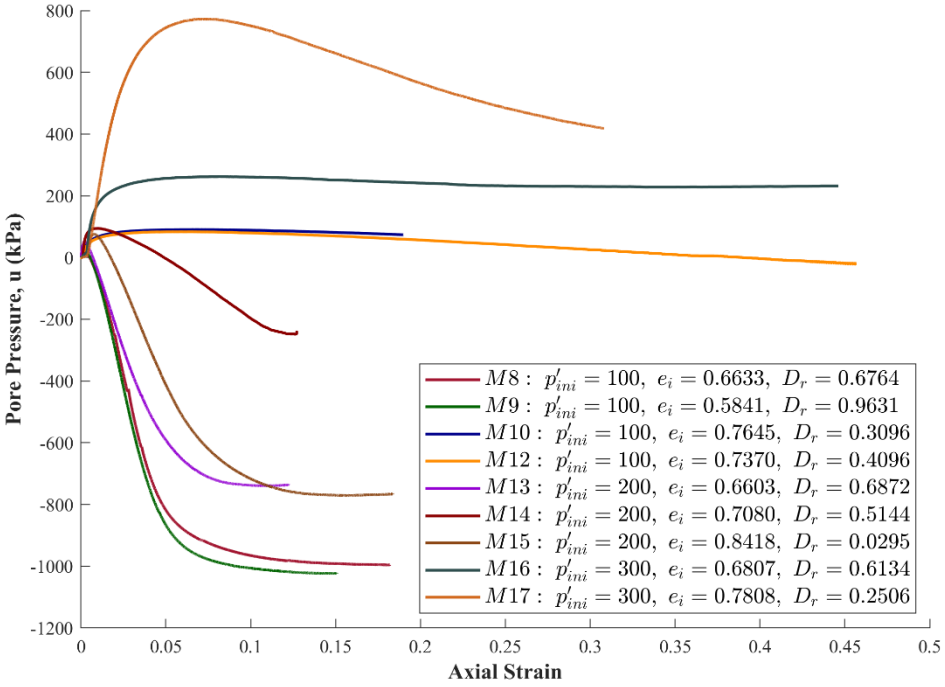

Figure 5.11: Change in Pore Pressure - Sydney Sand

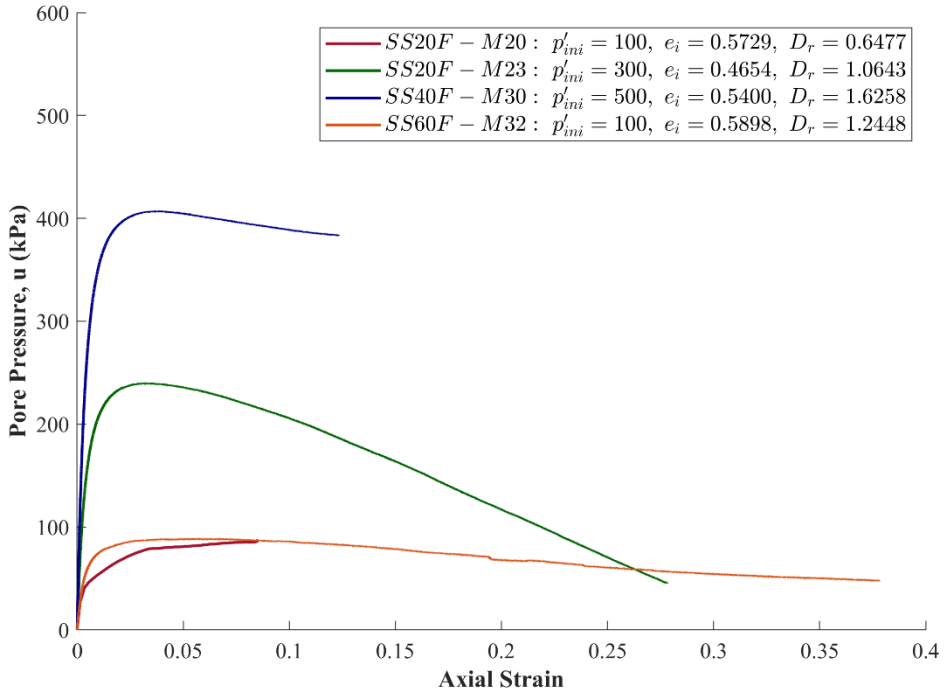

Figure 5.12: Change in Pore Pressure - Sydney Sand with Fines

Effect of fines content

Figures 5.7 to 5.10 and 5.13 to 5.18 present the stress-strain and normalised responses for Sydney Sand with 0%, 20%, 40%, and 60% fines under both drained and undrained conditions. In drained tests, the stress-strain response varies with fines content. For 0% fines, dense samples exhibit a clear peak followed by strain softening, which corresponds to dilation. As the fines content increases to 20% and 40%, the magnitude of the peak stress reduces and post-peak softening becomes less distinct, indicating a progressive reduction in dilative tendency. At 60% fines, the post-peak softening is minimal, and samples mostly show strain hardening behaviour, suggesting contractive response dominates. Loose samples at all fines contents show continuous strain hardening.

The volumetric strain behaviour in drained tests (Figures 5.19 to 5.22) provides clearer insight into this transition between contractive and dilative states. Dense samples with 0% fines display a distinct volumetric turning point, an initial phase of compression is followed by a reversal to dilation once shear strains exceed approximately 1–2%. The onset of this dilation coincides with the peak deviatoric stress, indicating that the soil structure is expanding as shear bands begin to form. With 20% fines, the turning point still exists but occurs later (at slightly higher axial strains, typically 3–4%) and with less volumetric rebound. At 40% fines, dilation is significantly muted; the volumetric turning point shifts further, and only a small amount of dilation is visible before the sample trends toward overall compression again. At 60% fines, the volumetric curve shows almost no reversal, dense samples largely remain contractive throughout, and any observed dilation is minor and localised.

This evolution of volumetric strain behaviour demonstrates that fines progressively suppress dilation by filling voids between coarse grains and reducing interparticle slip. The fines create a denser, more interlocked structure that resists expansion under shearing. As a result, the critical state is approached differently for each fines content: for low fines contents (0–20%),

dilation helps drive the soil to its CSL, whereas at higher fines (40–60%), the path is dominated by contraction. Consequently, observed approaches to the CSL in the figures are a combination of true convergence in some tests and trend-toward behaviour in others where localisation or apparatus limits intervene.

In undrained conditions, the stress-strain response and pore pressure development are also influenced by fines content. Loose samples across all fine fractions generate positive excess pore pressure during shearing, with a more rapid buildup at higher fines contents. This leads to greater reductions in effective stress and earlier onset of strain softening, particularly at 60% fines. Dense samples with 0% and 20% fines initially exhibit dilation during shearing, reducing pore pressure and increasing effective stress. However, as fines content increases to 40% and 60%, the extent of pore pressure reduction lessens, indicating a suppression of dilative behaviour under undrained conditions as well.

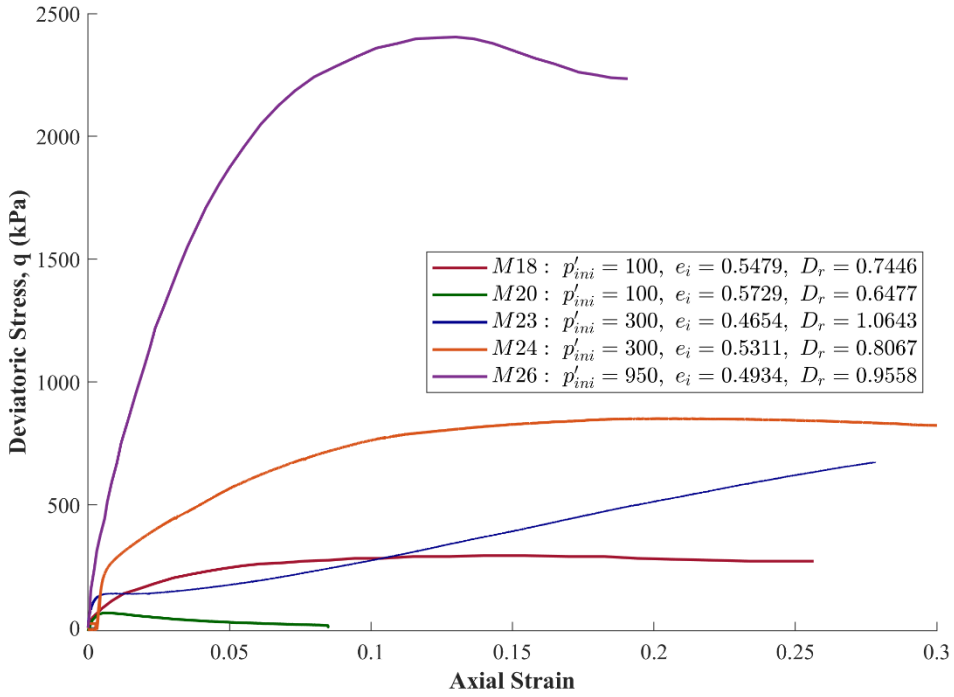

Figure 5.13: Stress Strain response - Sydney Sand with 20% Fines

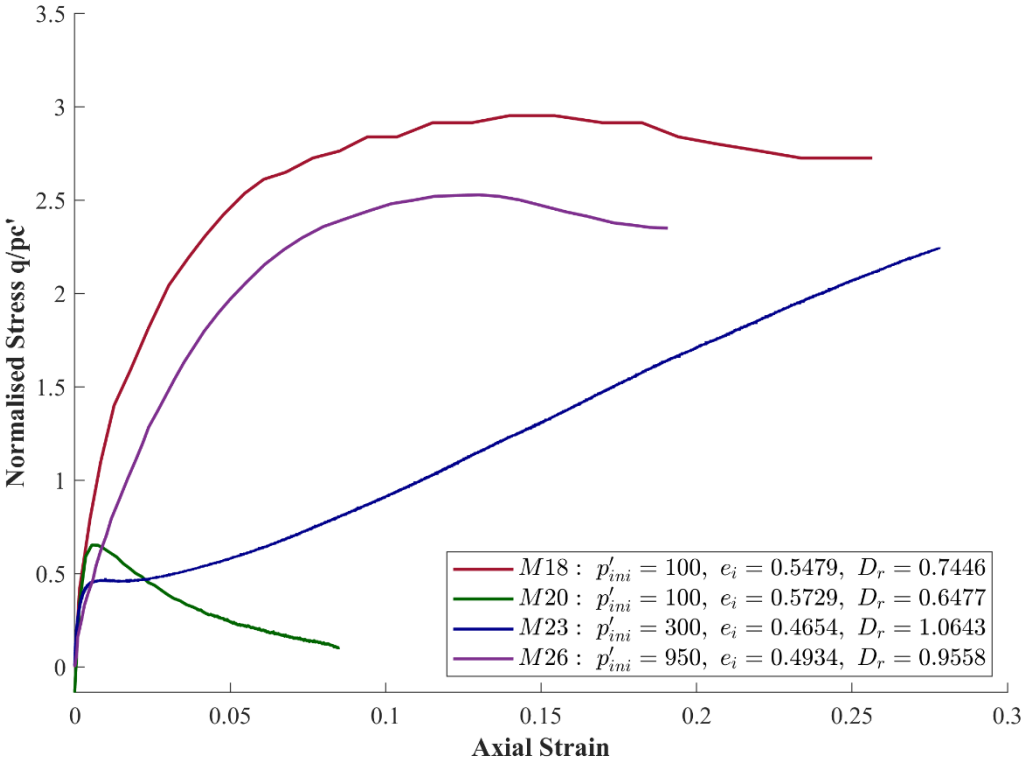

Figure 5.14: Normalised Stress vs Axial Strain - Sydney Sand with 20% Fines

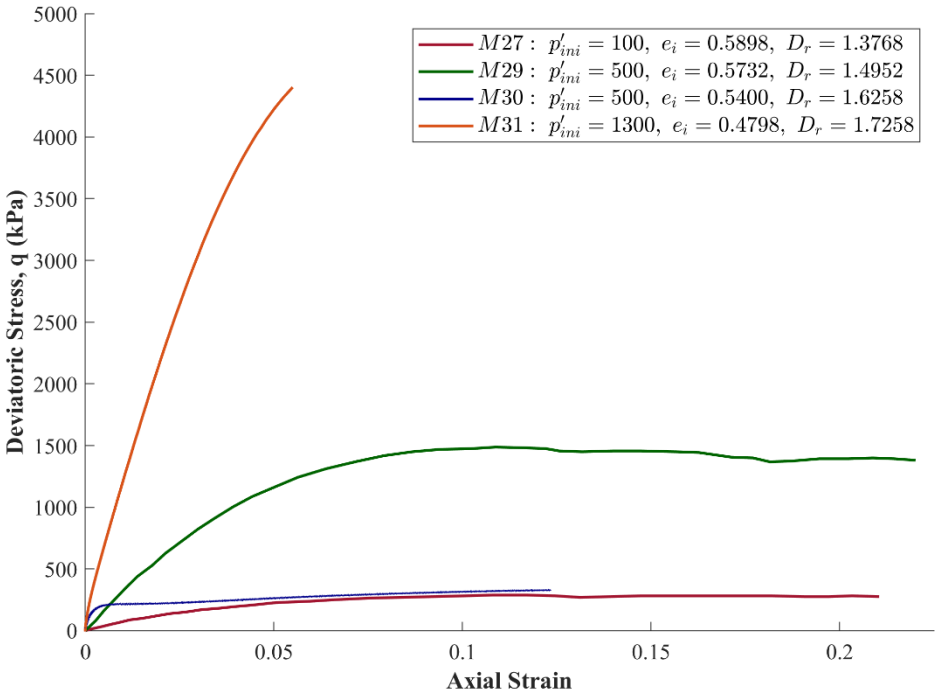

Figure 5.15: Stress Strain response - Sydney Sand with 40% Fines

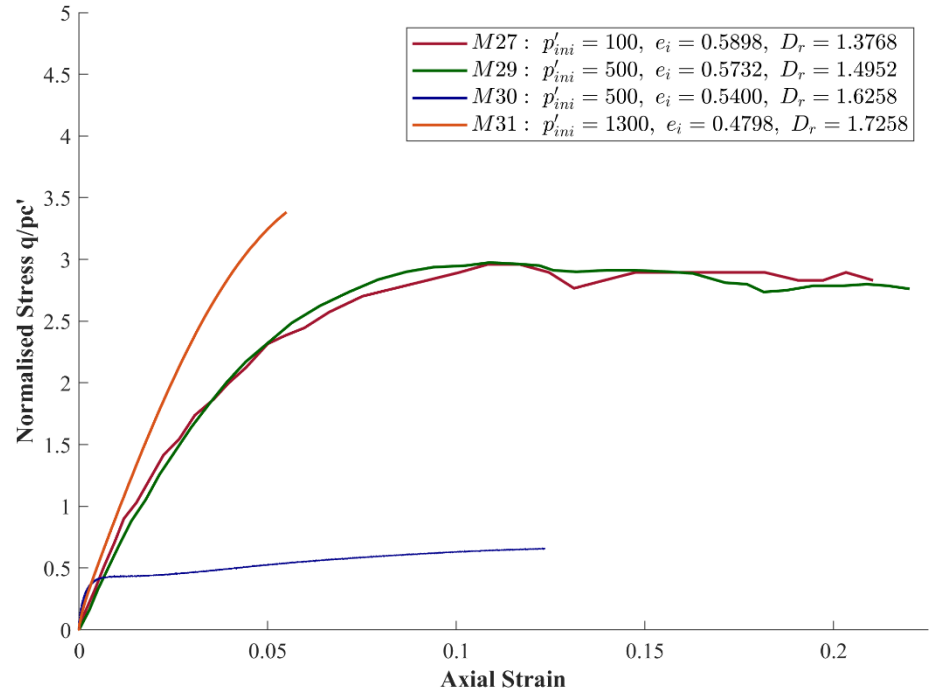

Figure 5.16: Normalised Stress vs Axial Strain - Sydney Sand with 40% Fines

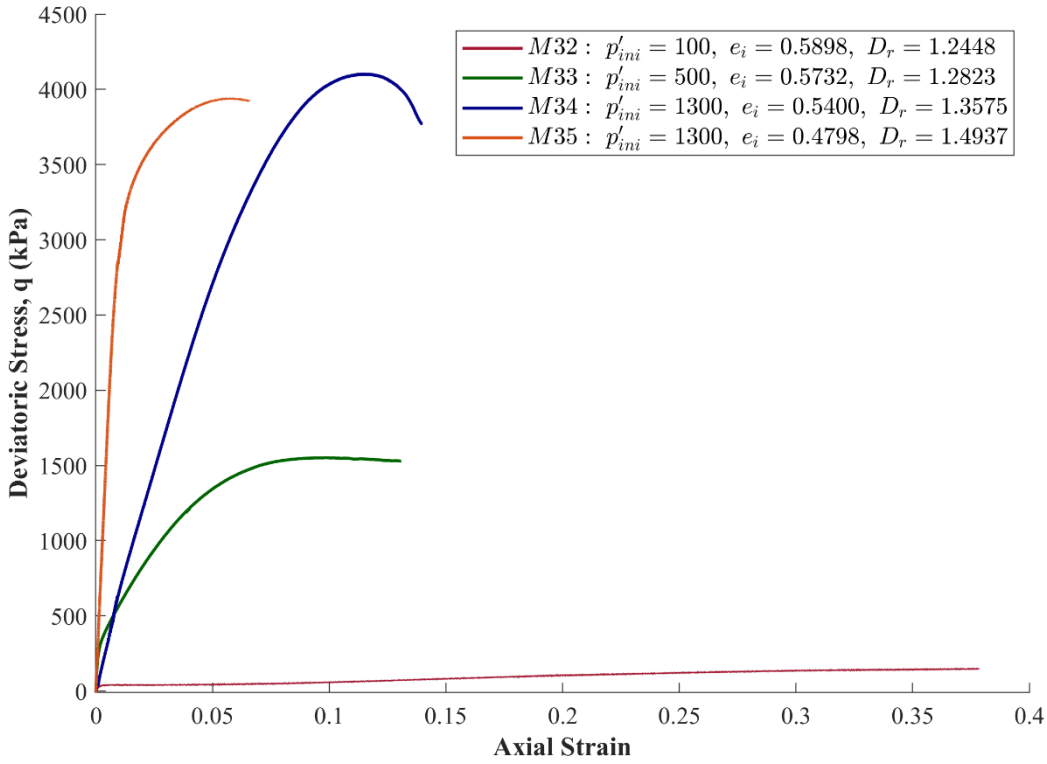

Figure 5.17: Stress Strain response - Sydney Sand with 60% Fines

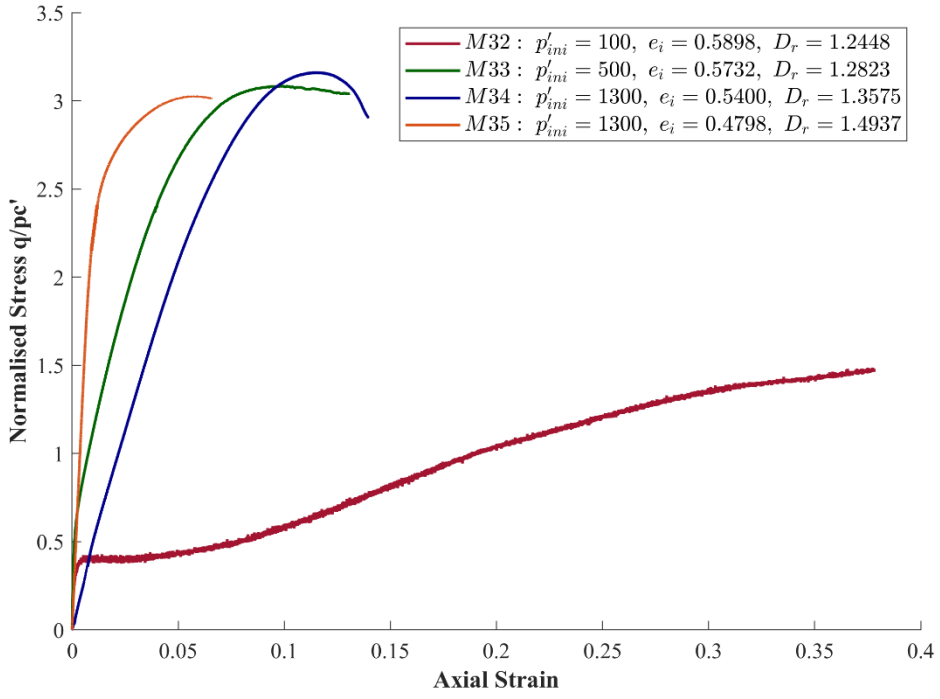

Figure 5.18: Normalised Stress vs Axial Strain - Sydney Sand with 60% Fines

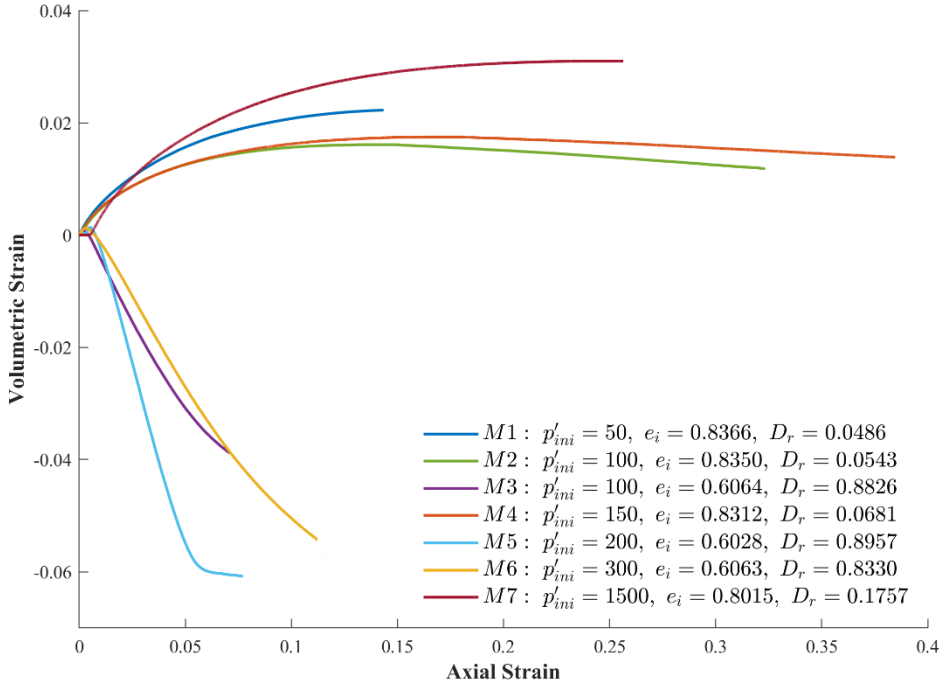

Figure 5.19: Volumetric response - Sydney Sand

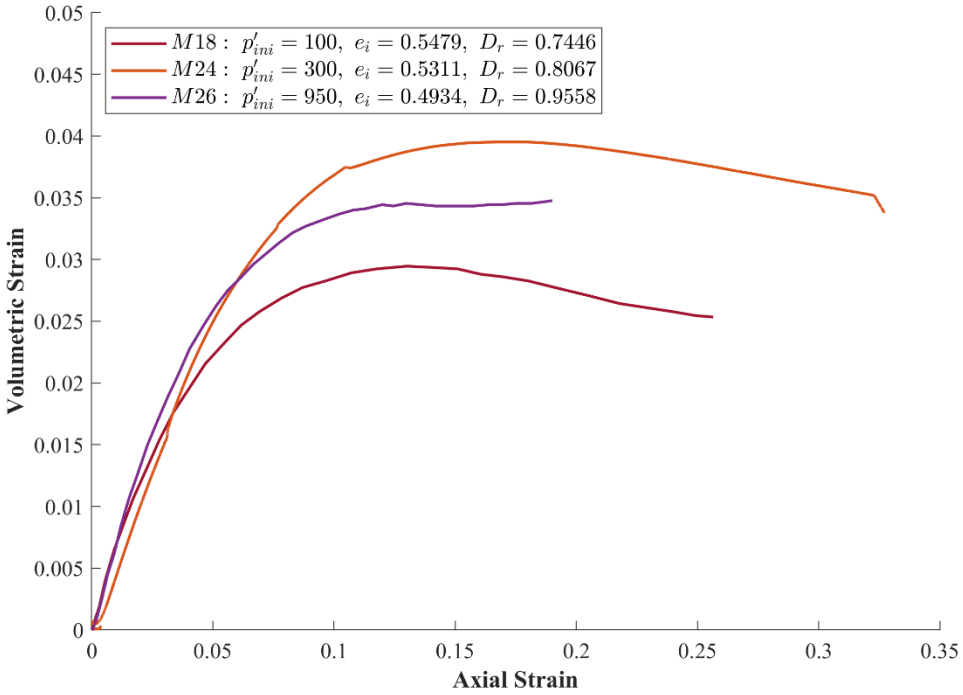

Figure 5.20: Volumetric response - Sydney Sand with 20% Fines

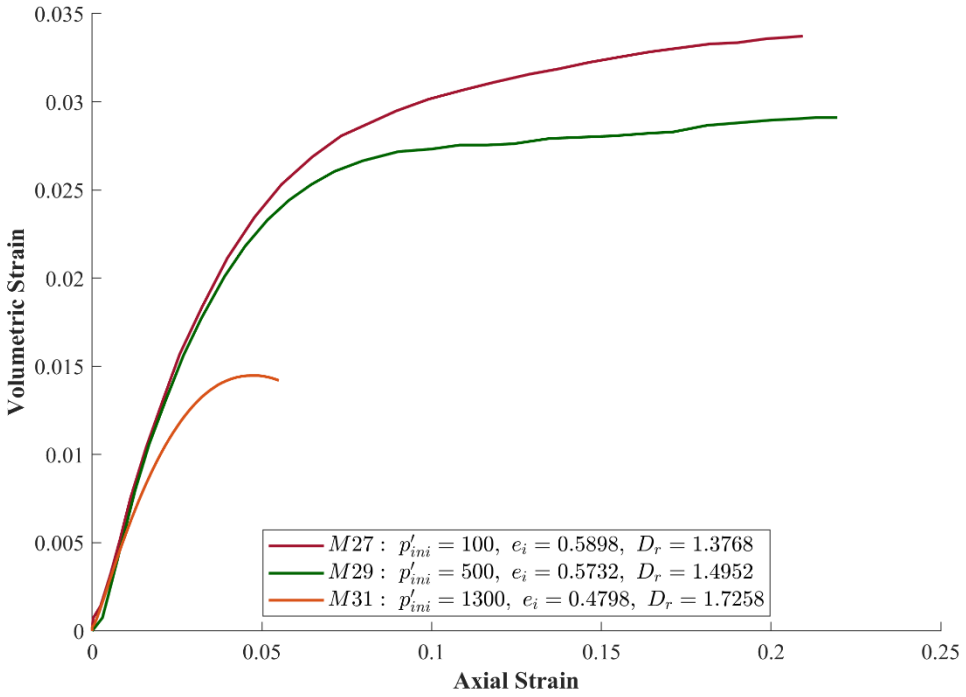

Figure 5.21: Volumetric Response - Sydney Sand with 40% Fines

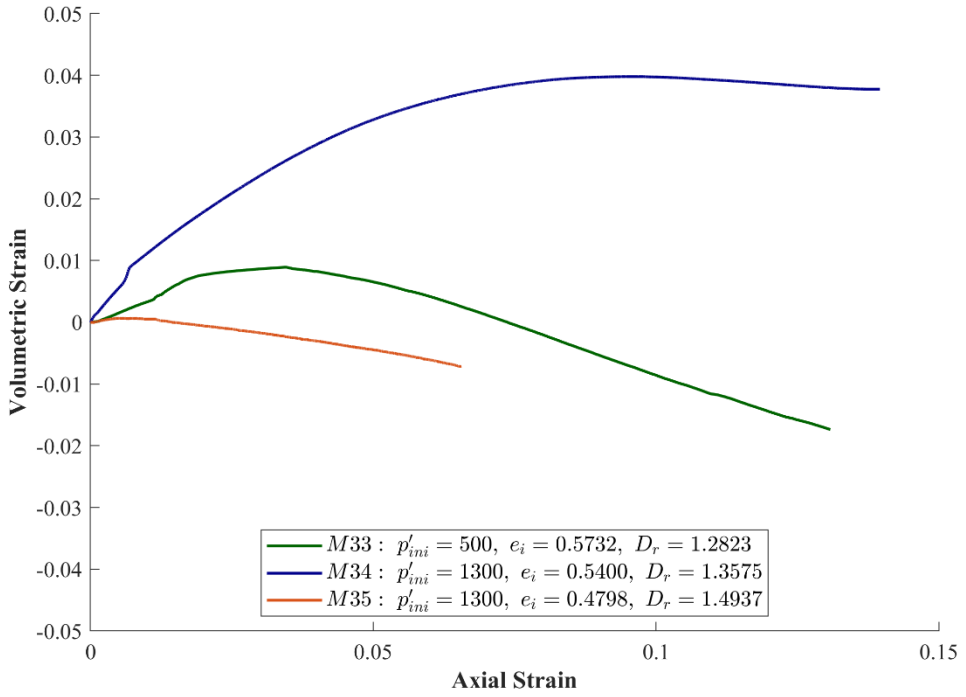

Figure 5.22: Volumetric response: Sydney with 60% Fines

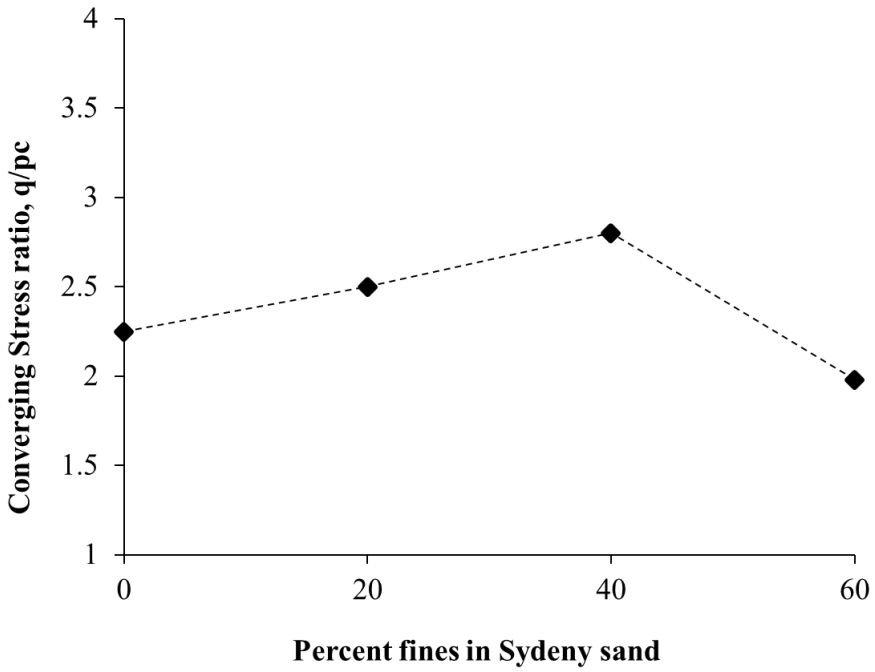

Figure 5.23: Comparison of Converging Stress Ratio - Sydney Sand Family

5.3.3 Critical State and CSL Parameters of Sydney Sand Family

The determination of the critical state line (CSL) is a crucial yet challenging task because the position of CSL has significant effect on model parameters of all models based on critical state. Ideally, all tests should be conducted until the soil reaches its critical state without strain localization. However, achieving this ideal condition is often difficult in practice. Most samples in this study failed at stress states with homogeneous deformation, indicating uniform shearing until failure or reaching critical state. However, there were some exceptions to this pattern.

In certain cases, particularly with dense samples sheared under drained conditions, shear planes formed during testing as mentioned in the earlier section. This development invalidates calculations based on overall volume change and can lead to misleading results at large strains. In several cases, stress values after shear plane formation dropped drastically. Additionally, the volumetric change curve becomes difficult to interpret after shear plane formation, rendering the test data unreliable beyond this point. While some researchers have proposed extrapolation techniques to address this issue (Zhang and Lei, 2024), this study opted for manual estimation of the CSL.

For all tests, CSL identification was based on a combination of (i) monitoring whether the stress–strain response had stabilised (shear stress becoming nearly constant with increasing strain), and (ii) examining void ratio changes to confirm that volumetric strain had levelled off. Tests that reached at least 15–20% axial strain without strain localisation typically achieved a clear plateau, and those end points were taken as true CSL values. For tests where shear planes formed early or the sample did not fully stabilise, the final reliable data point was recorded, and an extrapolation was made along the observed trend toward the CSL. This ensured that "approaching" tests still contributed data without biasing the fitted CSL.

An additional observation was made in dense undrained tests such as M8, M9, M13, and M16, where the stress path in the q-p' space exhibited a sharp dip. This behaviour does not indicate movement along the critical state line but rather reflects the collapse of effective confining stress due to excessive pore pressure buildup. As pore pressures approached the total confining stress, the effective stress reduced to near zero, leading to an artificial cap on the stress path. In reality, had the effective confining stress been sustained, through increased cell pressure capacity the sample would likely have continued mobilizing strength, reaching a true critical state at a higher stress level. This highlights a limitation of testing dense sands in triaxial systems with pressure capacity up to 1.8 MPa, where the equipment restricts the ability to simulate field-scale confinement for dense materials undergoing undrained shearing. These cases demonstrate the need to interpret such dips with caution and avoid mistaking them for the critical state.

Once CSL points were compiled, the data were fitted to the critical state equation (Eqn 8) using parameters λ, N_c, α_{csl}, and M. This regression-based fit served two purposes: (i) aligning the end-state points from tests that fully reached critical state, and (ii) ensuring that tests which only approached critical state trended consistently toward the fitted CSL. Where strain localisation had removed later data, only pre-localisation points were used for the fit to avoid bias. No artificial "post-peak correction" was applied; instead, the CSL was defined by combining all reliable test endpoints and trend-extrapolated values to maintain physical consistency with observed behaviour.

At least one or two tests for each sand–fines mixture were repeated at very similar initial void ratios (corrected to three decimal places) to confirm the existence of a unique CSL for that mixture. These repeat tests consistently produced nearly identical stress paths and converged on the same CSL location, demonstrating that the CSL was not a test artefact. The fact that repeated specimens with matching void ratios followed the same stress path also provides

strong evidence of the accuracy of the testing methodology and the reliability of the testing practice.

The repeated tests were plotted together and visually compared. Minimal deviations were observed between each pair in key behavioural indicators, including the onset of dilation, peak stress level, and peak volumetric strain in drained tests, as well as peak pore pressure and effective stress paths in undrained tests. This close alignment confirmed that the CSL identified for each mixture reflects a consistent and repeatable soil response.

The CSLs for various Sydney sand mixtures are presented in both stress path (q vs p') and void ratio vs mean effective stress (e vs log p') plots, as shown in Figures 5.24 to 5.33. These lines were plotted using critical state equation as in Eqn. 8 with parameters λ, N_c, α_{csl}, and M in both q-p space and e-log p' space. This particular form of CSL representation was chosen as it aligns with the constitutive model requirements. The derived critical state parameters from this fitted line for each sand mixture are summarized in Table 5.8: Critical State Parameters: Sydney Sand Family.

Table 5.8: Critical State Parameters: Sydney Sand Family

S.no	Material	ϕ_{cs}	M	λ	N_c	α_{csl}
1	Sydney Sand	30	1.2	0.39	24.5	6800
2	Sydney Sand - 20% Fines	33	1.330	0.58	95	6900
3	Sydney Sand - 40% Fines	36	1.462	0.6	113	7200
4	Sydney Sand - 60% Fines	36	1.462	0.562	98	9500

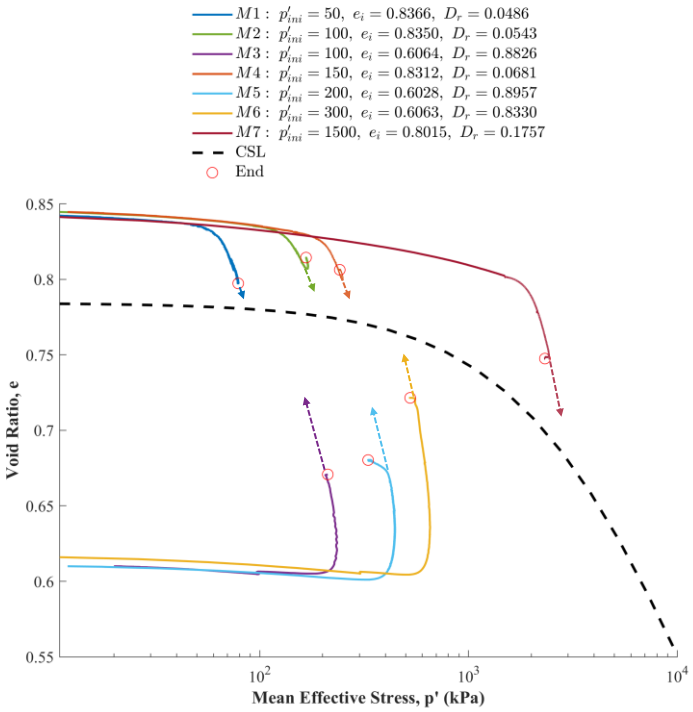

Figure 5.24: Critical State Response of Sydney Sand (Drained tests): *e vs logp'* space

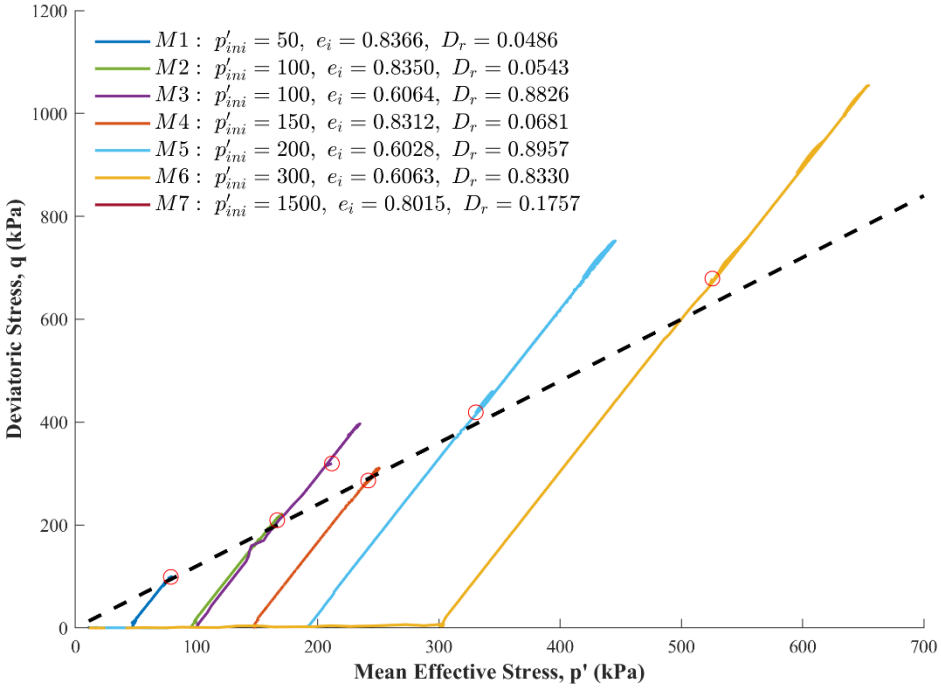

Figure 5.25: Critical State Response of Sydney Sand (Drained): *q vs p'* space

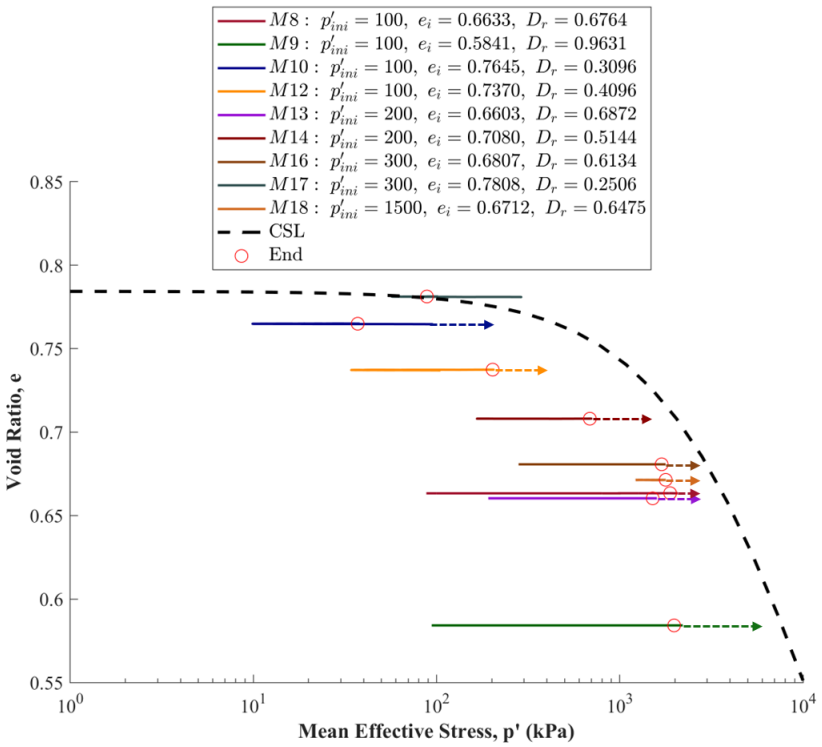

Figure 5.26: Critical State Response of Sydney Sand (Undrained tests): *e vs logp'* space

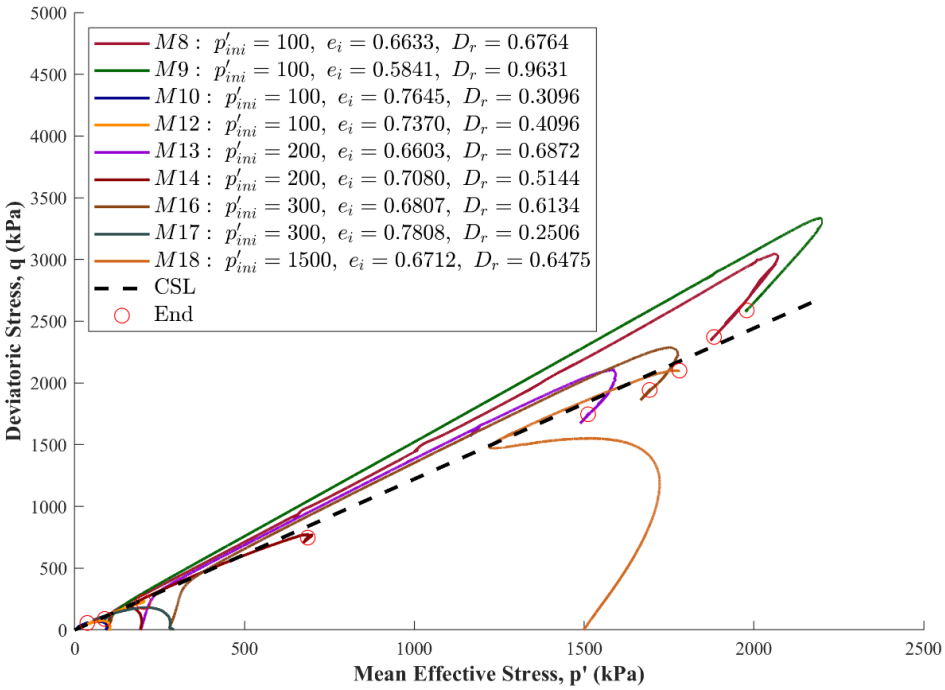

Figure 5.27: Critical State Response of Sydney Sand (Undrained tests): *q vs p'* space

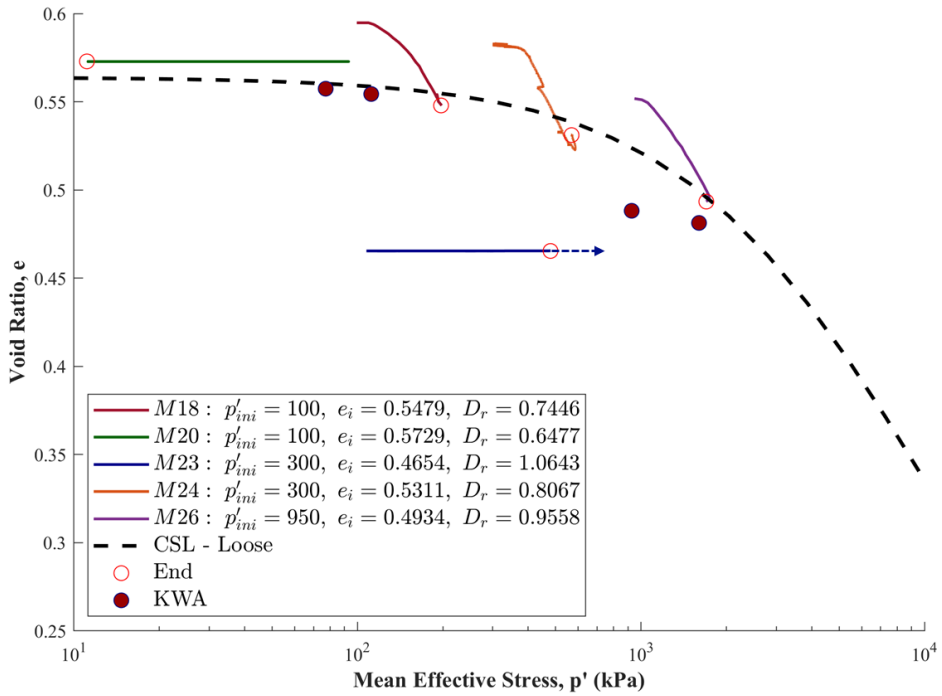

Figure 5.28: Critical State Response of Sydney Sand with 20% Fines (Drained and Undrained): *e vs logp'* space

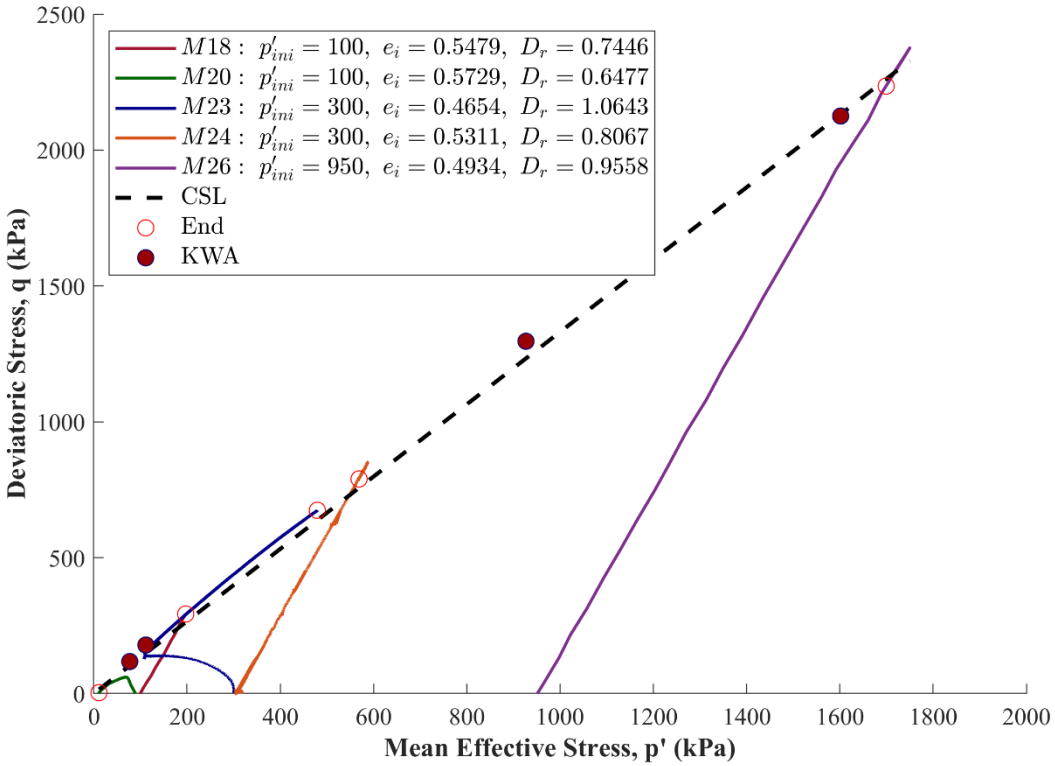

Figure 5.29: Critical State Response of Sydney Sand with 20% Fines (Drained and Undrained): *q vs p'* space

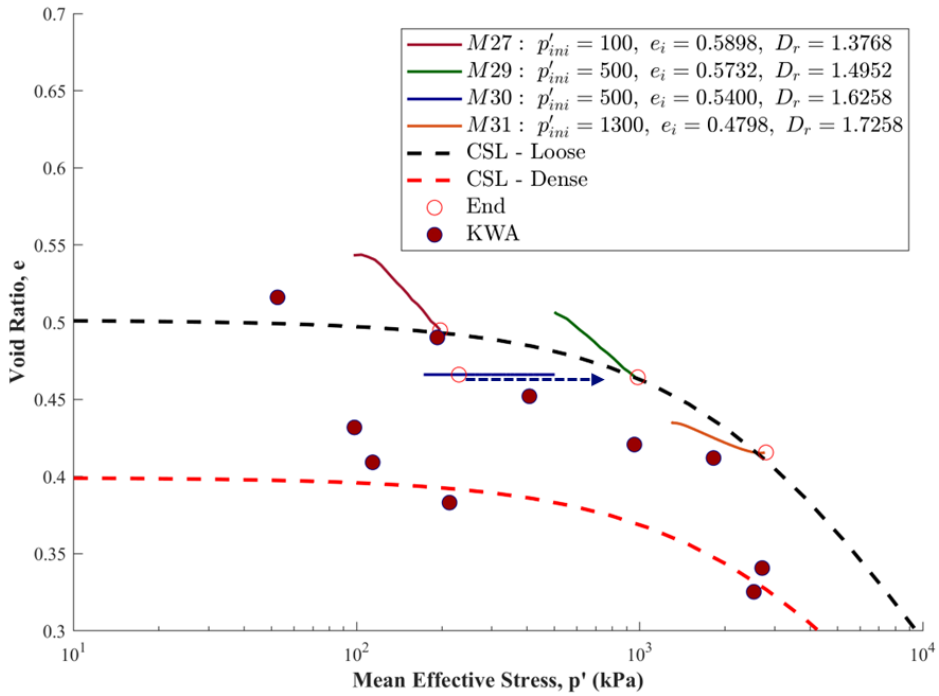

Figure 5.30: Critical State Response of Sydney Sand with 40% Fines (Drained and Undrained): *e vs logp'* space

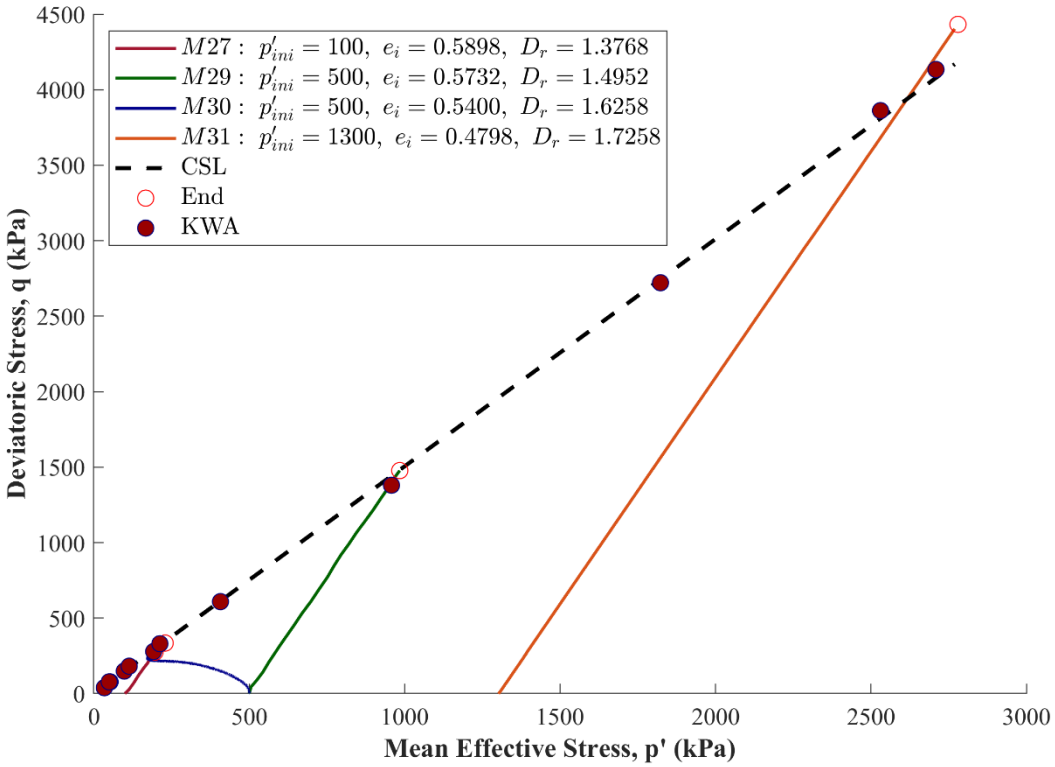

Figure 5.31: Critical State Response of Sydney Sand with 40% Fines: q vs p' space

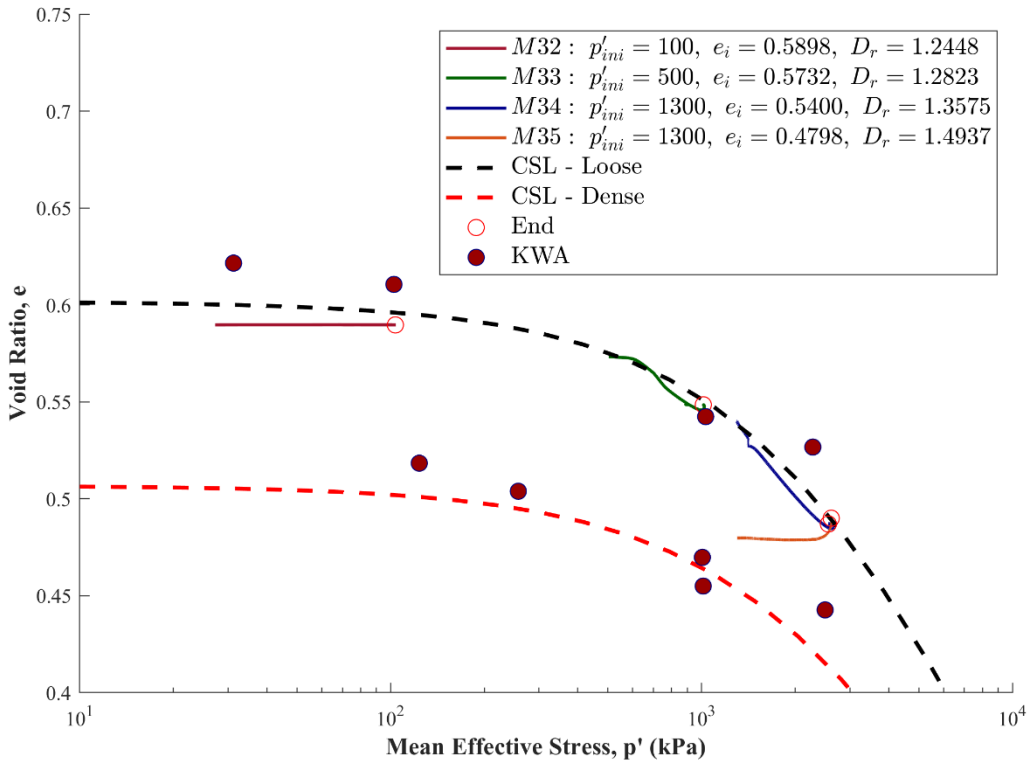

Figure 5.32: Critical State Response of Sydney Sand with 60% Fines (Drained): *e vs logp'* space

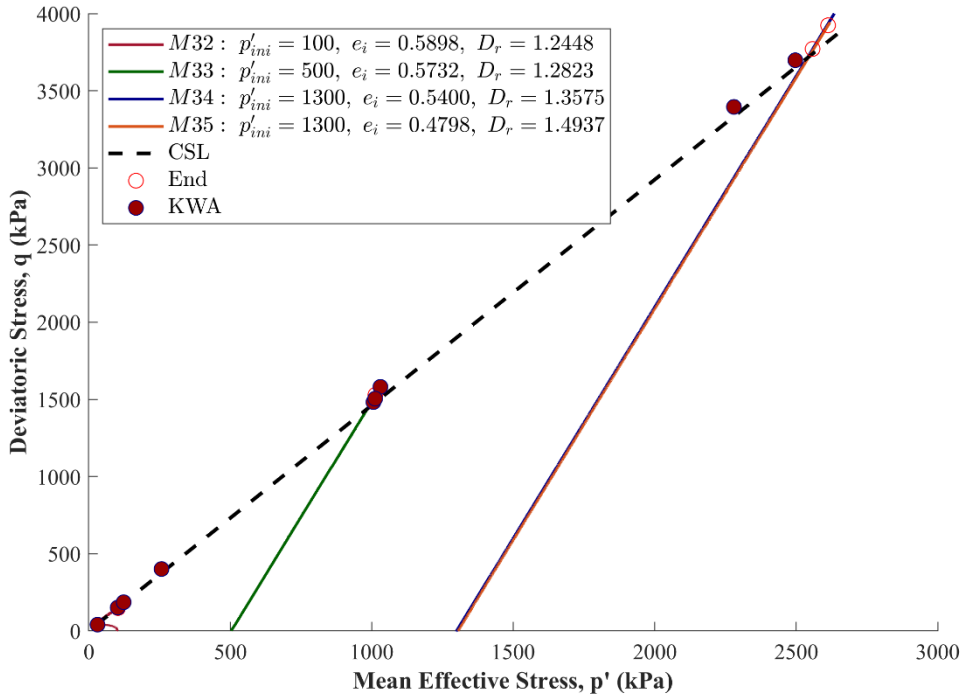

Figure 5.33: Critical State Response of Sydney Sand with 60% Fines (Drained): *q vs p'* space

Figures 5.24 and 5.25 present the drained triaxial test results for Sydney Sand (0% fines), plotted in e–log(σ_3') and q–p spaces, respectively. Although tests were conducted on both loose and dense specimens, many were terminated prematurely before reaching critical state conditions. This early termination was primarily due to shear band formation or limitations in the testing apparatus, such as the LVDTs reaching their maximum range. Despite not fully achieving large strains, the convergence of loose and dense test paths particularly in the q–p plots allowed for a reasonable estimation of the critical state line (CSL).

Figures 5.26 and 5.27 show undrained test results for Sydney Sand. In these tests, the extremely loose specimen (M17) reached critical state, as the stress and void ratio conditions were favourable for steady-state deformation. However, for the denser samples, critical state was not reached. As discussed earlier, this was not due to limitations in strain capacity but rather due to a rapid increase in pore pressure during shearing, which caused the effective confining stress (σ_3') to drop to zero. While mean effective stress (p') includes contributions from both axial and confining stress components, the vanishing of σ_3' significantly reduces p' and affects the ability of the sample to sustain further shear. This condition interrupted the path to critical state, especially in dense samples, where larger strains would otherwise be required.

Figures 5.28 to 5.33 present the CSL representation for SS20F, SS40F, and SS60F mixtures. In these cases, most tests both loose and dense clearly approached or reached the critical state in both e–log(σ_3') and q–p spaces. This improved clarity in critical state convergence is attributed to better confinement and more uniform shearing behaviour in fines-containing mixtures. Exceptions include a few medium-dense samples (e.g., M23 and M30), which deviated from the trend, not achieving large strains and maintaining effective confining stress. While Sydney Sand and Sydney Sand with 20% fines exhibited unique Critical State Lines (CSLs), Kwa (2019) reported that mixtures with 40% and 60% fines may display different CSLs for initially dense and loose samples, indicating a possible divergence in critical state

behaviour depending on initial conditions. This observation is particularly relevant because the constitutive model employed in this study assumes a unique CSL for each material. If dual CSLs do exist in transitional fines mixtures, as suggested by Kwa, it highlights a limitation of this modelling assumption. Transitional behaviour where the mechanical response is influenced by both material composition and initial density, or compaction method challenges the premise of a single critical state surface. Such discrepancies can affect the model's ability to capture post-yield behaviour and may result in inaccurate predictions under cyclic or complex loading conditions.

In this study, calibration parameters were derived from loose specimens, as most tests were conducted on samples prepared in a loose state. However, this simplification may not fully represent the behaviour of dense transitional mixtures. Interestingly, sample M35, although medium dense, approached the Critical State Line similarly to other dense specimens, but notably, it converged toward the same unique CSL that was defined by the loose samples. This behaviour is further discussed in the section on CSL trends in WGS mixtures.

The critical state friction angle (ϕ_{cs}) varied significantly across the samples. Pure silt exhibited the highest ϕ_{cs}, while sand-silt mixtures showed lower values. Notably, samples with 40% and 60% fines had ϕ_{cs} values similar to pure silt as also reported in Kwa (2019), whereas those with 20% fines had a ϕ_{cs} closer to pure sand. These findings suggest a non-linear relationship between fines content and ϕ_{cs}, with silt dominating frictional behaviour at higher fines contents (40% and 60%) and sand controlling at lower fines content (20%).

A closer examination of the Critical State Line slope (λ) reveals additional trends. For Sydney Sand with 0% fines, λ was 0.39, increasing to 0.58 for SS20F and peaking at 0.60 for SS40F, followed by a slight reduction to 0.562 for SS60F. This variation suggests that the addition of fines initially increases soil compressibility due to changes in particle arrangement and pore structure. The minor decrease in λ at 60% fines, as discussed earlier, may be attributed to a

shift in dominant fabric or a denser packing associated with silt-rich matrices. These observations are consistent with findings by Thevanayagam et al. (2002) and Lade et al. (1998), who reported that increasing fines content alters critical state parameters, especially when fines become the governing phase in soil behaviour.

5.3.4 Stress Strain Response of WGS Family

This section presents the results of confirmatory triaxial tests conducted on well-graded sand (WGS) mixtures with varying fines contents to validate and extend the findings reported by Kwa (2019). The WGS mixtures were prepared using the same grading envelope and material types used in the previous study. Four different fines content levels 18%, 28%, 40%, and 60% were used, denoted as WGS18F, WGS28F, WGS40F, and WGS60F respectively. The goal was to replicate the Critical State Line (CSL) and examine the effect of fines content on the mechanical behaviour of the soil under monotonic triaxial loading.

Figures 5.34 to 5.40, illustrate the stress-strain responses of the tested WGS mixtures under varying confining pressures. For each fines content, tests were conducted on loose to medium dense specimens at low (100 kPa) and high (500 kPa) effective confining pressures. Two tests were performed for each mixture to confirm the critical state line. These tests complement the dense sample tests previously conducted by Kwa (2019), enabling a more complete evaluation of the material's stress-strain response across a broader density range.

The stress–strain curves for the WGS mixtures exhibited typical strain-hardening behaviour, where deviatoric stress increased with axial strain until reaching a peak, followed by either strain-softening or a gradual transition to steady state. This observation is important because it reflects the inherent frictional resistance and interlocking among the angular particles in the well-graded sand, including the basalt aggregates. Strain-hardening in these mixtures suggests that particle rearrangement and dilation dominate the shearing process, which is typical of dense, granular materials with high angularity and a broad grain-size distribution. Almost all

samples demonstrated uniform deformation at failure, indicating a consistent failure mechanism across varying fines contents. However, the nature and extent of this response differed considerably with fines content, highlighting the influence of fine particles on load transfer, dilation potential, and post-peak behaviour.

For specimens with lower fines content (WGS18F and WGS28F), higher peak strengths and stiffer initial responses were observed across both confining pressure levels. These mixtures displayed a clearer and more pronounced transition from initial contraction to dilation in medium dense samples. In particular, the onset of dilation was observed around 5–7% axial strain, with the stress-strain response showing a post-peak reduction in deviatoric stress followed by a stable plateau, indicating a steady-state condition consistent with the critical state framework. This behaviour suggests a dominance of the coarse-grained skeleton, where grain interlocking and angularity contributed to a relatively dense and dilative structure under shear.

As the fines content increased (WGS40F and WGS60F), a progressive reduction in peak strength and stiffness was observed. These mixtures demonstrated more compressible behaviour, with the deviatoric stress developing gradually and the peak being less distinct, particularly in loose specimens. Medium dense samples of these mixtures exhibited little to no dilation, and the stress–strain response tended to plateau rather than soften after peak, indicating a more contractive or neutral behaviour approaching critical state. The presence of higher fines likely disrupted the force chains within the granular matrix, leading to reduced interparticle contact between coarse grains and a fabric more susceptible to compression.

Under higher confining pressure (500 kPa), the peak strength increased across all mixtures, as expected due to increased mean effective stress. However, the difference in behaviour among mixtures remained evident. The strength gain with pressure was more prominent in the low fines' mixtures, while the response in high fines specimens showed more subdued increases,

especially in loose states. The role of fines in altering the compressibility and contact mechanics of the mixture became more apparent under these conditions.

These test results indicate that mixtures with lower fines content are more dilative and stiffer, particularly at medium densities, while mixtures with higher fines are more contractive and compressible, resulting in lower peak strengths and a more gradual transition to critical state. These trends are consistent with expectations based on the influence of fines on particle packing, load transfer, and dilatancy mechanisms.

To further support the identification of critical state and assess test reliability, normalized stress ratio plots (q/p_c' vs axial strain) were generated for each fines content. These plots illustrate the convergence of stress ratio towards a constant value at large strain, indicating approach to critical state. A comparative summary across all mixtures is shown in Figure 5.42, highlighting clearer and faster convergence in low-fines mixtures, and more gradual, contractive behaviour in high-fines mixtures. These plots reinforce the reliability of the triaxial data and serve as an effective tool to validate the CSL assumption for each material.

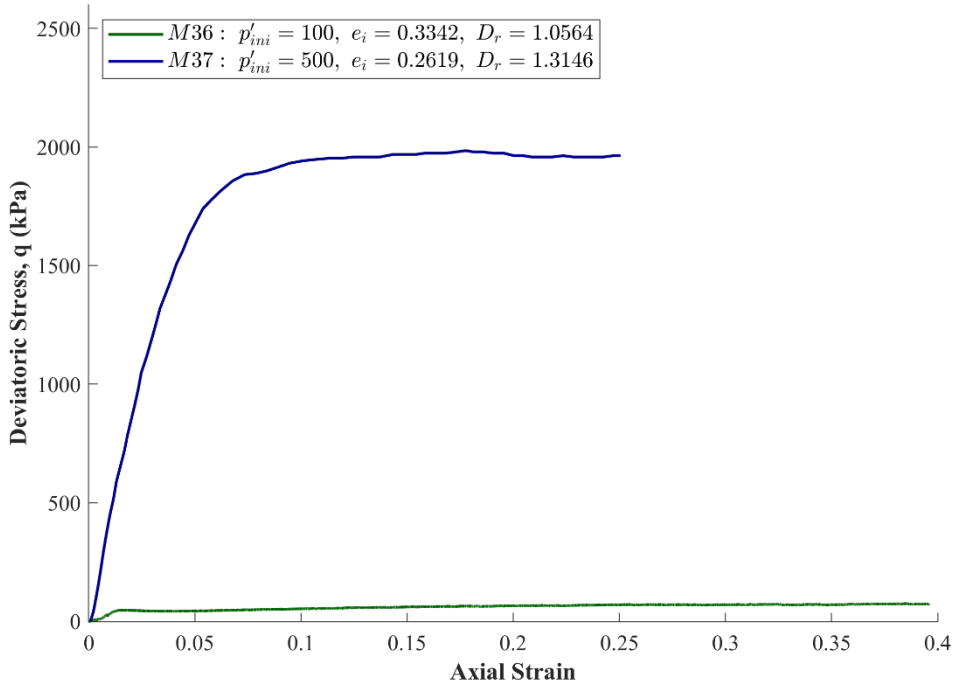

Figure 5.34: Stress Strain response: Well Graded Sand with 18% Fines

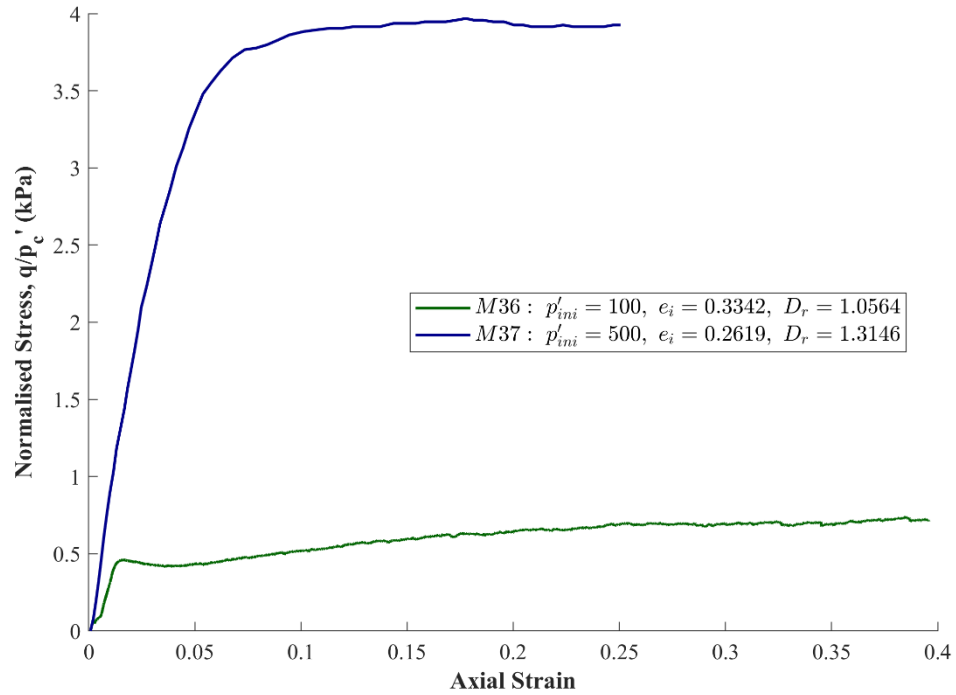

Figure 5.35: Normalised Stress vs Axial Strain - Well Graded Sand with 18% Fines

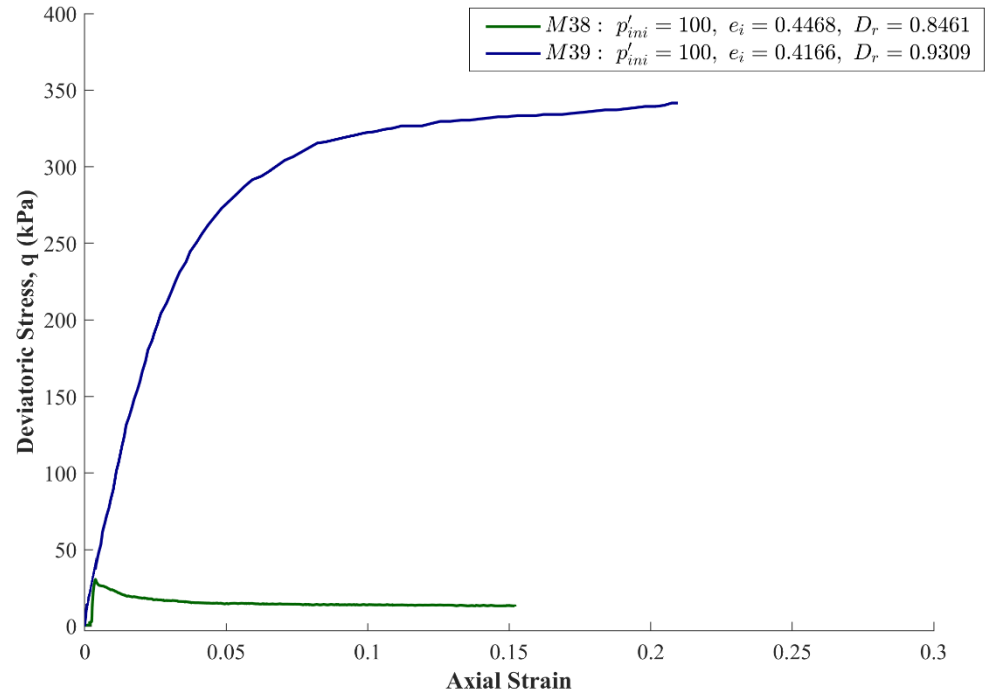

Figure 5.36: Stress Strain response: Well Graded Sand with 28% Fines

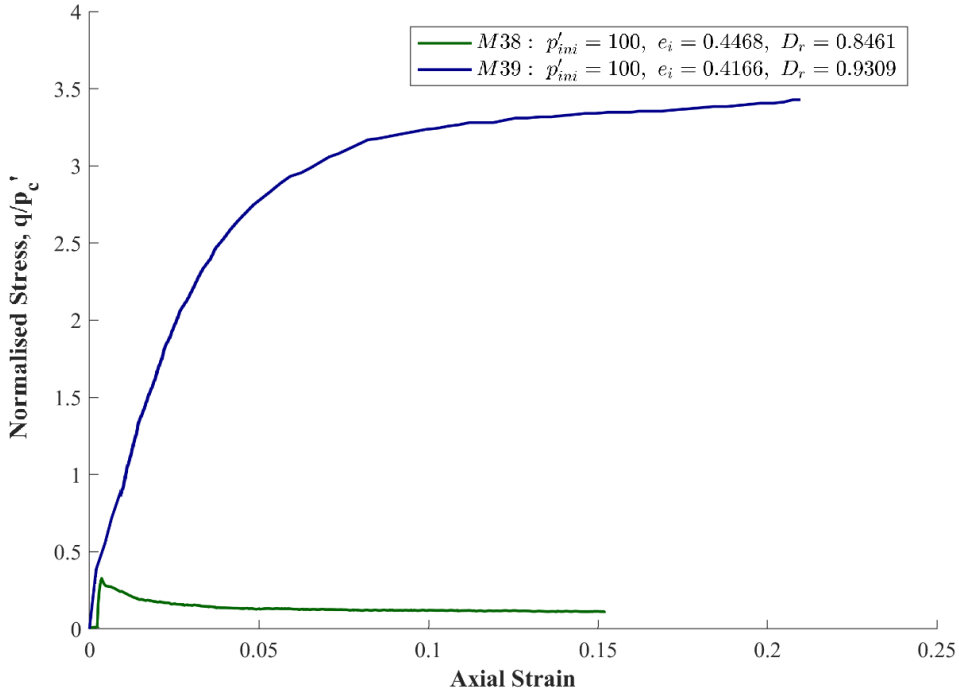

Figure 5.37: Normalised Stress vs Axial Strain - Well Graded Sand with 28% Fines

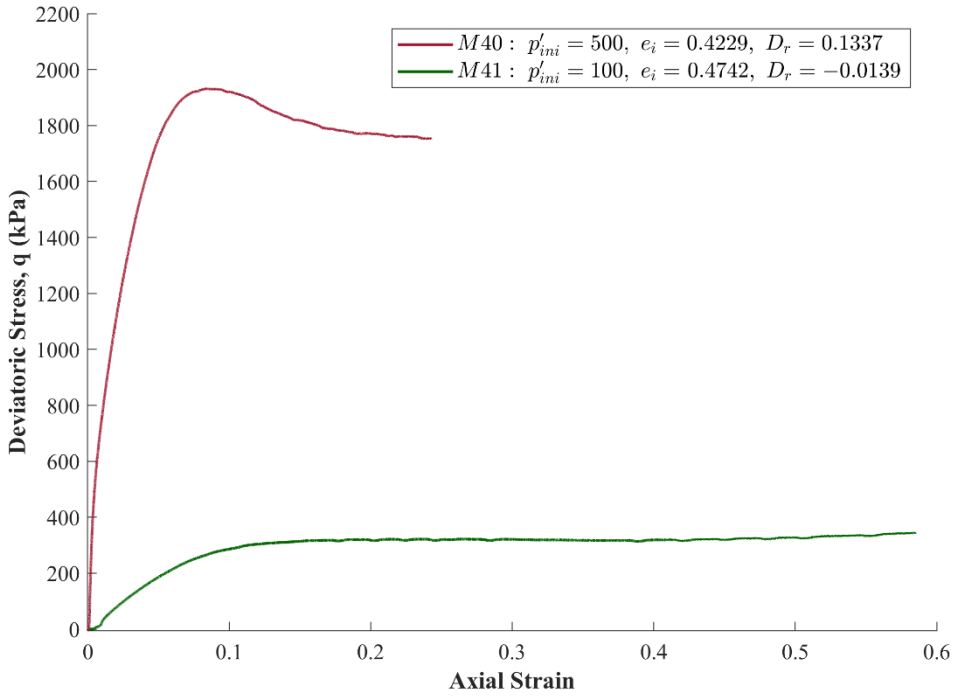

Figure 5.38: Stress Strain response: Well Graded Sand with 40% Fines

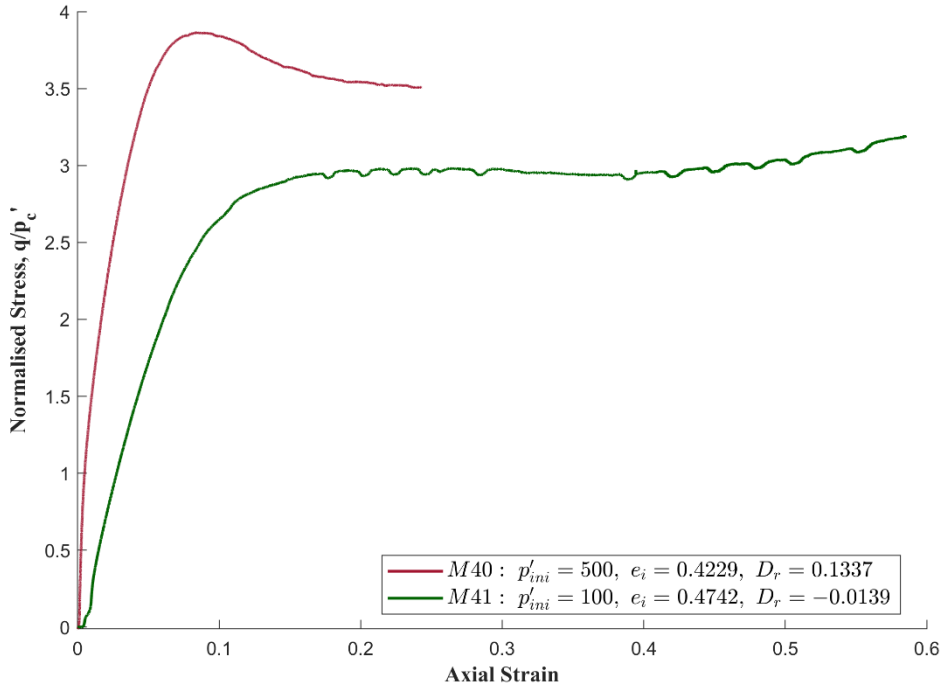

Figure 5.39: Normalised Stress vs Axial Strain - Well Graded Sand with 40% Fines

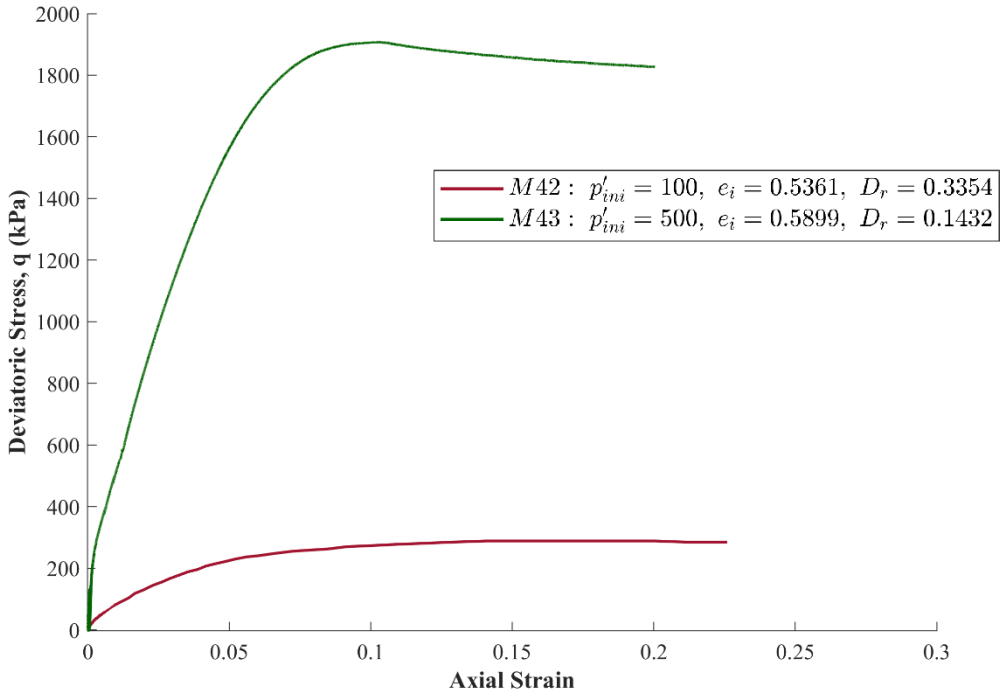

Figure 5.40: Stress Strain response: Well Graded Sand with 60% Fines

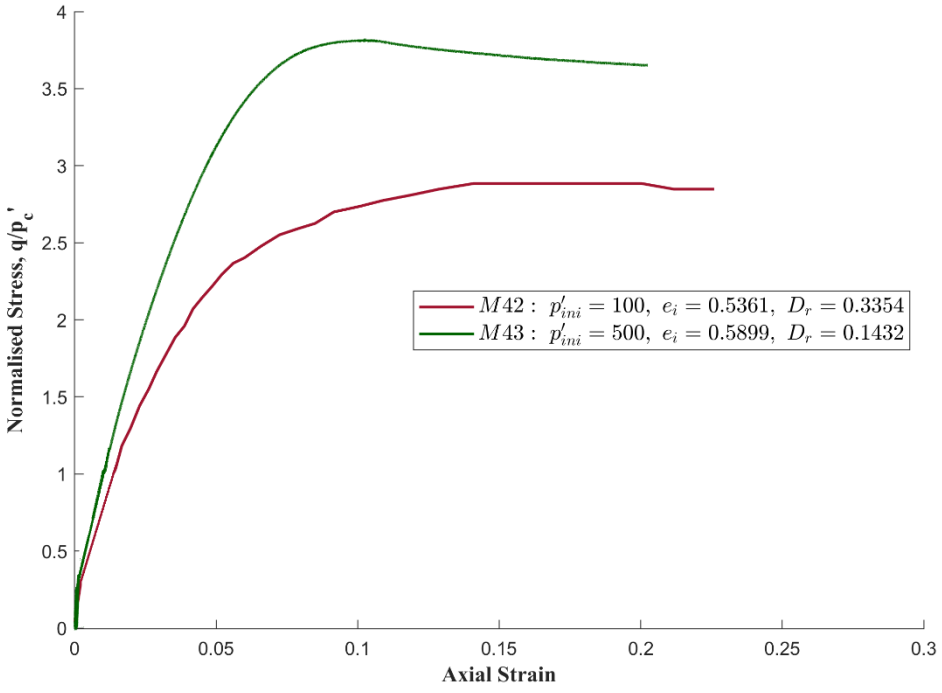

Figure 5.41: Normalised Stress vs Axial Strain - Well Graded Sand with 60% Fines

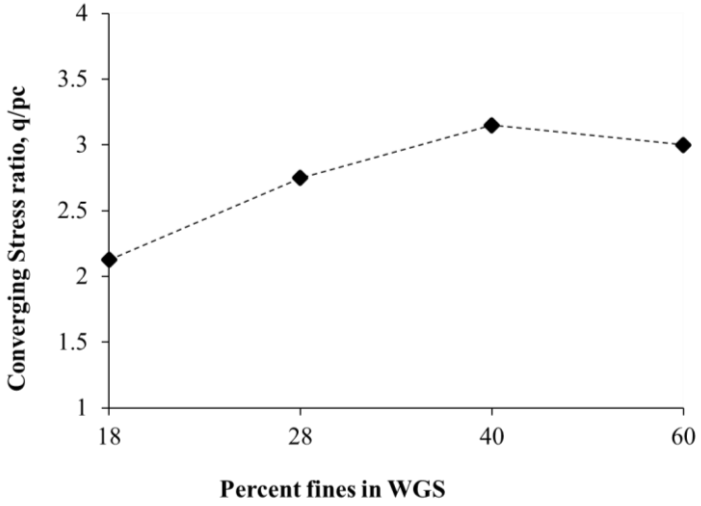

Figure 5.42: Comparison of Converging Stress Ratio - WGS Family

5.3.5 Volumetric Response of WGS Family

The volumetric responses of WGS samples are presented in Figure 5.43, providing valuable insights into the soil's behaviour under various stress conditions. These responses provide the compressibility and dilation characteristics of the mixtures under shear loading and complement the interpretations made from the stress–strain data discussed in the previous section. It is important to note that the volumetric responses for undrained tests are not plotted due to the constant volume nature of these tests and addressed in terms of pore pressure response. Additionally, a few drained tests were not recorded with their volumetric responses, and consequently, these are not included in the volumetric response graphs or the Critical State Line (CSL) plots in void ratio and stress space.

As expected, loose specimens across all fine's contents exhibited contractive behaviour throughout the shearing process. However, the magnitude and persistence of contraction varied with fines content. Specifically, WGS40F and WGS60F mixtures showed more pronounced volume reduction, consistent with their more compressible structure and lower peak strengths, as discussed in the stress–strain response section. These responses reflect the influence of

higher fines content, which tends to reduce intergranular contacts between coarse particles and results in a structure that compresses more readily under shear.

Medium dense specimens showed a more diverse range of volumetric behaviours, which is closely linked to their position relative to the CSL. In WGS18F and WGS28F, medium dense specimens typically displayed an initial contraction phase, followed by a distinct onset of dilation beyond approximately 5–7% axial strain. This transition corresponds to the phase where deviatoric stress peaks and begins to soften or stabilise, consistent with a dilative volumetric trend. The volume expansion observed in these cases supports the presence of a dense, interlocked granular skeleton resisting further compression.

In contrast, WGS40F and WGS60F medium dense specimens displayed significantly reduced dilation, and in many instances, the volumetric response remained contractive or stabilised at near-zero volume change. As previously noted, these specimens developed deviatoric stress gradually and exhibited minimal softening, indicating limited particle rearrangement and a more compressible, fines-dominated fabric. These volumetric trends observed across the WGS mixtures strongly align with the mechanical responses described in the stress–strain section. Mixtures with lower fines content consistently showed a dilative response in medium dense states, while those with higher fines content remained contractive throughout shearing.

As similarly discussed for Summary of saturated tests (Section 4.3.1), the interpretation of relative density (D_r) becomes increasingly unreliable in silty or fines-rich mixtures, such as SS40F, SS60F, WGS40F and WGS60F. D_r may give misleading indications of the sample's compactness or behavioural tendencies. Instead, a more robust interpretation can be made by evaluating the sample's position relative to its Critical State Line (CSL). In this framework, specimens that remain compressive during shearing are likely to have been initially located above the CSL, while those that exhibit dilation such as the medium dense WGS18F and WGS28F samples are inferred to have started below the CSL, consistent with a denser state.

This reinforces the importance of considering the state parameter in understanding soil behaviour, particularly in transitional or fines-dominated mixtures where conventional indices like D_r lose validity.

All specimens tested under drained conditions exhibited bulging failure without the formation of distinct shear bands, indicating largely uniform deformation. As previously discussed in the Sydney Sand's Critical State discussion (Section 4.3.3), this deformation pattern allows for reliable interpretation of volumetric strains up to and beyond peak stress. In contrast, dense specimens tested by Kwa (2019) often showed shear localisation, which can compromise volumetric data accuracy post-peak.

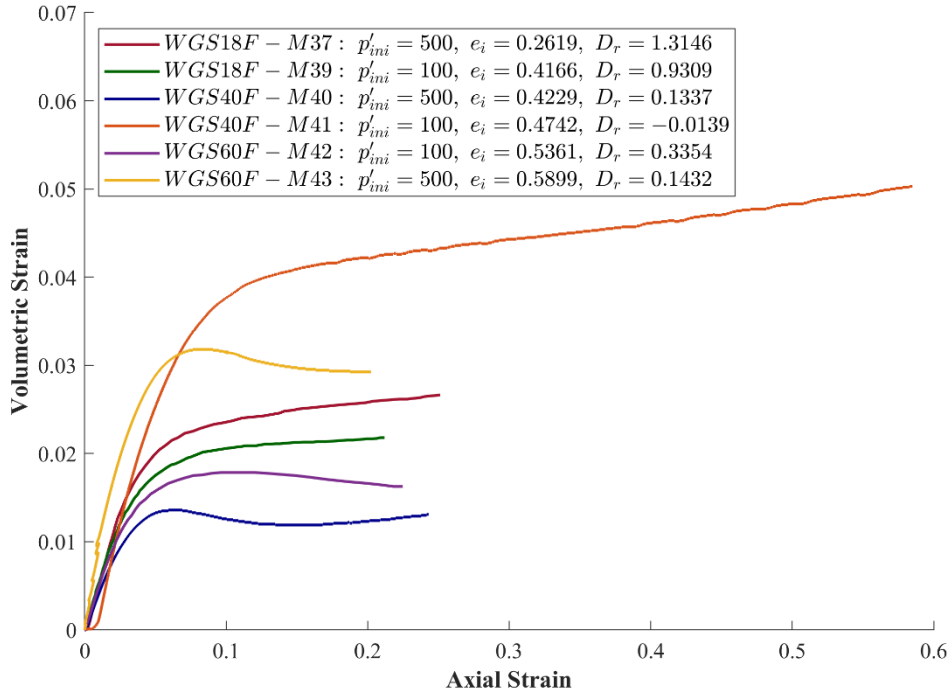

Figure 5.43: Volumetric Response: Well Graded Sand Family

5.3.6 Critical State and CSL Parameters of WGS Family

The critical state line (CSL) for WGS has been plotted in both stress space (p'-q) and void ratio-logarithmic mean effective stress space (e-log p') in Figures 5.44 to 5.51. These plots incorporate the consolidated results from all available test data, including those from the

current study and previous research by Kwa (2019). The critical state parameters derived from these plots are summarized in Table 5.9, demonstrating a strong correlation between the current study's findings and the CSL established by Kwa (2019).

For WGS with 18% fines (WGS18F), a unique and well-defined CSL was observed across all initial states tested, converged to a common CSL in e–log p′ space, indicating a stable soil fabric dominated by the coarse-grained skeleton. As the fines content increased (WGS28F, WGS40F, and WGS60F), the convergence pattern remained broadly consistent. Most samples, including those prepared at medium densities, continued to approach the same CSL, demonstrating that the critical state surface remains unified even as the fines content increases, at least under the current sample preparation method.

Interestingly, this observation differs from what was previously reported by Kwa (2019), who found that dense specimens of WGS and Sydney Sand mixtures, particularly those with higher fines content defined a separate critical state line, distinct from the CSL approached by looser samples. The key difference appears to lie in the sample preparation methodology. Kwa's dense samples were compacted using Fagerberg's Compaction Hammer D, which imparts a higher and more localised compaction energy. This method likely created a more interlocked particle fabric and led to a denser, anisotropic structure that evolved along a different critical state path during shearing. This divergence in CSL behaviour between the two studies underscores the critical role of fabric and initial packing structure in defining critical state conditions. While Kwa's results suggested a state-dependent CSL due to densification effects, the findings in the present study indicate that dense samples, when prepared under consistent, low-energy tamping methods, tend to evolve toward the same critical state as loose samples. It is therefore reasonable to consider dual CSL behaviour as a possible outcome of variations in soil fabric, particularly when dense states are achieved through different compaction techniques.

This is an important insight, as it underscores the need for consistent and well-documented sample preparation protocols when interpreting critical state behaviour, especially in soils with transitional fines content. It also highlights a limitation in the classical CSSM framework, which assumes a unique critical state surface regardless of initial state or fabric. The findings from the current study support the view that when prepared using tamping, transitional fines mixtures exhibit a consistent CSL across initial densities, while also confirming that dual CSL trends can emerge under alternative compaction methods, as reported by Kwa (2019). This reinforces the importance of fabric effects in critical state soil mechanics and provides valuable input for refining constitutive models to account for such behaviour.

Table 5.9: Critical State Parameters: WGS Family

S.no	Material	ϕ_{cs}	M	λ	N_c	α_{csl}
1	Well Graded Sand – 18% Fines	42	1.722	0.6	36	3500
2	Well Graded Sand – 28% Fines	40	1.636	0.58	55	5000
3	Well Graded Sand – 40% Fines	37	1.593	0.52	40.5	6000
4	Well Graded Sand – 60% Fines	37	1.506	0.45	26.3	6000

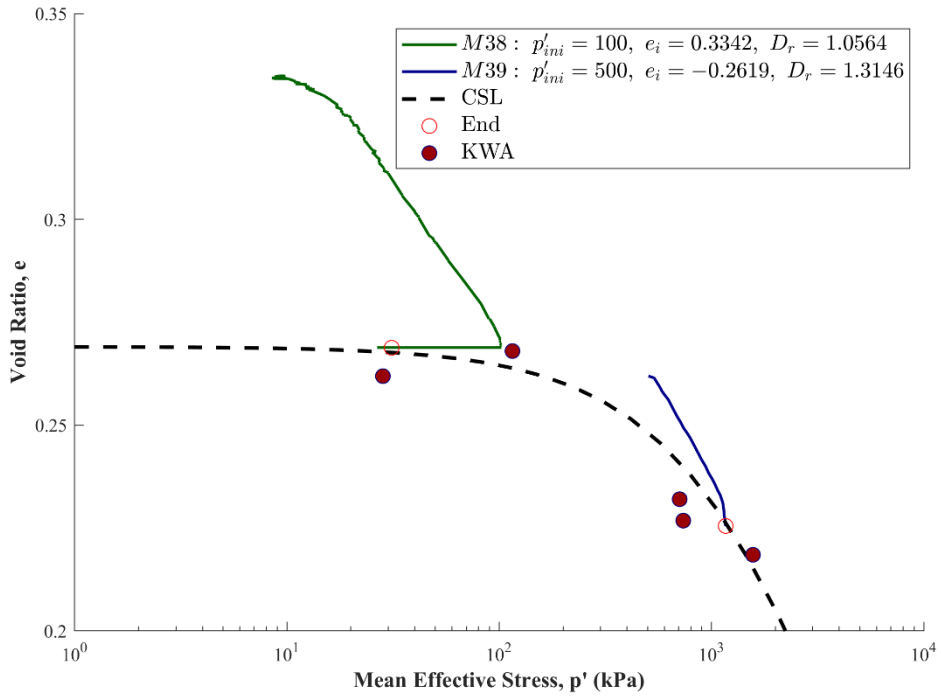

Figure 5.44: Critical State Response - Well Graded Sand - 18% Fines: *e vs logp'* space

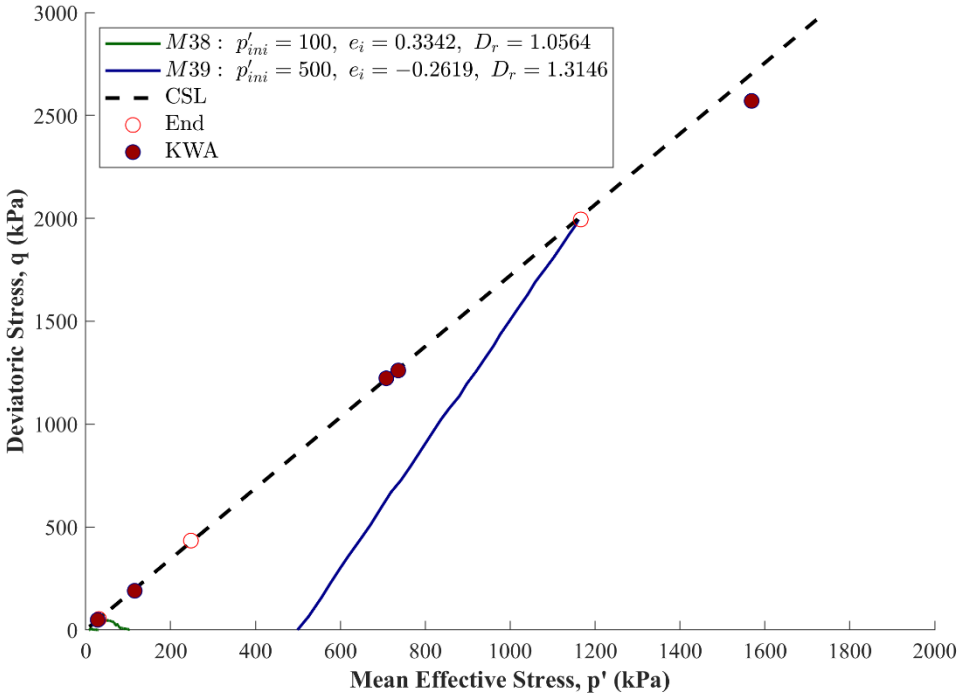

Figure 5.45: Critical State Response - Well Graded Sand with 18% Fines: *q vs p'* space

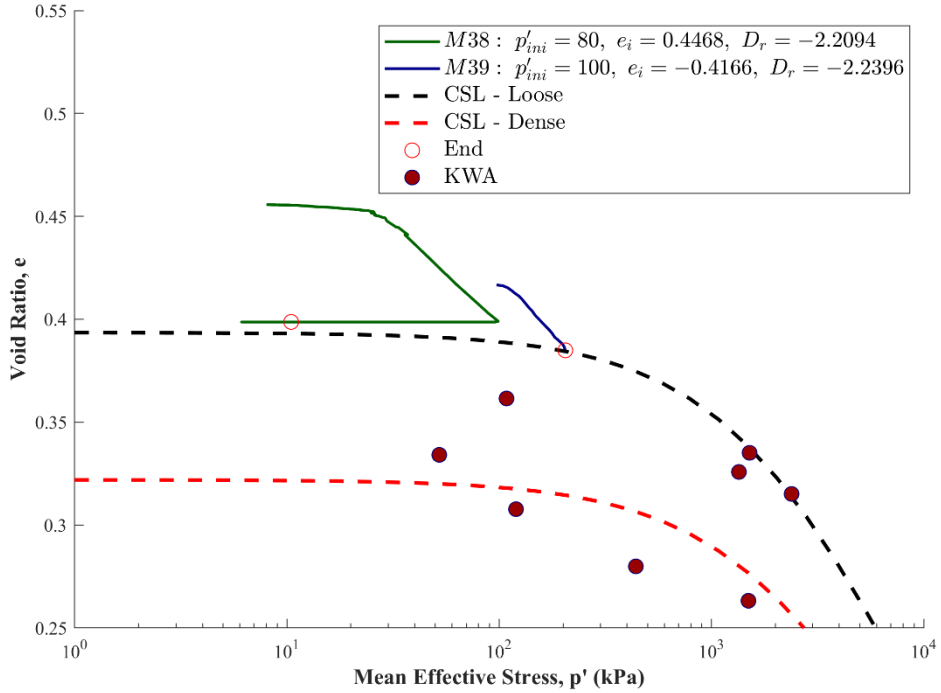

Figure 5.46: Critical State Response - Well Graded Sand - 28% Fines: *e vs logp'* space

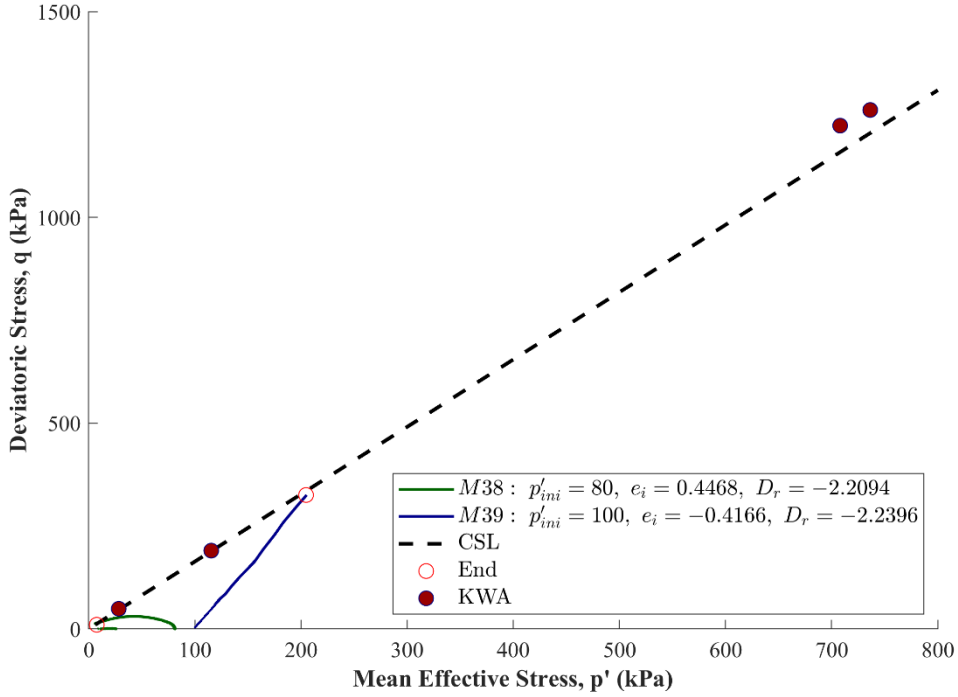

Figure 5.47: Critical State Response - Well Graded Sand with 28% Fines: *q vs p'* space

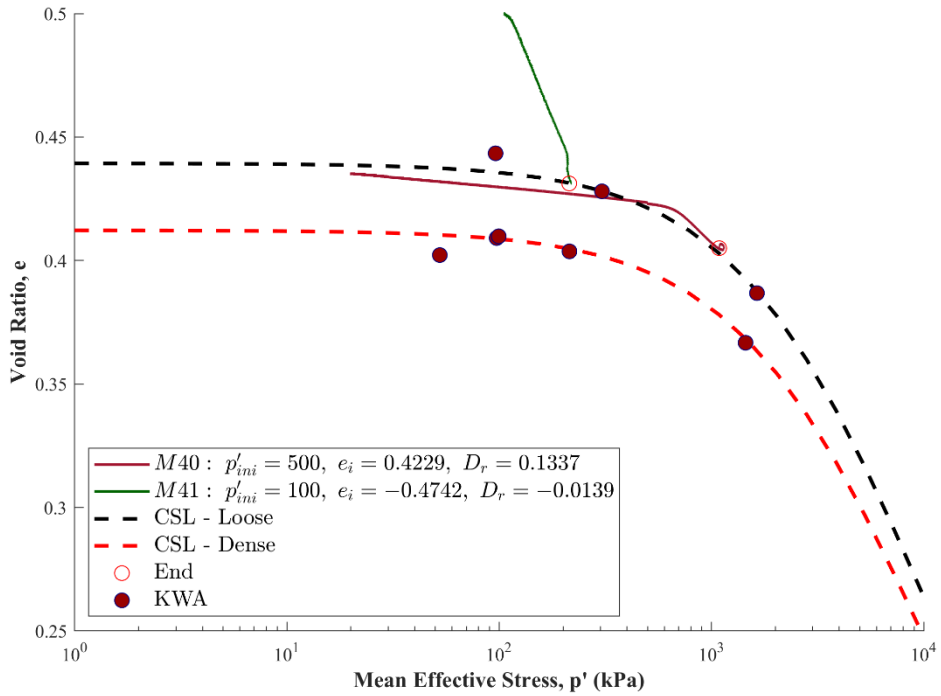

Figure 5.48: Critical State Response - Well Graded Sand - 40% Fines: *e vs logp'* space

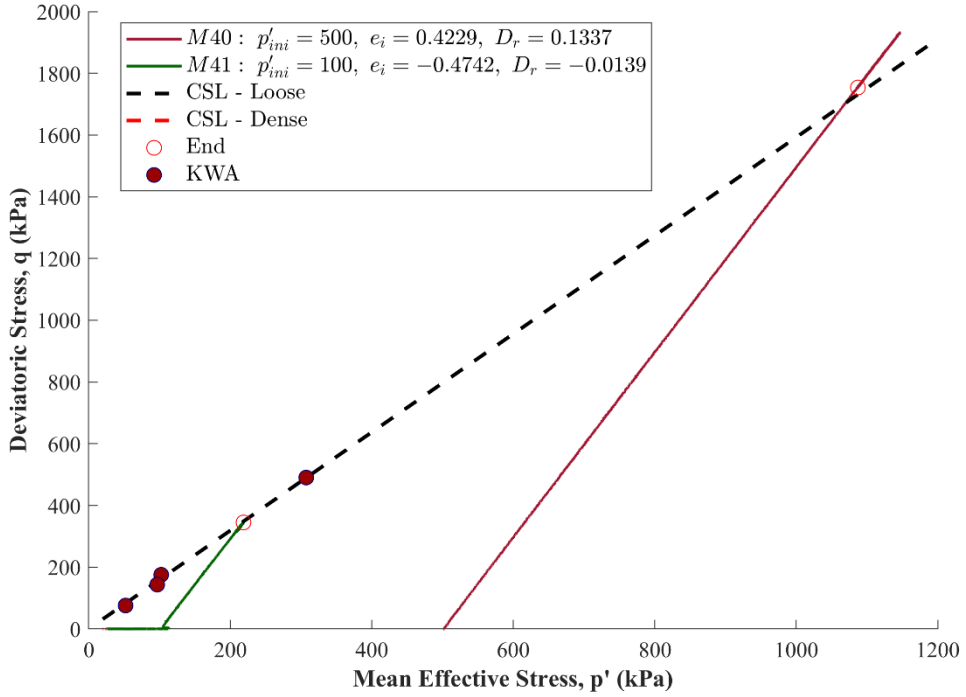

Figure 5.49: Critical State Response - Well Graded Sand with 40% Fines: *q vs p'* space

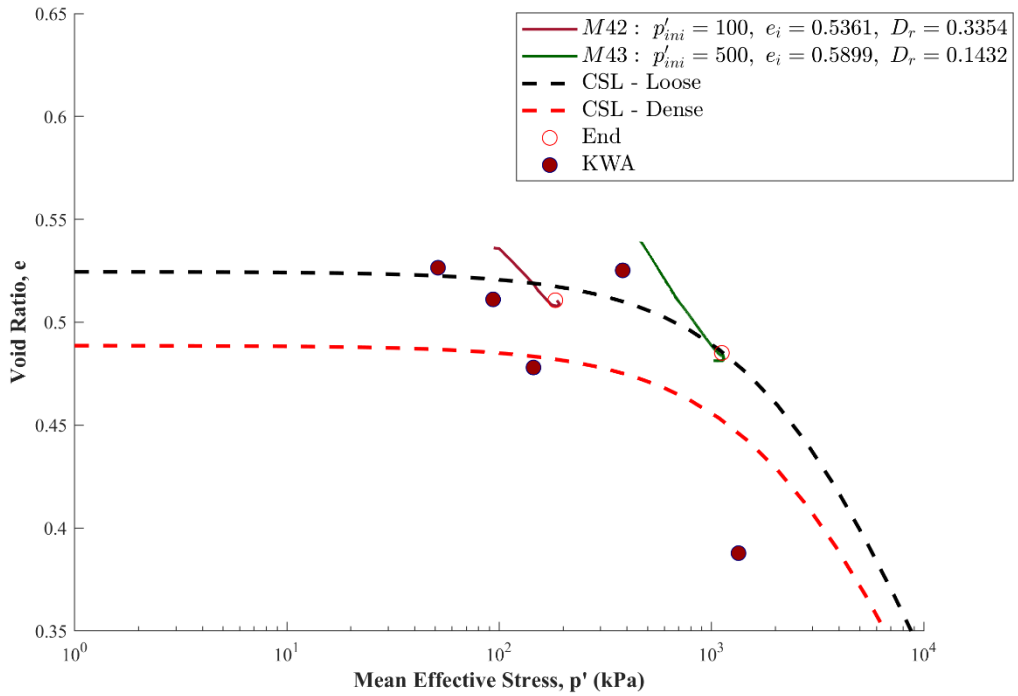

Figure 5.50:Critical State Response - Well Graded Sand - 60% Fines: *e vs logp'* space

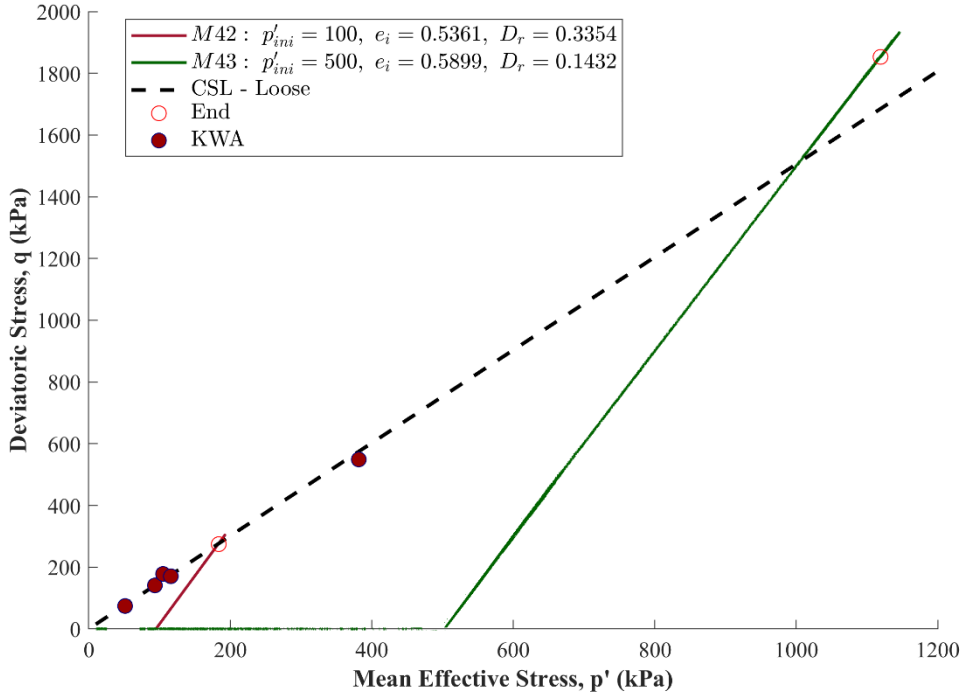

Figure 5.51: Critical State Response - Well Graded Sand - 60% Fines: *q vs p'* space

5.3.7 CSL Summary

The critical state parameters obtained from this comprehensive testing program serve as crucial inputs for the calibration and validation of advanced constitutive models. By establishing the Critical State Line (CSL), these models can capture the soil's behaviour across a wide spectrum of stress and density states for a range of particle size distributions. This enhanced capability enables reliable predictions of soil response under diverse loading conditions, a factor of paramount importance in geotechnical design and analysis involving varied soil compositions. The study's approach of calibrating the models with two distinct soil types - Sydney sand and Well Graded Sand (WGS) made from basalt aggregates, each with different fines contents - provides a robust foundation for understanding and predicting soil behaviour. Sydney sand, with its range of fines contents, represents a typical quartz-based soil commonly encountered in many geotechnical projects. On the other hand, WGS, being a manufactured sand composed of basalt aggregates with particle sizes ranging from 9.5 to 0.15mm, offers insights into the behaviour of materials with different mineralogical compositions and particle size distributions. The inclusion of a manufactured sand like WGS also provides valuable insights into the performance of engineered materials in geotechnical applications, bridging the gap between natural soils and custom-designed geomaterials. This dual-soil approach ensures that the calibrated models are versatile and applicable to a broader range of geological conditions.

By systematically varying the fines content in both soil types, the research captures the nuanced effects of particle size distribution on critical state behaviour. Within the framework of Critical State, the experimental results obtained from eight soil mixtures ranging from clean Sydney Sand (SS0F) to fines-rich Well-Graded Sand (WGS60F), demonstrate how particle size distribution and fines content fundamentally govern the location, shape, and uniqueness of the CSL in both q–p′ and e–log p′ spaces. These variations have direct implications for the accurate formulation and validation of constitutive models that rely on critical state concepts.

In the Sydney Sand family, the clean sand (SS0F) showed a distinct and consistent CSL across densities, characterised by a critical stress ratio M = 1.2 and a CSL slope λ = 0.39. With increasing fines content, the CSL shifted upward and steepened (λ = 0.60 for SS40F), indicating greater compressibility, while M increased to 1.462 in SS40F and SS60F. A slight decrease in slope at 60% fines (λ = 0.562) was observed, likely due to increased particle-to-particle friction and reduced rearrangement potential in a fines-dominated matrix.

These deviations in CSL slopes at higher fines contents may not only be a function of packing density but could also reflect the influence of mineralogy and particle shape. Quartz-based Sydney Sand fines, being sub-rounded, allow for greater rearrangement at moderate contents, but when fines dominate, inter-particle friction increases, and compressibility reduces. By contrast, the angular, rough-textured basalt fines in WGS mixtures create interlocking structures that steepen or flatten CSL trends differently. Thus, both mineralogical differences (quartz vs basalt) and particle morphology (rounded vs angular) provide a plausible explanation for the observed non-linear CSL behaviour.

While earlier studies, such as Kwa (2019), reported dual CSLs for Sydney Sand mixtures with high fines content particularly under dense conditions compacted using Fagerberg's hammer, this aspect could not be evaluated here as no dense specimens were tested for SS40F and SS60F in the current program. As such, the effect of high-energy compaction and its influence on packing structure was not explored for the Sydney Sand family in this study.

In practical terms, this presents a modelling challenge: if the soil exhibits multiple critical states for the same material but different fabric conditions, constitutive models assuming a single CSL will fail to capture the correct post-yield path and may mis predict liquefaction or softening thresholds under cyclic or large strain loading.

In contrast, the WGS mixtures provided an opportunity to assess CSL behaviour across varying densities and packing structures. WGS18F displayed a steep CSL (λ = 0.65, M = 1.722),

reflecting the interlocked, compressible nature of angular particles. As fines content increased, the CSL gradually flattened ($\lambda = 0.45$, $M = 1.506$ at WGS60F), consistent with a transition to a fines-supported matrix and reduced dilatancy. Importantly, medium dense specimens of WGS mixtures prepared using moist tamping also converged to the same CSL as loose samples, suggesting that fabric remained broadly consistent across density ranges. This differs from Kwa (2019), where dual CSLs emerged in dense samples compacted, highlighting the influence of sample preparation. The role of compaction-induced fabric on CSL behaviour is discussed in detail in Section 4.3.6 (WGS Family), where dense WGS samples were tested, allowing for a more complete interpretation.

The position and shape of the CSL in e–log p′ space also highlight the differences in compressibility across mixtures. Sydney Sand, with or without low fines, displayed relatively flatter CSLs indicative of stiff, low-compressibility behaviour. As fines content increased, the CSLs became steeper, particularly for SS20F and SS40F, due to enhanced compressibility. However, the CSL steepness decreased at 60% fines, likely due to fines-dominated packing inhibiting volumetric strain. For WGS mixtures, the steepest CSL appeared at WGS18F and gradually flattened with increasing fines, reflecting a similar reduction in compressibility despite finer gradation. This non-linear trend confirms that both initial gradation and fines content affect not only the slope of the CSL but also its trajectory, and that their interaction is challenging to be captured by any critical state-based constitutive framework.

This extended dataset allows for the development of more sophisticated constitutive models that can account for the transitional behaviour observed in soils with varying fines contents.

5.4 Cyclic Mechanical Behaviour of Sands

Cyclic triaxial tests play a critical role in understanding the evolution of soil behaviour under repeated loading and provide a foundation for calibrating constitutive models that incorporate memory surfaces, accumulation of strain, and semi-fluidized states. In this study, a targeted

program of drained and undrained cyclic triaxial tests was conducted across selected soil mixtures, specifically designed to capture a diverse range of soil responses and stress histories. The focus of this study is not to generate a complete behavioural database, but rather to evaluate the ability of the revised constitutive model to replicate distinct cyclic responses across varying gradations and initial states. Accordingly, a limited number of cyclic tests were strategically chosen to explore key behavioural features, including cyclic densification, fabric change, and critical state attainment under both drained and undrained conditions.

To comprehensively assess the soil behaviour, a diverse range of loading conditions was employed. Some samples were initially subjected to number of cycles of cyclic loading, followed by monotonic shearing to failure. This approach allowed for the evaluation of critical state conditions after cyclic preloading, providing insights into the soil's stress history effects (Wichtmann & Triantafyllidis, 2016). Additionally, tests involving up to 1000 cycles were performed to investigate potential ratcheting behaviour. Ratcheting, or the accumulation of plastic strain under cyclic loading, is a critical consideration in long-term stability analyses of geotechnical structures (Escribano et al., 2019).

During stress-controlled cyclic testing, a common challenge encountered was the overshooting of deviatoric stress beyond the target value. This issue arises from the lag in pore pressure generation and the system's delayed response in reversing the loading direction. To mitigate this effect, reducing the shearing rate is recommended, allowing for better synchronization between applied stress and pore pressure response (Vaid & Sivathayalan, 1996).

Drained cyclic tests were performed on clean Sydney Sand (SS0F) and on Sydney Sand mixtures containing 20%, 40%, and 60% feldspar fines. Undrained cyclic tests were conducted only for the mixtures containing fines, as the cyclic behaviour of clean Sydney Sand in undrained conditions has already been extensively investigated by Mohammadi (2020), whose data was directly used for model validation. All samples were prepared at loose initial states,

consistent with the goal of exploring strain accumulation, densification, and the approach to critical state from the contractive side.

Each specimen was isotropically consolidated and subjected to cyclic loading with fixed deviatoric stress amplitude, using either single-stage or multi-stage loading tests. A representative test for each material and condition is presented in Figures 5.52 to 5.59. In multi-stage tests, such as the one illustrated in Figure 5.53, deviatoric stress amplitude was increased in increments (e.g., 100, 200, 400, and 800 kPa). The response to each increment showed a progressive increase in accumulated strain. For example, while the transition from 100 to 200 kPa induced minimal change in axial strain accumulation, the jump from 200 to 400 kPa led to a threefold increase in strain, and at 800 kPa, axial strains exceeded 0.9%, indicating onset of flow.

In undrained cyclic tests (e.g., Figure 5.54 and Figure 5.57), excess pore pressure build-up progressively reduced the effective stress, consistent with the onset of cyclic mobility. However, in some dense specimens (e.g., SS20F), the apparatus reached a point where the effective confining pressure approached zero, compromising control over the stress path. This behaviour, previously observed in monotonic undrained tests, suggests the sample had not yet reached critical state, but further interpretation was limited by the apparatus constraints under insufficient effective stress conditions. This behaviour was observed in C9 (Figure 5.54), only when the sample was sheared monotonically after two stages of cyclic loading. The cyclic deformation is minimal compared to the monotonic shearing.

A particularly important observation was made in all drained cyclic tests on loose specimens: repeated cyclic loading caused clear cyclic densification. This was evident in the reduction of void ratio after cycling, and the resulting post-cyclic monotonic shearing behaviour exhibited characteristics of dense samples, including dilation and upward curvature in the e–log p′ space. This pattern was observed consistently in SS0F, SS20F, SS40F, and SS60F. Despite being

prepared loose, the cumulative effect of 100 cycles, each contributing less than 0.001 axial strain acted as a dynamic compaction mechanism, pushing the soil into a denser state. During post-cyclic monotonic shearing, all samples followed a dilative path that approached the loose state CSL, rather than the dense CSL reported in Kwa (2019). This deviation is likely due to the absence of high-energy compaction methods like Fagerberg's hammer in this study. Hence, while void ratios post-cycling may reach values associated with dense states, the resulting soil fabric appears more consistent with dynamically densified loose samples than with statically compacted dense ones.

Due to apparatus discrepancies including frequency misapplication and missing volume change measurements, cyclic test results of WGS soil mixtures were not included. Two tests were attempted for each WGS mixture but were excluded from interpretation due to reliability concerns. This limited their inclusion in the main cyclic analysis.

To support interpretation of cyclic test behaviour, summary plot for Sydney Sand in Figure 5.60 presents the evolution of void ratio and mean effective stress (e–log p′) after cycling for SS0F. This plot confirms that the critical state is ultimately attained after cyclic densification. This further supports the role of repeated loading in promoting fabric rearrangement and strain hardening, even in initially loose states.

It is acknowledged that failure data is missing for some drained cyclic tests, particularly due to the fact that many samples continued to accumulate strain without reaching a defined failure envelope during cycling. Moreover, cyclic drained loading inherently increases density, reducing the likelihood of instability or flow failure during the cycles themselves. Instead, failure tended to occur during subsequent monotonic shearing and was accompanied by dilation in most cases. The final states of these materials, show clear convergence toward their respective CSLs, reaffirming the applicability of CSSM even in cyclic contexts.

This interpretation is critical for model calibration. A constitutive model designed to capture cyclic response must simulate not only stress-strain loops and strain accumulation but also the evolution of void ratio and effective stress toward the critical state. The results from this study provide valuable benchmarks for model validation, particularly in their ability to capture cyclic densification, delayed dilation, and CSL convergence under both drained and undrained loading conditions.

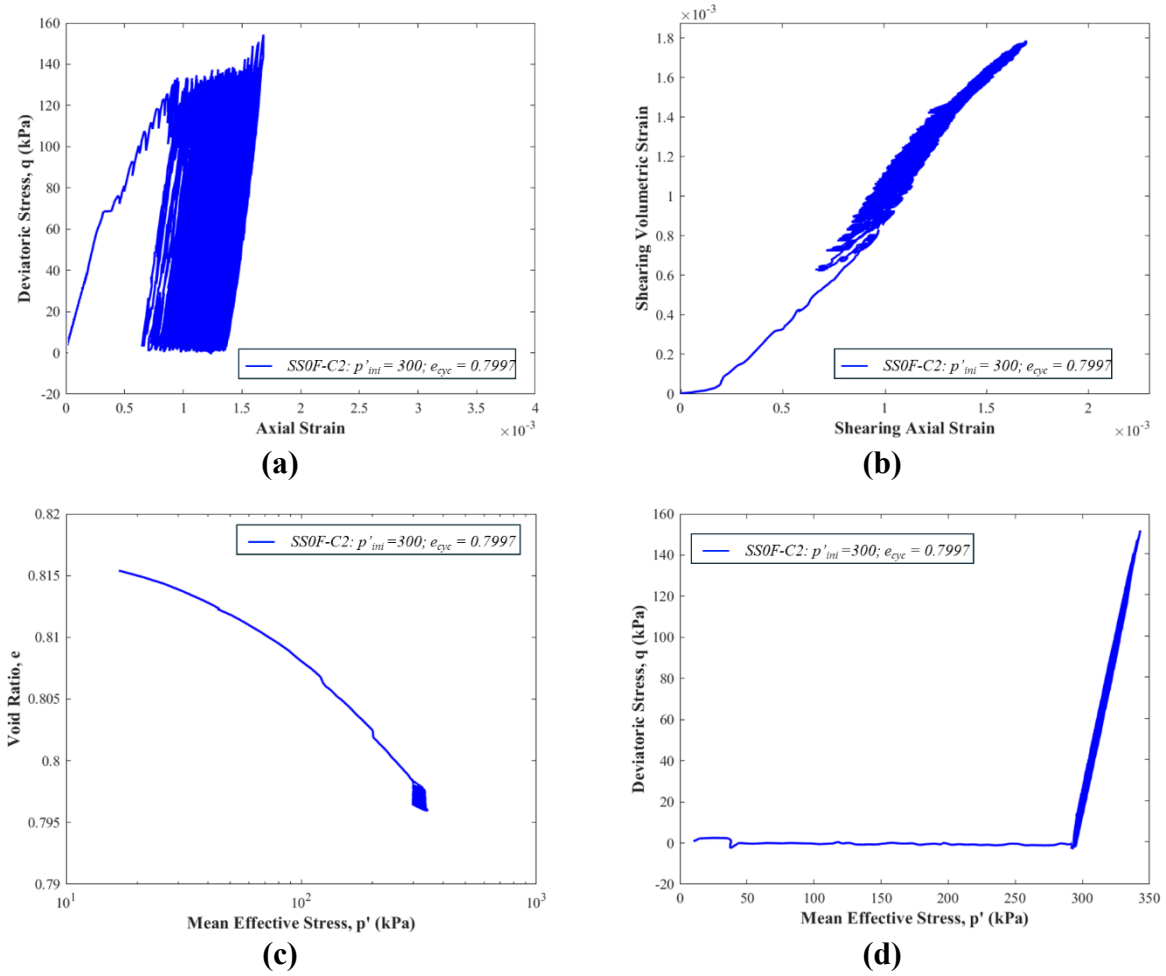

Figure 5.52: Drained cyclic behaviour of Sydney Sand: (a) Stress strain response, (b) Volumetric response, (c) Stress path in void ratio vs log p' space, (d) Stress path in q vs p' space

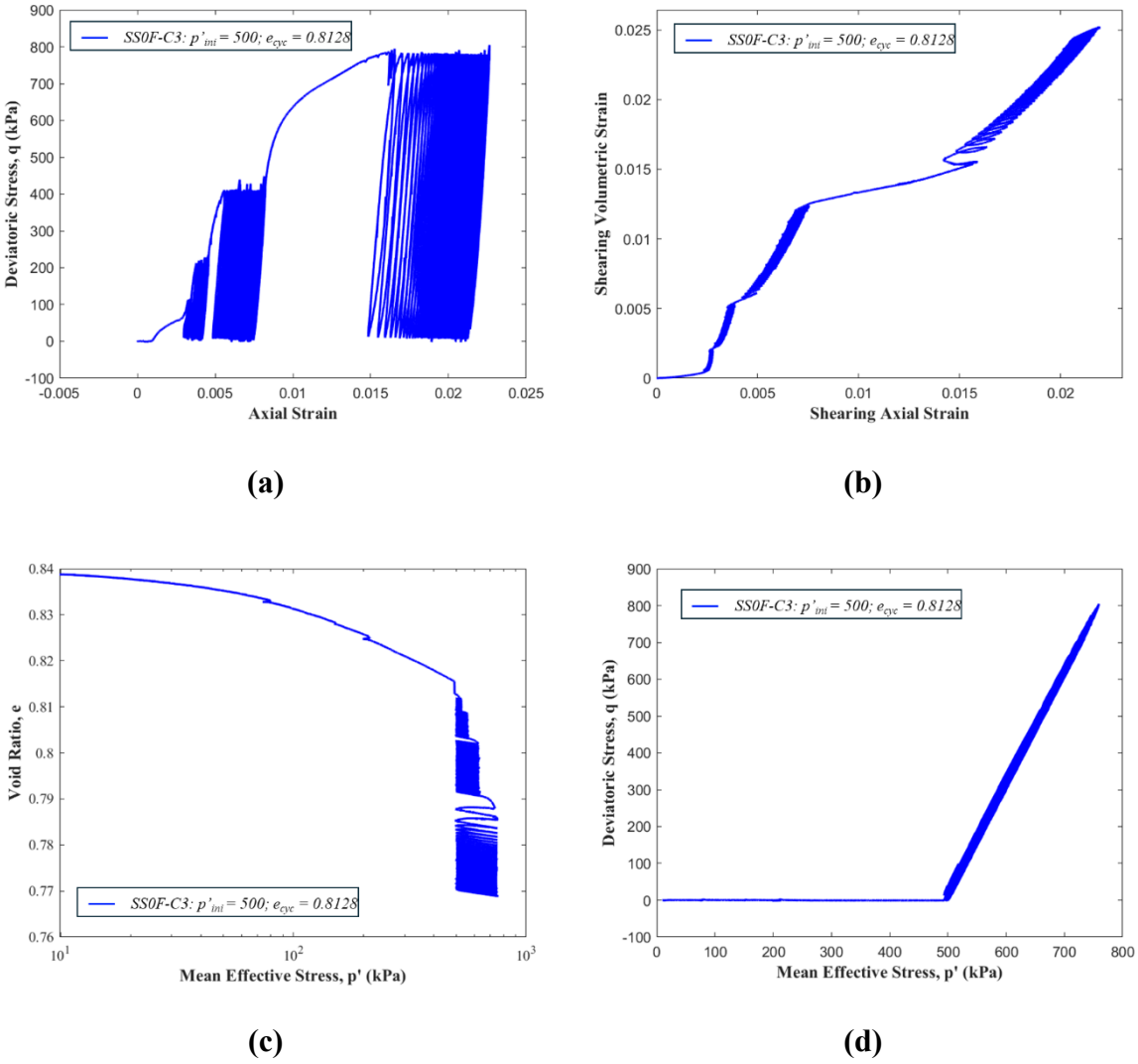

Figure 5.53: Drained cyclic behaviour of Sydney Sand - Multistage: (a) Stress strain response, (b) Volumetric response, (c) Stress path in void ratio vs log p' space, (d) Stress path in q vs p' space

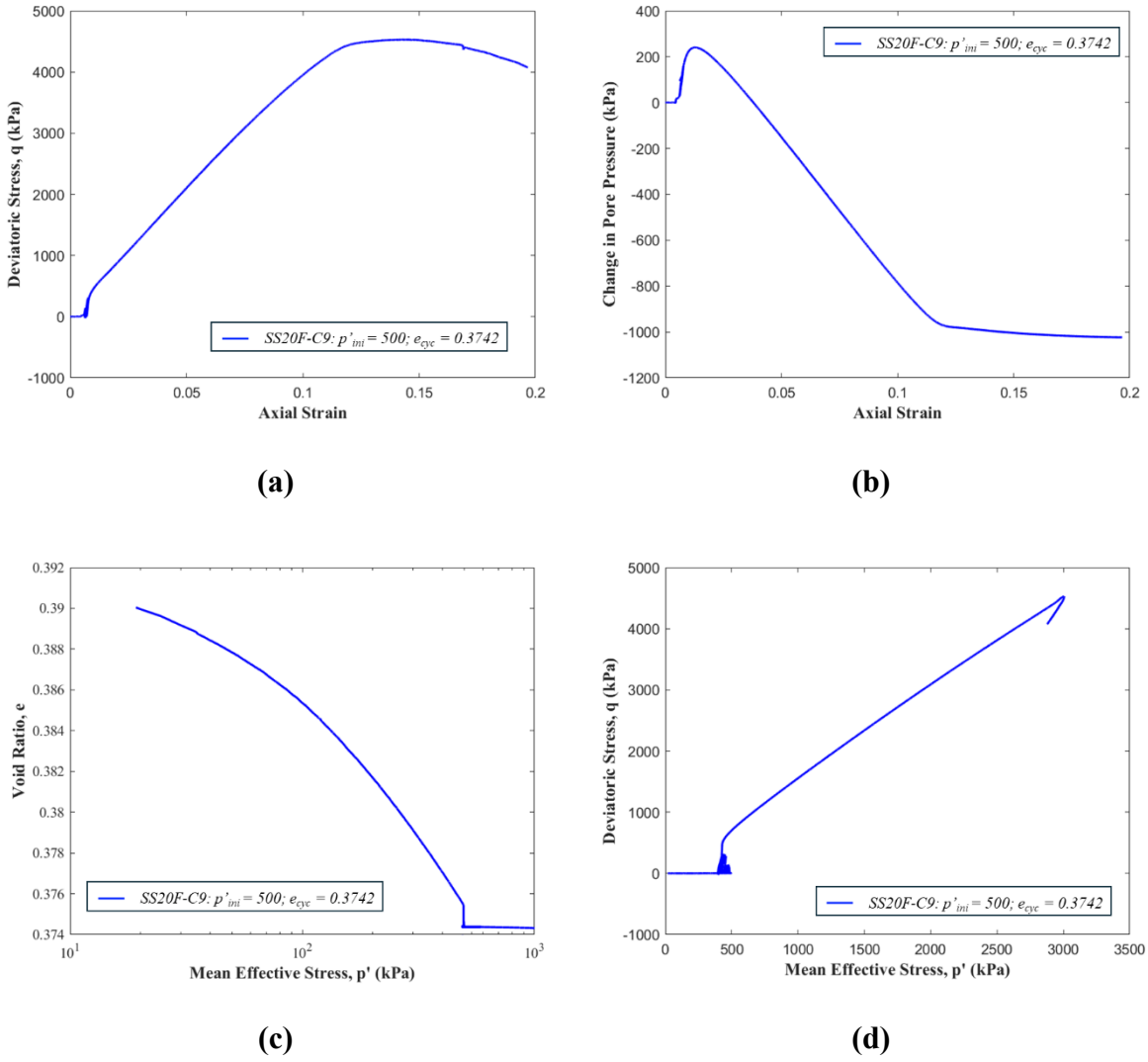

Figure 5.54: Undrained cyclic behaviour of Sydney Sand with 20% Fines: (a) Stress strain response, (b) Pore Pressure response, (c) Stress path in void ratio vs log p' space, (d) Stress path in q vs p' space

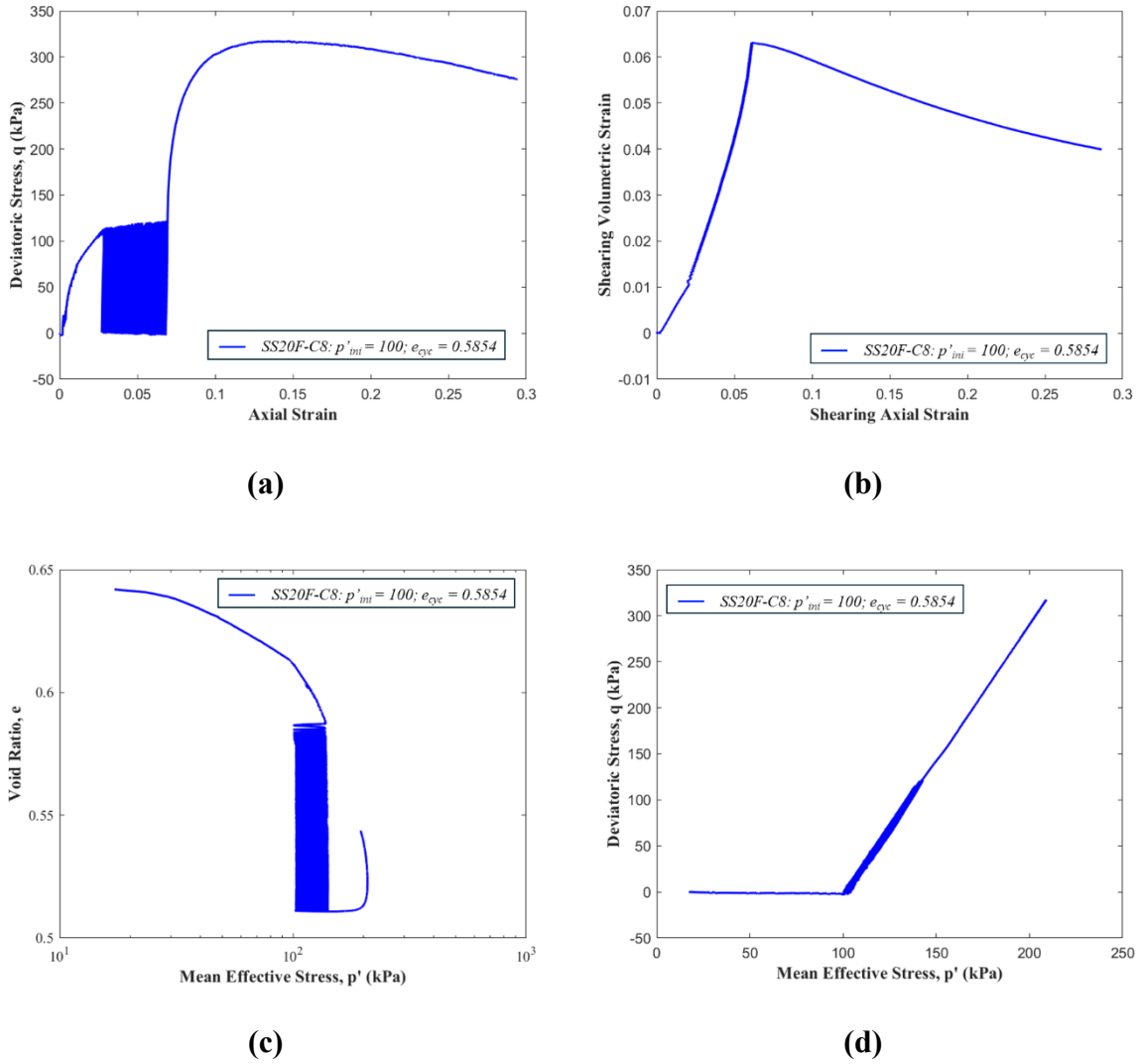

Figure 5.55: Drained cyclic behaviour of Sydney Sand with 20% Fines: (a) Stress strain response, (b) Volumetric response, (c) Stress path in void ratio vs log p' space, (d) Stress path in q vs p' space

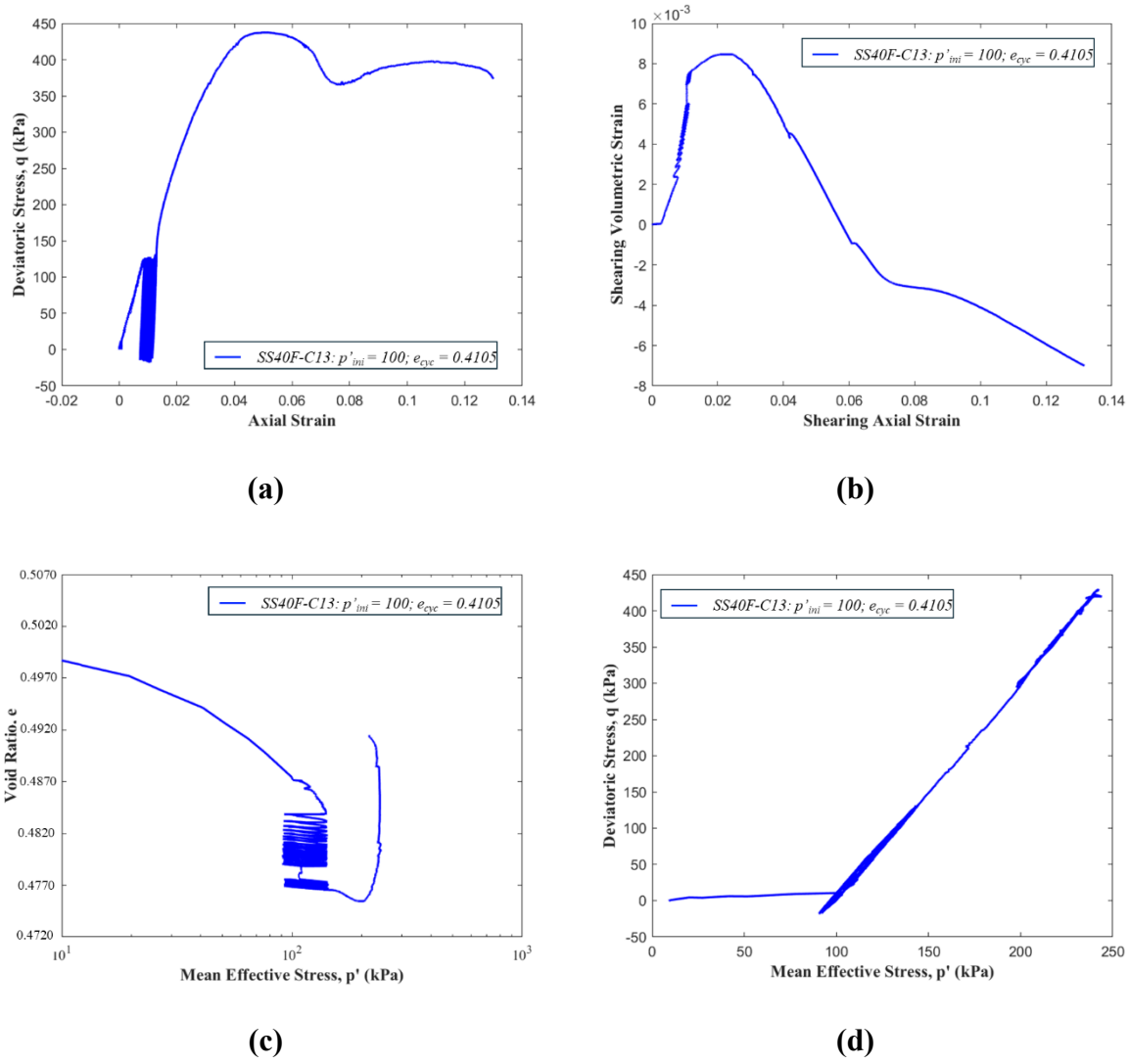

Figure 5.56: Drained cyclic behaviour of Sydney Sand with 40% Fines: (a) Stress strain response, (b) Volumetric response, (c) Stress path in void ratio vs log p' space, (d) Stress path in q vs p' space

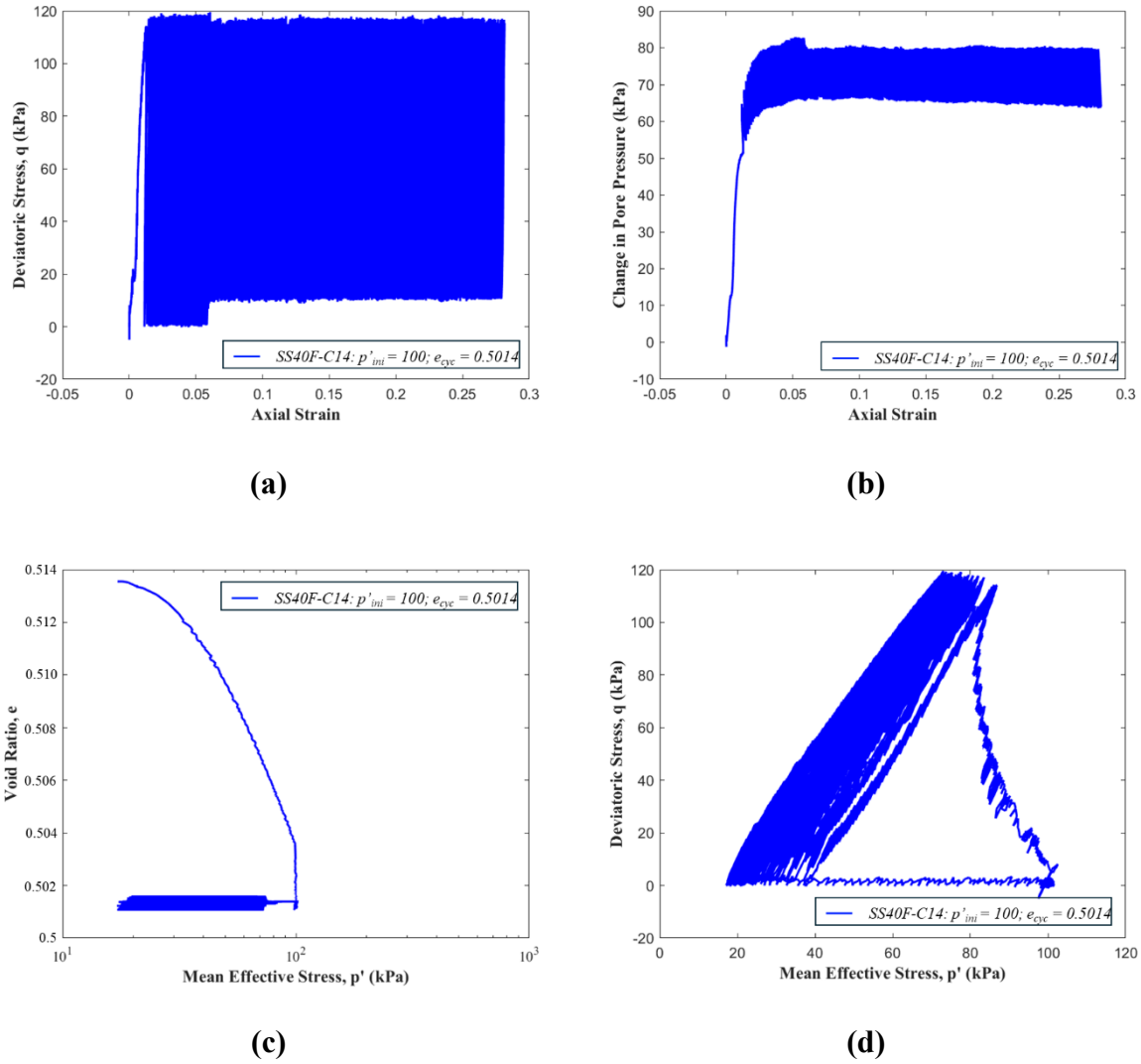

Figure 5.57: Undrained cyclic behaviour of Sydney Sand with 40% Fines: (a) Stress strain response, (b) Pore Pressure response, (c) Stress path in void ratio vs log p' space, (d) Stress path in q vs p' space

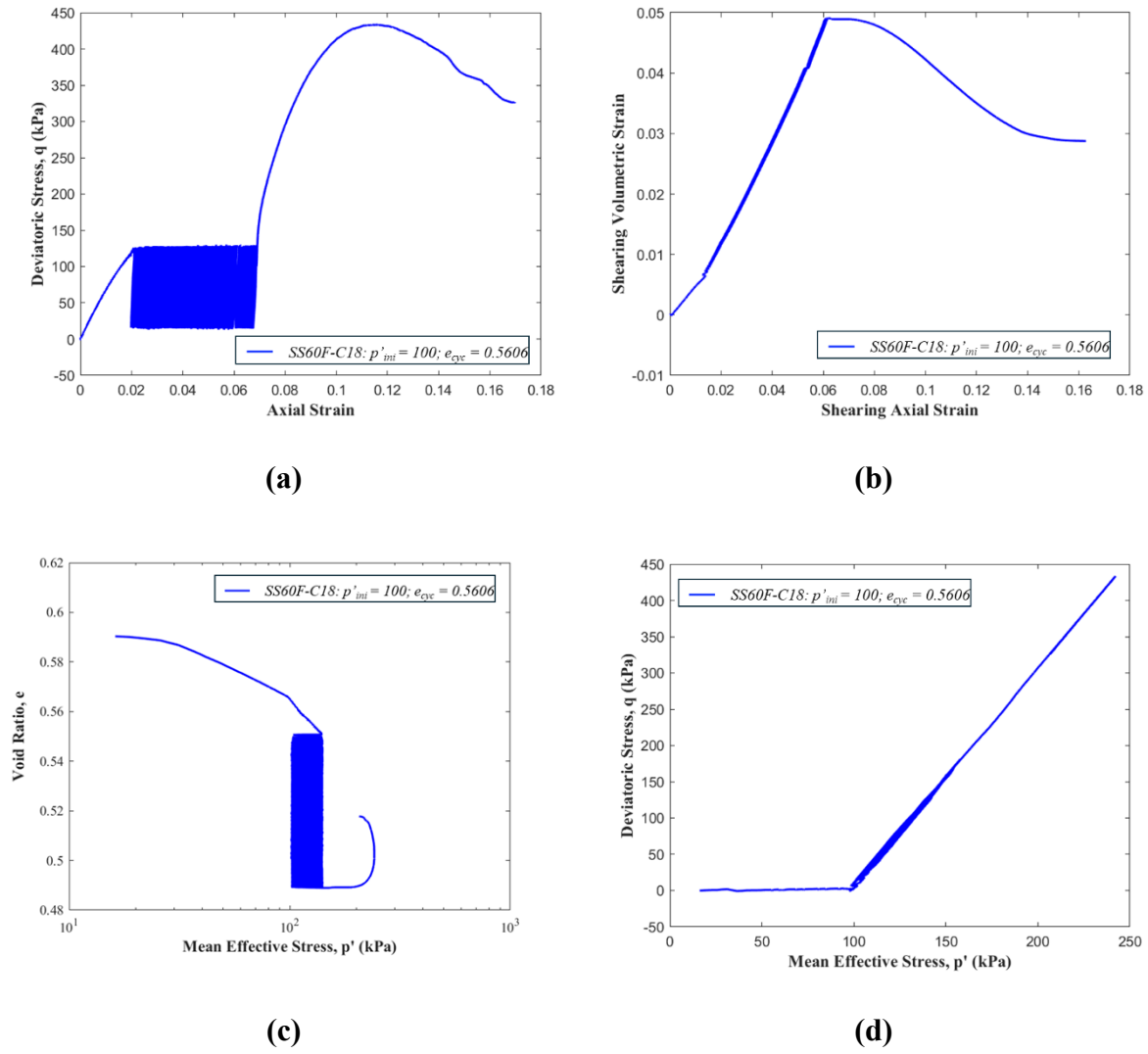

Figure 5.58: Drained cyclic behaviour of Sydney Sand with 60% Fines: (a) Stress strain response, (b) Volumetric response, (c) Stress path in void ratio vs log p' space, (d) Stress path in q vs p' space

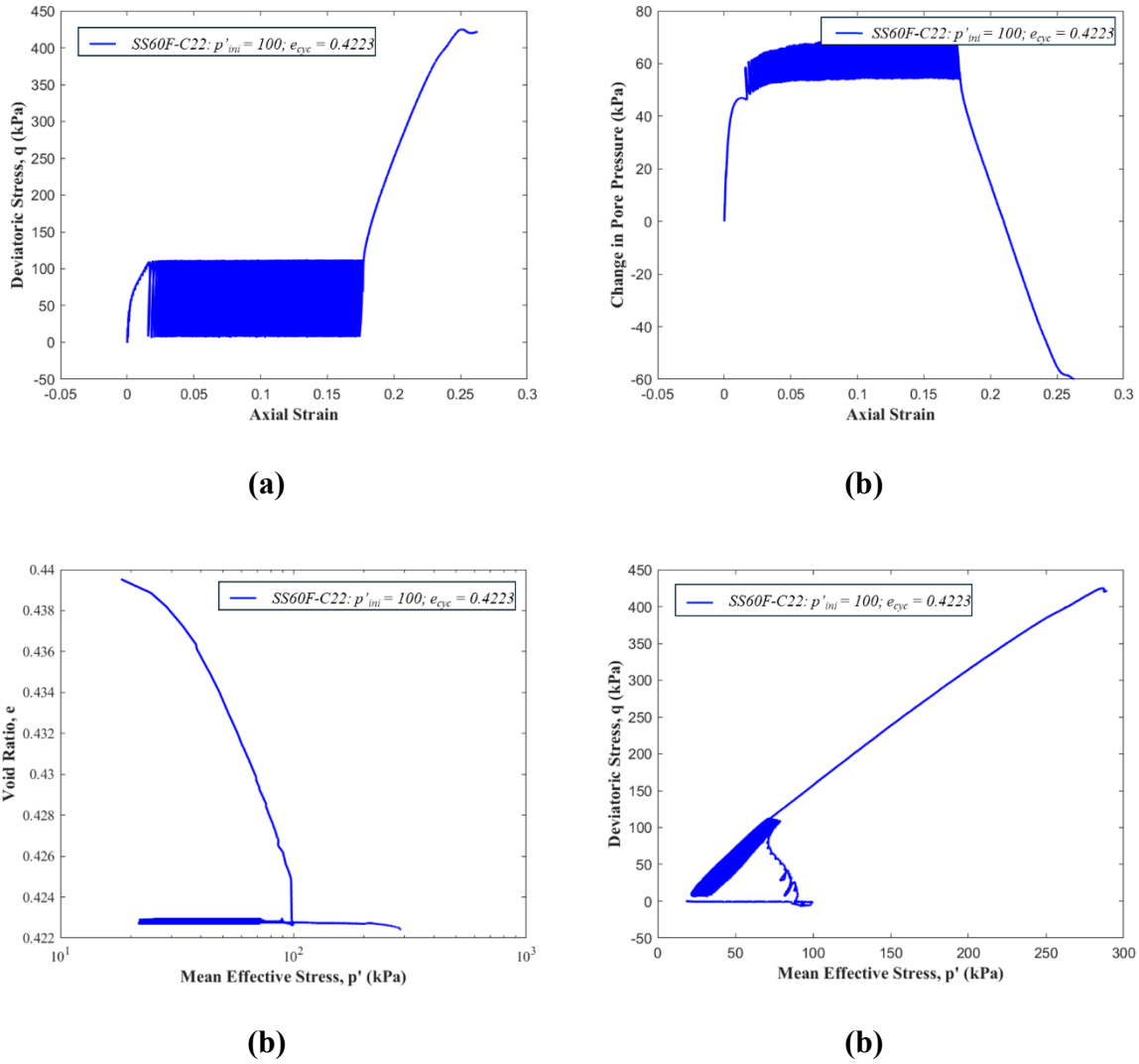

Figure 5.59:Undrained cyclic behaviour of Sydney Sand with 60% Fines: (a) Stress strain response, (b) Pore Pressure response, (c) Stress path in void ratio vs log p' space, (d) Stress path in q vs p' space

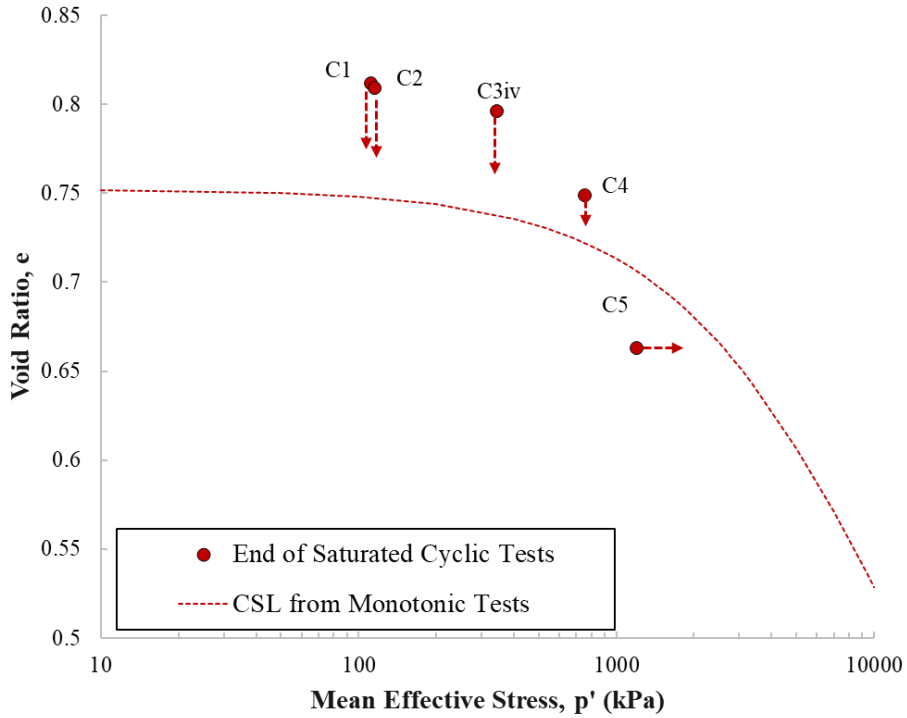

Figure 5.60: CSL Summary of Saturated Cyclic Tests: Sydney Sand

5.5 Behaviour of Unsaturated Sands

The behaviour of unsaturated sands differs from saturated conditions due to the influence of suction and partial saturation on strength and stiffness. Unlike saturated tests, unsaturated loading involves simultaneous control and monitoring of suction and water retention, requiring slower, carefully controlled procedures. These effects are particularly relevant under cyclic and monotonic loading where, suction evolution influences stress paths and deformation. A key parameter governing this behaviour is the Soil-Water Characteristic Curve (SWCC), which links suction to degree of saturation and is essential for defining effective stress in unsaturated soils. The next section presents the SWCC tests conducted for each soil mixture to support interpretation and model calibration.

5.5.1 Soil Water Characteristics Curve (SWCC)

The hydraulic response of soil is fundamental to understanding its unsaturated behaviour, making the determination of the Soil-Water Characteristic Curve (SWCC) a crucial aspect of any model of unsaturated soil behaviour. This section presents and analyses the results of SWCC experiments conducted on the different soil types used in this study. Sydney sand with varying fines content and Well Graded Sand (WGS) made from basalt aggregates. However, SWCC Sydney sand and many other sands of similar PSD is well studied (Rahman and Lo 2008; Prodan et al., 2024) and experimental data is available. These experiments provide valuable insights into the relationship between soil suction and moisture content, which is essential for predicting soil behaviour under partially saturated conditions.

The following subsections provide the specific SWCC results for each soil type, examining key parameters such as air-entry value, residual water content, and the shape of the curves. These parameters are critical for understanding how each soil retains and releases water under various suction levels. By comparing the SWCCs of Sydney sand with different fines contents and the WGS, we can gain insights into how particle size distribution and mineralogy affect a soil's water retention properties.

5.5.2 Hydraulic Response of Sydney Sand Family

For Sydney Sand and its variants with 20%, 40%, and 60% fines content, the SWCC was determined using the HYPROP apparatus (Peters and Durner, 2006), a state-of-the-art device capable of measuring soil water retention properties with high precision. It's important to note that the HYPROP apparatus is specifically designed to plot the drying curve of the SWCC, which represents the soil's behaviour as it loses moisture. This limitation should be considered when interpreting the results, as hysteresis effects between drying and wetting cycles are not

captured in this data. While the moist soil sample of known moisture content and void ratio is allowed to dry in the atmosphere, the mass and tension of the soil is monitored continuously. Goodness-of-fit analysis confirmed that the Fredlund–Xing model captured the measured data exceptionally well for Sydney Sand mixtures (R^2 = 0.9996 for SS0F, 1.000 for SS20F, 0.9820 for SS40F, and 0.9954 for SS60F). These values indicate that almost all variability in measured saturation could be explained by the fitted curves, with only minor deviations at the very dry end of the curve where HYPROP readings are less reliable.

As part of the current study scope, only drying SWCC curves were measured. Wetting paths and associated hysteresis effects were not captured. In addition, a constant suction level was maintained during unsaturated cyclic triaxial testing, meaning that dynamic changes in suction and degree of saturation due to volume change were not tracked. From a modelling perspective, the Fredlund-Xing model was used for fitting the SWCCs, where only the parameters 'm' and 'n' differ between drying and wetting paths. Since hysteresis was not simulated, its impact on triaxial modelling results is expected to be minimal. Nonetheless, this represents a limitation of the current work. In reality, matric suction and degree of saturation can evolve during cyclic loading due to volume change and moisture redistribution. This effect, while not captured here, may influence long-term suction evolution and should be explored in future studies.

It is noted that the residual suction values obtained from the HYPROP-based SWCCs do not fully agree with the suction equilibration and degree of saturation observed in the triaxial tests performed in this study. This mismatch likely results from differences in boundary conditions (drying path versus constant-suction triaxial loading), stress state, and sample disturbance during re-packing. Hence, while the SWCC data provide useful reference trends, the absolute suction values should be interpreted with caution when compared against mechanical test conditions.

The recorded values are fitted with SWCC fitting equation given by Fredlund-Xing model (1994) as discussed in chapter 2 in equation 31, reproduced in equation 40. The SWCC parameters that are necessary for model simulations are listed in Table 21.

$$S_w^{\alpha} = S_{rw} + (1 - S_{rw}) * \left(ln \left[exp(1) + \left(\frac{p_c^*}{P^{\alpha}} \right)^{n_x^{\alpha}} \right] \right)^{-m_x^{\alpha}} \quad 40$$

Where, S_w^{α} is volumetric moisture content at suction p_c^*, $(1 - S_{rw})$ is residual water content, S_{rw} is saturated water content, P^{α} is parameter related to air entry value, Air Entry Value (AEV) parameter – suction where desaturation begins; reflects pore entry threshold, $n_x^{w,d}$ is Pore-size distribution index – controls the steepness of the SWCC, and $m_x^{w,d}$ is Fitting parameter – adjusts the shape of the curve; As fines content increased, a general reduction in saturated volumetric water content (S_{rw}) and a shift in air entry value (AEV) were observed. SS0F exhibited the highest S_{rw} and steepest desaturation (high n), reflecting a uniform sand matrix with rapid drainage. In contrast, SS60F showed a more gradual desaturation (low n) and a higher AEV (P^{α}), indicating finer pore structure and stronger water retention. The transition from SS20F to SS60F revealed increased hysteresis potential and more complex pore-size distributions, consistent with the presence of fines. These trends are reflected in the fitted Fredlund-Xing parameters in Table 5.10 and the fitted curves presented in Figure 5.65.

Table 5.10: SWCC parameters for Sydney sand with fines

Material	S_{rw}	P^{α}	n	m
SS0F	42.7	0.020	10	1.0
SS20F	37.99	0.0250	4.29	0.63
SS40F	24.71	0.4879	3.75	1.85
SS60F	28.46	0.3808	1.9802	0.495

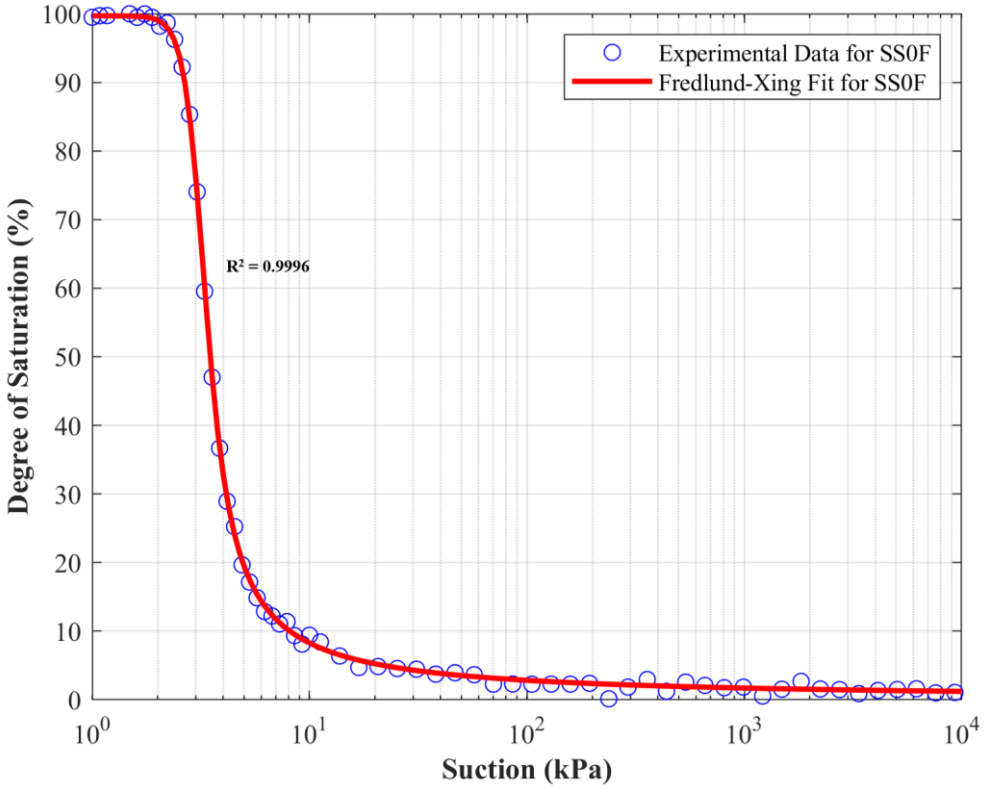

Figure 5.61: SWCC of Sydney sand fitted with Fredlund-Xing Model

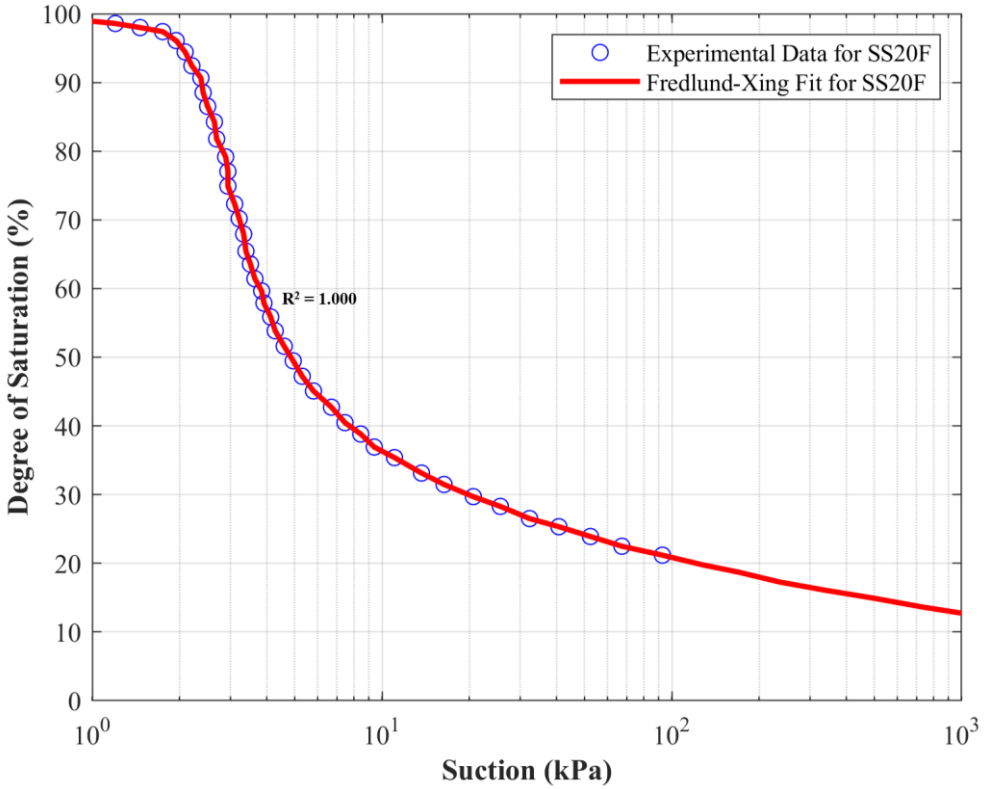

Figure 5.62: SWCC of Sydney sand with 20% Fines fitted with Fredlund-Xing Model

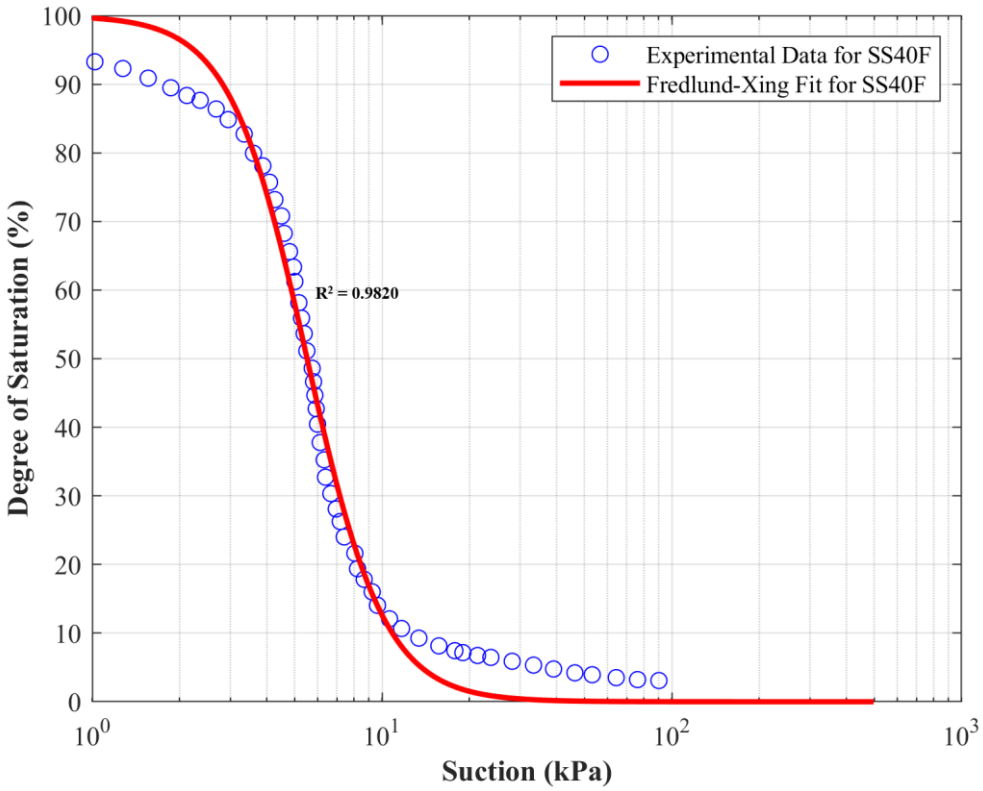

Figure 5.63: SWCC of Sydney sand with 40% Fines fitted with Van Fredlund-Xing Model

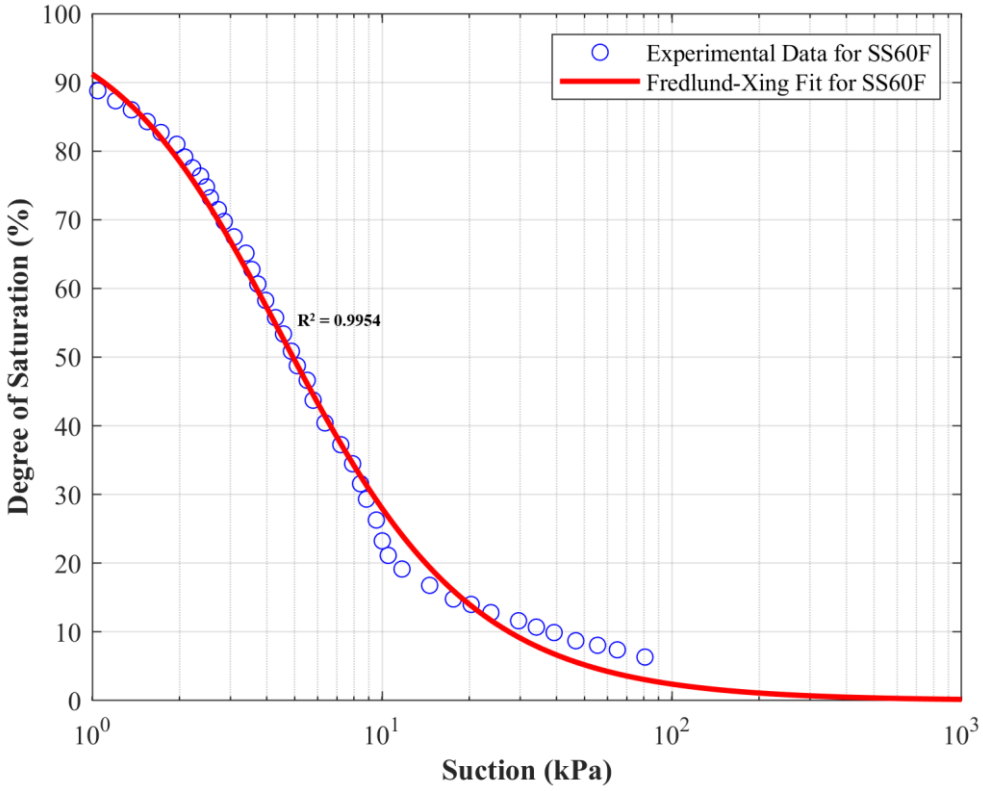

Figure 5.64: SWCC of Sydney sand with 60% Fines fitted with Fredlund-Xing Model

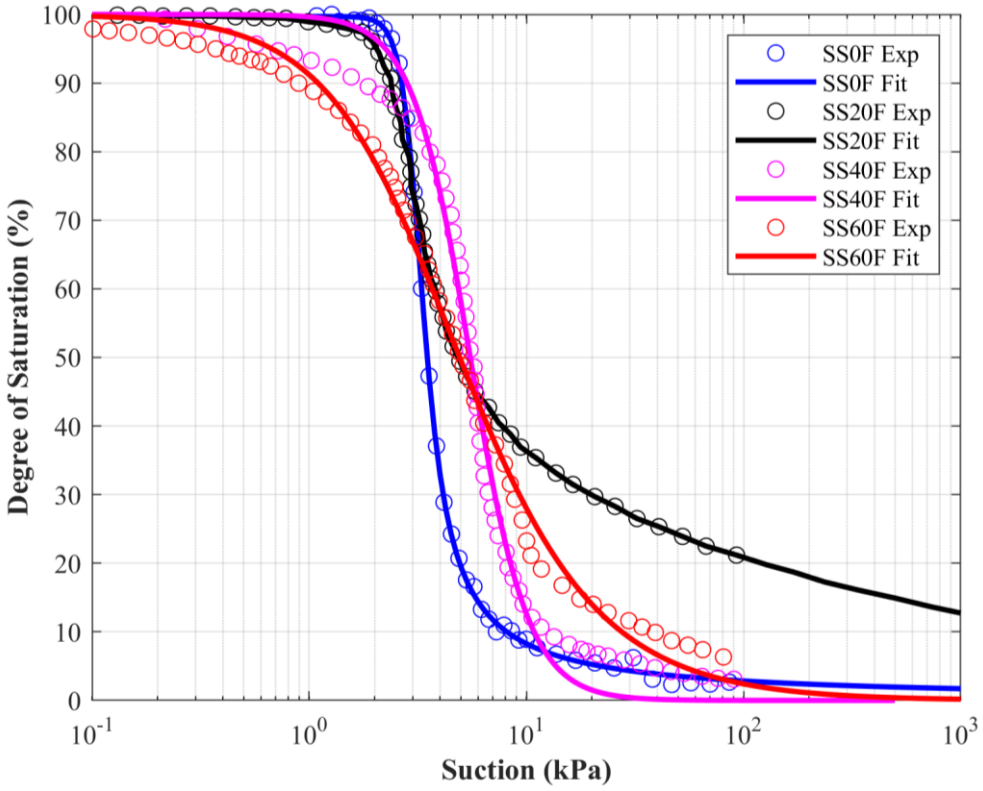

Figure 5.65: SWCC of Sydney Sand Family fitted with Fredlund-Xing Model

5.5.3 Hydraulic Response of WGS Family

In contrast to Sydney Sand family, the SWCC for the Well Graded Sand (WGS) was determined using the pressure plate apparatus, a more traditional method that allows for both drying and wetting cycles to be measured. The Fredlund–Xing model provided a good fit to WGS data but with slightly lower R^2 values for some drying branches – for example, WGS18F Drying (R^2 = 0.9486) and WGS28F Drying (R^2 = 0.7381). These lower values reflect natural scatter in pressure plate measurements at high suctions and the more irregular pore structure of WGS. Wetting branches fitted better overall (R^2 typically > 0.86), confirming that the model still captures the dominant water retention trends despite some drying-path variability.

These results, reported by Kwa (2019), are presented in Table 5.11. The use of different experimental methods for the two soil types provides a comprehensive view of soil-water interactions across a range of materials and testing conditions. The SWCC of WGS family is also fitted with modified Fredlund-Xing model. Notable hysteresis was observed between

drying and wetting curves for all mixtures, with higher θ_s and AEV (α) values typically reported in the drying branch. As fines content increased, both air entry values and residual saturation levels varied, indicating increased water retention and finer pore distributions. These behaviours are illustrated in the individual SWCC plots shown in Figures 5.66 to 5.69, corresponding to WGS18F, WGS28F, WGS40F, and WGS60F respectively.

Table 5.11: SWCC fitting parameters for WGS sand family

Material	S_{rw}	P^{α}	n	m
WGS18F Drying	0.795	1.757	2.1	2.3
WGS18F Wetting	0.603	0.628	2.1	2.3
WGS28F Drying	0.726	2.772	15	19
WGS28F Wetting	0.603	0.988	15	19
WGS40F Drying	0.748	4.039	10	7.5
WGS40F Wetting	0.681	0.088	10	7.5
WGS60F Drying	0.805	3.580	15	1.27
WGS60F Wetting	0.675	0.347	15	1.27

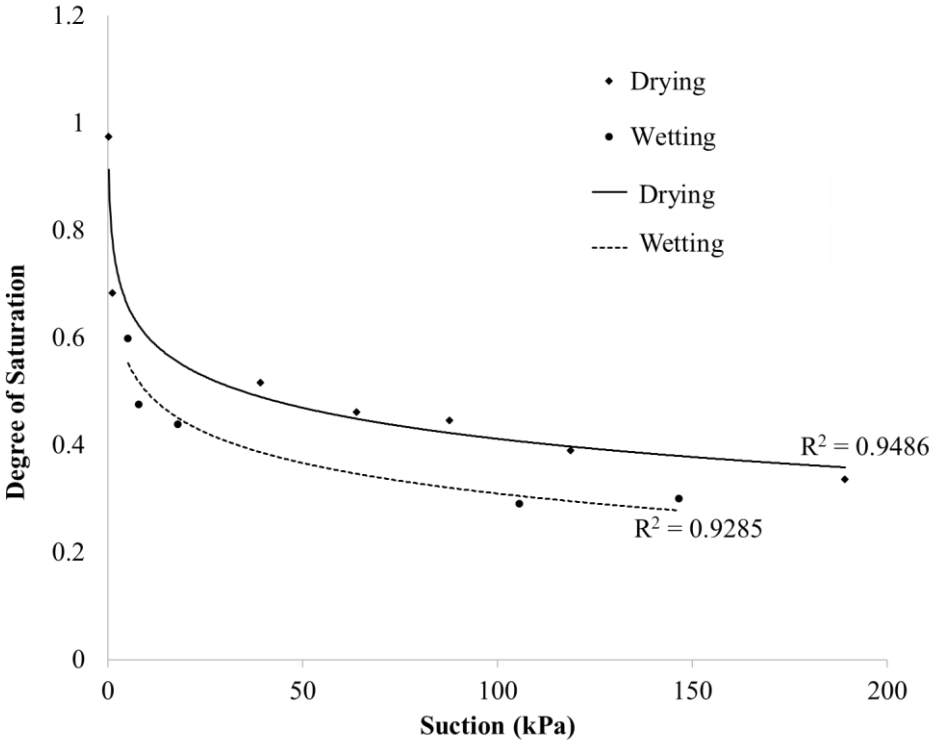

Figure 5.66: SWCC of Well Graded Sand with 18% Fines

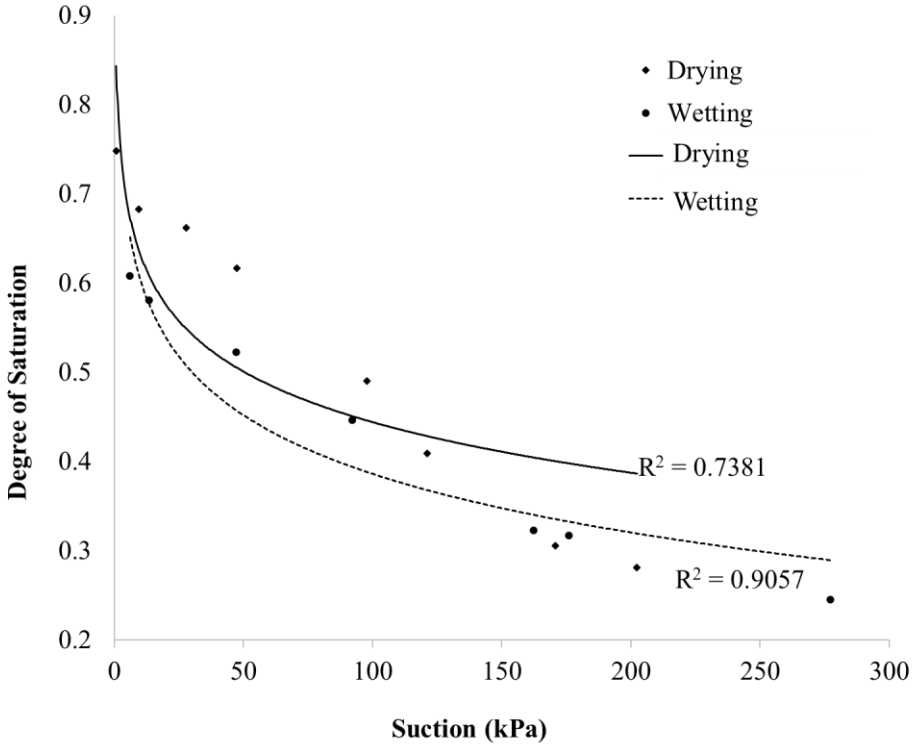

Figure 5.67: SWCC of Well Graded Sand with 28% Fines

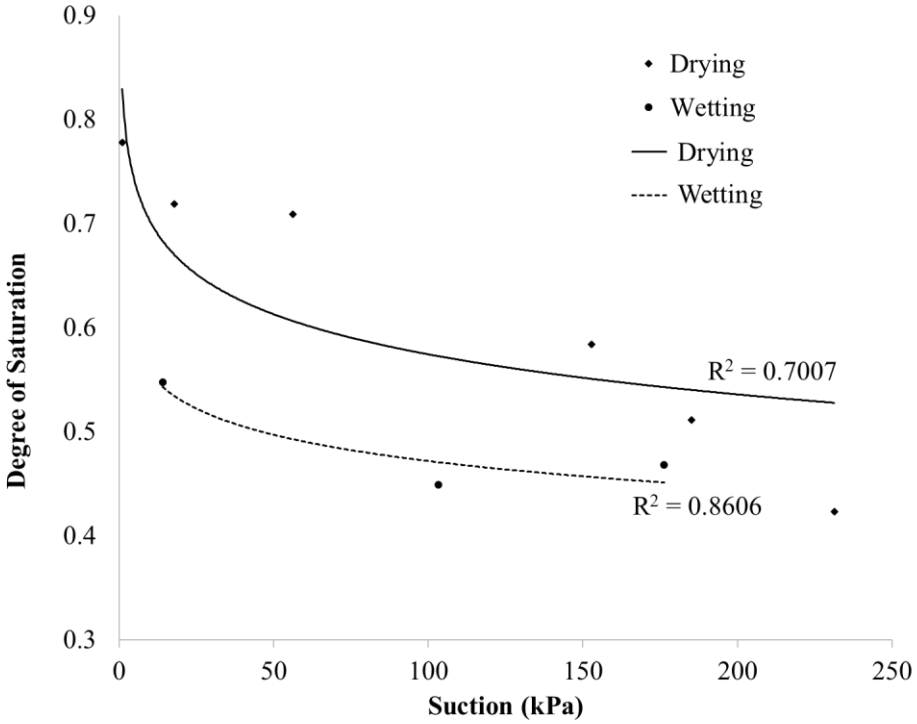

Figure 5.68: SWCC of Well Graded Sand with 40% Fines

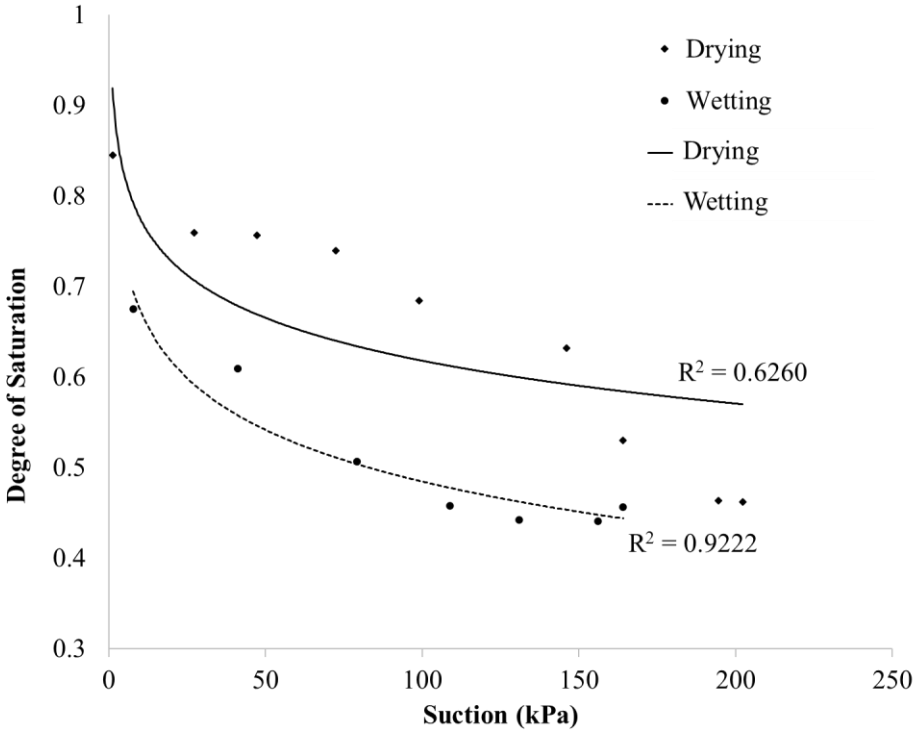

Figure 5.69: SWCC of Well Graded Sand with 60% Fines

5.6 Triaxial Testing on Unsaturated sands

This section presents the unsaturated behaviour of the sands under both monotonic and cyclic triaxial tests focusing on stress-strain response, volumetric changes, stress path and degree of saturation. The behaviour of unsaturated soils is compared with their fully saturated counterparts to interpret the effects of suction. Due to time constraints, the number of triaxial tests conducted was limited. The study encompasses a few tests for each of the two drainage conditions for Sydney sand mixtures under both monotonic and cyclic loading. For WGS mixtures, given the availability of ample unsaturated cyclic test data (Kwa, 2019), a two triaxial tests for each mixture were performed, one monotonic and one cyclic.

It is important to note that the hydraulic condition in unsaturated triaxial tests is always considered drained, as water can migrate internally even when external valves are closed. Therefore, such tests are more accurately classified as constant suction tests (drained) or constant water content tests (undrained), rather than strictly based on external drainage control. In this study, a constant suction of 10 kPa was maintained for all mixtures except clean Sydney Sand, where suction equilibration could not be achieved reliably due to its poorly graded and highly permeable nature. The suction boundary was created by applying a fixed pore-water pressure at the base of the specimen through the HAEPD disc, while the top of the sample was left vented to atmospheric air pressure.

While this boundary condition was kept constant throughout shearing, the internal suction within the specimen was allowed to evolve naturally as the soil volume changed during compression or dilation. No active feedback system was used to dynamically correct these changes, meaning the tests are more accurately described as “nominal constant suction”, the applied boundary suction remained fixed, but minor redistribution of suction inside the specimen occurred during shearing.

Although 10 kPa is higher than the air-entry values (AEV) determined for all the tested mixtures, this does not invalidate the testing condition. On the contrary, suction values above the AEV still correspond to unsaturated states, especially in fine or well-graded sands. In this range, the soil is nearly saturated, and air is occupied by larger pores, while water remains continuous within finer pores. This region represents an important transition zone where suction begins to affect strength and stiffness, even though significant air invasion has begun in coarse pores.

There are several reasons why selecting a suction slightly above the 10 kPa are appropriate and useful:

- It lies above the AEV for all materials, ensuring the samples are partially saturated and that suction actively contributes to mechanical strength and stiffness.
- Much higher suction values (well above 10 kPa) would substantially increase equilibration time, sometimes requiring several weeks for dense or low-permeability specimens.
- At moderate suction (just above AEV), the degree of saturation remains high enough to preserve realistic stress transfer through pore water while still exhibiting measurable suction effects.
- Constitutive models, particularly those based on critical state or bounding surface frameworks, aim to capture soil behaviour in this near-saturated regime, where partial desaturation enhances strength without inducing abrupt structural changes.
- The selected suction value is consistent with lightly desaturated field conditions commonly encountered in engineered fills and shallow subgrades.

By maintaining a manageable suction level (10 kPa), full equilibrium was achieved in most specimens within 5–10 days, enabling reliable observations of the mechanical response of unsaturated soils. This approach ensured that a clear initial suction state was defined before shearing began, while acknowledging that small, natural variations in internal suction occurred

during loading. Establishing suction equilibrium prior to shearing was crucial for ensuring that the initial stress state was well-defined and that the observed behaviour reflected true unsaturated soil response. This provides a strong foundation for validating the model under realistic unsaturated conditions, particularly in the near-saturated regime that is of primary interest in geotechnical applications.

During the consolidation stage, unsaturated soils often exhibit different volumetric responses compared to saturated soils; however, the assumption that unsaturated soils always undergo higher volume changes due to the compressibility of air voids is not universally valid. This behaviour is highly dependent on the degree of saturation at the time of loading, the soil's initial density, and the applied net mean stress. In unsaturated soils, when a significant volume of the pore space is occupied by air, the system becomes more compressible than a fully saturated soil. However, as the degree of saturation increases and the air phase becomes discontinuous or trapped, its compressibility effect diminishes, and the soil begins to behave more like a saturated system.

These variations in equilibrium suction significantly influenced the degree of saturation at the time of loading and consequently affected the compressibility of the soils during the consolidation phase. Even though the net mean stress was consistently applied at 100 kPa across all tests, the compression behaviour differed due to the variable saturation states and air content within the pores. Soils with higher fines content and denser packing tended to retain more water due to their finer pore structure, resulting in higher degrees of saturation and lower suction at equilibrium. However, depending on the soil fabric and moisture distribution, the presence of partially saturated air voids may still contribute to increased compressibility under loading.

Therefore, the volumetric compression observed during the consolidation stage of the unsaturated triaxial tests in this study reflects a combined effect of initial density, fines content, suction equilibration, and degree of saturation.

The effective stress in the unsaturated condition used in this study is adopted from the Bishop's equation (Bishop and Blight, 1963) as shown in equation 41.

$$\sigma' = \sigma - u_a + \chi(u_a - u_w) \quad 41$$

Where, σ' is the effective stress, σ is total stress, u_a is pore air pressure, u_w is porewater pressure, and χ is effective stress parameter which is equal the degree of saturation in this study that ranges from 0 to 1. The unsaturated setup is supplemented with a pore air pressure transducer to measure the pore air pressure as mentioned in Chapter 3. This method of calculating effective stresses were common both in cyclic and monotonic unsaturated tests. However, the more detailed behaviour is discussed in further sections.

5.6.1 Monotonic Behaviour of Unsaturated Soils

Once suction equilibrium was achieved, each specimen was consolidated under an isotropic net stress of 100 kPa. A target suction of 10 kPa was applied across all tests; however, clean Sydney Sand (SS0F) presented challenges in achieving this equilibrium due to its uniformly graded nature and high permeability. Despite maintaining the applied suction for extended durations, the loosely packed structure of SS0F resulted in rapid moisture redistribution and early onset of desaturation, making sustained equilibrium at 10 kPa difficult to maintain. Consequently, most SS0F specimens equilibrated at slightly lower suction values (typically 6–7 kPa for denser samples and <5 kPa for looser ones). In contrast, the Sydney Sand mixtures containing fines (SS20F, SS40F, SS60F) successfully achieved and maintained the target 10 kPa suction. This was facilitated by their finer grain structure and lower permeability, which allowed better retention of matric suction after a prolonged equilibration period (often 7–10

days). The increased fines content not only enhanced water retention capacity but also slowed down hydraulic equilibration, enabling a stable suction profile across the sample before shearing.

Although a prolonged equilibration period was adopted to ensure uniform suction distribution prior to shearing, suction equilibrium during the loading phase was not actively monitored or verified. It was assumed that the low strain rate used in monotonic testing would allow sufficient time for suction redistribution throughout the specimen. While this assumption is generally reasonable for sandy soils with relatively high permeability, volume changes during shearing, particularly in denser or finer-grained samples may cause internal suction gradients to develop. However, limited direct mid-plane suction measurements were performed on selected tests (see Appendix). Preliminary readings showed that suction values fluctuated by less than ±2 kPa during shearing, indicating that the assumption of quasi-uniform suction was broadly valid for the test conditions adopted. Nevertheless, without continuous real-time monitoring, it is not possible to confirm spatial uniformity of suction throughout loading. This introduces some uncertainty in interpreting effective stress and stiffness evolution in unsaturated tests. Future studies should incorporate direct suction measurements during shearing to better validate this assumption and improve confidence in model calibration.

Subsequently, the sample is sheared using a stress-controlled mechanism at a constant rate of 0.05 mm/minute. The stress–strain responses of the unsaturated samples followed trends broadly similar to those observed in saturated drained tests. Loose specimens displayed strain-hardening behaviour, with continuous compaction until reaching a critical state. In contrast, denser specimens developed clear peak deviatoric stresses followed by strain softening associated with volumetric dilation. However, in all unsaturated cases, the stress at peak and critical states was consistently higher than those observed in the saturated counterparts. This upward shift of the critical state surface, visible when comparing effective stress paths in q–p′

space with CSLs from saturated tests, demonstrates the reinforcing effect of suction in increasing shear strength and modifying the critical state condition. For example, Figures 4.67–4.70 show that even in tests that began in a loose state, the equilibrium suction caused densification, shifting their behaviour toward dilative response similar to medium-dense or dense saturated specimens.

This behaviour is supported by volumetric strain and degree of saturation trends shown in subfigures (b) and (e) of Figures 5.53 to 5.56. All specimens exhibited reduced volumetric change compared to saturated specimens (as in Figures 5.19 to 5.22) with similar initial void ratios. This is due to the additional effective stress provided by matric suction, which increases the stiffness of the soil skeleton and suppresses excessive compression. The degree of saturation trends further validates these responses: in loose specimens, saturation steadily increased due to compaction and reduction in void space. In denser specimens, saturation initially increased but eventually decreased during dilation, as expansion of pore space caused a redistribution and possible air-entry into larger pores. This observation reflects the dynamic coupling between hydraulic and mechanical processes in unsaturated soils. In some cases, this phenomenon explains sudden strength drops or brittle failures where suction collapse or entrapped air rapidly reduced effective stress. In particular, suction collapse tends to occur when dilation induces cavitation in the pore fluid, breaking capillary menisci and causing a sudden loss of suction. Entrapped air bubbles can also expand rapidly under decreasing pore water pressure, leading to abrupt reductions in effective stress and brittle stress–strain response. These mechanisms are consistent with the sudden stress drops observed in some SS0F and SS20F tests.

Table 5.12 provides a clear summary of how unsaturated behaviour manifested across the tested sand–fines mixtures. For instance, clean Sydney Sand specimens (UM1–UM5), although prepared at relatively loose states ($e_{ini} > 0.72$), developed low degrees of saturation (S_{r_ini} =

0.12–0.19) and displayed dilation after consolidation. This led to marginal reductions in void ratio or minimal compaction. Under saturated conditions at similar densities, such loose specimens would typically exhibit compressive behaviour. The observed dilation here suggests that even at low S_r, suction-induced strengthening was sufficient to suppress compressive strains. but sudden desaturation during dilation may have contributed to brittle behaviour in some cases. In these loose specimens, suction collapse and redistribution of water–air phases likely caused sharp transitions in stiffness, giving rise to the abrupt post-peak drops recorded in stress–strain curves.

SS20F specimens (UM8, UM9) followed a similar trend, with moderate degrees of saturation (S_r = 0.32–0.46) and limited changes in void ratio, again pointing to the stiffening effect of suction. With increasing fines content, specimens such as SS40F (UM10) and SS60F (UM11) started at higher saturation levels (S_{r_ini} = 0.49–0.65), yet surprisingly exhibited dilative behaviour typically associated with dense states. Notably, the SS60F specimen reached a post-shearing saturation of S_{r_f} = 0.62, behaving in a manner contrary to saturated expectations, where high fines content is generally associated with increased compressibility. This counterintuitive dilative response at high Sr suggests that suction redistribution during shear, combined with the finer-grained matrix resisting collapse, created a transient stiffening effect. However, when air entrapment was triggered in some tests, localised brittle failures and sudden reductions in shear resistance were observed.

These findings highlight that the relationship between suction, fines content, and deformation behaviour is more nuanced than predicted by classical saturated frameworks. While the effective stress ($\sigma' = u_a + S_r \cdot (u_w - u_a)$) implies greater influence of suction at higher S_r, the observed dilation in high-fines specimens suggests that suction-induced stiffness potentially enhanced by fabric changes or suction hardening offsets the expected compressibility. Conversely, the relatively muted dilation in clean sand raises questions about whether those

samples were looser than assumed or experienced limited suction mobilisation due to entrapped air. Such entrapped air pockets can redistribute unevenly under loading, producing non-uniform suction fields that explain the sudden brittle failures observed in some unsaturated tests. Overall, these results point to a complex interplay between saturation, fines, and fabric evolution under unsaturated conditions.

The trend across mixtures indicates that increasing fines content results in higher degrees of saturation at equilibrium suction, particularly under the same net confining stress. This behaviour is attributable to the improved water retention capacity provided by the finer matrix. At a fixed suction of 10 kPa, samples with more fines held significantly more water, thereby achieving higher saturation and, in turn, a denser mechanical response. Consequently, their strength and stiffness were higher than the clean sand specimens. However, the effect of fines was not linear. While SS20F and SS40F showed notable increases in saturation and shear resistance, the SS60F sample began to approach a saturation state where further strength gains from suction diminished, possibly indicating transition toward cohesive-like behaviour.

Importantly, the tests conducted here were limited to a single consolidation pressure of 100 kPa. As a result, mapping a full critical state line in e–log p′ or q–p′ space for the unsaturated state was not possible. Nevertheless, the data clearly shows that unsaturated samples reached effective stress states above the saturated CSL, validating the assumption that suction shifts the critical state surface upwards in both spaces. This also aligns with the modified critical state frameworks for unsaturated soils, which incorporate suction as an additional stress state variable.

In interpreting this behaviour, several key mechanisms come into play. Matric suction contributes directly to the effective stress via inter-particle tension, enhancing the shear strength of the soil skeleton (Fredlund & Rahardjo, 1993). The capillary water held between particles forms menisci, which increase normal stresses and interlocking, improving resistance

to shearing (Lu & Likos, 2004). The enhanced strength is particularly notable in denser or finer-grained samples that retain suction more effectively. Furthermore, the hysteretic nature of the soil-water characteristic curve (SWCC) means that degree of saturation changes during shearing do not follow a single path, leading to complex hydro-mechanical interactions such as partial desaturation during dilation or re-saturation during compaction. Each of these redistribution processes can create abrupt shifts in effective stress, directly linked to the brittle stress–strain responses observed in some tests. The fact that these phenomena were observed across multiple gradations reinforces their physical relevance, rather than being artefacts of equipment or preparation.

These findings provide critical insight into the role of suction in modifying the critical state response. The presence of suction allows the soil to behave in a stiffer and stronger manner, even when prepared in loose states. This is particularly important in predicting field behaviour under partial saturation and highlights the need to incorporate suction into advanced constitutive models. The observations made here serve as reference benchmarks to fine-tune model parameters, ensuring accurate simulation of the mechanical behaviour of unsaturated sandy soils with varying particle size distributions.

Table 5.12: Summary of Monotonic Unsaturated tests

Test No	Test Label	p_i'	Suction	e_{ini}	e_f	DOS_{ini}	DOS_f
UM1	MUD_SS0F100i	100	-6	0.7846	0.8650	0.1938	0.1187
UM2	MUD_SS0F100ii	100	-7	0.7813	0.8422	0.1209	0.1121
UM3	MUD_SS0F100iii	100	-7	0.7871	0.7955	0.1188	0.1176
UM4	MUD_SS0F100iv	100	-6	0.7665	0.6923	0.1358	0.1504
UM5	MUD_SS0F100v	100	-6	0.7231	0.7069	0.1488	0.1522
UM6	MUD_SS0F100vi	100	-10	0.5898	0.6869	0.4723	0.4055
UM7	MUD_SS0F100iii	100	-10	0.6113	0.7718	0.4557	0.3609
UM8	MUD_SS20F100iii	100	-10	0.6455	0.6670	0.3241	0.3137
UM9	MUD_SS20F100iii	100	-10	0.5574	0.5419	0.4496	0.4624
UM10	MUD_SS40F100iii	100	-10	0.5212	0.5275	0.6530	0.6451
UM11	MUD_SS60F100iii	100	-10	0.6954	0.5471	0.4919	0.6252

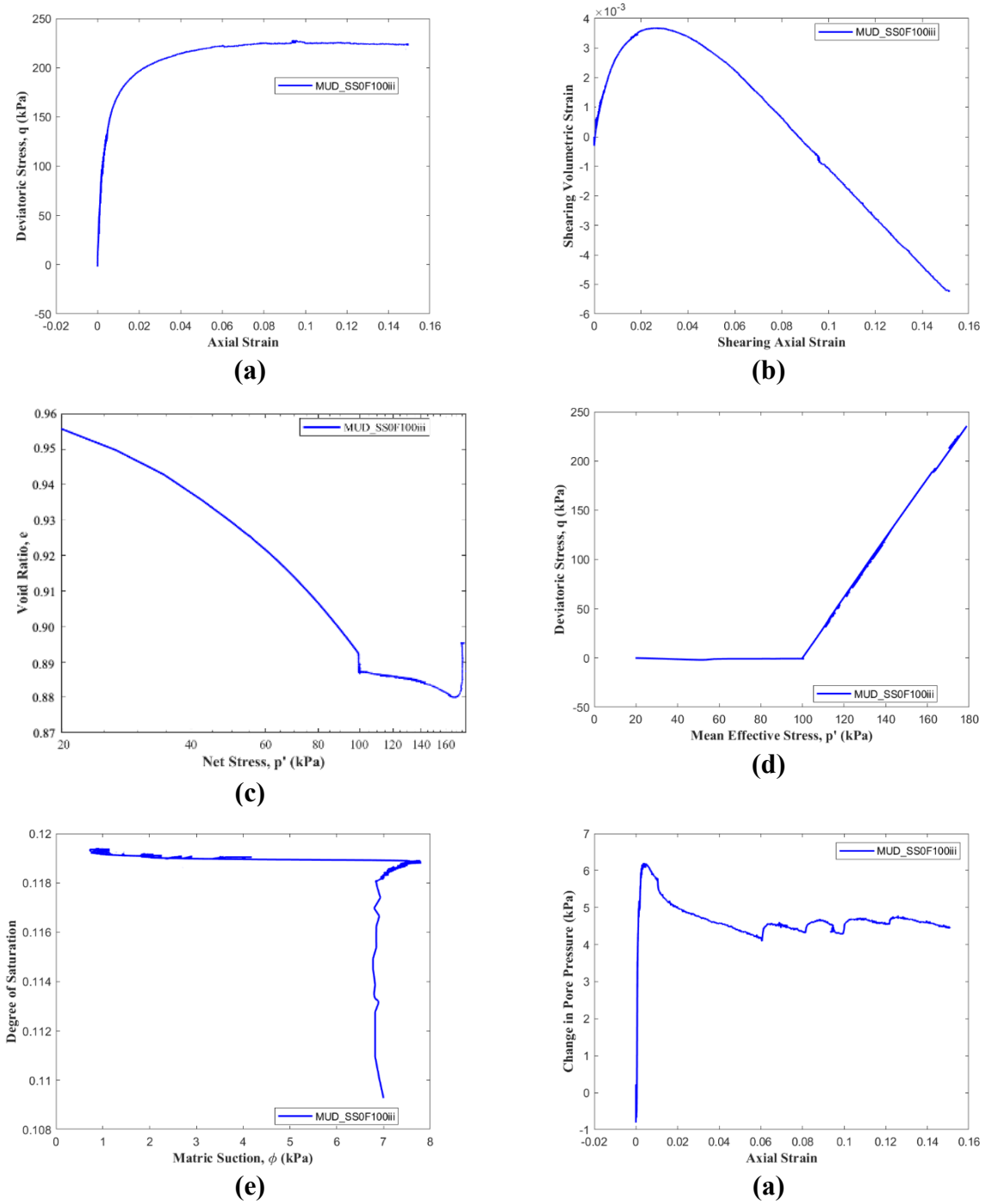

Figure 5.70: Monotonic unsaturated behaviour of Sydney sand (a) Stress Strain response, (b) Volumetric response, (c) Stress path in void ratio vs log p' space, (d) Stress path in q vs p' space, (e) Change in degree of saturation vs Matric suction, (f) Pore pressure response.

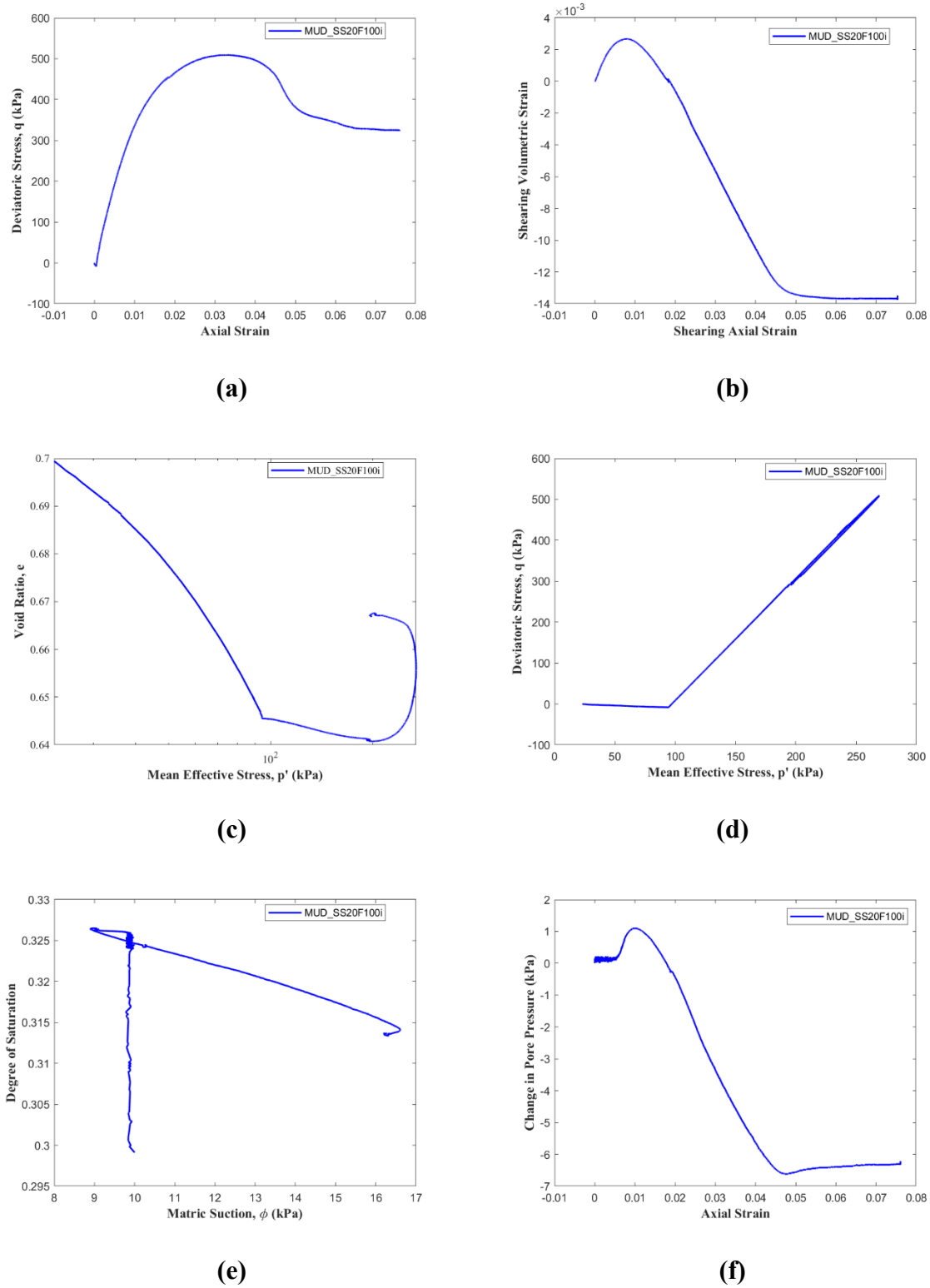

Figure 5.71:Monotonic unsaturated behaviour of Sydney sand with 20% fines (a) Stress Strain response, (b) Volumetric response, (c) Stress path in void ratio vs log p' space, (d) Stress path in q vs p' space, (e) Change in degree of saturation vs Matric suction, (f) Pore pressure response.

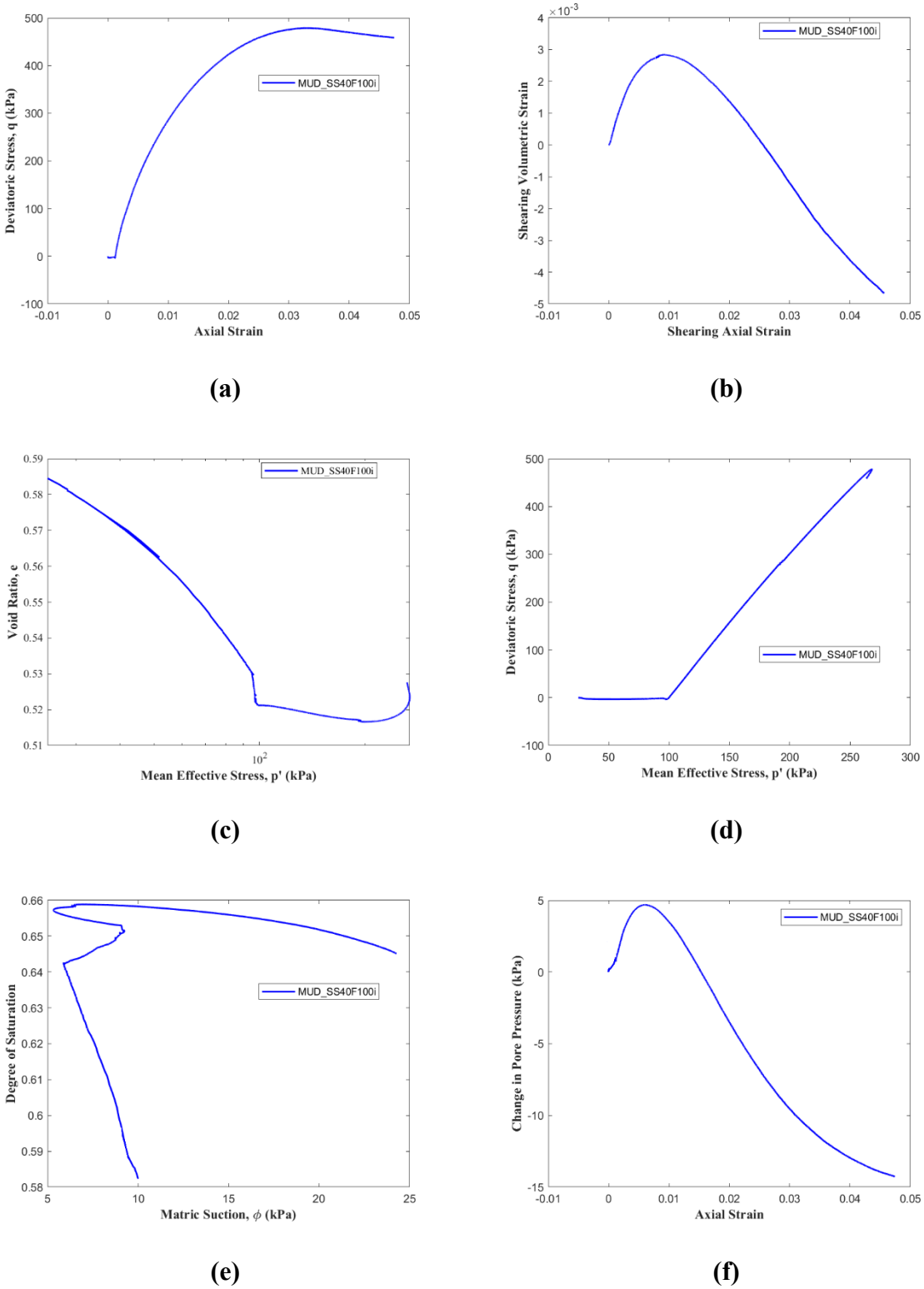

Figure 5.72: Monotonic unsaturated behaviour of Sydney sand with 40% fines (a) Stress Strain response, (b) Volumetric response, (c) Stress path in void ratio vs log p' space, (d) Stress path in q vs p' space, (e) Change in degree of saturation vs Matric suction, (f) Pore pressure response.

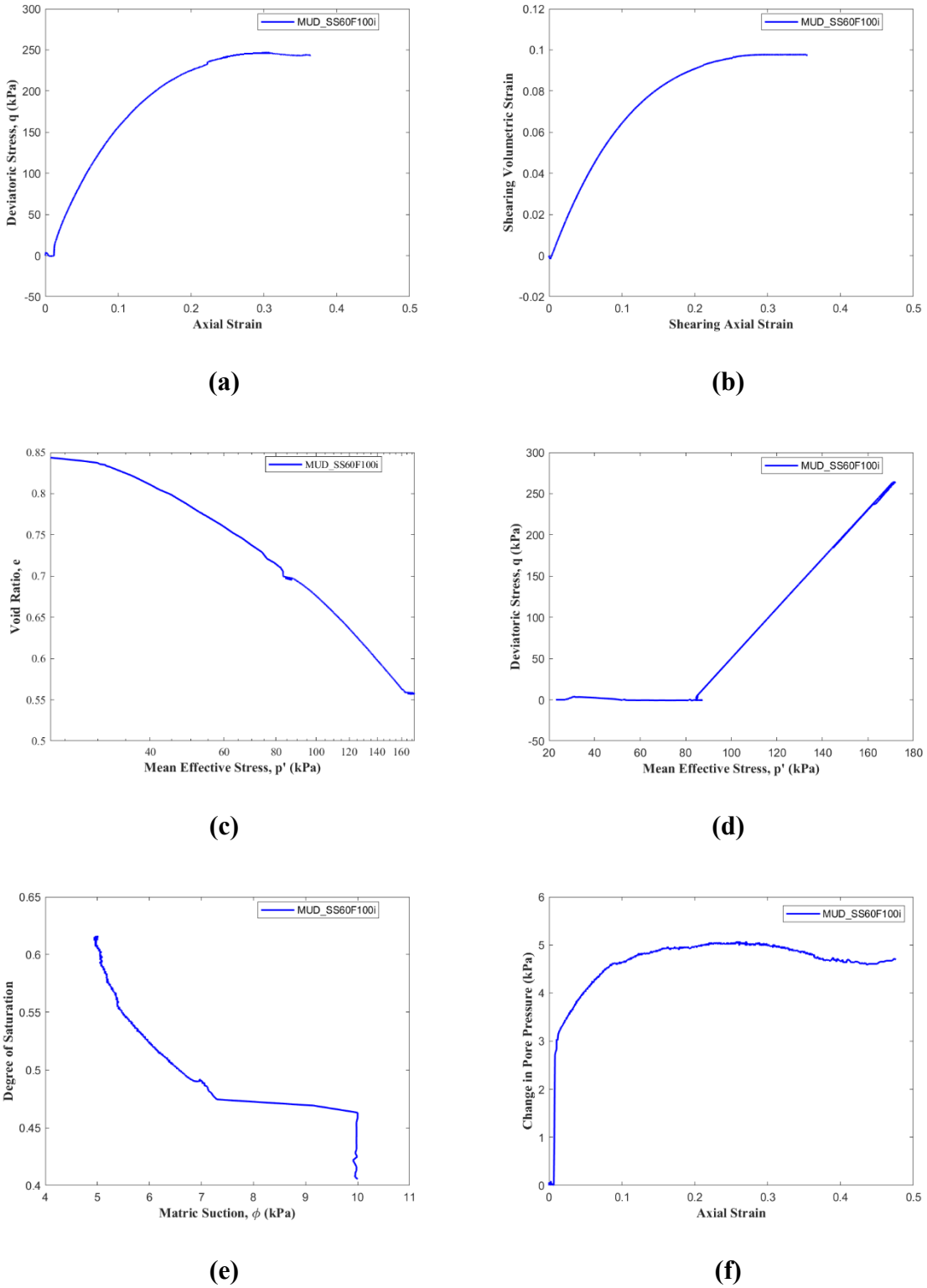

Figure 5.73: Monotonic unsaturated behaviour of Sydney sand with 60% fines (a) Stress Strain response, (b) Volumetric response, (c) Stress path in void ratio vs log p' space, (d) Stress path in q vs p' space, (e) Change in degree of saturation vs Matric suction, (f) Pore pressure response.

5.6.2 Cyclic Behaviour of Unsaturated Soils

This section presents the results and interpretation of a selected set of unsaturated cyclic triaxial tests, summarised in Table 5.13. The primary aim of these tests was to evaluate the cyclic response of partially saturated sands and well-graded soil mixtures under controlled suction conditions and to assess the applicability of the proposed constitutive model in capturing the evolving cyclic behaviour of unsaturated soils. Given the complexity of performing cyclic tests under unsaturated conditions, particularly with respect to suction equilibration and saturation stability, only a limited number of cyclic tests were performed, with one representative test per material.

All tests were conducted under constant suction conditions, meaning that any change in degree of saturation during cyclic loading was driven by both volume change and deformation. The tests were primarily carried out at a mean net stress of 100 kPa and a fixed suction of 10 kPa, consistent with the boundary conditions adopted in the monotonic unsaturated test series. An exception was made for clean Sydney Sand, where a lower suction of 6 kPa was used to reflect the relatively coarse and poorly graded nature of the material and its lower water retention capacity.

It is important to acknowledge that while a constant suction was applied and maintained throughout cyclic testing, suction equilibrium within the specimen during repeated loading was not mapped throughout the specimen (i.e., distributed internal suction sensing was not employed). In monotonic tests, the low shearing rate was considered sufficient for suction equilibrium, but during cyclic loading, even at relatively low frequencies (0.05 Hz), the transient nature of stress cycles may have prevented complete suction redistribution across the sample. This is particularly relevant for coarse or heterogeneous soils like clean Sydney Sand. Although the boundary suction was held constant, internal variations in suction could influence stiffness, degree of saturation, and effective stress evolution. These potential inconsistencies

may have had minor effects on the stress path evolution or saturation response. Future studies should consider employing embedded tensiometers or slower loading steps between cycles to better track suction equilibration within the sample during cyclic loading. Notwithstanding, preliminary internal measurements presented in Appendix A (Figure A.1) indicate small fluctuations about the set suction with no systematic drift; these data are spatially limited and thus considered preliminary, but they support the view that suction changes during cycling were small.

No explicit cyclic failure criterion was adopted in this study. Instead, the tests were terminated after a pre-set number of cycles (generally ≤100 cycles) or when equipment limitations were reached. In one case, a denser sand–fines mixture was subjected to 3000 cycles to evaluate long-term densification. Failure was not defined in terms of double-amplitude axial strain, as is typical in saturated liquefaction testing. Instead, post-cyclic monotonic shearing was used to assess the response, with specimens judged against their proximity to or divergence from the critical state line (CSL). Thus, the interpretation of failure was based on whether the soil fabric, after cyclic loading, had evolved towards a contractive or dilative state.

The cyclic response of the constant suction tests is illustrated in Figures 5.74 to 5.80, covering various soil gradations and fines contents. While the test program aimed to maintain a constant loading frequency of 0.05 Hz, equipment-related challenges, particularly with the stress-controlled actuator, led to frequency fluctuations in some tests. In the case of the WGS 60% fines mixture, these control issues were significant enough to affect the reliability of the test outcome; hence, the results for this test are not included in the discussion. These limitations reflect the broader experimental challenge of maintaining precise stress and suction control under repeated loading in unsaturated soil testing. Although Table 5.13 provides an overview of the test conditions, only those tests with consistent loading frequency and stable equipment performance were considered in the following analysis and comparison with saturated test data.

The cyclic response observed in the unsaturated tests was broadly consistent with the behaviour seen in saturated cyclic tests in terms of accumulation of plastic strain and progressive densification. However, a notable distinction was the magnitude of void ratio reduction, which was significantly greater in the unsaturated specimens. This is primarily due to the presence of compressible pore air in unsaturated soils, which allows for larger volume changes during loading, unlike saturated samples where the incompressibility of water restricts volumetric contraction. The unsaturated specimens showed a more gradual accumulation of plastic axial strain over cycles. This difference is primarily due to the presence of matric suction in the unsaturated samples, which contributes to apparent cohesion and enhances the initial cyclic resistance, thereby delaying the onset of instability (Ghayoomi et al., 2011). As a result, the unsaturated soils did not experience effective stress collapse; instead, they underwent progressive densification driven by volumetric contraction.

Associated changes in degree of saturation were also observed in loose specimens, S_r increased steadily due to void ratio reduction and expulsion of pore air; in contrast, denser specimens often showed small reductions in S_r during dilation phases, indicating localised desaturation as void space expanded. These hydro-mechanical couplings are fundamental to the unsaturated cyclic response and must be captured in advanced constitutive modelling.

For instance, a relatively loose clean sand sample exhibited notable axial strain (~4.7%) during the first cycle but experienced minimal strain accumulation over the remaining 100 cycles. Despite the limited number of cycles, the sample densified slightly and behaved like a medium-dense material during subsequent monotonic shearing. It reached a critical state well above the saturated CSL, reflecting the stiffening effect of suction and the increase in effective stress due to volume contraction.

In contrast, a denser sand-fines mixture subjected to 3000 cycles experienced only minor axial strain (~1%) per cycle. However, the cumulative effect of cyclic densification was significant,

leading to a void ratio reduction that brought the sample close to a dilative state. During post-cyclic monotonic shearing, this sample approached the unsaturated critical state line and showed clear signs of dilation, indicating that densification under cyclic loading can shift the mechanical response toward that of a dense material.

Extremely loose samples, particularly those with higher fines content (40% and 60%), responded quite differently. These specimens exhibited large initial strains during early cycles and underwent substantial volumetric contraction. However, the overall densification was insufficient to shift the samples into a dilative regime. When sheared monotonically after cyclic loading, these soils continued to compress, never reaching the critical state, and failing in a contractive manner. This illustrates how insufficient initial density can limit the beneficial effects of cyclic densification in unsaturated soils. Minimal number of cycles could also be the reason for this phenomenon. The influence of fines is critical here: while low to moderate fines improved water retention and enhanced suction stabilisation, excessive fines increased compressibility and promoted contractive behaviour under cyclic loading.

Well-graded soils with intermediate fines content, such as 18% and 28%, generally followed trends similar to those of sand-fines mixtures with 20% fines. They exhibited moderate strain accumulation and underwent gradual densification over several hundred to a few thousand cycles. In one case, a sample reached a significantly lower void ratio but did not fail under post-cyclic monotonic loading, suggesting enhanced resistance due to the combined effect of particle interlocking and suction. In contrast, samples with 40% fines displayed a mix of contractive and dilative behaviour depending on their initial void ratio and fines packing structure.

The stress paths from these tests, plotted in both void ratio vs. log(p') and q vs. p' spaces (Figures 5.74 to 5.80), reveal the evolution of stress states under cyclic loading. In denser specimens, the stress path gradually approached the critical state in a manner consistent with

dilation. In looser specimens, the stress path remained below the CSL and moved horizontally or downward, indicating continued contraction and the absence of a critical state condition.

A critical comparison for Sydney Sand with saturated behaviour is shown in Figure 5.81, where the critical state lines for saturated and unsaturated conditions are overlaid. The unsaturated CSLs consistently appear above those of the saturated counterparts across all tested gradations. This shift is attributed to the contribution of matric suction, which increases the soil's apparent cohesion and effective stress, enhancing cyclic resistance and delaying the onset of failure. Importantly, the location of the unsaturated CSL is not fixed but varies with the degree of saturation and fines content, as will be quantified in the next chapter.

In summary, the cyclic behaviour of unsaturated soils exhibits a complex interplay between suction, fines content, and density. Loose samples with high air content can densify under repeated loading but may not reach the critical state unless sufficiently compacted. Denser specimens, on the other hand, show more stable responses and are more likely to exhibit dilative behaviour upon shearing. These observations emphasise the need to consider not just the initial density but also the evolving saturation and suction conditions in cyclic stability assessments. The experimental findings clearly demonstrate that unsaturated CSLs are elevated compared to saturated ones, and the shift in critical state behaviour must be captured in constitutive models for accurate prediction of cyclic soil response.

Table 5.13: Summary of Cyclic Unsaturated tests

Test NO	Test Label	p_i'	*Suction*	e_{cyc}	e_f	DOS_{cyc}	DOS_f	q_{amp}	*CSR*	No of cycles
UC1	CUD_SS0F100i	100	-6	0.9225	0.8665	0.0976	0.1037	175	0.875	100
UC2	CUD_SS0F100ii	100	-10	0.5282	0.5261	0.1097	0.1240	75	0.375	3000
UC3	CUD_SS20F100	100	-10	0.5456	0.5498	0.5336	0.5560	70	0.350	2536
UC4	CUD_SS40F100	100	-10	0.8503	0.7256	0.3980	0.4027	135	0.675	20
UC5	CUD_SS60F100	100	-10	0.9487	0.7963	0.4420	0.5307	125	0.625	20
UC6	CUD_WGS18F100	100	-10	0.2525	0.2883	0.5387	0.5516	65	0.325	516
UC7	CUU_WGS28100	100	-10	0.5213	0.4777	0.5285	0.5766	115	0.575	900
UC8	CUD_WGS40F100	100	-10	0.5591	0.4716	0.5891	0.7242	65	0.325	220
UC9	CUU_WGS60F100	100	-10	0.4704	0.4347	0.5336	0.5560	130	0.650	2500

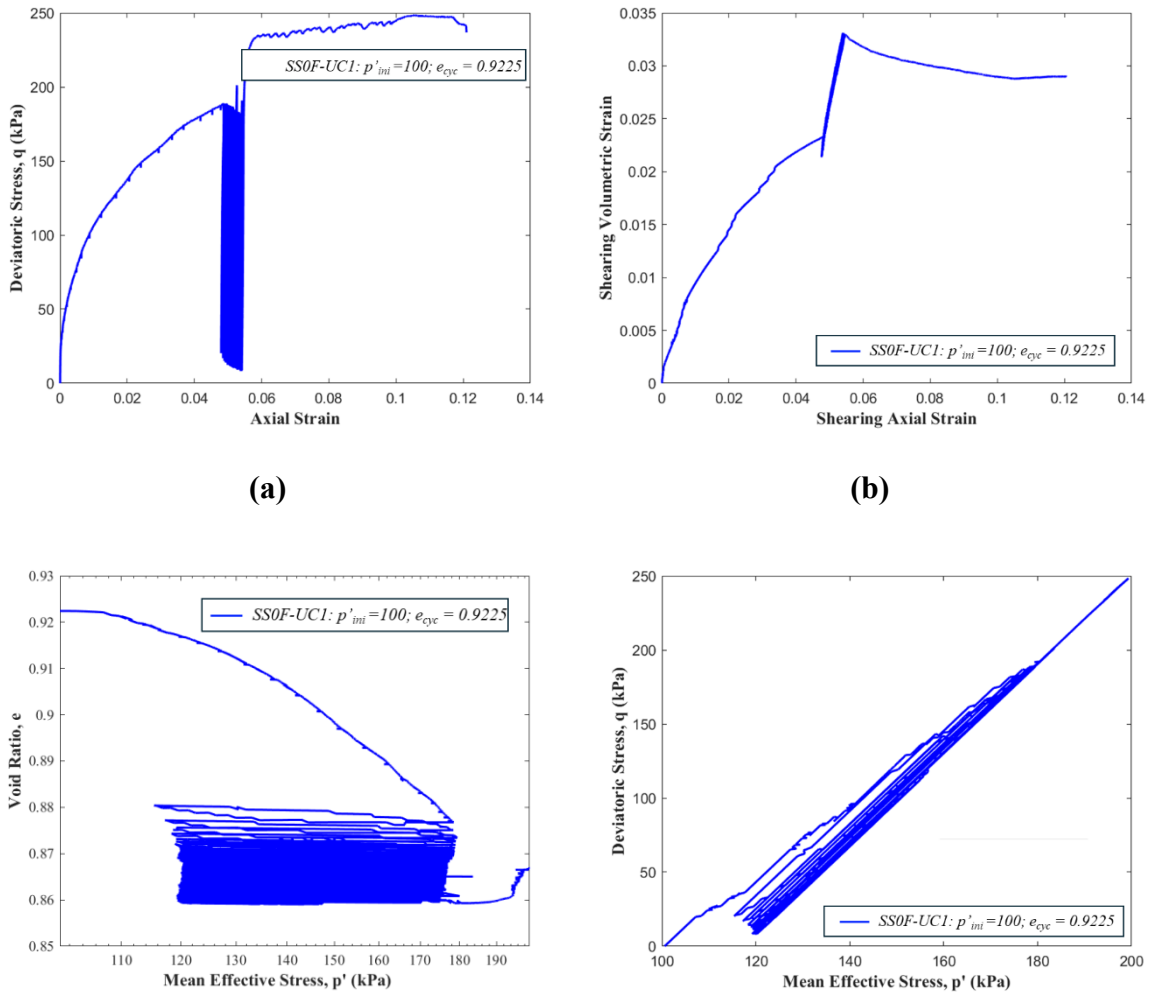

Figure 5.74: Cyclic unsaturated behaviour of Sydney sand (a) Stress Strain response, (b) Volumetric response, (c) Stress path in void ratio vs log p' space, (d) Stress path in q vs p' space.

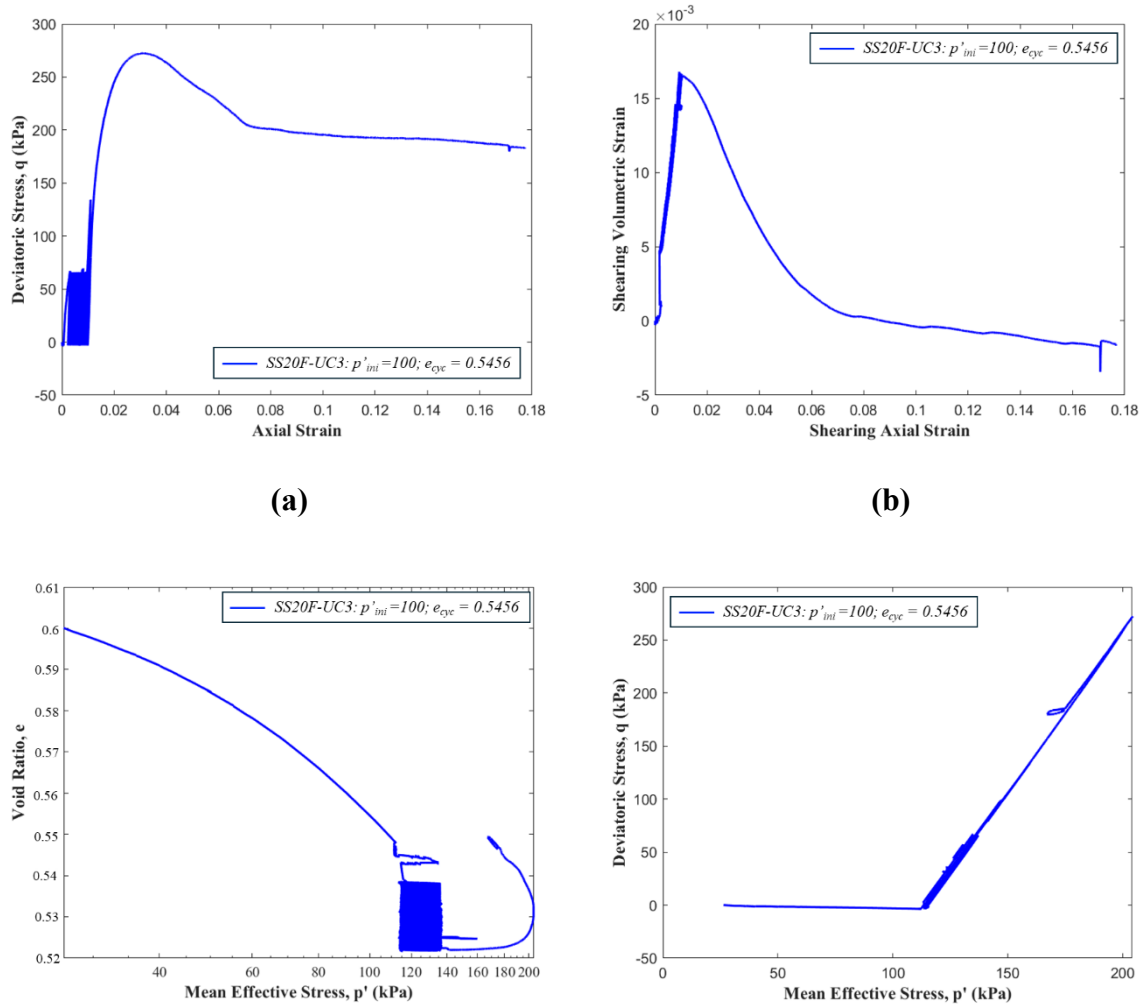

Figure 5.75: Cyclic unsaturated behaviour of Sydney sand with 20% Fines(a) Stress Strain response, (b) Volumetric response, (c) Stress path in void ratio vs log p' space, (d) Stress path in q vs p' space.

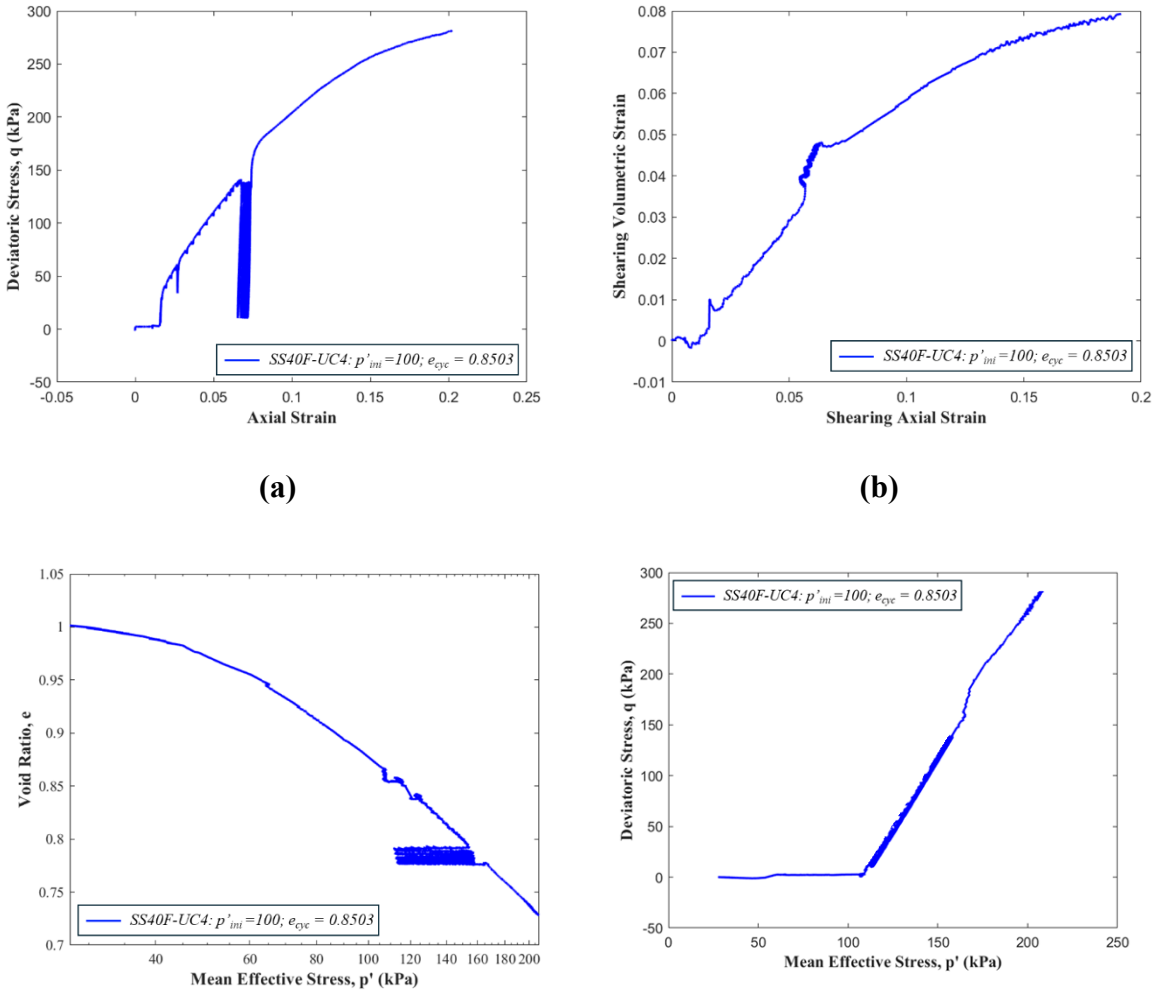

Figure 5.76: Cyclic unsaturated behaviour of Sydney sand with 40% Fines(a) Stress Strain response, (b) Volumetric response, (c) Stress path in void ratio vs log p' space, (d) Stress path in q vs p' space.

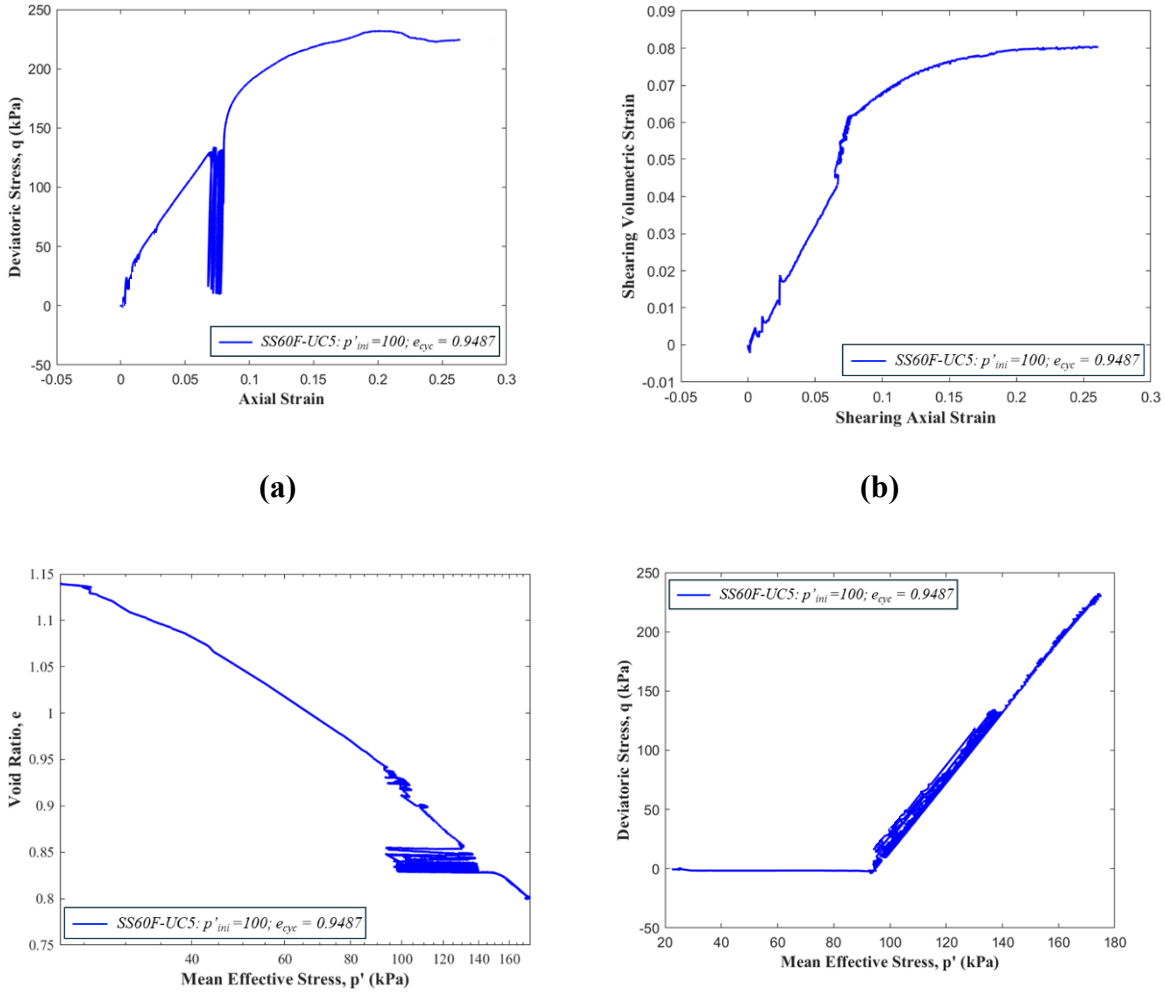

Figure 5.77: Cyclic unsaturated behaviour of Sydney sand with 60% Fines(a) Stress Strain response, (b) Volumetric response, (c) Stress path in void ratio vs log p' space, (d) Stress path in q vs p' space.

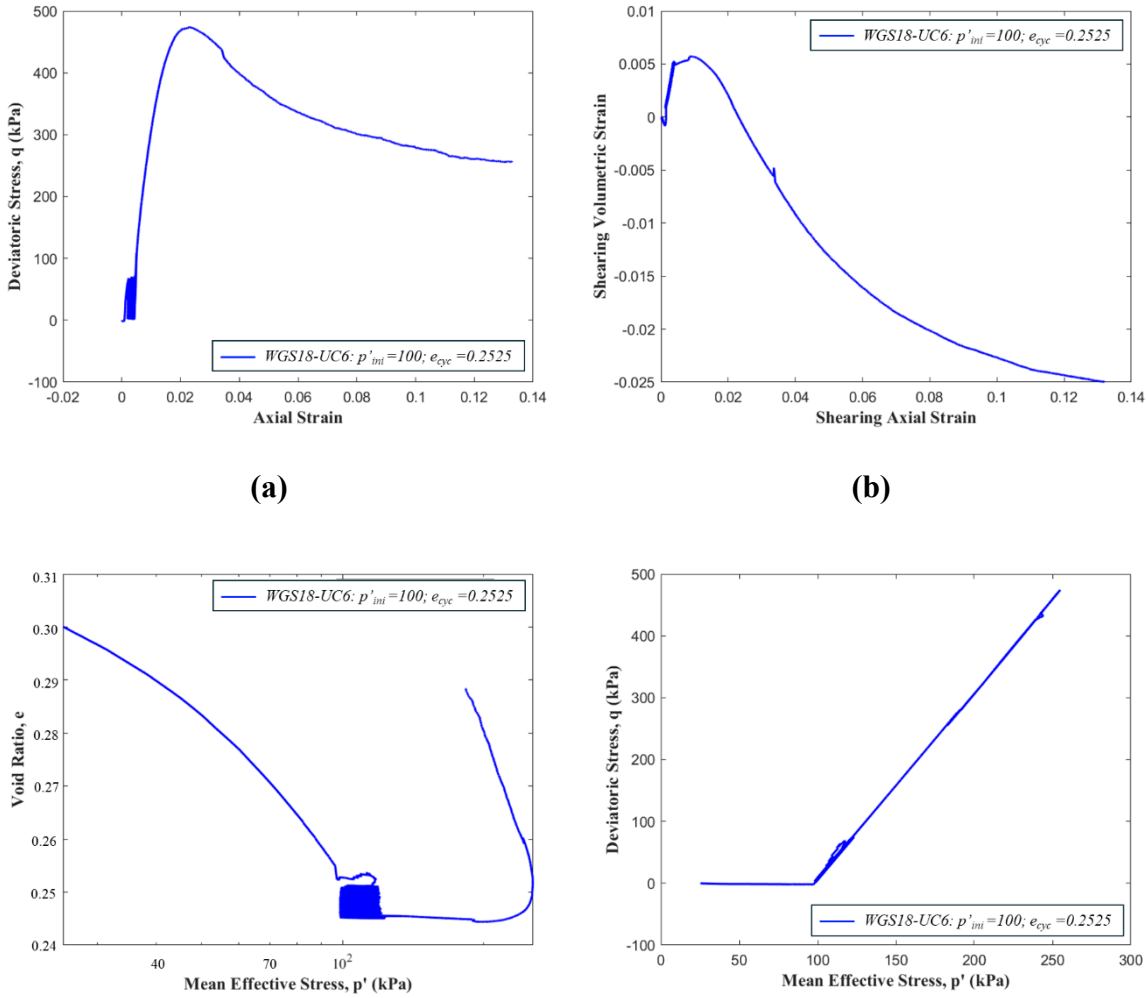

Figure 5.78: Cyclic unsaturated behaviour of WGS with 18% Fines(a) Stress Strain response, (b) Volumetric response, (c) Stress path in void ratio vs log p' space, (d) Stress path in q vs p' space.

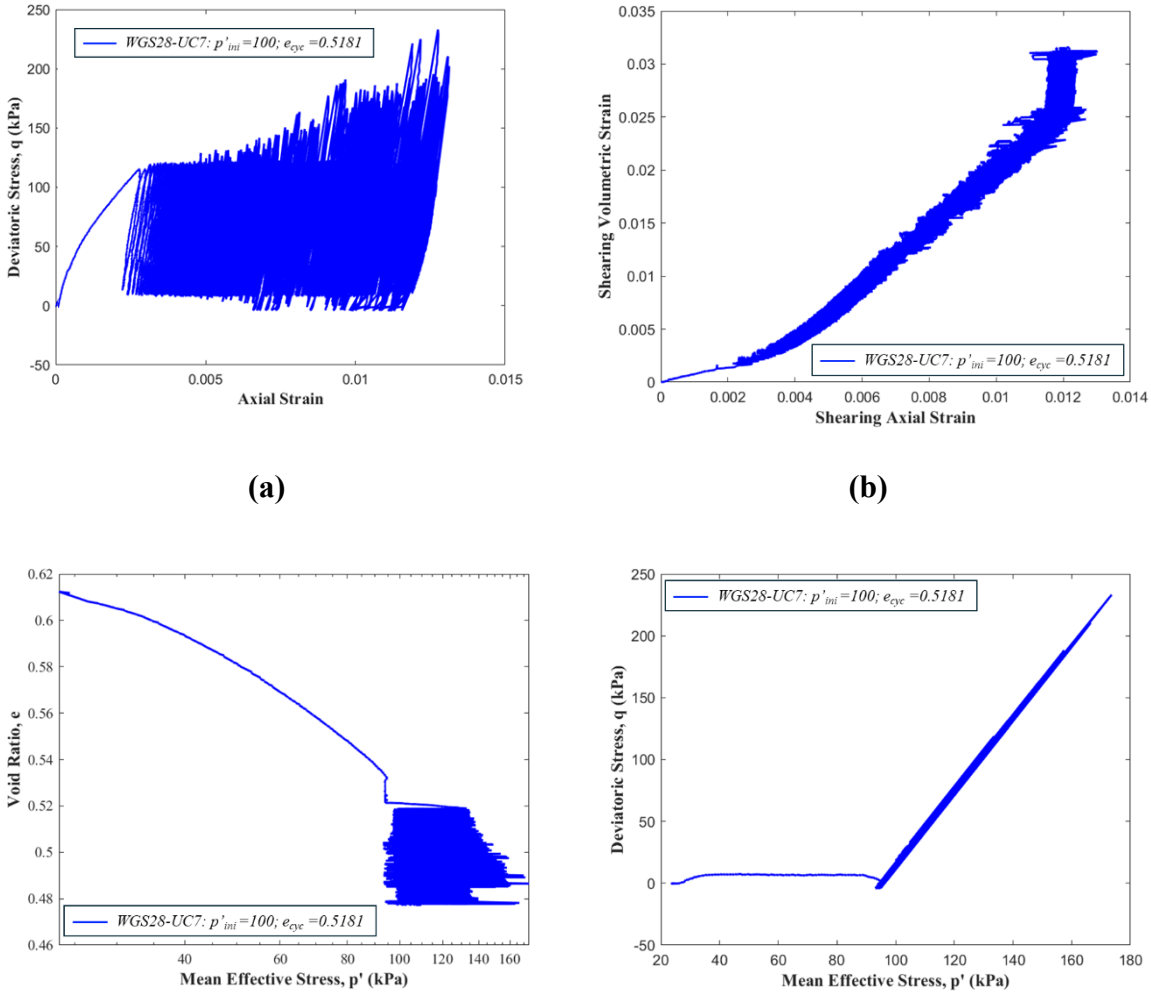

Figure 5.79: Cyclic unsaturated behaviour of WGS with 28% Fines(a) Stress Strain response, (b) Volumetric response, (c) Stress path in void ratio vs log p' space, (d) Stress path in q vs p' space.

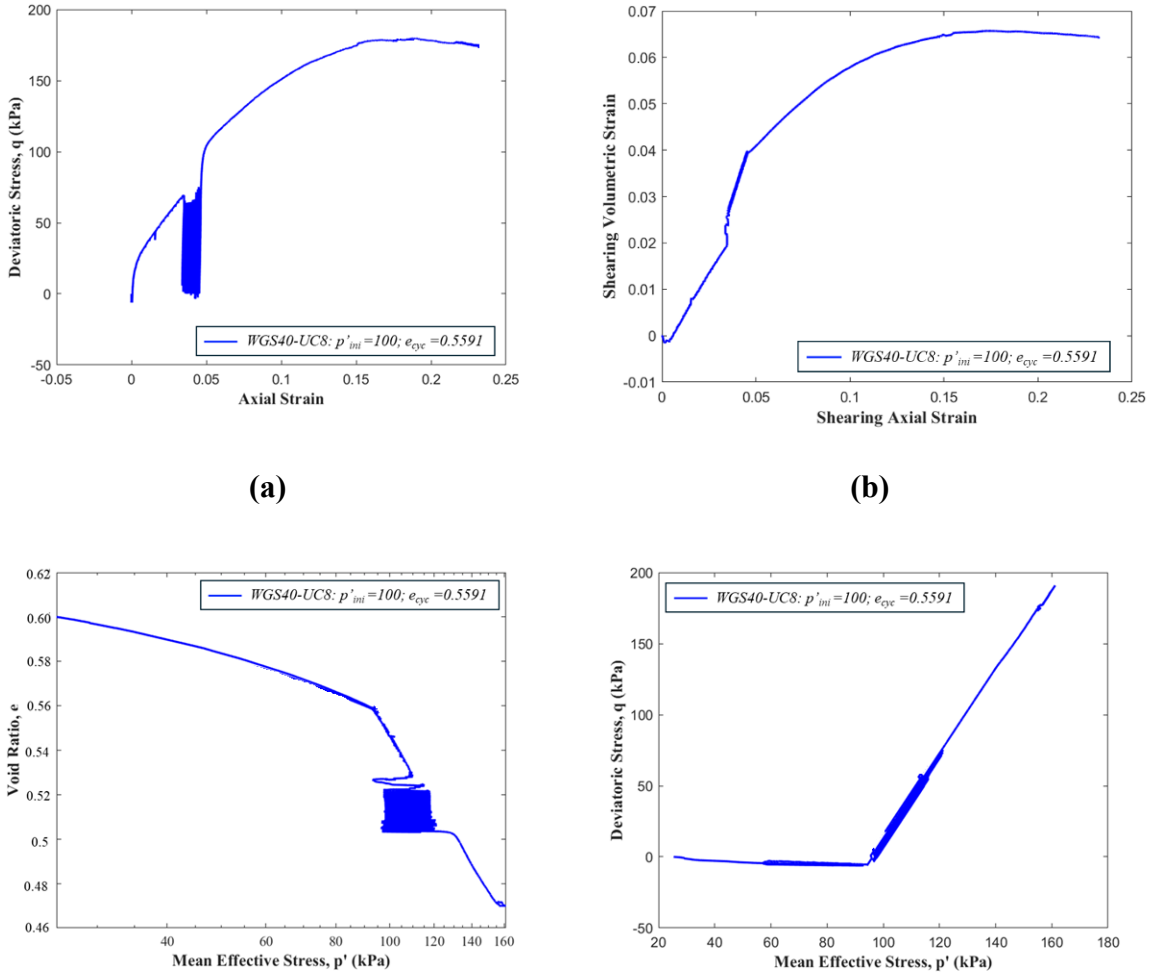

Figure 5.80: Cyclic unsaturated behaviour of WGS with 40% Fines(a) Stress Strain response, (b) Volumetric response, (c) Stress path in void ratio vs log p' space, (d) Stress path in q vs p' space.

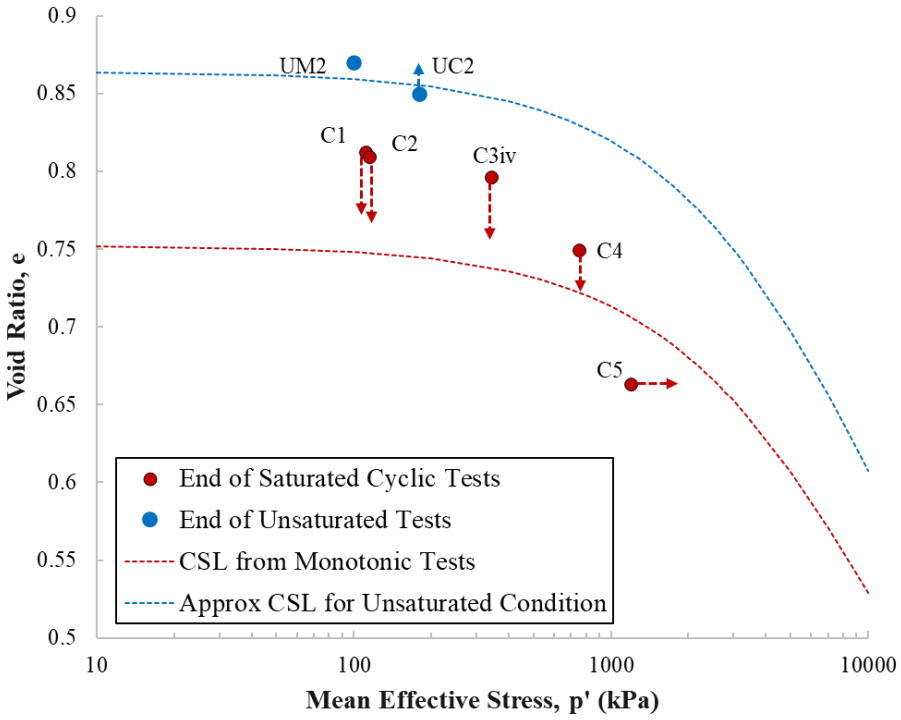

Figure 5.81: CSL Summary of Saturated and Unsaturated condition: Sydney Sand

5.7 Summary

In summary, this chapter presents a series of experiments designed to determine the essential model parameters for both the original and revised models. These experiments include 1-D compression tests, triaxial tests, and soil-water characteristic curve (SWCC) determinations, each chosen for its efficacy in providing specific types of data.

The 1-D compression tests were conducted to derive compression parameters, which are tabulated in Table 5.2. Critical state parameters, obtained through triaxial testing, are presented in Table 5.8 and Table 5.9. The SWCC parameters, crucial for understanding the hydraulic behaviour of unsaturated soils, are listed in Table 5.10 and Table 5.11. While the aforementioned tests were primarily used for parameter determination and model calibration, the unsaturated tests served a different purpose. These tests were specifically conducted to validate the model's performance under partially saturated conditions. The material parameters, derived from the saturated tests, were further calibrated along with curve-fitting parameters.

These calibrated parameters were then used to simulate each of the unsaturated tests performed in this study, as well as available data from Kwa (2019) and Amirabbas (2020).

It is worth noting that the unsaturated tests were not designed with strict consistency in the number of cycles or cyclic stress ratio (CSR). This variability, although initially unintended, proved beneficial in validating the model's versatility across a range of loading conditions which will be addressed in future research. Further calibration and simulations are explained in the following chapter.

Chapter 6
Model Simulations

6.1 Introduction

Numerical modelling of soil behaviour relies on accurately calibrated constitutive parameters to ensure realistic simulation of mechanical responses under a variety of loading paths. Calibration is a crucial step in constitutive modelling, as it governs the ability of the model to replicate experimentally observed behaviours, including volume change, strain softening or hardening, and stress path evolution. This chapter presents the comprehensive calibration strategy adopted for the constitutive model used in this study, which includes parameter derivation, simulation procedures, and validation against experimental data from triaxial tests. The focus of this chapter is on the calibration of model parameters for simulating monotonic triaxial tests on both saturated and unsaturated conditions for Sydney Sand and Well-Graded Sand (WGS) mixtures with varying fines content. Following this, attempts were made to simulate saturated and unsaturated cyclic triaxial tests to assess the model's capability in capturing cyclic stiffness degradation, stress reversal, and strain accumulation under repeated loading. The parameters associated with elastic stiffness, critical state, yield surface, dilatancy, and kinematic hardening are calibrated using experimental results generated in this study and, where necessary, supplemented with data from published triaxial tests on similar soils, i.e., Mohammadi (2020) and Kwa (2019), to improve confidence and robustness in the parameter selection.

However, it is important to note that not all model components were calibrated from scratch. Specifically, the parameters governing the memory surface and the semi-fluidised state, which primarily influence cyclic and post-cyclic behaviour were not fully calibrated in this study due to limitations in available test data. Instead, these parameters were adopted from pre-existing, well-validated simulations of sands with similar particle size distributions and fines content. This decision was based on a rational and pragmatic modelling philosophy, acknowledging that soils with comparable gradation and mineralogy often exhibit similar behavioural trends

under cyclic loading. While this introduces a degree of approximation, minor fine-tuning was performed based on comparative simulations to ensure the trends remained realistic. Nevertheless, the reader is advised that these parameters were not subject to full calibration within the scope of this work, and thus any findings related to cyclic or post-liquefaction behaviour should be interpreted with this limitation in mind.

6.2 Calibration Techniques

As discussed in Chapter 2, the model parameters can be categorised into groups depending on the material characteristic they describe. These groups are Elasticity, Critical state, Kinematic hardening, Dilatancy, Memory Surface, Semifluidised State, and stress integration and unsaturated soil parameters. Calibration for each of the parameter groups is described below, and the full calibration workflow is summarised in a schematic as shown in Figure 6.1, which maps parameter groups to the experimental tests from which they are derived. This flowchart provides a step-by-step reference for researchers and practitioners, ensuring transparency and reproducibility of the calibration process. Calibration for each of the categories is described below.

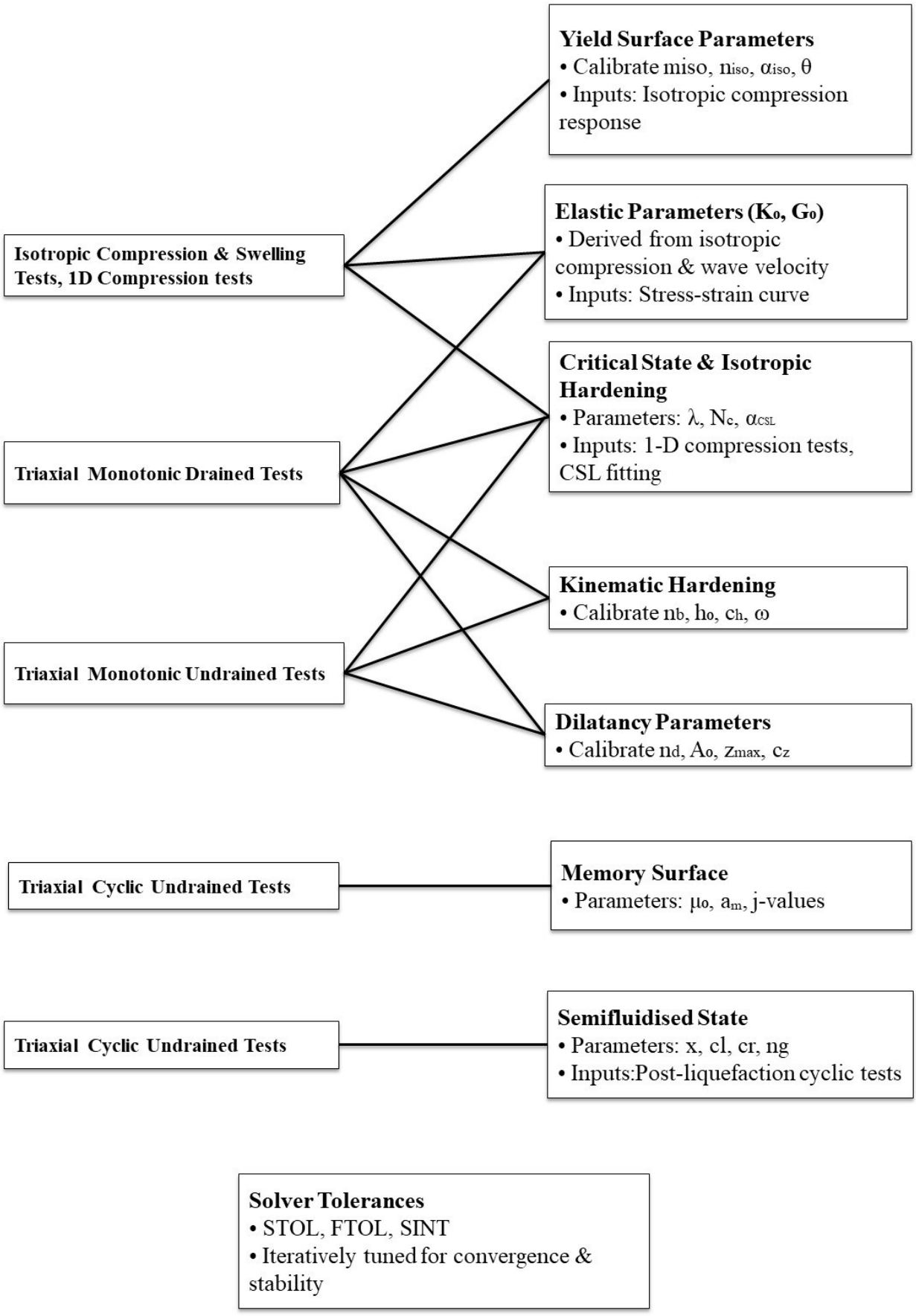

Figure 6.1: Calibration workflow schematic showing parameter groups

6.2.1 Elasticity

The parameters, the bulk and shear moduli, are dependent on stress and dry density as specified by equations 10 and 11. These equations have two dimensionless constants K_0 and G_0 that control the magnitudes of the moduli. Alternatively, with the help of isotropic swelling test (unloading stage of isotropic compression test), K_0 can be determined with help of following relation given by Ghorbani and Airey (2021):

$$K_0 = -3\frac{\left(p_2'^{\frac{1}{3}} - p_1'^{\frac{1}{3}}\right)}{p_a^{\frac{1}{3}}(ln\, e_2 - ln\, e_1)} \qquad 42$$

Where p_1' and p_2' are mean effective stress of the soil at the beginning and end of swelling respectively and e_1 and e_2 are corresponding void ratios.

This expression can be applied to the unloading curve of 1-D compression test (Oka F et al., 1999) at high stress when plotted in terms of p' vs e. Here p' is calculated with vertical stress and $K_{0,nc}$ (coefficient of earth pressure at rest, not to be confused with material parameter K_0);

$p' = (\sigma'_v + 2K_{0,nc}\sigma'_v)/3$

The parameter G_0, which represents the elastic shear modulus in Equation 10, can be determined from stress–strain responses or through elastic wave velocity measurements in the laboratory or field. In this study, G_0 for Sydney sand under monotonic shearing was estimated by fitting Equation 10 to the initial segment of the deviatoric stress–strain data obtained from drained triaxial tests. As shown in Figure 6.2, a value of $G_0 = 186$ was selected for Sydney sand.

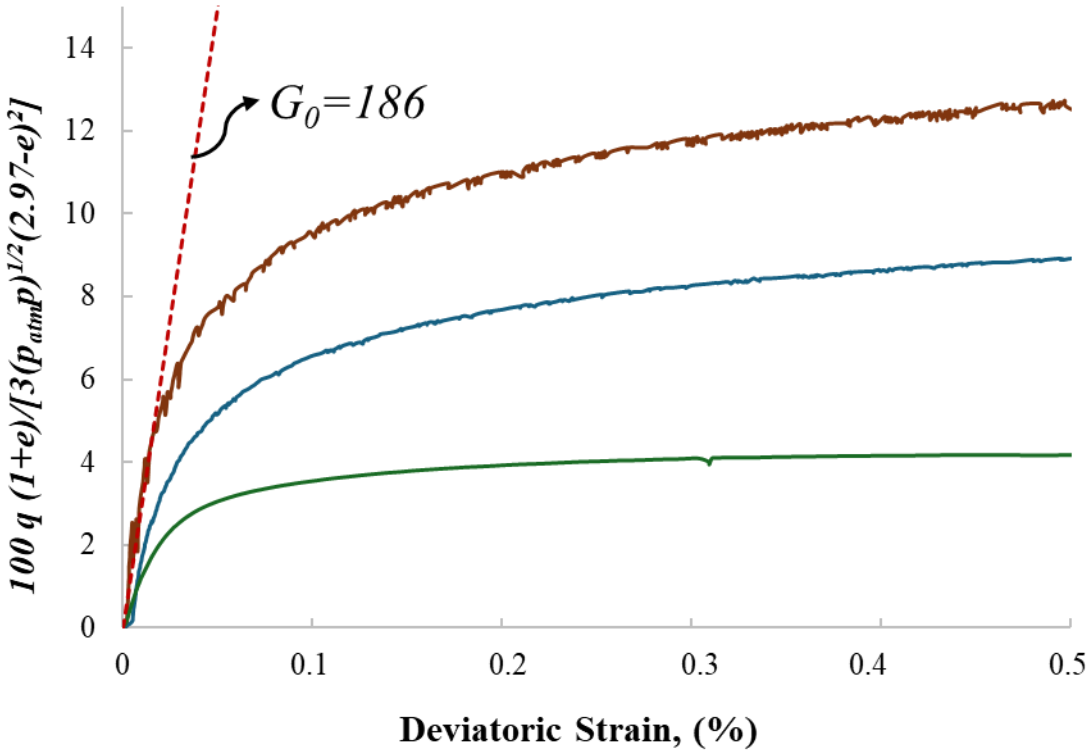

Figure 6.2: Calibration of G_0 for Sydney Sand

6.2.2 Critical State and Isotropic Hardening parameters

The isotropic hardening parameters can be derived from the LCC line which can be plotted using 1-D compression test at high stress states (Burland, 1990; Wood, 1990). The compression curve is constructed by plotting equation 12 enabling parameter λ and of N_l to be estimated. Here λ is the slope of the limiting compression line and it also controls the slope of the critical state line along with α_{csl} as shown in equation 12 and 18. The plotted line is adjusted to asymptotically fit the compression curve at high-stress levels, where the slope of the compression curve stabilises. Once this fitting is achieved, the coefficients of the line provide the value of N_l, as illustrated in Figure 5.1 and Figure 5.4 in chapter 5.

The critical state parameters are denoted differently depending on the coordinate space in which they are represented. Given the advantages of using bi-logarithmic space, as discussed in previous sections (Been & Jefferies, 1985; Li & Wang, 1998), this approach has been

adopted in the original model. Using drained and undrained triaxial tests performed on soil samples with various relative densities and initial stress conditions, the CSL is plotted in terms of void ratio and mean effective stress.

The experimentally derived CSL is then fitted using Equation 18 by adjusting N_c, and α_{csl}, while λ parameter remains fixed, as it has already been determined from the LCC Equation 12. The parameters λ and α_{csl} influences the slope of the CSL, while N_c is the value of void ratio on the CSL when $p_c'+\alpha_{csl} = 1$. The final parameters used for simulations are derived from the best-fit curves presented in Figures 6.3 to 6.10.

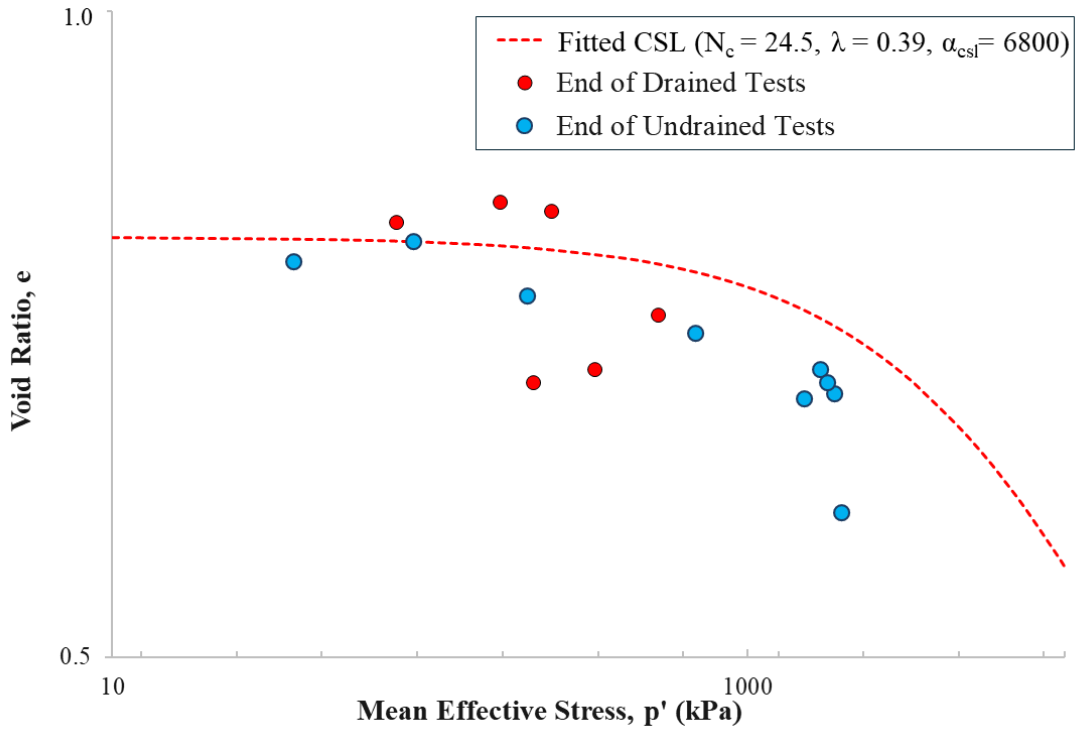

Figure 6.3: Fitted CSL Parameters for Sydney Sand

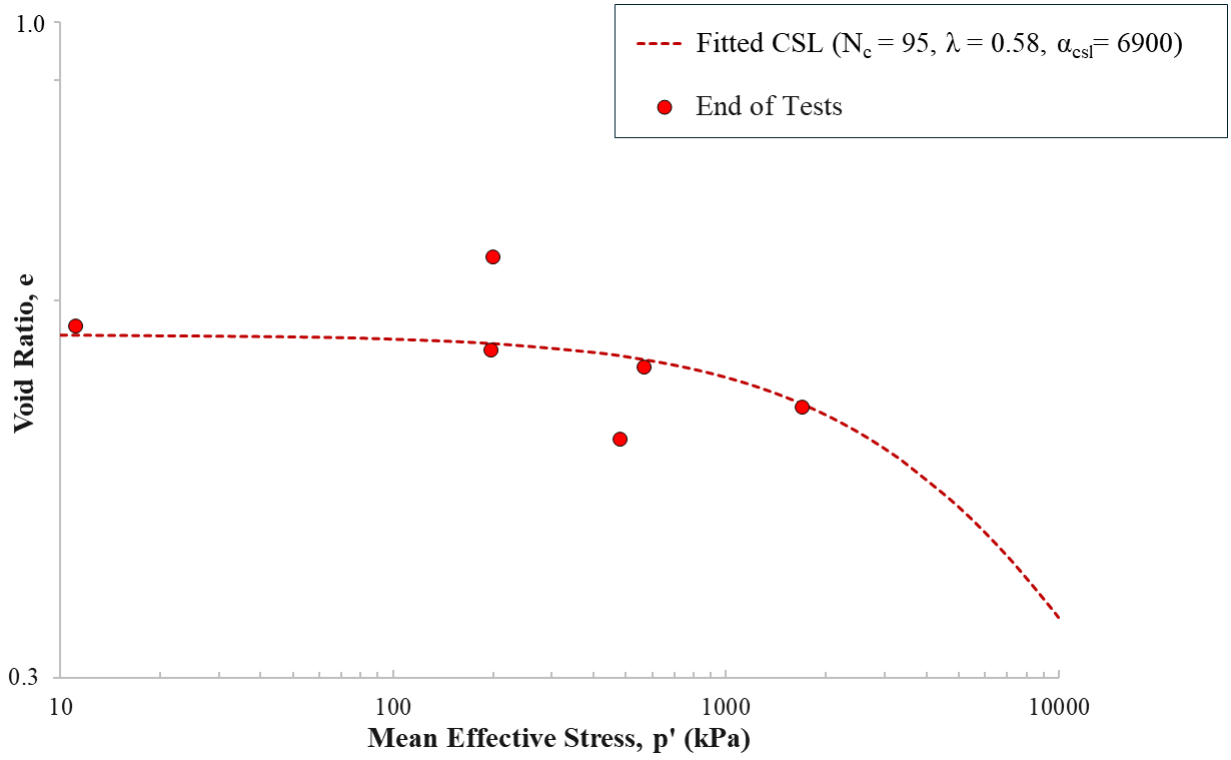

Figure 6.4: Fitted CSL Parameters for Sydney Sand with 20% Fines

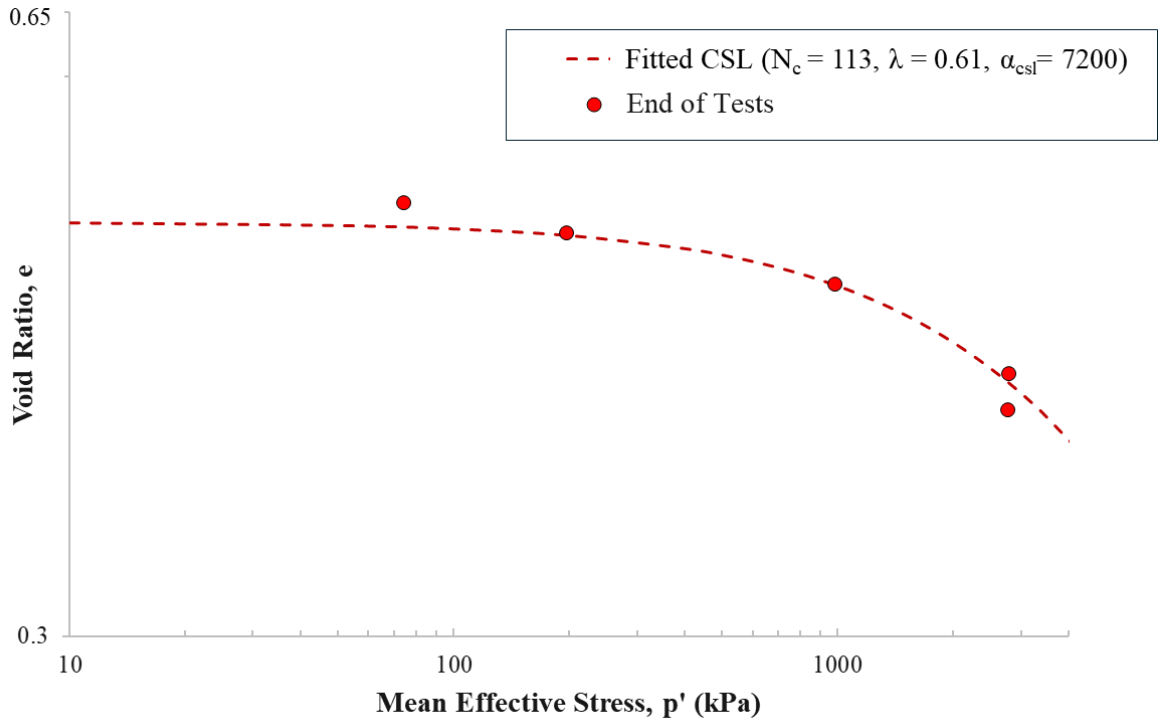

Figure 6.5: Fitted CSL Parameters for Sydney Sand with 40% Fines

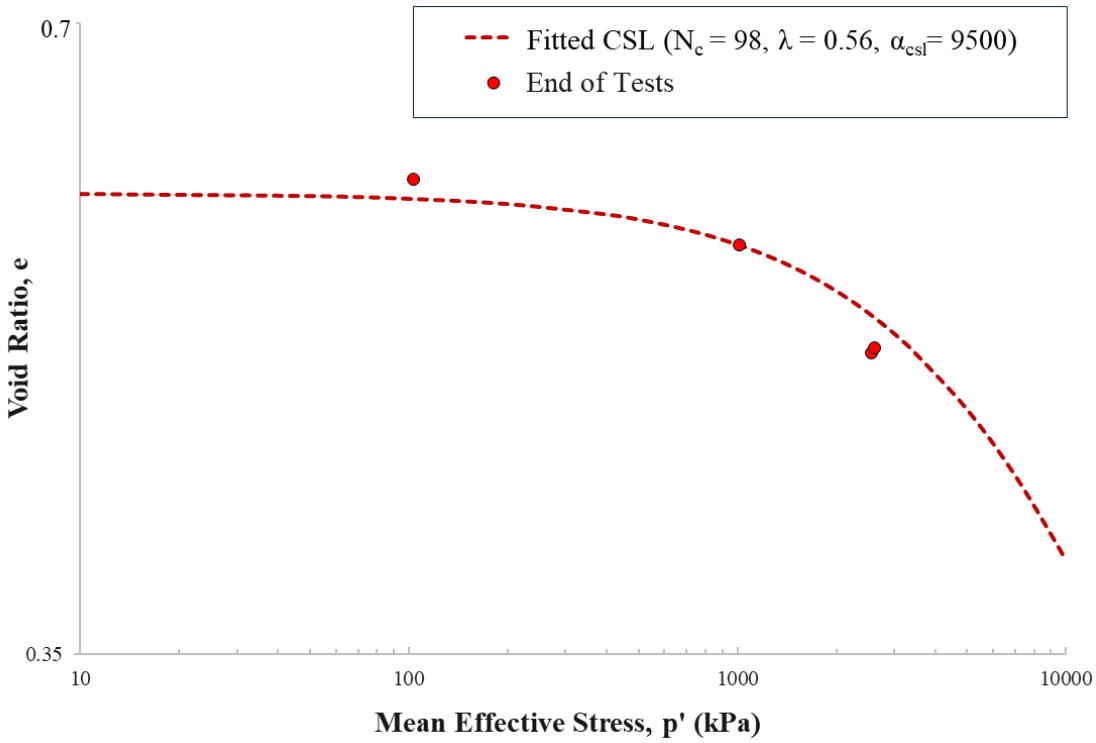

Figure 6.6: Fitted CSL Parameters for Sydney Sand with 60% Fines

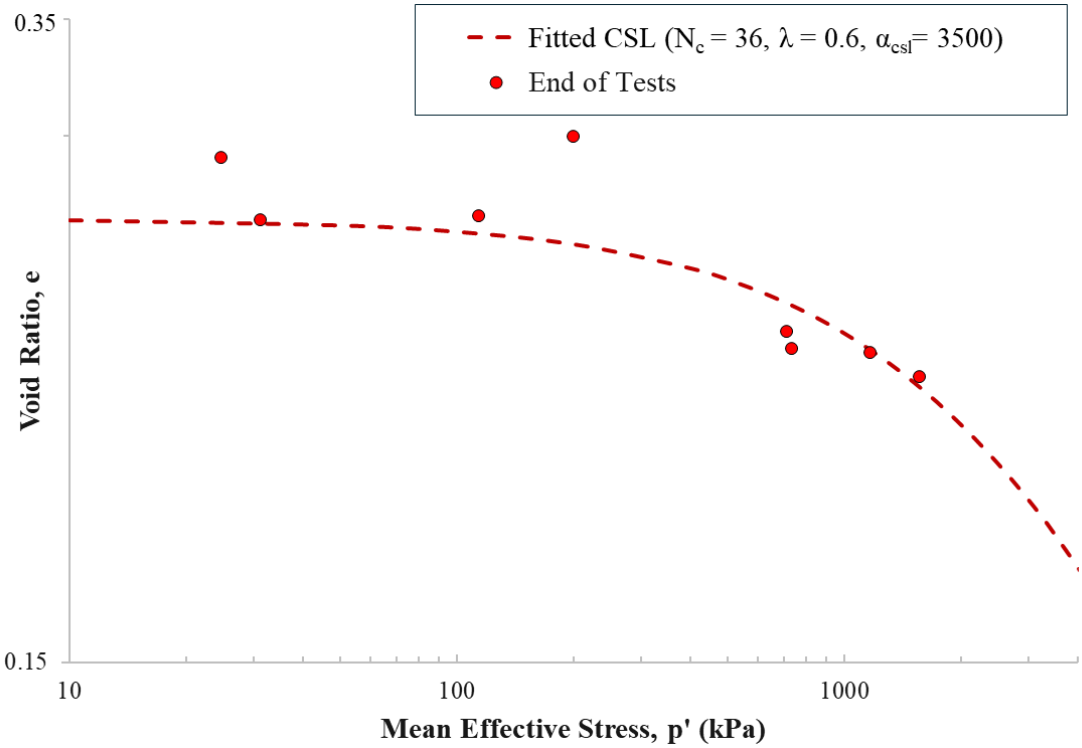

Figure 6.7: Fitted CSL Parameters for WGS with 18% Fines

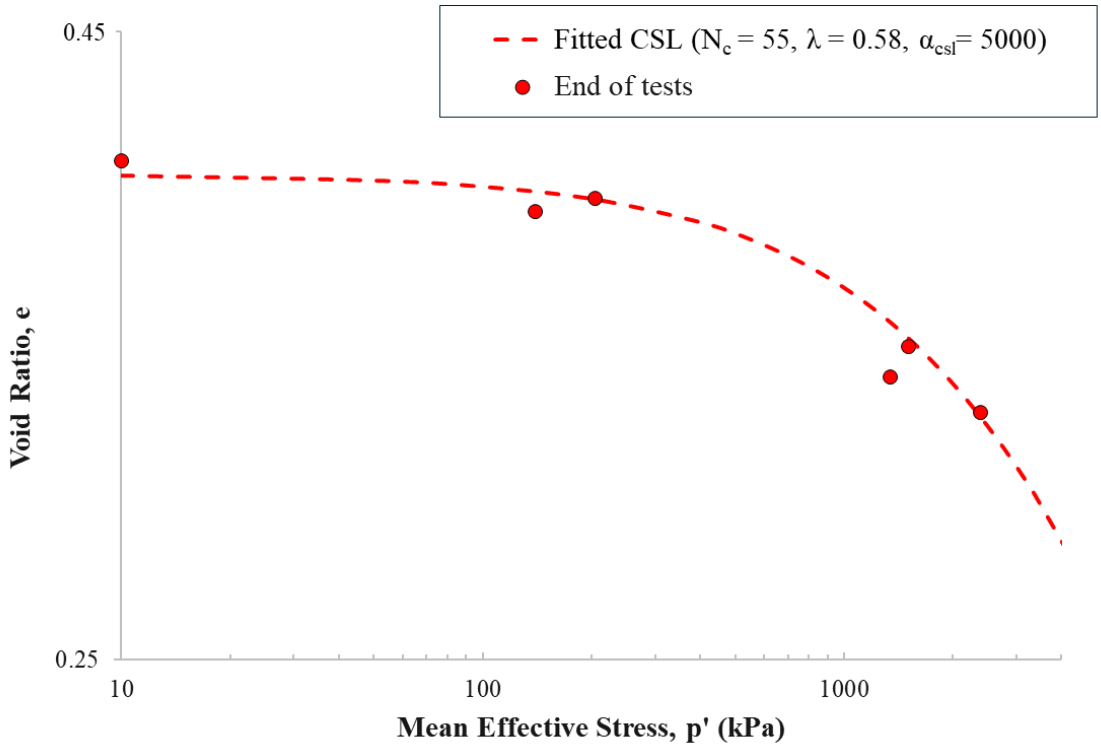

Figure 6.8: Fitted CSL Parameters for WGS with 28% Fines

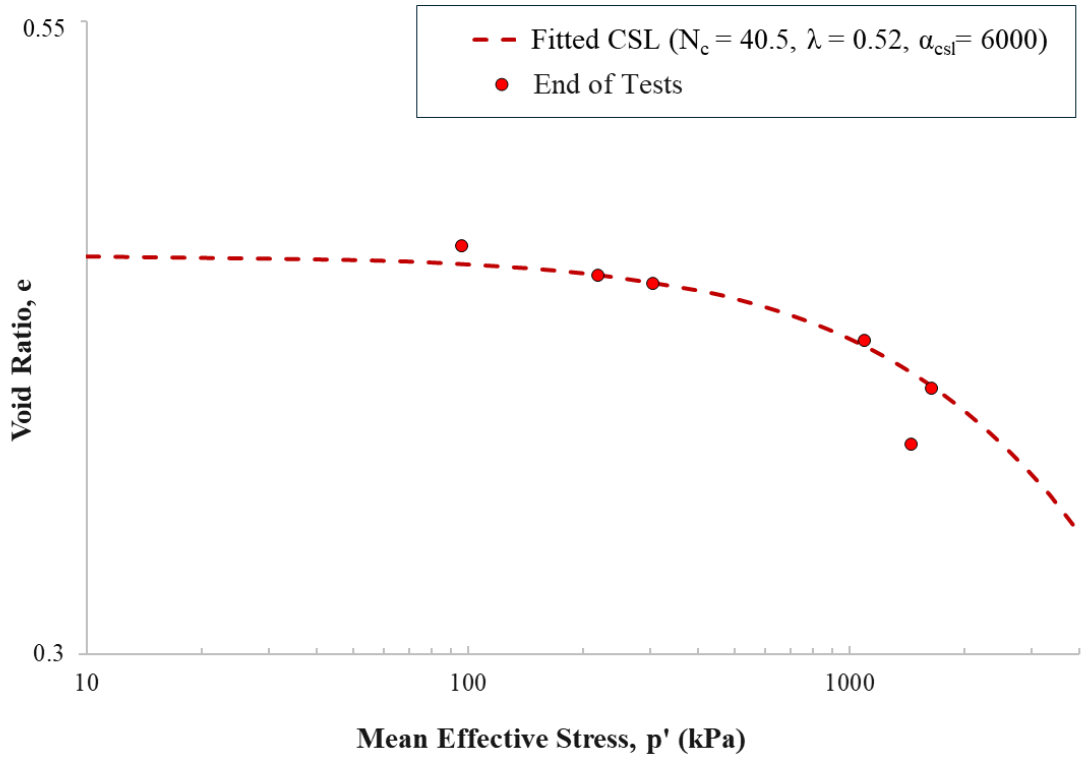

Figure 6.9: Fitted CSL Parameters for WGS with 40% Fines

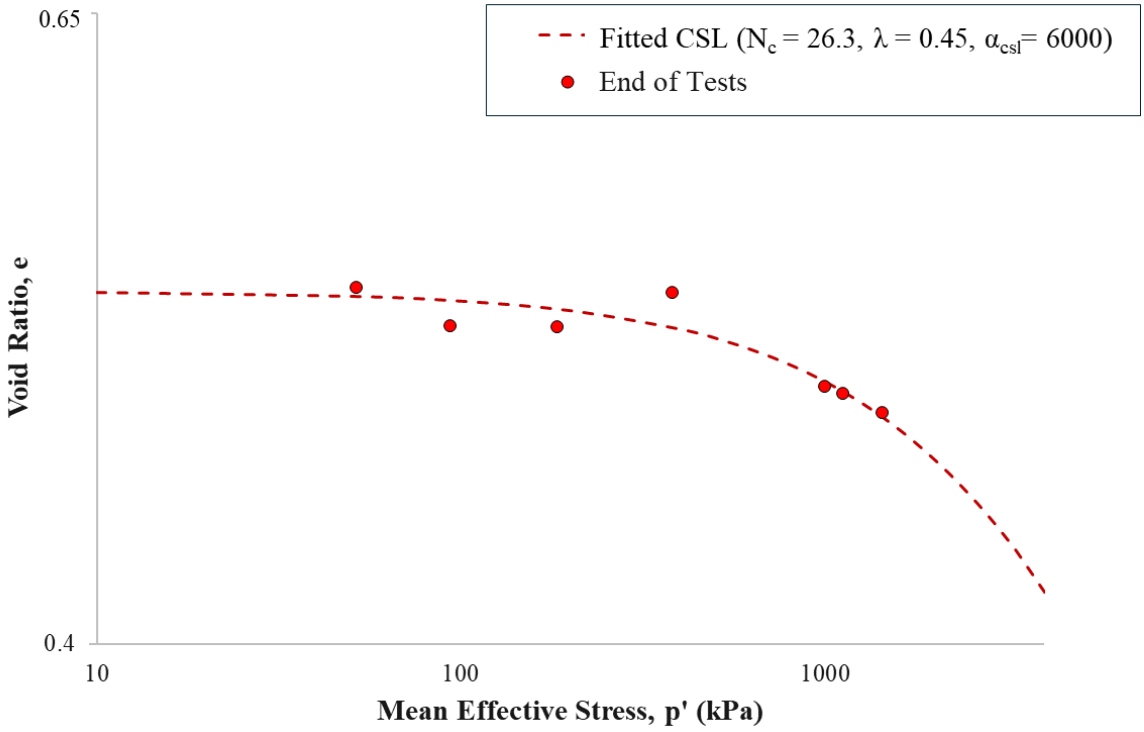

Figure 6.10: Fitted CSL Parameters for WGS with 60% Fines

The fitted CSL is refined by adjusting the model parameters. While ensuring a good fit, it is crucial to avoid the use of unrealistic parameter values purely for curve fitting purposes. The accuracy of the CSL fitting depends on both the quantity and quality of the experimental data. For instance, in SS60 (Sydney Sand with 60% fines), where the number of experiments is limited, the fit is less reliable. Conversely, despite a high number of experiments, WGS28 (WGS with 28% fines) also exhibits a poor fit, highlighting the importance of balancing data quality and test coverage over a range of net consolidation stress and void ratios.

To account for the shift in the CSL for partially saturated soil, the model proposed by Gallipoli et al. (2003), has been used. The bonding effect caused by water menisci at inter-particle contacts is incorporated through the variable ξ, which is defined as the product of a suction-dependent function $f(s)$ and the air saturation $(1 - Sr)$. This formulation captures both the increasing number of water menisci as saturation decreases and the growing intensity of the capillary force with rising suction. The function $f(s)$ is derived from the theoretical capillary force solution by Fisher (1926) for two identical spheres and increases monotonically from 1.0 (at zero suction) to a maximum of approximately 1.5. In this study, the bonding variable ξ serves as a normalising parameter that governs the deviation of the mechanical response of unsaturated soils from that of their saturated state. The effect of this bonding is reflected in the void ratio response through a non-linear function that relates the void ratio in unsaturated conditions e to its saturated counterpart e_s, both measured at the same average skeleton stress. The relationship is expressed by the following equation:

$$\frac{e}{e_s} = 1 - b_1[1 - exp(-b_2.)\,\xi\,] \qquad 43$$

where b_1, and b_2 are fitting parameters corresponding to a and b in the original model. These parameters control the magnitude and sensitivity of void ratio change with respect to bonding.

Furthermore, the function $f(\xi)$ can be interpreted as the difference between the intercepts of the Critical State Line (CSL) and the Limiting Compression Curve (LCC) under unsaturated conditions when compared to their saturated counterparts.

6.2.3 Yield Surface

While the model is capable of simulating isotropic compression tests with a minimal number of parameters, the yield surface parameters m_{iso}, n_{iso}, α_{iso}, and θ are not directly known and must be calibrated. Given that the elastic, critical state, and isotropic hardening parameters are already established, the calibration of yield surface parameters is performed by adjusting them to match specific features of the isotropic compression response, particularly where significant behavioural changes occur.

The parameter m_{iso}, which defines the slope of the isotropic yield surface, is adopted from the literature (Dafalias & Manzari., 2004, Taiebat & Dafalias., 2007 and Ghorbani & Airey., 2019) and is fixed at $0.05M_c$. The material parameter θ, which governs the transition of the Loading Collapse Curve (LCC) from the Initial Compression Line (ICL), is calibrated by observing the curvature of the ICL in a semi-logarithmic plot of mean effective stress versus void ratio. This controls the transition of LCC from ICL and it can be calibrated by observing the curvature of ICL in (semi log) plot of mean effective stress and void ratio. A more gradual transition corresponds to a higher value of θ, whereas a sharper curve indicates a lower value.

Similarly, the bounding surface parameters n_{iso} and α_{iso} are determined by matching the slope of the Normal Compression Line (NCL) with the experimental data. These parameters influence the rate at which the yield surface expands under isotropic loading. The final values of θ, n_{iso}, and α_{iso}, are selected based on the best fit between the simulated response and the experimental data, ensuring consistency in the shape and evolution of the yield surface.

6.2.4 Kinematic Hardening

The kinematic hardening parameters (i.e., n^b, h_0, c_h and ω) were estimated from the results of drained and undrained triaxial tests by fitting these with simulated plots of the triaxial tests. The maximum stress where the stress reversal starts before reaching the CSL in triaxial tests is controlled by the n^b parameter. For loose samples, this phenomenon does not occur as the sample is directly approaching the critical state. However, for the dense samples, this phenomenon occurs when a stress reversal occurs before reaching critical state (Shown in Figure 6.11). n^b can be defined as the slope of the line formed by plotting bounding state parameter (ψ_b – state parameter at peak stress ratio) versus its corresponding stress ratio $ln(M/M^b)$ for the stress reversal points of a number of drained and undrained triaxial tests, where M is slope of critical state line and M^b is slope of bounding surface The calibrated values of n^b are shown in Figures 6.14 and 6.15.

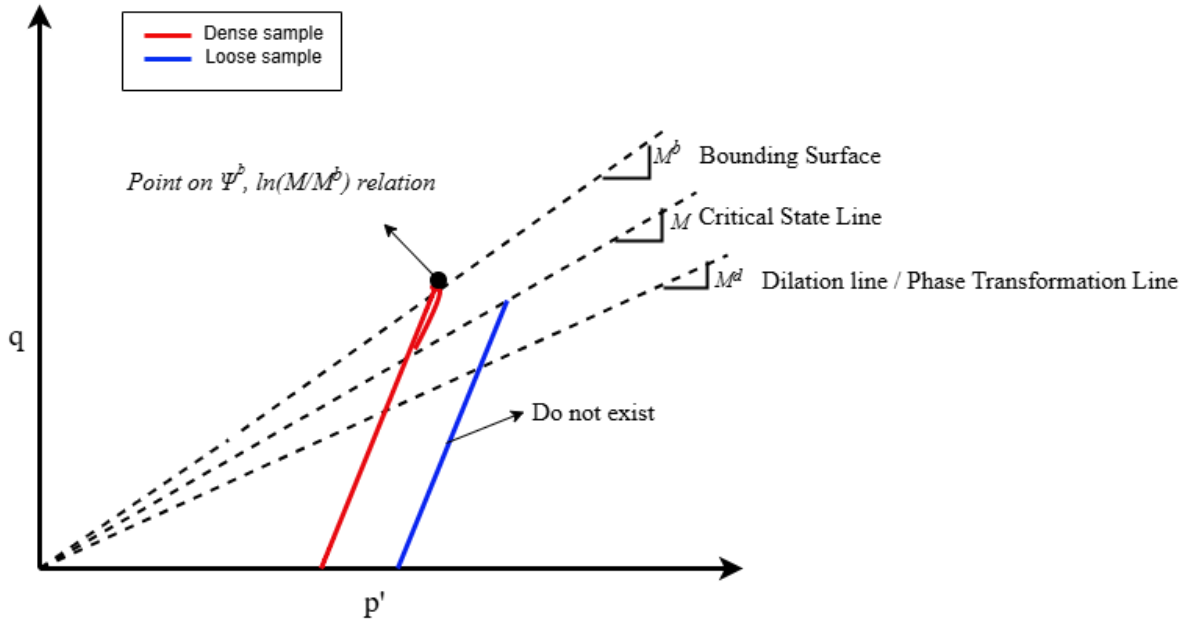

Figure 6.11: Location of Kinematic parameter – To plot n^b in Drained Tests

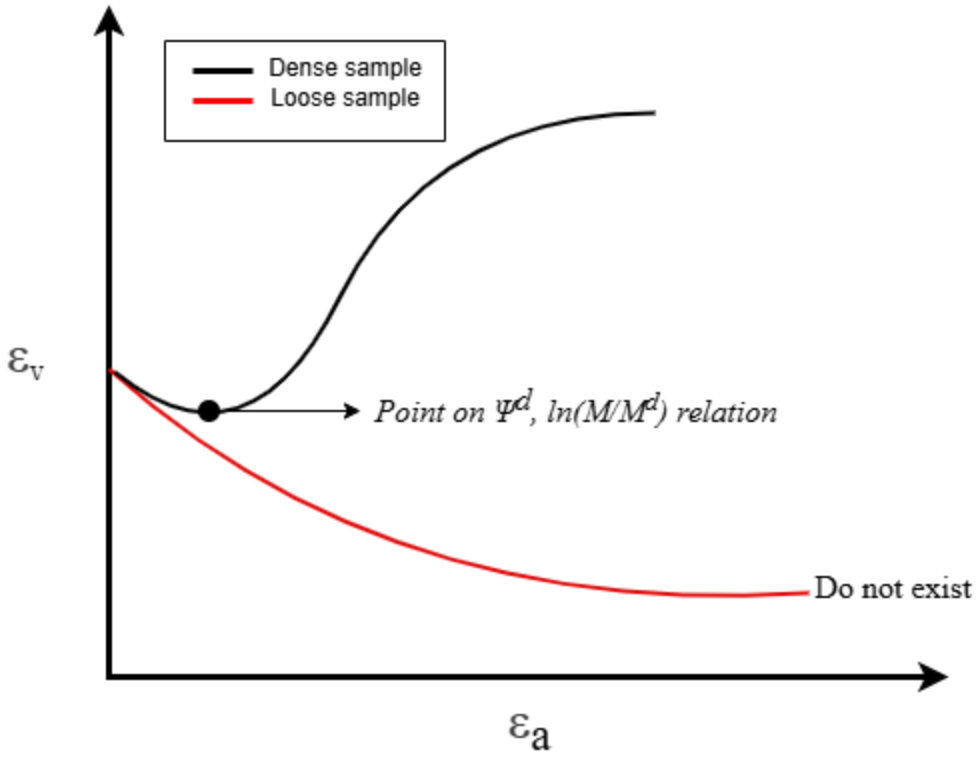

Figure 6.12: Location of Kinematic Parameter – To plot n^d for Drained Tests

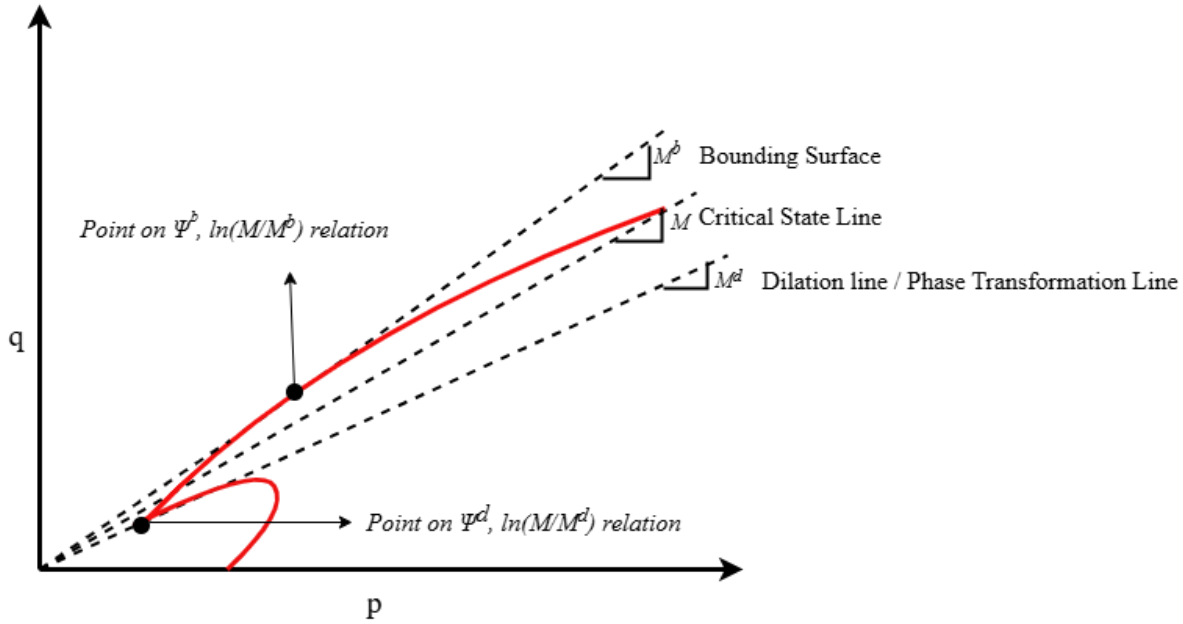

Figure 6.13: Location of Kinematic Parameters in Undrained Test

The experimental tests performed in this study alone were not sufficient to reliably determine all the kinematic hardening and dilatancy parameters. Therefore, additional data from the triaxial tests reported by Kwa (2019) were utilised to support the calibration.

The parameters, h_0, c_h, which govern the rate of kinematic hardening, were calibrated using a trial-and-error approach based on comparisons with experimental stress–strain behaviour from drained and undrained triaxial tests. In particular, the calibration followed the guidance of equation 22 which describes the evolution of the back-stress ratio and its influence on deviatoric stress development.

During the calibration process, initial values for h_0 and c_h were assumed based on published literature (e.g., Taiebat and Dafalias, 2008), and then systematically adjusted to reproduce the shape and progression of the stress–strain response. The key comparison involved the simulated or interpreted stress ratio (q/p') versus axial strain curves against the experimentally observed curves. The parameter h_0 controls the initial stiffness of the kinematic hardening rule, hence affecting how quickly the stress path curves after yielding. A larger h_0 results in faster kinematic translation and sharper hardening behaviour, while a smaller value results in more gradual hardening. The parameter c_h governs the rate at which this hardening rate decays with ongoing plastic strain.

Therefore, each trial involved modifying h_0 and ch, then plotting the stress ratio versus axial strain to observe how well the simulated response followed the experimental data, especially focusing on the initial post-yield curvature, peak stress ratio, and the stress reversal behaviour for dense and loose samples. The final values were selected when a reasonable match was achieved between experimental and modelled behaviour for a range of densities and test conditions.

Parameter ω is a switch for enabling and disabling the stress overshooting module in this model. If $\omega=10^6$, then the module is enabled and if $\omega=0$, then it is disabled.

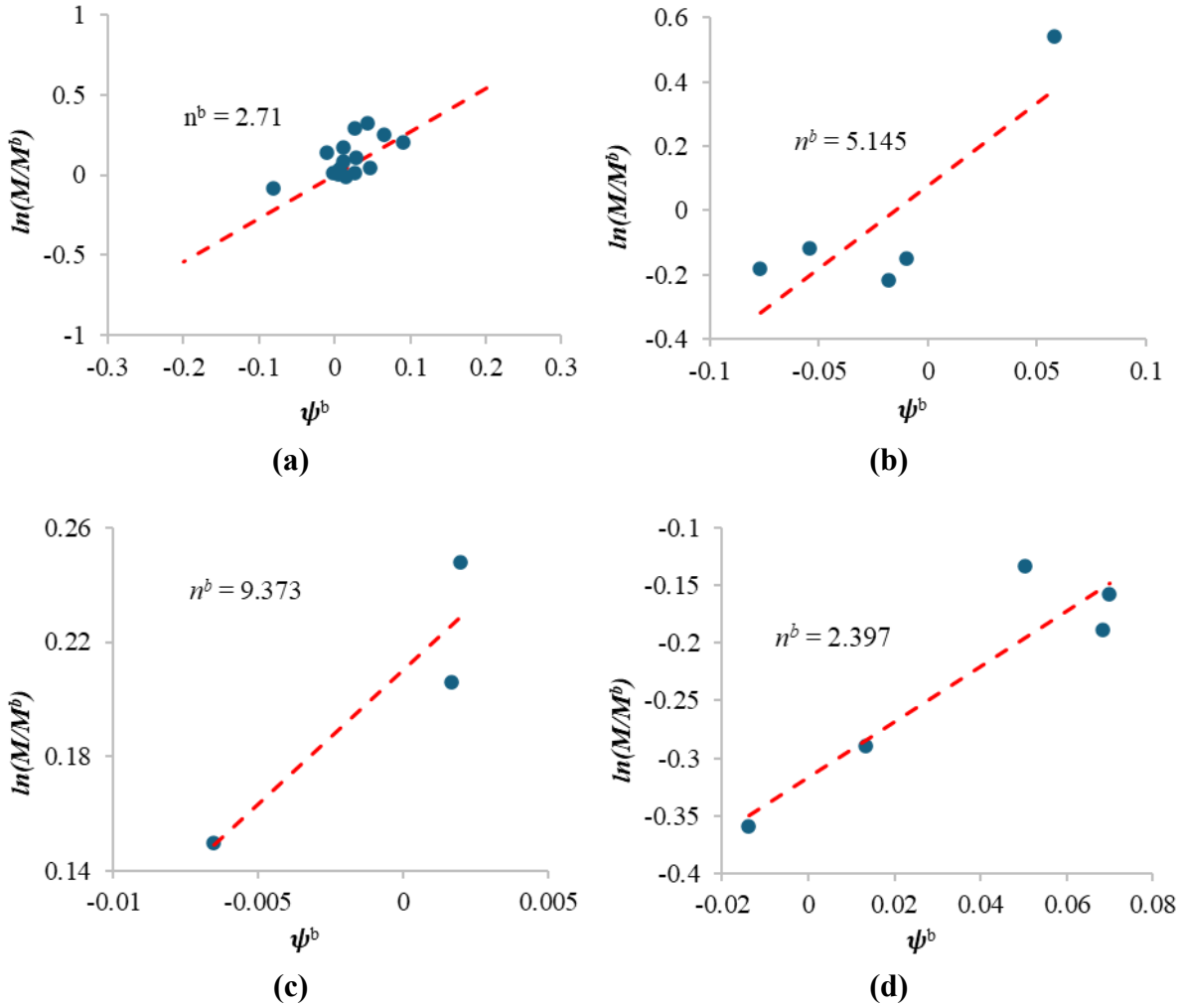

Figure 6.14: Calibration of bounding surface parameter (n^b) - (a) Sydney Sand, (b) Sydney Sand with 20% Fines, (c) Sydney Sand with 40% Fines, (d) Sydney Sand with 60% Fines.

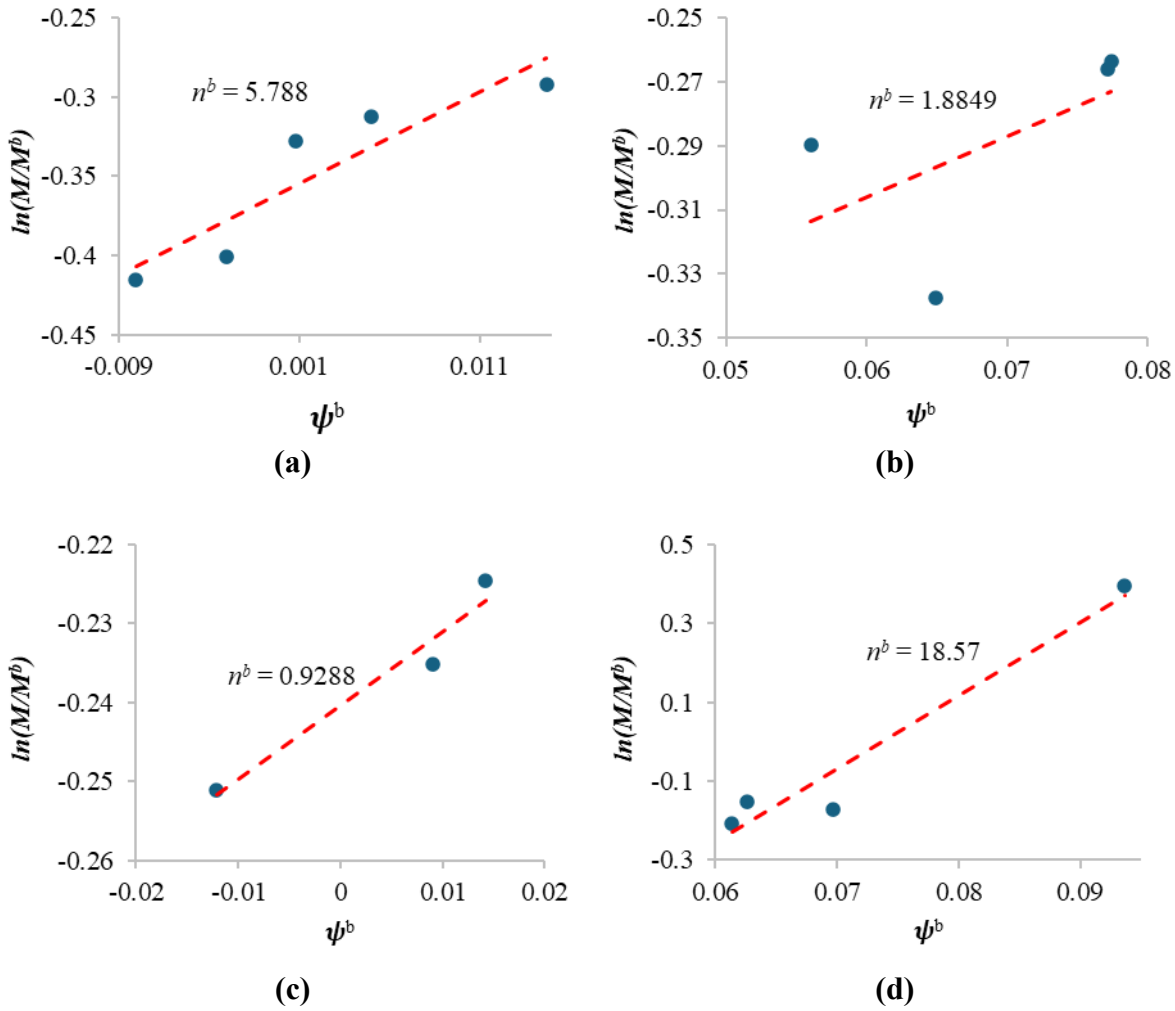

Figure 6.15: Calibration of bounding surface parameter (n^b) - (a) WGS with 18% Fines, (b) WGS with 28% Fines, (c) WGS with 40% Fines, (d) WGS with 60% Fines.

6.2.5 Dilatancy

The dilatancy parameters are n^d, A_0, z_{max} and c_z which are calibrated with the help of equations 23, 25, & 26. n^d is calibrated like n^b but of the parameter is determined from points where the first stress reversal takes place in the q-p' plot of undrained tests as shown in Figure 6.12. The parameter n^d can be defined as the slope of the line formed by the plot between state parameter ψ_d and its corresponding stress ratio $ln(M/M^d)$ of number of drained and undrained triaxial tests as illustrated in Figure 6.16 and Figure 6.17. In drained tests the points used to determine n^d are where the change in volumetric strain ($\delta\varepsilon_v/\delta\varepsilon_a$)is maximum and in undrained tests, where the change in pore pressure ($\delta u/\delta\varepsilon_a$) is maximum.

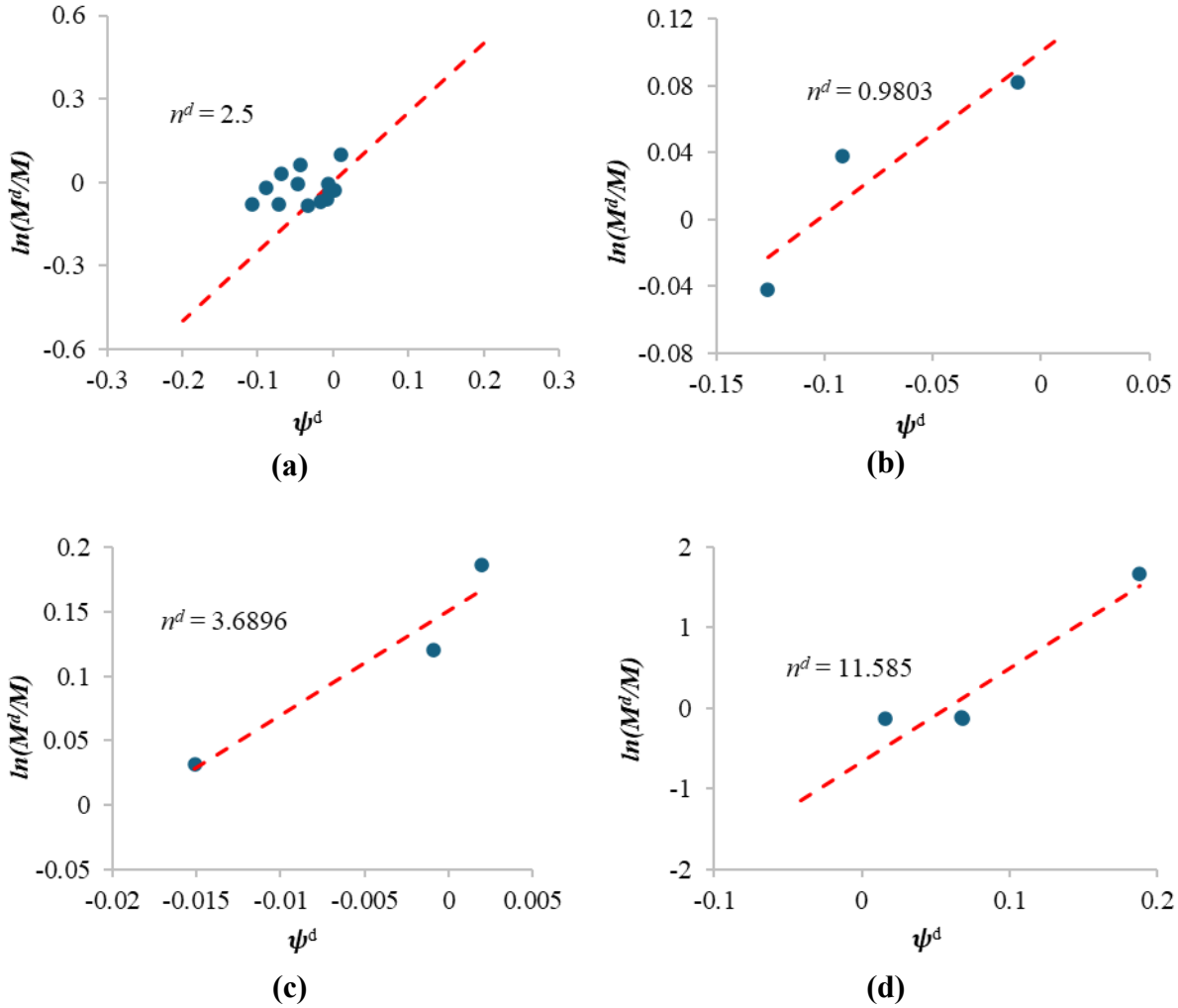

Figure 6.16: Calibration of dilation parameter (n^d) - (a) Sydney Sand, (b) Sydney Sand with 20% Fines, (c) Sydney Sand with 40% Fines, (d) Sydney Sand with 60% Fines

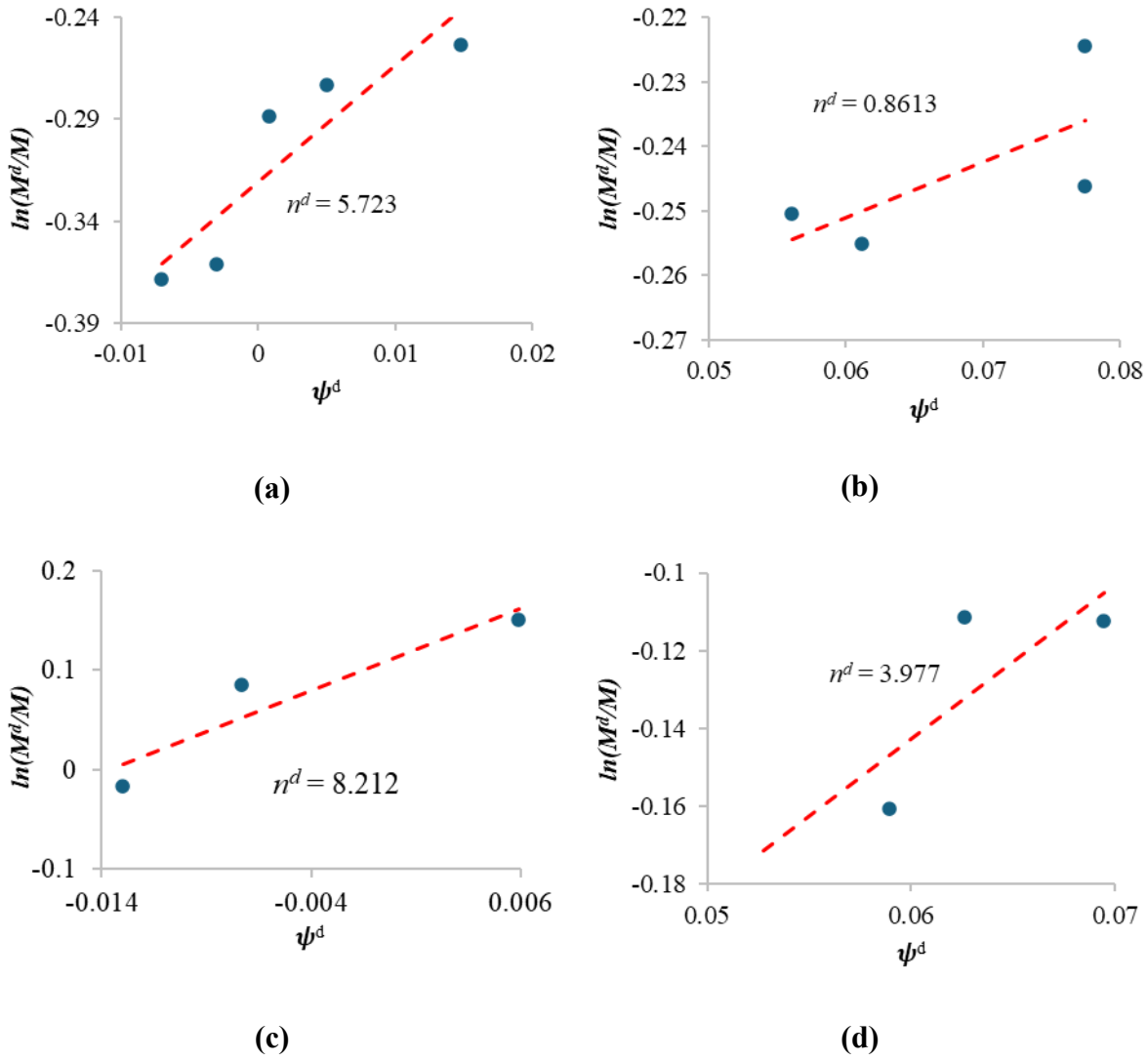

Figure 6.17: Calibration of dilation parameter (n^d) - (a) WGS with 18% Fines, (b) WGS with 28% Fines, (c) WGS with 40% Fines, (d) WGS with 60% Fines.

z_{max} and c_z are calibrated using a trial-and-error method by fitting the curve for unloading path of a cyclic drained or undrained triaxial tests, particularly the stress strain response. However, they do not impact the performance of the monotonic tests.

6.2.6 Memory Surface

The memory surface parameters can be calibrated with a series of drained cyclic triaxial tests with different void ratio, e_0. However, due to the limited number of cyclic tests performed there are insufficient data to fully calibrate the model parameters. The procedure described here is

the one followed by Chen et al. (2024) using the comprehensive data available for Karlsruhe Sand. The tests are simulated with estimated parameters and compared with experimental data to fit the curve. μ_0 is calibrated by comparing the results of first few cycles of a cyclic drained test with roughly estimated values for other unknown parameters. The variation of results with respect to change in μ_0 is shown in Figure 6.18.

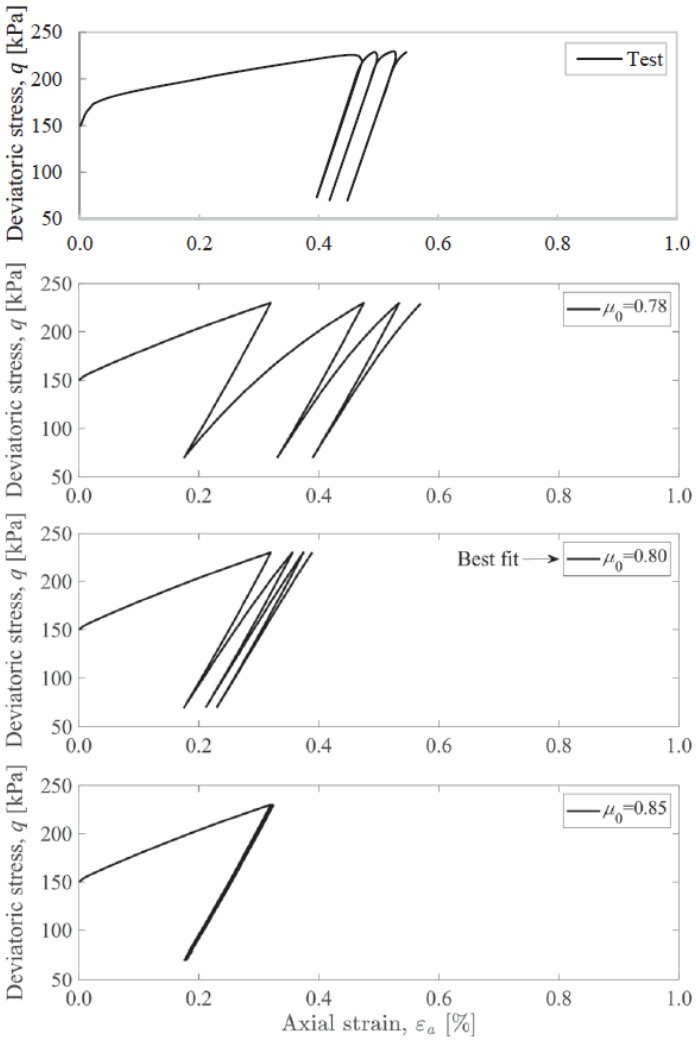

Figure 6.18: Calibration of parameter μ0 on Karlsruhe Sand by Wichtmann, (2005) (after Chen et al, 2024).

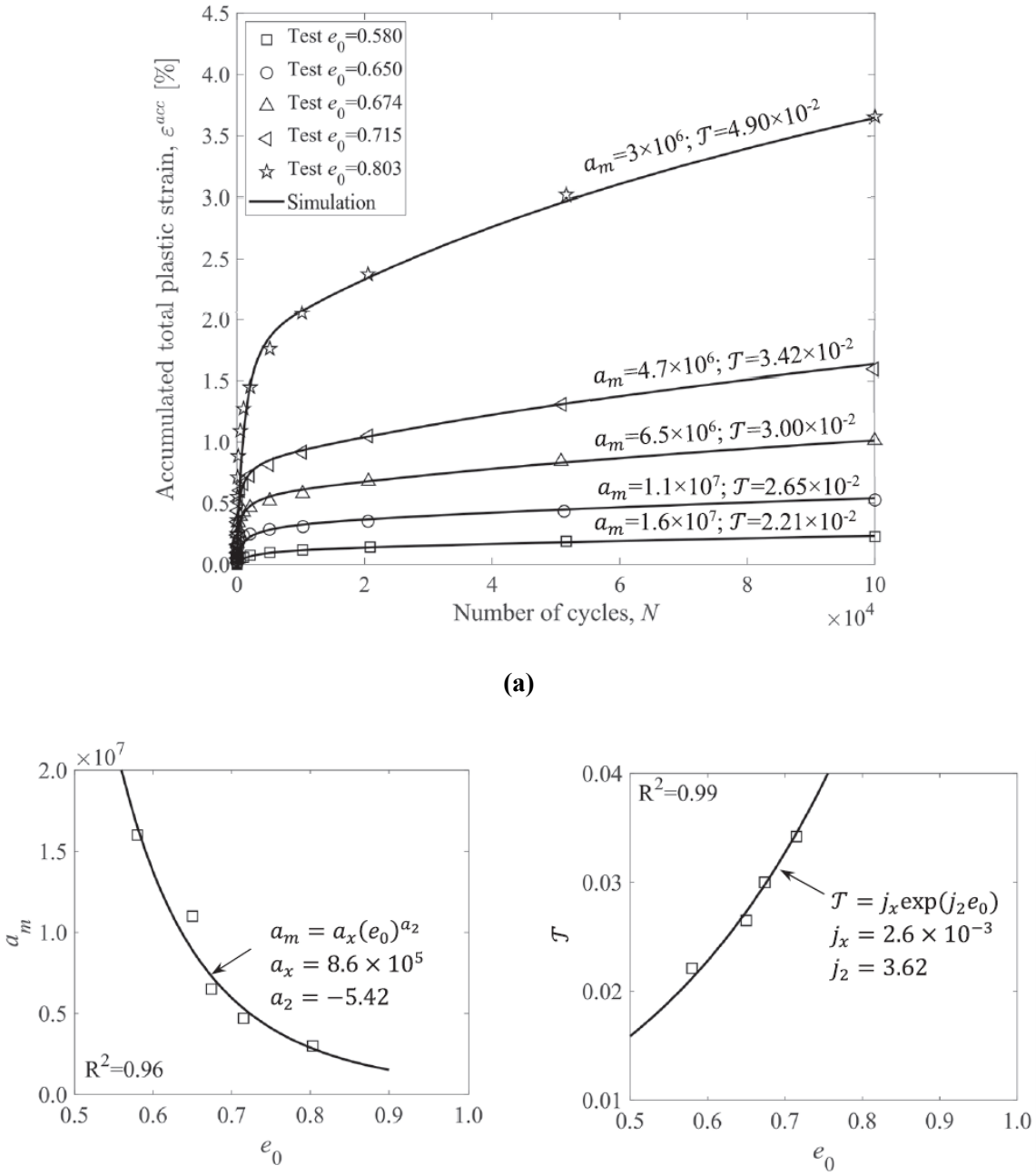

Figure 6.19: Calibration of a_2 and j_2 using Karlsruhe Sand by Wichtmann, (2005) (a) a_m and $\mathcal{T}$ at various void ratio with η_{ave} = 0.75; (b) Calibration of a_2; (c) calibration of j_2. (after Chen et al., 2024)

a_m and $\mathcal{T}$ are initially estimated to a constant value for the simulations to compare the plot of number of cycles N vs accumulated plastic strain ϵ_p^{acc}. Gradually, the values of a_m and $\mathcal{T}$ are increased until the N-ϵ_p^{acc} plot from each experiment agree with simulations. Following this, the values of a_m and $\mathcal{T}$ determined from the initial fitting are applied to tests with different

initial void ratios. The data is then plotted with a_m versus e_0 and $\mathcal{T}$ versus e_0, as shown in Figure 6.19. These plots allow the dependency of a_m and $\mathcal{T}$ on the initial void ratio to be visualized. Once these relationships are established, the relationships between (a_m–e_0) and ($\mathcal{T}$–e_0) are determined using the least squares method. Through this statistical approach, the constants a_2 and j_2 are accurately derived, indicating specific trends in the data.

With these constants in hand, the calibration proceeds by estimating additional parameters, a_1 and j_1, based on data from tests where only the amplitude of the cyclic loading parameter q_{amp} is varied, while other conditions are kept constant. This process ensures that the effects of q_{amp} on the model parameters are accurately captured.

The same procedure is then applied to estimate j_3 using tests where only the mean effective stress p_{ave} differs, with all other conditions remaining constant. This allows the calibration of parameters related to the soil's response to different levels of confining stress.

Similarly, j_4 is estimated by analysing tests in which the stress ratio η_{ave} is varied, with all other conditions kept constant. This step ensures that the model can accurately account for the effects of different stress paths. Finally, the values of a_0 and j_0 are determined through a trial-and-error process to best approximate the experimental data across a range of conditions, including variations in q_{amp}, e_0, p_{ave}, and η_{ave}. During this final calibration phase, the values of the previously determined parameters a_1, a_2, j_1, j_2, j_3, and j_4 may be fine-tuned to ensure that the model achieves the best overall fit to the experimental data. Due to similarity of Karlsruhe and Sydney Sand, the same parameters have been assumed to be applicable. As discussed later, some attempt has been made to adjust the parameters to obtain better fits.

6.2.7 Semifluidised State

In the calibration process of the Sf state parameters such as x, c_l, c_r, and n_g were adjusted to ensure the model can capture the cyclic shearing behaviour of soil in the semifluidised state in

post liquefaction stage. The parameter x, controls the maximum amplitude of post-liquefaction shear strain, was calibrated after sensitivity analyses. Increasing x leads to a higher maximum strain amplitude which can be compared with the experimental results of undrained triaxial tests where the soil liquefied. The parameter c_l, is responsible for governing the pace of strain accumulation after liquefaction. Similarly, n_g can be calibrated by reflecting the observed number of cycles versus the accumulated strain. For c_r, calibration is achieved by comparing the rate of recovery during drained loading; a value of 0 is selected, if the data is for multiple liquefaction stages, ensuring the model could simulate the response in subsequent undrained cyclic shear tests after reconsolidation.

Even though the calibration procedure for the memory surface and semifluidised state is well-documented and theoretically well understood, practical constraints related to computational efficiency pose significant challenges. The calibration of these parameters requires an iterative process, where multiple trial simulations are run to fine-tune the model's response to experimental data. Given that each individual simulation takes between 7 and 30 minutes, the total computational cost of running an extensive set of simulations for each parameter can become infeasible, especially when dealing with a wide range of soil conditions and cyclic loading scenarios.

Additionally, the memory surface parameters influence the long-term accumulation of plastic strains under cyclic loading, requiring multiple loading cycles to be simulated accurately. This significantly extends the computation time, as each cycle contributes incrementally to the evolution of strain, making it computationally prohibitive to test numerous variations in parameter values. Similarly, the semifluidised state parameters control post-liquefaction behaviour and require a high number of cycles to fully capture the strain evolution in liquefied soil conditions. Since liquefaction and post-liquefaction behaviour are time-dependent and

path-dependent, achieving precise calibration would require a large number of sensitivity analyses across multiple stress paths and initial conditions.

Given these constraints, a rational and pragmatic approach is necessary. Instead of performing exhaustive calibration for every new dataset, parameters for the memory surface and semifluidised state are adopted from preexisting simulations of soils with similar particle size distributions and grading characteristics. This approach is justified based on extensive prior research, which has demonstrated that soils with comparable grading, mineralogy, and fines content exhibit similar cyclic and post-liquefaction behaviours under equivalent loading conditions. Studies (Been & Jefferies, 1985; Manzari & Dafalias, 2004; Taiebat & Dafalias., 2007, Ghorbani & Airey, 2019) have shown that memory surface evolution and semifluidised state transitions primarily depend on particle rearrangement mechanisms and effective stress paths, which are closely related to grain size distribution, void ratio, and confining stress. Therefore, transferring parameters from well-validated simulations of similar soil types ensures that the model remains realistic while maintaining computational efficiency.

While this method introduces a degree of approximation, the fundamental principles guiding soil behaviour remain intact. The adopted values undergo minor fine-tuning based on comparative simulations to ensure reasonable agreement with observed trends. This strategy allows for a balanced trade-off between computational feasibility and the accuracy of cyclic and post-cyclic predictions, ensuring that the model remains practical for engineering applications without compromising its scientific validity.

Other than the listed parameters, the calibration of STOL (Stress Tolerance), FTOL (Force Tolerance), and SINT (Integration Tolerance) is essential for ensuring the accuracy and stability of the model while maintaining computational efficiency. STOL is calibrated by performing simulations with varying tolerances to balance the accuracy of stress integration with computational cost, ensuring minimal error in stress calculations. FTOL is adjusted to

control the convergence criteria for force equilibrium, optimizing the balance between accuracy and iteration count during the simulation. SINT is calibrated by testing different integration tolerances to ensure the stability of the solution during complex loading conditions, such as cyclic loading, while also considering computational efficiency. Together, these parameters are fine-tuned through iterative testing to achieve a robust and reliable model suitable for accurately simulating soil behaviour.

6.3 Structure of the program

The constitutive model was designed to solve wide range boundary value problems. For the simulations the model has been implemented in a program that can apply various triaxial test conditions. These include saturated drained, saturated undrained, and unsaturated tests under both monotonic and cyclic loading. Additionally, the model supports isotropic compression tests for both saturated and unsaturated states. The model can simulate the following tests:

Triaxial Tests:

- Saturated Drained Triaxial Compression
- Saturated Undrained Triaxial Compression
- Saturated Drained Cyclic Triaxial Test (Stress-Controlled)
- Saturated Undrained Cyclic Triaxial Test (Stress-Controlled)
- Unsaturated Drained Triaxial Test (Constant Suction)
- Unsaturated Drained Triaxial Test (Constant Volumetric Water Content)
- Unsaturated Cyclic Triaxial Test (Constant Suction)
- Unsaturated Cyclic Triaxial Test (Constant Volumetric Water Content)

Isotropic Compression and Consolidation Tests:

- Saturated Isotropic Compression
- Unsaturated Isotropic Compression
- Isotropic Consolidation

- Cyclic Isotropic Consolidation

Oedometer Tests:

- K_0 - Loading (Earth Pressure at Rest / Oedometer Test)

Variations in Cyclic Tests:

- Constant P Cyclic Test
- Custom Cyclic Strain-Controlled Test
- Cyclic Loading with Strain Control
- Cyclic Undrained Strain-Controlled Triaxial Test
- Simple Shear Test (Stress-Controlled)
- Unsaturated Cyclic Shear Test (Constant Suction)

Each analysis type corresponds to a specific material type and model type, requiring a distinct set of inputs to ensure accurate representation. While the model type ultimately refers to the same constitutive framework, different features are activated depending on the nature of the test being simulated. The input parameters vary depending on the test conditions (defined as Analysis type in the model). Monotonic tests require only the fundamental soil parameters such as elasticity, isotropic hardening, kinematic hardening, and critical state properties. Unsaturated tests necessitate additional parameters, including the soil-water characteristic curve (SWCC) and suction-dependent mechanical properties to account for partial saturation effects. Cyclic loading tests require further parameters related to stress overshooting, memory surface effects, and the semifluidised state, in addition to the abovementioned parameters which are crucial for modelling cyclic degradation and liquefaction behaviour.

The core structure of the model is built upon a set of governing material parameters that define soil behaviour under these test conditions. These parameters are categorised based on the mechanical response they control. Elastic properties govern the immediate, recoverable response of the material to loading. Plasticity parameters, including isotropic and kinematic

hardening, dictate the evolution of the yield surface and the accumulation of plastic strains. Critical state parameters define the ultimate strength and volumetric behaviour of the soil as it approaches a steady-state condition. Unsaturated soil parameters include the soil-water characteristic curve (SWCC) and suction-dependent mechanical properties, which are essential for modelling partial saturation effects. Lastly, cyclic loading parameters address stress overshooting, memory surface effects, and the semifluidised state, all of which play a crucial role in simulating cyclic degradation and liquefaction behaviour.

Once the appropriate analysis type and material properties are specified, the model progresses through a structured computational sequence. The process begins with initialisation, where material parameters and initial stress states are defined, including boundary conditions and suction values for unsaturated soils. During the loading application phase, the model applies incremental loads and computes stress-strain responses based on the governing constitutive equations. Elastic and plastic strain computation follows, distinguishing between elastic and plastic components using a predefined yield function and associated flow rule. To maintain accuracy, the model performs bounding surface corrections, where the stress state is continuously checked against the bounding surface to ensure a realistic transition between elastic and plastic behaviour. Plastic corrections are applied iteratively based on the distance between the stress state and the bounding surface. In cyclic loading scenarios, the model updates parameters governing strain accumulation, ratcheting, hardening/softening, and stress return mapping iteratively to reflect changes in soil behaviour over successive loading cycles. The final stage involves validation, where the simulation results are compared against experimental data to assess the accuracy of the model. In this study, saturated and unsaturated triaxial tests under monotonic loading have been extensively validated, while cyclic loading tests have been verified to a limited extent due to the availability of experimental data. A schematic representation of the algorithmic workflow of the model is provided in the flowchart

in Figure 6.20. This flowchart illustrates the step-by-step computational sequence, detailing the progression from material property definition to final validation.

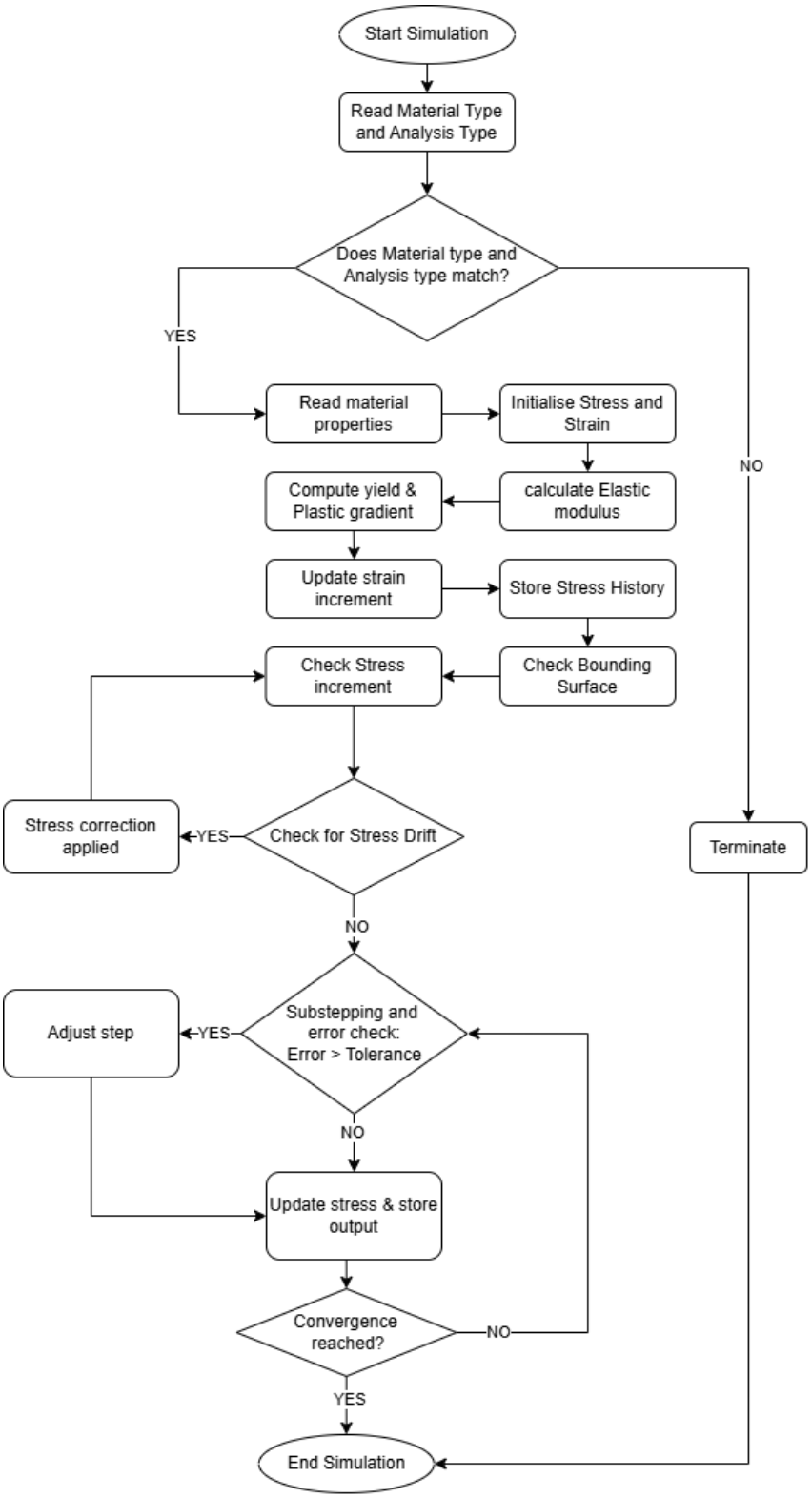

Figure 6.20: Schematic representation of the algorithmic workflow of the model

6.4 Simulations

The simulation process commenced with saturated monotonic tests, utilizing a minimal set of material parameters to establish a baseline response. Following this, the model was extended to unsaturated conditions by incorporating Soil-Water Characteristic Curve (SWCC) parameters and suction states, allowing for a more comprehensive validation of the model at different degrees of saturation. Building upon the successful simulation of monotonic tests in both saturated and unsaturated conditions, these results confirmed the correctness of the selected material parameters while maintaining minimal computational runtime.

To enhance the robustness of the analysis, R^2 values were computed for stress–strain, CSL fits (both q–p′ and e–log p′), and volumetric/pore pressure responses, and are presented in Tables 6.2, 6.3 and 6.5. While many R^2 values were above 0.90 (with several exceeding 0.98), it is important to note that soil behaviour is highly non-linear, meaning that a high R^2 does not necessarily equate to a perfect behavioural match. Therefore, R^2 was used in combination with visual inspection of peak stress behaviour, dilation points, and volumetric change trends to judge the quality of model fits.

Since monotonic tests are computationally less demanding compared to cyclic tests, they served as an efficient preliminary step to validate the model before proceeding to more complex cyclic simulations. This approach significantly reduced the need for parameter corrections or adjustments during the computationally expensive cyclic simulations, ensuring a more efficient and reliable simulation process.

To accurately capture the cyclic response, additional parameters governing memory surface evolution and state-dependent cyclic behaviour were incorporated. Finally, the simulations were further expanded to cyclic loading under unsaturated conditions, integrating both SWCC and cyclic-specific parameters to evaluate the complex interplay between saturation and cyclic loading effects.

Since the calibration and structural formulation of the model have been discussed earlier, the following sections focus solely on the simulation results, evaluating their performance and ability to capture the observed soil behaviour.

6.4.1 Simulations of Monotonic saturated tests

Monotonic simulations were conducted under both drained and undrained conditions on the Sydney Sand (Sydney sand, Sydney sand with 20%, 40%, & 60% fines) and WGS sand (WGS with 18%, 28%, 40%, & 60% fines) families, utilizing the material parameters presented in Table 6.1. Since the calibration process does not yield perfectly optimized parameters, a margin of error is introduced across all simulations, resulting in curves that do not exactly match the experimental data. Nevertheless, key aspects of soil behaviour such as peak stress ratio, adherence to the critical state line, dilation behaviour, and volumetric changes are reasonably well captured when compared to experimental results.

Table 6.1:Model parameters for Sydney sand and WGS sand family

Type	Symbol	SS0F	SS20F	SS40F	SS60F	WGS18F	WGS28F	WGS40F	WGS60F
Elasticity	G_0	186	172	168	160	210	190	176	182
	K_0	120	105	112	135	126	133	129	128
Kinematic Hardening	n^b	2.71	5.15	9.37	2.40	5.79	1.88	0.93	18.57
	c_h	0.968	0.9	0.89	0.82	0.88	0.85	0.79	0.86
	h_0	12	9.2	8.6	7.07	5.5	5.1	3.6	2.5
Dilatancy	n^d	2.5	0.98	3.69	11.59	5.72	0.86	8.21	3.98
	A_d	0.4	0.7	0.8	0.8	0.6	0.8	0.8	0.9
	c_z*	600	600	600	600	600	600	600	600
	z_{max}*	4	4	4	4	4	4	4	4
	N_l	27.5	97	100	150	172	91.5	49.4	27.2
	λ	0.39	0.58	0.6	0.56	0.6	0.58	0.52	0.45
Critical State	N_c	24.5	95	113	98	36	55	41.5	26.3
	α_{csl}	6800	6900	7200	9500	3500	5000	6000	6000
	M	1.2	1.33	1.462	1.462	1.722	1.636	1.593	1.506

*These values influence the unloading stage of monotonic tests but did not affect the current set of simulations. Therefore, they were kept constant across all materials.

One representative test of each kind (Monotonic Saturated Drained and Monotonic saturated Undrained) for each material is presented below. Numerical simulations of drained triaxial tests are presented and analysed to evaluate the model's ability to replicate experimentally observed soil behaviour. Key response variables commonly examined in laboratory tests are considered, including the stress path in q–p' space, the evolution of mean effective stress and void ratio, and the stress-strain response in deviatoric strain and axial strain space. Additionally, volumetric strain is assessed against axial strain during the shear stage, explicitly excluding

volumetric changes that occur during the consolidation phase. This approach ensures that the simulated response is compared primarily based on the shearing-induced mechanical response rather than consolidation-induced densification effects.

6.4.2 Effect of Density

The effect of density in soil mechanics is fundamentally linked to changes in void ratio (e), as density variations directly influence the soil structure and its response to loading.

The ability of the model to capture soil behaviour across different densities is assessed by examining its predictions in q–p' and e–p' space. The state parameter, defined as $\psi = e - e_{cs}$, is a crucial indicator of whether a soil sample is initially loose ($\psi > 0$) or dense ($\psi < 0$) relative to the critical state line (CSL). The evolution of the state parameter determines whether a soil specimen undergoes contractive or dilative behaviour, which in turn influences strain softening, hardening, and instability mechanisms.

When comparing Figure 6.24 (loose sample) and Figure 6.21 (dense sample), clear trends emerge that align with critical state soil mechanics principles (Roscoe & Burland, 1968). In Figure 6.24, the stress path of the loose specimen shows a downward trend in e–p' space, indicating contraction toward the critical state line. This is expected because loose soils exhibit positive excess pore pressure generation (or effective stress reduction in drained conditions), leading to a reduction in void ratio and eventual approach toward the CSL.

Conversely, Figure 6.21 for the dense specimen exhibits an upward trend in e–p' space, signifying a tendency to dilate during shear. This behaviour occurs because dense sands initially contract slightly but then develop negative excess pore pressure (or increased mean effective stress in drained conditions), causing volumetric expansion. The stress-strain response in dense sands is thus characterized by strain-hardening behaviour, leading to an increase in effective stress and resistance to further deformation (Jefferies & Been, 2015).

These trends validate the model's ability to replicate the dependence of soil behaviour on density. The observed numerical results confirm that the model appropriately captures the transition from contractive to dilative behaviour as the soil moves from loose to dense states. Furthermore, the correct directional approach toward the CSL in e–p' space suggests that the model successfully integrates state-dependent hardening/softening mechanisms.

A similar evaluation is conducted for undrained triaxial tests, where the soil deforms at constant volume, and changes in pore water pressure (u) govern the evolution of effective stress. As the model does not directly compute pore water pressure, the focus remains on stress paths and stress-strain relationships to infer undrained behaviour.

Comparing Figure 6.24 (loose sample) and Figure 6.22(dense sample) reveals that the model replicates experimentally observed undrained soil behaviour, particularly in terms of how mean effective stress (p') and void ratio (e) evolve toward the critical state.

In Figures 6.24 and 6.32, the stress path of the loose sample exhibits a continuous decrease in mean effective stress (p') while approaching the critical state. Since undrained conditions prevent volume change, contraction manifests as an increase in pore water pressure, leading to a reduction in effective stress and ultimately bringing the sample to the CSL at a diminished stress level. This response is characteristic of contractive undrained behaviour, where the soil lacks sufficient initial fabric resistance, causing progressive loss of strength and potential instability.

The evolution of void ratio (e) and effective stress (p') in the loose sample further confirms this behaviour. The sample approaches the CSL at a progressively lower stress state, as the current void ratio remains above the critical state line ($e > e_{cs}$), indicating contractive tendencies. This is consistent with the fundamental principle that loose samples tend to reach critical state at lower stress levels due to their limited resistance to compression-induced densification.

In Figures 6.22, 6.26, 6.28 and 6.30, the stress path for the medium dense sample initially follows a downward trajectory in q–p' space, similar to the loose case. However, upon reaching the yield surface, the stress path reverses direction and trends upward, indicating an increase in effective stress due to dilation. This behaviour is characteristic of dense sands, which initially generate excess pore pressure due to contractive tendencies, but subsequently constrained dilation causes, reducing pore pressure and increasing effective stress as shear progresses. The void ratio (e) and effective stress (p') trends further confirm this behaviour. Initially, the stress path follows a diminishing effective stress trend, but after reaching the yield surface, it transitions toward a higher stress state, as the void ratio moves toward the CSL from below ($e < e_{cs}$). This confirms that when the initial void ratio is below the CSL, the sample stabilizes at a higher stress state, while when it is above the CSL, the sample reaches the CSL at a lower stress state.

These observations demonstrate that the model correctly captures state-dependent stress path evolution, accurately replicating the expected undrained behaviour for both loose and dense conditions.

6.4.3 Effect of fine content and Grain size distribution

Sydney sand, with increasing percent fines (20%, 40%, and 60%), demonstrates a progressive disturbance in the model's ability to accurately simulate dilation behaviour. Dilation in soils refers to the increase in volume that occurs when dense granular materials are subjected to shear. This behaviour is particularly significant in sands, where an initially dense specimen may exhibit slight contraction before reaching a critical strain level, at which point dilation becomes dominant. The transition from contractive to dilative behaviour is commonly characterised by two key parameters: the point of dilation and the dilation angle, both of which significantly influence the model's ability to capture peak strength and volumetric behaviour.

The point of dilation marks the stress or strain state at which volumetric contraction ceases, and dilation begins, closely associated with the phase transformation point in dense samples (Ishihara, 1993; Lade & Pradel, 1990). This transition is evident in volumetric strain versus axial strain plots, where a reversal in volumetric strain trends signifies the onset of dilation. Additionally, in undrained conditions, dilation manifests as a reduction in excess pore pressure, leading to an increase in mean effective stress (p') (Been & Jefferies, 1985). The ability to correctly capture this transition point is crucial, as it directly affects the accuracy of peak stress predictions and the evolution of volumetric behaviour during shearing. If the onset of dilation is misrepresented, the model may incorrectly predict peak strength values and post-peak softening trends, leading to errors in stress path evolution and strain hardening/softening responses. However, it is important to note that not all samples exhibit a clear phase transformation point. Loose sands, especially at high fines content, remain contractive throughout shear, meaning the model's deviation in these cases is more closely related to misrepresentation of peak stress and contractive volumetric trends rather than the failure to capture a dilation transition.

Similarly, the dilation angle (ϕ_d), defined as the ratio of volumetric strain increment to shear strain increment ($\phi_d = d\varepsilon v/d\gamma$), determines the extent of dilation (Bolton, 1986). A higher dilation angle corresponds to greater volume expansion during shear, typically observed in coarse-grained, well-compacted, and angular materials. If the dilation angle is underestimated, the model fails to capture the full dilative response, resulting in lower peak stress predictions and a misrepresentation of volumetric behaviour. For Sydney sand family, the model captures the dilation behaviour reasonably well at low fines content but progressively deviates from experimental results as the percentage of fines increases. The introduction of finer particles disrupts the granular structure, altering the interparticle contacts and reducing the dilative tendency of the soil. Consequently, the model struggles to reproduce both peak stress and

volumetric trends, leading to inconsistencies in stress-strain response and effective stress evolution.

While Sydney sand, a poorly graded sand (SP) with sub-rounded to sub-angular particles, exhibits a relatively accurate representation of dilation behaviour, the accuracy of the model diminishes as the fines content increases. The model performs well for clean Sydney sand and 20% fines, but deviates significantly at 40% and 60% fines, where the dilation response weakens and shifts toward a more contractive behaviour, aligning with findings in fine-content-dependent soil responses (Thevanayagam et al., 2002). The resulting misrepresentation of dilation trends affects the ability to correctly predict peak stress and causes volumetric behaviour to diverge from experimental results, particularly in the post-peak region, where dilation effects are dominant.

In contrast to Sydney sand, the well-graded sand (WGS) presents an inherently different particle size distribution and packing structure, significantly influencing its shear resistance and dilation behaviour. Even at a low fines content of 18%, WGS still exhibits some dilative response, and the model performs relatively well in capturing peak stress and volumetric behaviour. However, deviations become increasingly evident as the fines content rises to 28%, 40%, and 60% fines, where the mechanical response transitions toward a more contractive behaviour.

The presence of a wider grain size range in WGS results in tighter particle packing, increasing the coordination number and affecting both contraction and dilation tendencies (Santamarina & Cho, 2004). The inclusion of angular fines within a well-graded matrix enhances shear resistance, leading to a more complex stress-strain response compared to the more uniform Sydney sand (Vallejo & Mawby, 2000). While angular fines contribute to increased shear strength due to greater interlocking effects, at higher fines content, they fill the voids between larger grains, reducing overall dilation tendencies. The model's misrepresentation of dilation

behaviour at high fines content is therefore not solely due to angularity but rather the evolving coordination number and stress transmission within the soil skeleton (Mitchell & Soga, 2005). The inability to accurately capture the phase transformation point and dilation angle in WGS leads to errors in peak strength predictions and an overestimation of contraction behaviour, causing further deviation from experimental results. This discrepancy is most evident in dense WGS samples, where the model fails to reproduce the transition from contractive to dilative response, leading to underestimation of peak stress values and inaccurate post-peak volumetric trends.

For both Sydney sand and WGS families, the stress path in q–p' space shows distinct trends depending on the initial density and fines content. At low fines content, both sands exhibit an initial contractive response followed by dilation, approaching the critical state at relatively higher stress levels. However, as the percentage of fines increases, the stress path shifts, indicating a progressive loss of dilative response.

For Sydney sand, the stress path closely matches experimental results at low fines content but deviates significantly as fines increase beyond 40%, leading to weaker dilation and a reduced effective stress state at critical state equilibrium. The misrepresentation of the dilation angle affects peak stress predictions, causing the model to underestimate post-peak resistance.

For WGS, the stress-strain response and q–p' trajectory show a more pronounced contractive behaviour at increasing fines content, suggesting that the model underestimates the effect of interparticle angularity and grain structure on dilation. Due to this, peak stress predictions are increasingly inaccurate, and the model struggles to capture the transition from contractive to dilative response effectively.

6.4.4 Implications and limitation of Saturated tests

With simulations of saturated monotonic drained and undrained tests on Sydney sand and well-graded sand (WGS) families, the results highlight the model's capability and limitations in

capturing dilation behaviour, peak strength, and volumetric response across varying densities, fines contents and grading characteristics.

While the model successfully replicates the dilation behaviour of Sydney sand at low fines content, its accuracy deteriorates as the percentage of fines increases. The discrepancies become more pronounced in WGS, where a more complex grain size distribution and angular fines influence interparticle interactions, leading to deviations in stress-strain behaviour, dilation onset, and volumetric response. These findings suggest that certain fundamental aspects of soil fabric evolution and state-dependent behaviour require refinement within the current constitutive framework (Been & Jefferies, 1985; Thevanayagam et al., 2002; Santamarina & Cho, 2004).

The model parameters underpinning these simulations are provided in Table 6.1, and the fit quality is further supported by R^2 values summarised in Table 6.2 for the Sydney Sand family and Table 6.3 for the WGS family, which complement the visual curve assessments presented in the figures.

Table 6.2: R^2 values for model simulations of Sydney Sand family under monotonic saturated loading conditions.

S.No	Test Label	CSL – qp'	Stress – Strain response	CSL – e log p' space	Volumetric / Pore Pressure Response
1	MSD_SS0F50L	0.9916	0.9683	0.9848	0.9272
2	MSD_SS0F100L	0.9941	0.9048	0.9264	-5.3909
3	MSD_SS0F200MD	0.9908	0.7191	0.5608	0.5851
4	MSD_SS0F300MD	0.9900	0.6694	0.8686	0.9923
5	MSD_SS0F1500L	0.9988	0.8536	0.9566	0.1949
6	MSD_SS0F1500MD	0.9820	0.6755	0.5855	0.9700
7	MSU_SS0F100Di	0.9926	0.3475	0.9999	0.4652
8	MSU_SS0F100Dii	0.9495	-5.3322	0.9999	-3.7646
9	MSU_SS0F100Diii	0.9895	0.9180	0.9999	0.7619

10	MSU_SS0F100Li	0.5583	-4.0367	0.9999	0.2536
11	MSU_SS0F200Di	0.9531	0.8833	0.9999	0.9209
12	MSU_SS0F200Dii	0.9619	0.8610	0.9999	0.9045
13	MSU_SS0F200Diiii	-0.859	-5.5389	0.9999	-1.2793
14	MSU_SS0F200Li	0.9161	0.8728	0.9999	0.9876
15	MSU_SS0F300Di	0.9727	0.9365	0.9999	0.8436
16	MSU_SS0F300Li	0.7808	-12.7952	0.9999	-1.9159
17	MSU_SS0F1500L	-1.1747	0.7440	0.9999	0.8433
18	MSD_SS20F100L	0.9786	0.8365	0.7341	0.7542
19	MSD_SS20F300L	0.9678	0.5325	0.8756	0.7256
20	MSU_SS20F100L	0.6985	0.6154	0.9999	0.6771
21	MSU_SS20F300L	0.9111	0.6521	0.9999	0.8533
22	MSD_SS40F500L	0.9957	0.7511	-8.8876	0.7997
23	MSD_SS40F1300L	0.9993	-0.0294	0.9553	0.2834
24	MSU_SS40F500L	0.1431	0.5208	0.0189	0.9999
25	MSD_SS60F500L	0.9980	0.8567	0.8841	-6.5016
26	MSD_SS60F1300MD	0.9985	-1.0150	-0.0357	0.8900

Table 6.3: R^2 values for model simulations of WGS family under monotonic saturated loading conditions.

S.No	Test Label	CSL – qp'	Stress – Strain response	CSL – e log p' space	Volumetric Response
1	MSD_WGS18F500MD	0.9975	0.6101	0.9123	0.7618
2	MSU_WGS18F100L	0.8913	0.8541	0.9999	0.8871
3	MSD_WGS28F100L	0.9852	0.6624	0.8967	0.6315
4	MSU_WGS28F100L	0.9612	0.9125	0.9999	0.9185
5	MSD_WGS40F100L	0.9870	0.8931	0.9311	0.8762
6	MSD_WGS40F500L	0.9973	0.8669	0.9717	0.7086
7	MSD_WGS60F100MD	0.9996	0.9164	0.9351	0.9462
8	MSD_WGS60F500MD	0.9993	0.7112	0.8680	0.7810

A key limitation of the model is its difficulty in accurately capturing the phase transformation point and dilation angle, particularly at higher fines contents. Since these parameters govern the onset and extent of dilation, any misrepresentation directly affects peak stress predictions and post-peak volumetric trends (Bolton, 1986; Lade & Pradel, 1990). In dense sands, failure to accurately predict the transition from contractive to dilative behaviour leads to underestimation of strain hardening effects and overprediction of contraction, affecting the accuracy of effective stress paths in q–p' space. In loose sands with high fines content, the model struggles to capture the correct peak stress and volumetric evolution, leading to an early approach to the critical state at lower stress levels than observed experimentally (Shire et al., 2013).

Additionally, the model does not fully account for the influence of particle angularity, evolving coordination number, and fines fraction on stress transmission mechanisms (Mitchell & Soga, 2005; Rahman et al., 2008). As observed in WGS, the presence of angular and well-graded fines alters the force chains within the granular matrix, significantly affecting shear resistance and dilation tendencies. The model underestimates the stabilising effect of angular fines at low fines content and overestimates contractive tendencies at higher fines content, leading to deviations in post-peak behaviour and critical state approach (Vallejo & Mawby, 2000). These issues indicate the need for state-dependent modifications that incorporate fabric evolution and fines-content-dependent stress-dilatancy relationships (Thevanayagam, 1998; Santamarina et al., 2001).

Future refinements should focus on enhancing the constitutive framework to incorporate fabric-dependent behaviour and evolving grain-scale interactions (Thevanayagam, 2007). Implementing a more advanced stress-dilatancy model that considers the effect of varying fines content, grading characteristics, and interparticle angularity may improve the model's ability to predict dilation onset, peak stress evolution, and volumetric strain trends more accurately

(Been & Jefferies, 1985; Bolton, 1986). Moreover, a coupled effective stress approach that explicitly accounts for pore pressure evolution in undrained tests could enhance the model's capability in simulating transient loading effects, liquefaction potential, and cyclic mobility (Ishihara, 1993; Lade & Pradel, 1990). Addressing these limitations will enable a more comprehensive representation of soil behaviour across a wider range of soil gradations and fines content distributions, making the model more applicable to real-world geotechnical scenarios.

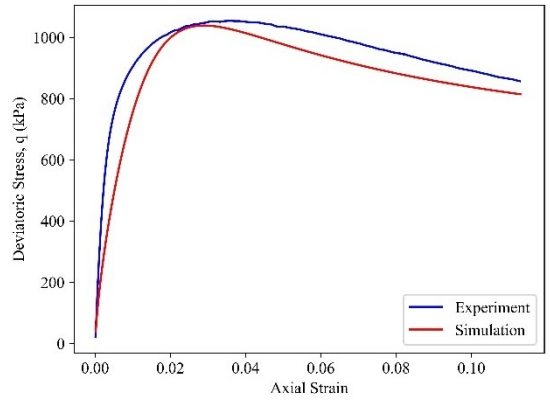

(a)

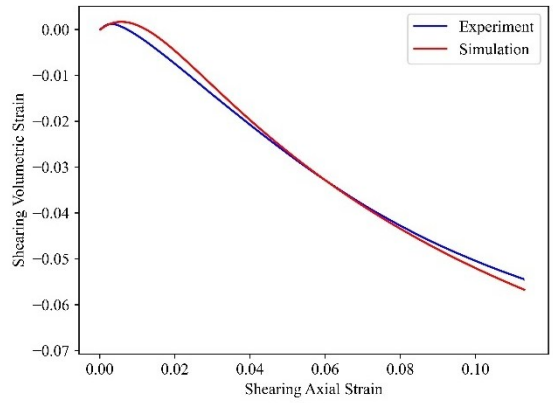

(b)

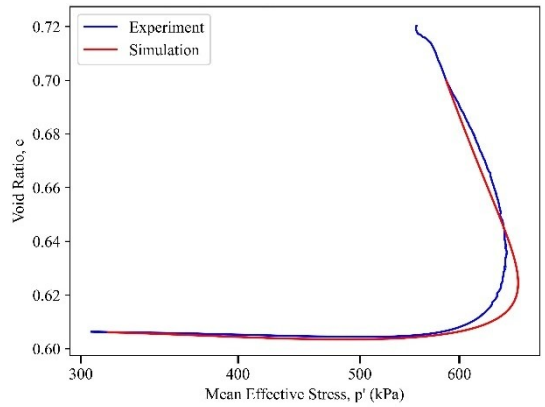

(c)

Figure 6.21: Simulation of Monotonic saturated Drained test: Sydney Sand, p'_{ini} = 300 kPa; e = 0.6063

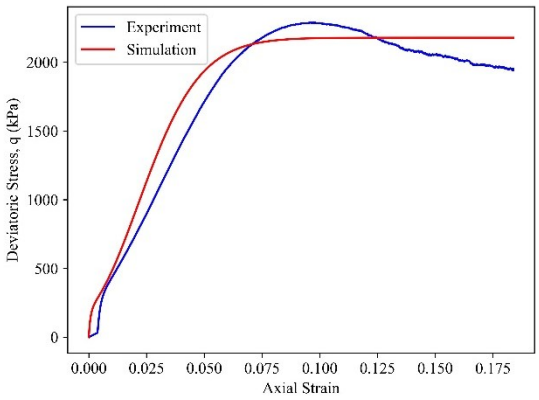

(a)

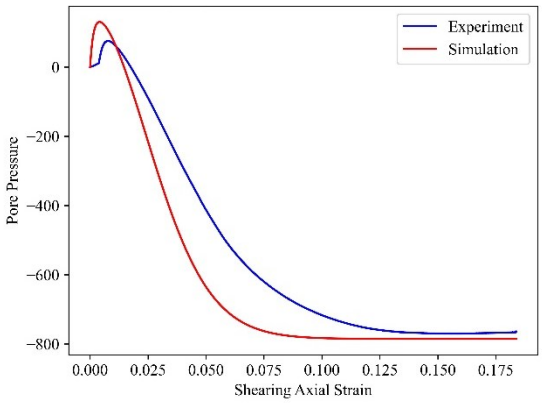

(b)

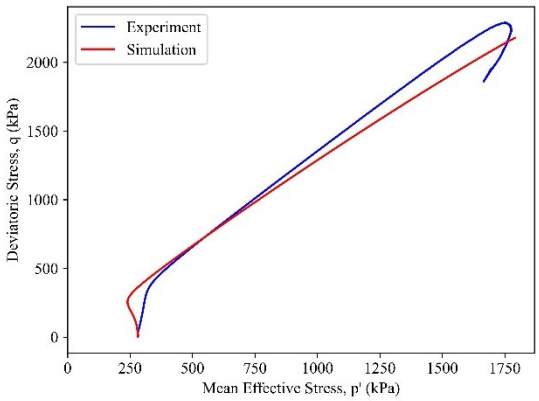

(c)

Figure 6.22: Simulation of Monotonic saturated Undrained test: Sydney Sand, p'_{ini} = 200 kPa; e = 0.6806

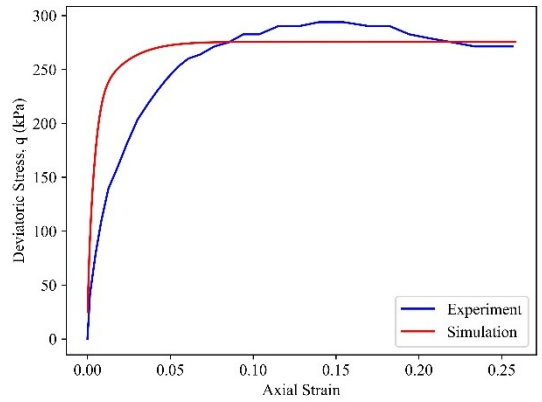

(a)

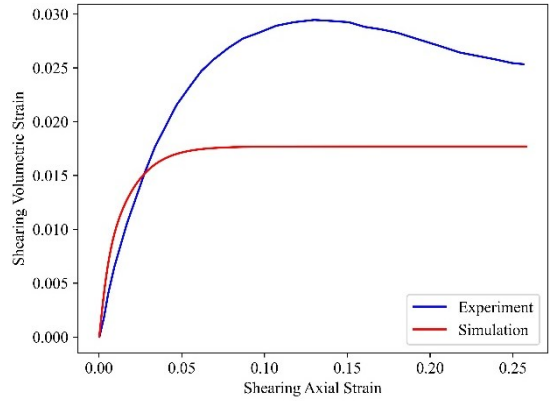

(b)

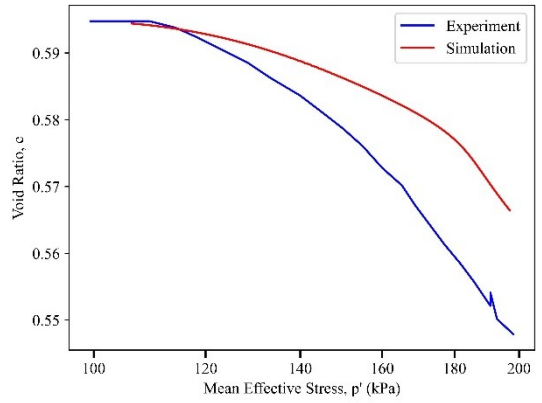

(c)

Figure 6.23: Simulation of Monotonic saturated Drained test: Sydney Sand with 20% Fines, p'_{ini} = 100 kPa; e = 0.5947

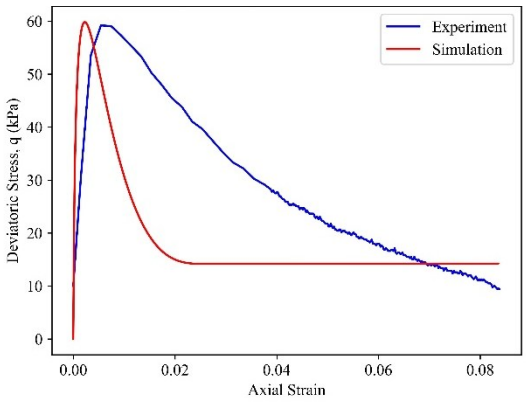

(a)

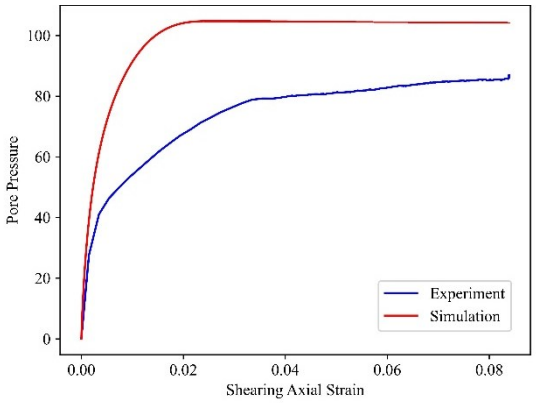

(b)

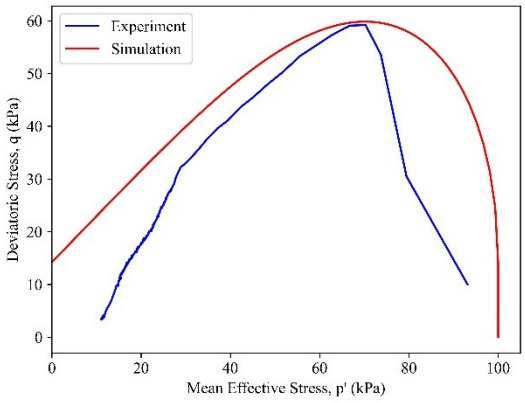

(c)

Figure 6.24: Simulation of Monotonic saturated Undrained test: Sydney Sand with 20% Fines, p'_{ini} = 100 kPa; e = 0.6265

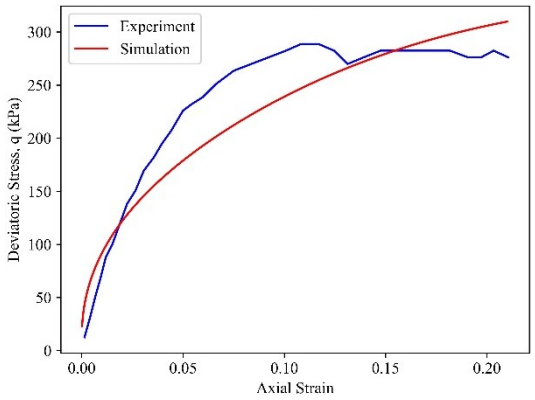

(a)

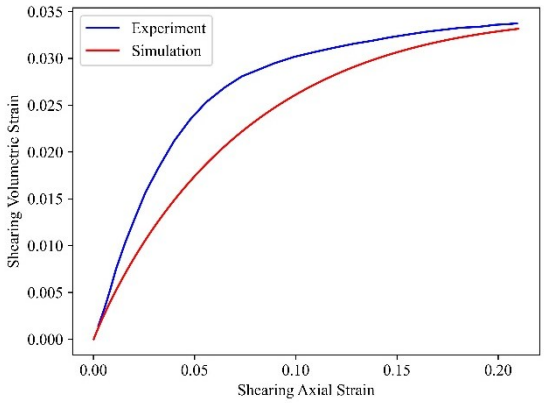

(b)

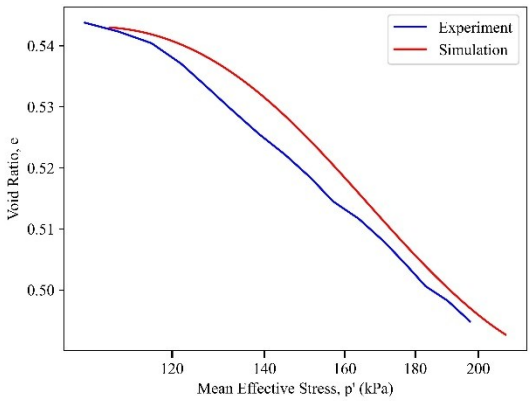

(c)

Figure 6.25: Simulation of Monotonic saturated Drained test: Sydney Sand with 40% Fines, p'_{ini} = 100 kPa; e = 0.5432

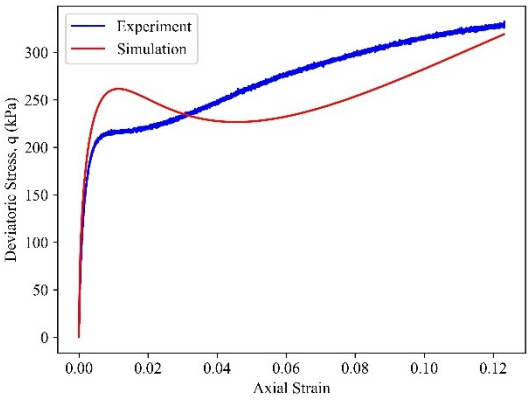

(a)

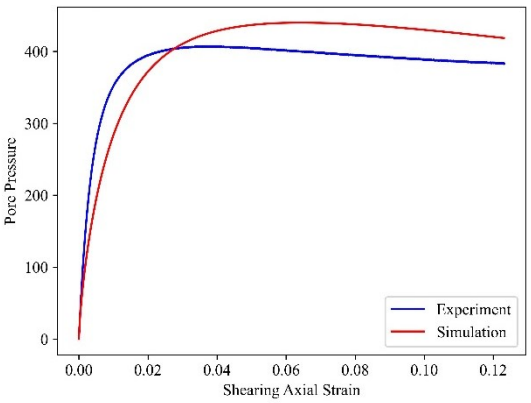

(b)

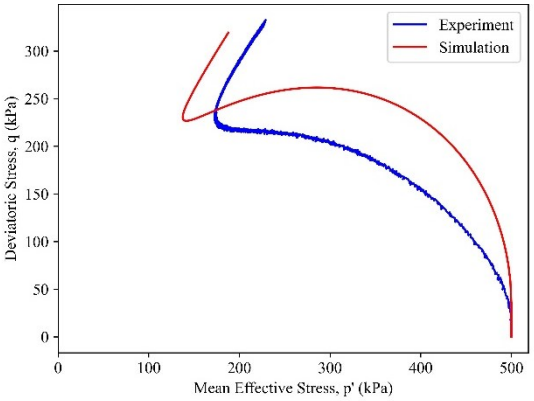

(c)

Figure 6.26: Simulation of Monotonic saturated Undrained test: Sydney Sand with 40% Fines, p'_{ini} = 500 kPa; e = 0.4660

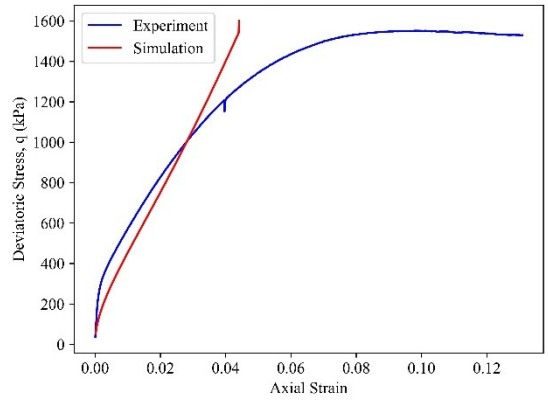

(a)

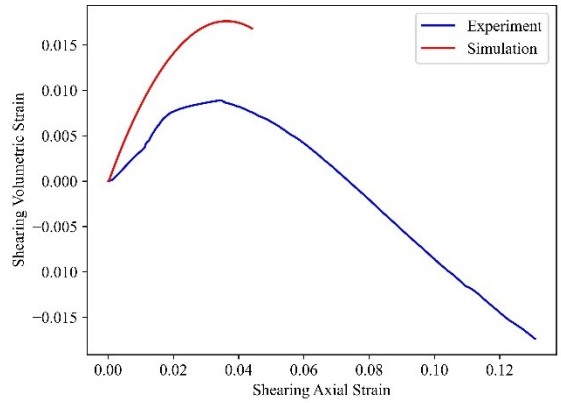

(b)

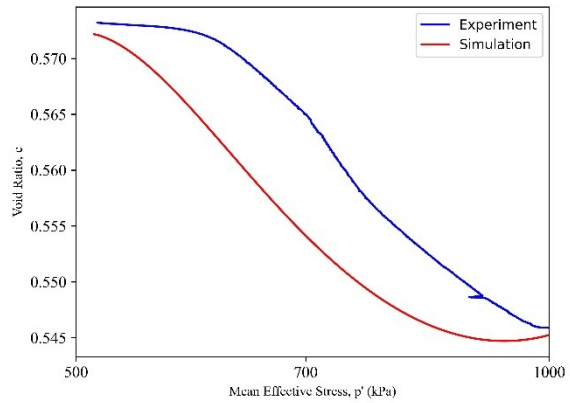

(c)

Figure 6.27: Simulation of Monotonic saturated Drained test: Sydney Sand with 60% Fines, p'_{ini} = 500 kPa; e = 0.5732

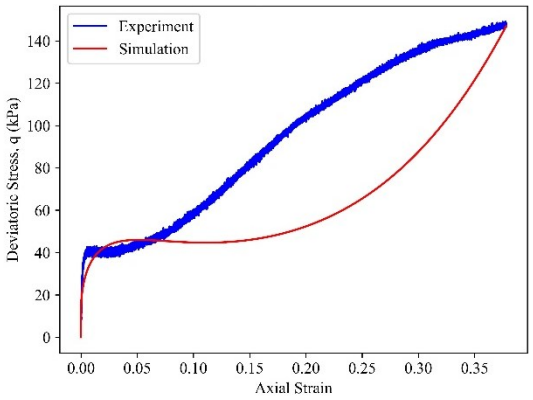

(a)

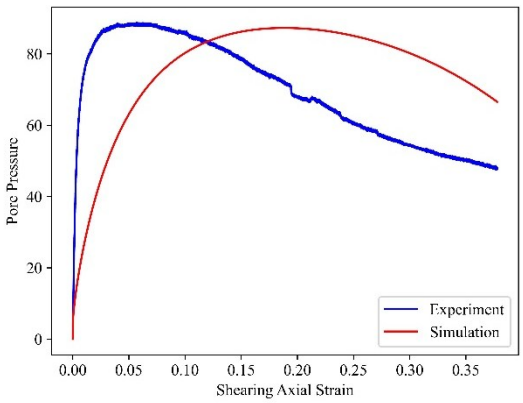

(b)

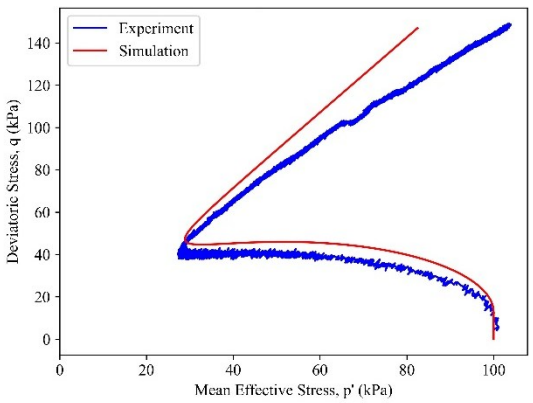

(c)

Figure 6.28: Simulation of Monotonic saturated Undrained test: Sydney Sand with 60% Fines, p'_{ini} = 100 kPa; e = 0.5898

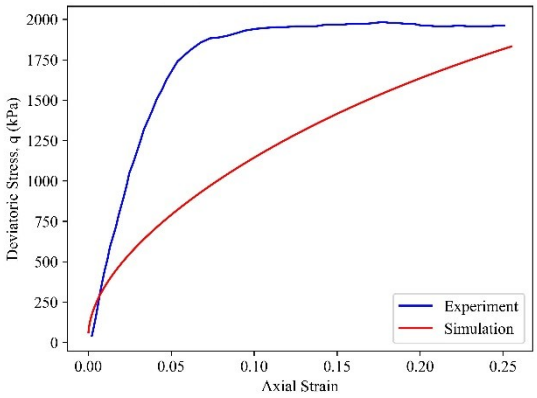

(a)

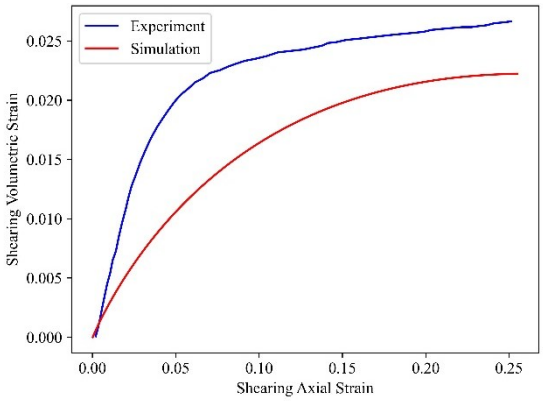

(b)

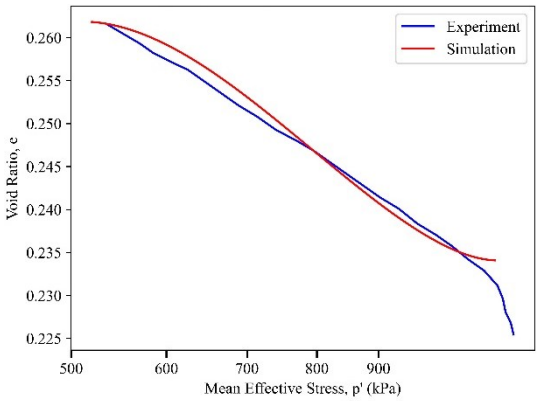

(c)

Figure 6.29: Simulation of Monotonic saturated Drained test: WGS with 18% Fines, p'_{ini} = 500 kPa; e = 0.2619

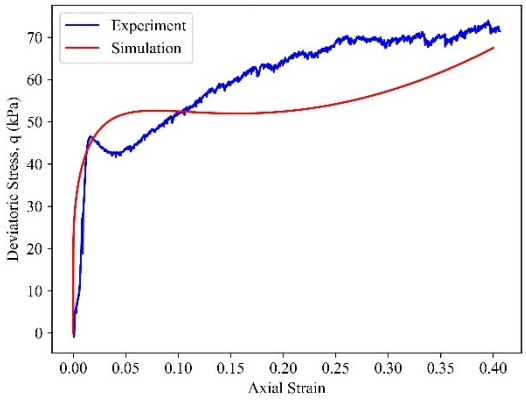

(a)

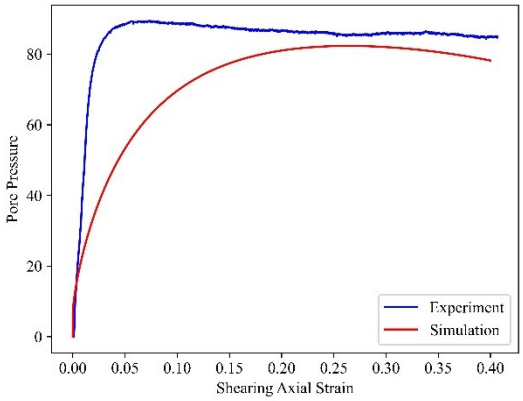

(b)

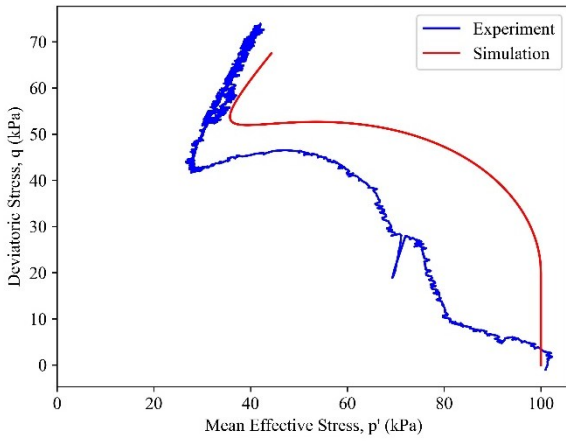

(c)

Figure 6.30: Simulation of Monotonic saturated Undrained test: WGS with 18% Fines, p'_{ini} = 100 kPa; e = 0.2955

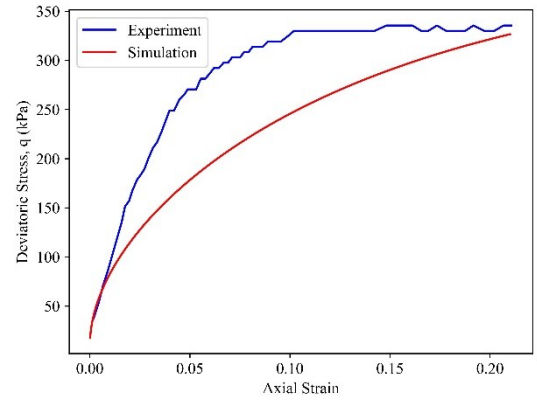

(a)

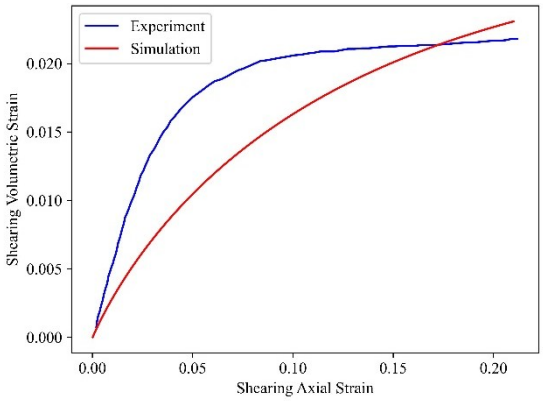

(b)

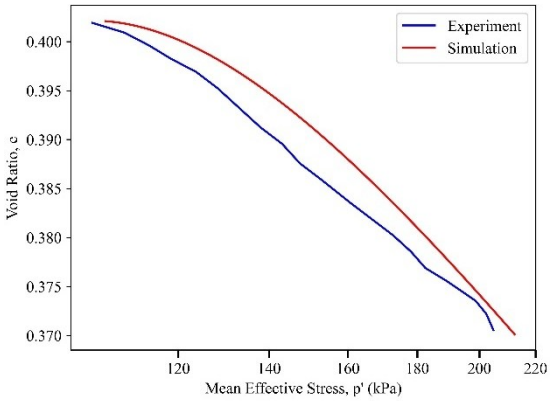

(c)

Figure 6.31: Simulation of Monotonic saturated Drained test: WGS with 28% Fines, p'_{ini} = 100 kPa; e = 0.4022

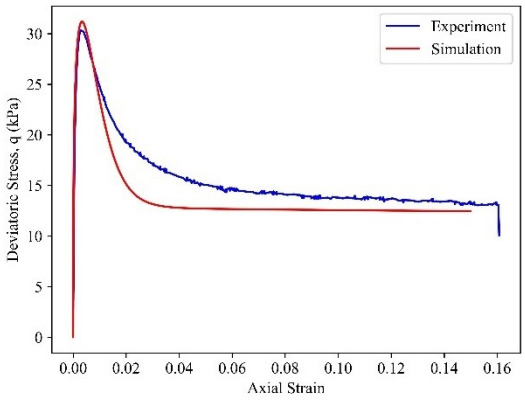

(a)

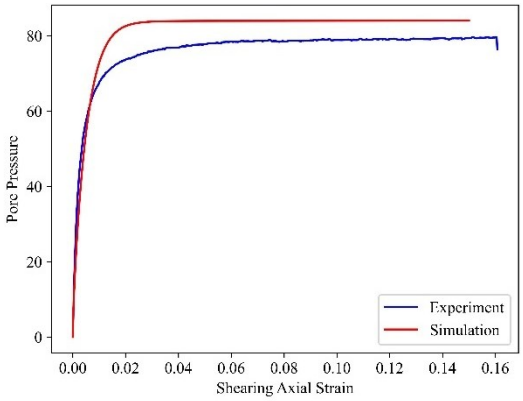

(b)

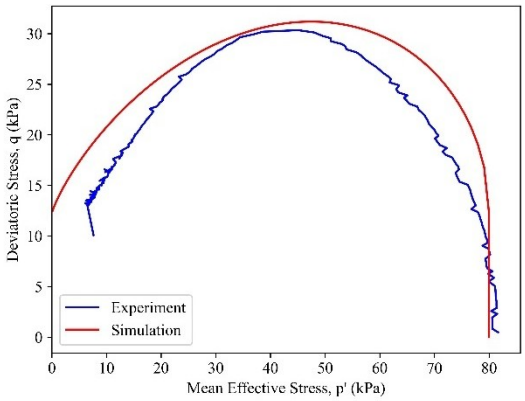

(c)

Figure 6.32: Simulation of Monotonic saturated Undrained test: WGS with 28% Fines, p'_{ini} = 80 kPa; e = 0.4218

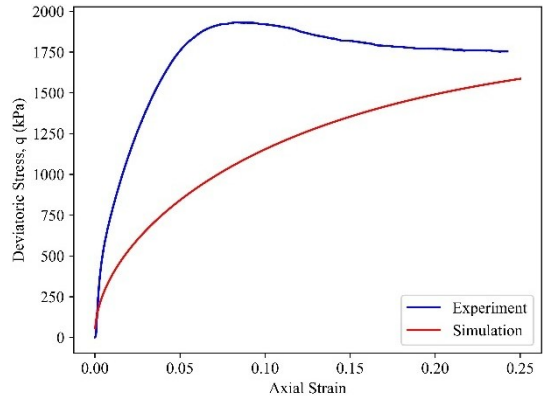

(a)

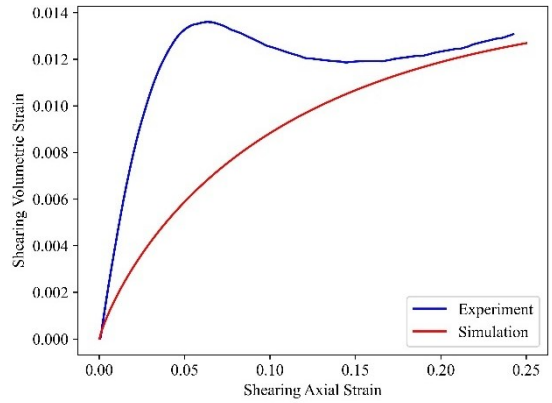

(b)

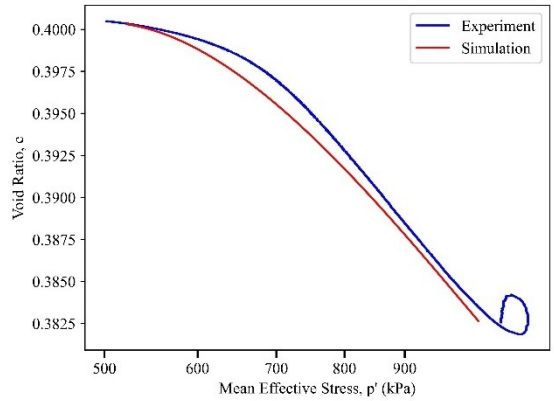

(c)

Figure 6.33: Simulation of Monotonic saturated Drained test: WGS with 40% Fines, p'_{ini} = 500 kPa; e = 0.4005

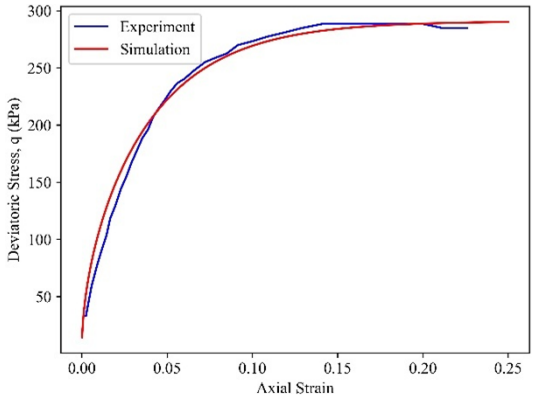

(a)

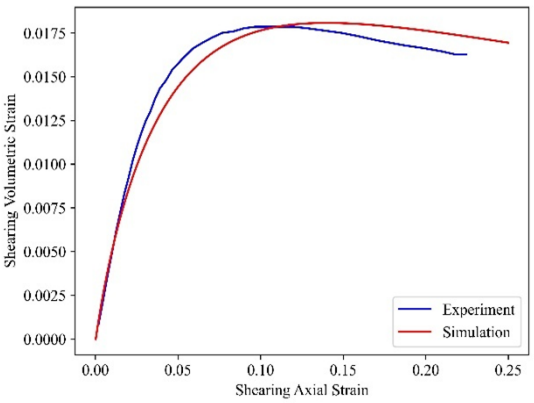

(b)

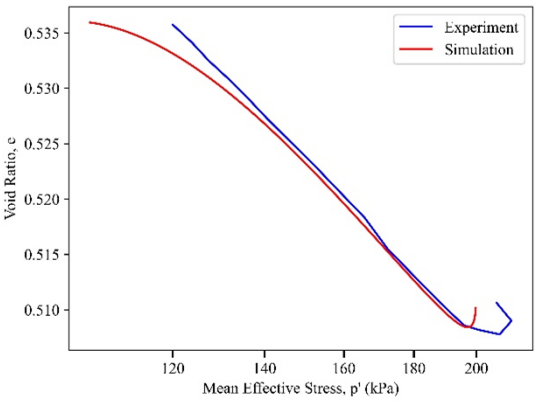

(c)

Figure 6.34: Simulation of Monotonic saturated Drained test: WGS with 60% Fines, p'_{ini} = 100 kPa; e = 0.5361

6.4.5 Simulations of Monotonic unsaturated tests

The behaviour of unsaturated soils is significantly influenced by matric suction, degree of saturation, and capillary effects, which alter their strength and deformation characteristics compared to their fully saturated counterparts (Fredlund & Rahardjo, 1993; Alonso et al., 2010). In this section, monotonic unsaturated triaxial tests were simulated on Sydney sand and well-graded sand (WGS) families, including Sydney sand, Sydney sand with 20%, 40%, and 60% fines, and WGS with 18%, 28%, 40%, and 60% fines, to evaluate the impact of grading and fines content on mechanical response under unsaturated conditions. The introduction of fines alters the pore structure, suction effects, and state-dependent behaviour, influencing stress-strain response, peak strength, and volumetric trends (Gallipoli et al., 2003; Lu & Likos, 2004; Tarantino, 2009).

Compared to saturated conditions, unsaturated soils require modifications in key constitutive parameters due to the role of suction in governing mechanical response. Elasticity parameters, increase with suction, resulting in higher stiffness under low-strain conditions (Alonso et al., 1990; Wheeler et al., 2003). Similarly, plastic hardening behaviour changes due to suction-dependent yield surface expansion and stress history effects, affecting the hardening modulus and transition between elastic and plastic deformation (Gens & Alonso, 1992; Tarantino & Tombolato, 2005). Additionally, kinematic hardening parameters require adjustment to account for the anisotropic effects of suction-induced stress paths, which alter loading-unloading behaviour (Sheng et al., 2008; Wheeler et al., 2003).

A major difference in unsaturated soil behaviour lies in the modification of critical state parameters, as the critical state line (CSL) is no longer unique but shifts depending on suction and fines content (Toll, 1990; Wheeler et al., 2003). Higher suction levels generally lead to lower void ratios at the critical state and higher mean effective stress, resulting in a suction dependent strength increase (Vanapalli et al., 1996; Wheeler & Sivakumar, 2000). However,

the role of fines content is still complex, as increased fines influence both pore water retention and capillary effects, leading to either increased cohesion or enhanced contractive behaviour, depending on suction conditions (Gallipoli et al., 2003; Tarantino, 2009).

To effectively model the influence of suction and degree of saturation, the behaviour of unsaturated soil is incorporated through the Soil-Water Characteristic Curve (SWCC), using the Fredlund and Xing (1994) model. The SWCC governs the relationship between suction and degree of saturation, allowing the model to accurately simulate the transition from partially saturated to saturated states (Fredlund & Xing, 1994). This integration ensures that suction-induced effects, such as pore water retention, capillary stress transmission, and hydraulic hysteresis, are reflected in the evolution of effective stress and stiffness with changing moisture conditions (Ng & Pang, 2000; Lu & Likos, 2004). By incorporating SWCC parameters as shown in Tables 5.10 and 5.11 shown in chapter 5, the model can simulate suction-dependent volume changes and strength behaviour, which is particularly crucial when analysing the effect of fines and grading on suction-induced dilatancy (Tarantino, 2009; Wheeler et al., 2003).

As fewer unsaturated tests have been conducted compared to saturated counterparts, the exact modification of constitutive parameters remains constrained by limited experimental data. Therefore, except for critical state parameters, which were calibrated based on previously used methods, most of the parameters that required updating were increased with rational reasoning while running the simulations. These adjustments ensured that the stress-strain response, peak strength, and volumetric behaviour aligned with experimental trends observed in similar unsaturated soil studies (Ng & Pang, 2000; Rahardjo et al., 2004; Sheng et al., 2008). The final calibrated values, representing the best simulation results, are presented in Table 6.1, capturing the effects of suction, fines content, and grading on the overall mechanical response.

The model parameters underpinning these unsaturated simulations are provided in Table 6.4, and the fit quality is further supported by R^2 values summarised in Table 6.5, which

complement the visual curve assessments presented in the figures. These R^2 values are presented for key response components — stress–strain, CSL in q–p′ space, CSL in e–log p′ space, and volumetric/pore pressure behaviour — offering a quantitative check alongside the qualitative curve matching.

Table 6.4: Model parameters for unsaturated simulations

Type	Symbol	SS0F	SS20F	SS40F	SS60F	WGS18F	WGS28F	WGS40F	WGS60F
Elasticity	G_0	290	270	270	260	320	295	285	290
	K_0	305	210	210	220	225	235	230	225
Kinematic Hardening	n^b	4.5	7.5	11.5	5.0	8.2	4.25	1.95	22.5
	c_h	0.968	0.9	0.89	0.82	0.88	0.85	0.79	0.86
	h_0	12	9.2	8.6	7.07	5.5	5.1	3.6	2.5
Dilatancy	n^d	1.8	0.75	2.5	8.2	4.8	0.5	6.25	2.18
	A_d	1.33	0.4	0.2	0.8	0.6	0.8	0.8	0.9
	c_z*	600	600	600	600	600	600	600	600
	z_{max}*	4	4	4	4	4	4	4	4
	N_l*	27.5	97	100	150	172	91.5	49.4	27.2
	λ	0.39	0.58	0.6	0.56	0.6	0.58	0.52	0.45
Critical State	N_c	36	116	116	128	58	72	63.5	59.7
	α_{csl}	4400	3600	3200	2800	3500	5000	6000	6000
	M	1.6667	1.8182	1.9259	1.9259	1.9821	1.8210	1.7826	1.7211

*These parameters but did not affect the current set of simulations. Therefore, they were left unchanged from their saturated counterparts and remained constant across all materials.

Table 6.5: R^2 values for model simulations of Sydney Sand family under monotonic unsaturated loading conditions

S.No	Test Label	CSL – qp'	Stress – Strain response	CSL – e log p' space	Volumetric Response
1	MUD_SS0F100i	0.9888	0.8686	0.8765	0.9102
2	MUD_SS0F100ii	0.9940	0.5444	0.5265	0.9412
3	MUD_SS0F100iii	0.9750	0.9877	0.9940	0.9008
4	MUD_SS0F100iv	0.9945	0.7376	0.9705	0.6004
5	MUD_SS0F100v	0.9949	0.9379	0.8043	0.5202
6	MUD_SS0F100vi	0.9914	-0.4463	0.7841	0.2665
7	MUD_SS0F100vii	0.9662	0.7970	0.6921	0.9325
8	MUD_SS20F100i	0.9985	0.3893	0.8125	0.8592
9	MUD_SS20F100ii	0.9958	-2.1064	0.8812	0.4354
10	MUD_SS40F100	0.9901	0.7354	0.8179	0.9610
11	MUD_SS60F100i	0.9934	0.8839	0.8872	0.7535

6.4.6 Observations in Simulations

A critical aspect of unsaturated test preparation is that most samples are prepared in a dense state to prevent collapse during sample preparation before applying suction. This practical limitation introduces an unintended bias, as fewer tests are conducted on loose specimens, thereby restricting the evaluation of the effect of fines on contractive soil structures (Gallipoli et al., 2003; Lu & Likos, 2004). The impact of density and suction on soil behaviour is particularly relevant when examining post-peak softening and stress-dilatancy evolution, both of which are challenging to capture accurately in numerical simulations.

Moreover, due to the partially saturated nature of the soil, even dense and stiff samples exhibit higher void ratios compared to their saturated counterparts. This is because the presence of air within the void spaces and suction effects alters the packing density, making the void ratio an unreliable parameter for direct comparison between saturated and unsaturated states (Wheeler & Sivakumar, 2000; Lu & Likos, 2004). The presence of air reduces the degree of saturation, causing even highly compacted samples to behave differently than fully saturated dense specimens. As a result, evaluating soil behaviour based purely on void ratio comparisons between saturated and unsaturated conditions can lead to misinterpretations, necessitating a state-dependent assessment that accounts for suction effects on soil fabric and stiffness (Alonso et al., 1990; Toll, 1990).

All the unsaturated simulations were conducted in terms of effective stress, incorporating the effect of suction using Bishop's effective stress equation (Bishop, 1959) as mentioned in Chapter 5. Almost all the unsaturated tests were conducted as constant suction tests, allowing for a direct assessment of how suction influences soil behaviour under monotonic loading conditions. Compared to their saturated counterparts, the simulation of unsaturated triaxial tests shows promising results in replicating key mechanical trends. While the simulations do not exactly match the experimental results in terms of absolute stress-strain response and volumetric strain magnitudes, they successfully reproduce the general stress-strain behaviour, volumetric contraction and dilation trends, and the approach toward the critical state. The slight offset in values between experimental and simulated results suggests that further refinements may be necessary to better capture suction-dependent soil stiffness and hardening characteristics, particularly in the transitional phase between contractive and dilative response (Ng & Pang, 2000; Rahardjo et al., 2004).

Furthermore, to simplify the study and account for apparatus limitations, most of the unsaturated tests were conducted within a suction range of 6–15 kPa. While this range is

sufficient to capture moderate suction effects, it limits the ability to comprehensively evaluate the impact of suction over a broader range, particularly in the higher suction regime, where soil behaviour transitions further from saturation-controlled responses to true unsaturated state-dependent mechanics (Vanapalli et al., 1996; Tarantino, 2009; Lu & Likos, 2004). Future studies could benefit from extending the suction range to examine its influence on strength, dilatancy, and critical state evolution in both coarse- and fine-grained soils.

Due to the strengthening effect of suction, many of the tested samples exhibited high stiffness, which, in turn, resulted in the formation of distinct shear planes during testing. Once a shear plane develops, the soil undergoes localized deformation, making volumetric strain measurements unreliable. This presents a challenge in both experimental data interpretation and numerical simulations, as the volumetric response after shear band formation is no longer representative of the overall sample behaviour. Consequently, in the simulations as shown in Figures 6.37 and 6.38, the transition beyond shear plane formation is not smooth and does not fully align with the experimental observations. This discrepancy highlights the need for refinements in the constitutive framework to better incorporate strain localization and post-failure mechanisms (Sheng et al., 2008; Wheeler et al., 2003).

However, as shown in the stress path plots in p–q space (part (a) of Figures 6.35 to 6.40), the model reproduces the experimental response for all sand mixtures, confirming the critical state slope under unsaturated conditions. In contrast, the volumetric behaviour is not captured as accurately, resulting in noticeable discrepancies in the void ratio evolution and, consequently, in the stress–strain response.

Overall, these findings underscore the importance of considering density effects, strain localization, and suction range limitations in both experimental design and constitutive modelling. Improving the ability of simulations to capture localized deformation and post-peak behaviour requires further refinement of stress-dilatancy relationships, particularly in the

presence of suction-dependent hardening and strain-softening effects. The promising trends observed in the critical state approach and a reasonable trend of stress-strain response, and volumetric behaviour, indicate that the current modelling framework is capable of simulating key unsaturated soil mechanisms but requires additional refinement to improve numerical-experimental agreement in absolute values

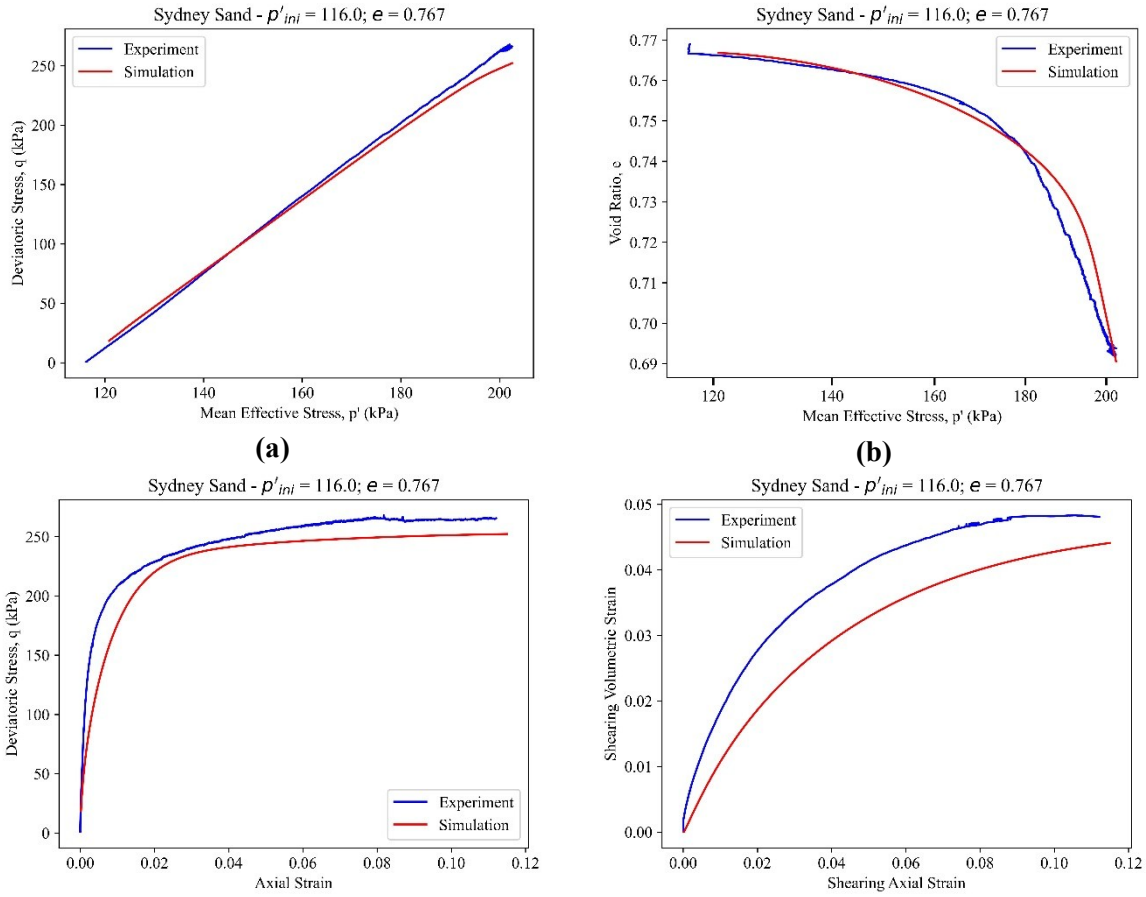

Figure 6.35: Simulation of Monotonic unsaturated – Constant suction test: Sydney sand, p'_{ini} = 116 kPa; p_{suc}=10; e = 0.7670

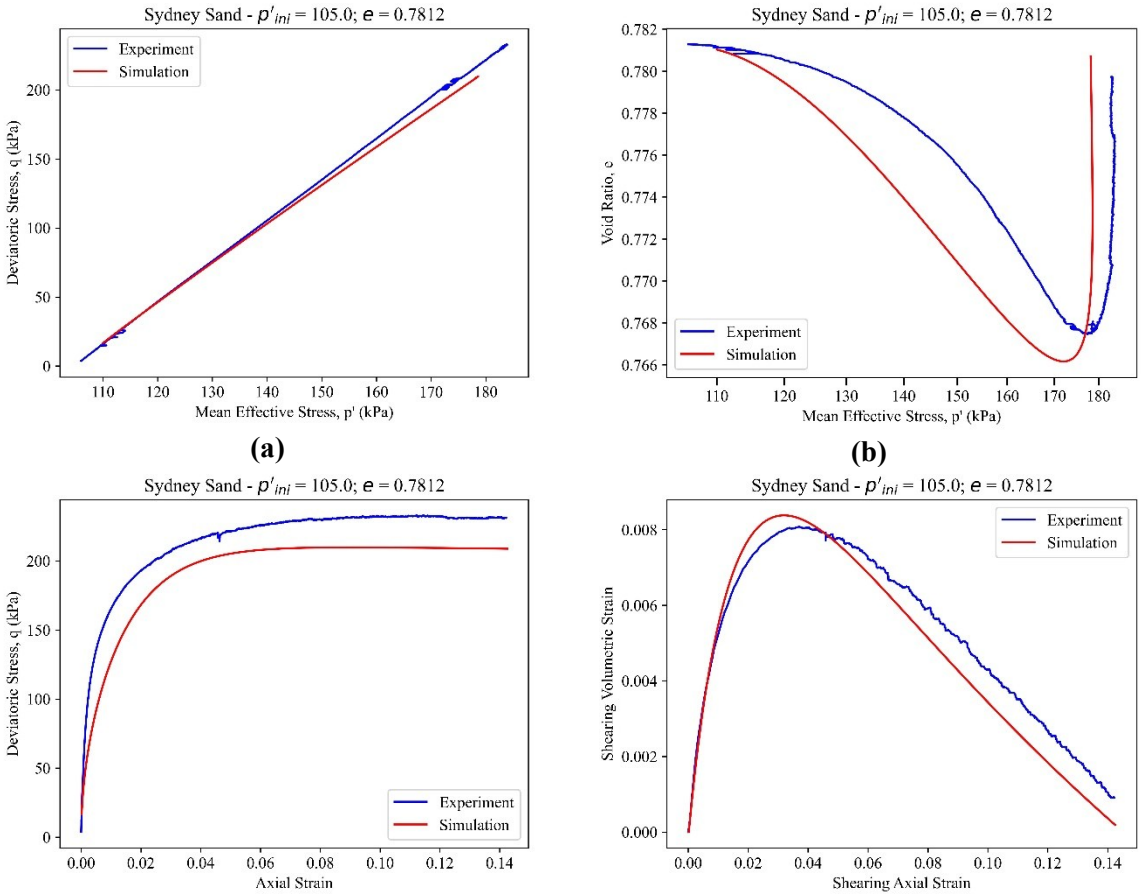

Figure 6.36: Simulation of Monotonic unsaturated – Constant suction test: Sydney sand, p'_{ini} = 105 kPa; p_{suc}=10; e = 0.7812;

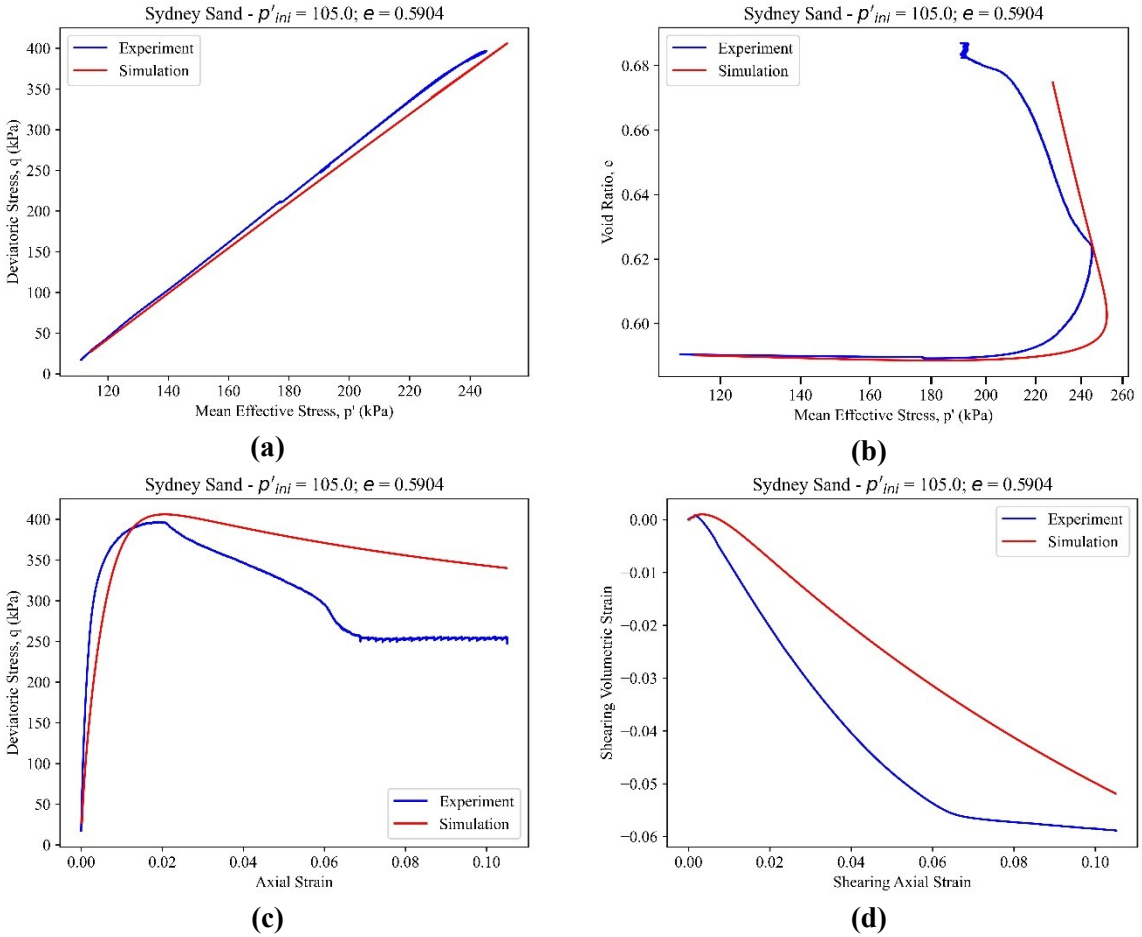

Figure 6.37: Simulation of Monotonic unsaturated – Constant suction test: Sydney sand, p'_{ini} = 105 kPa; p_{suc}=10; e = 0.5904;

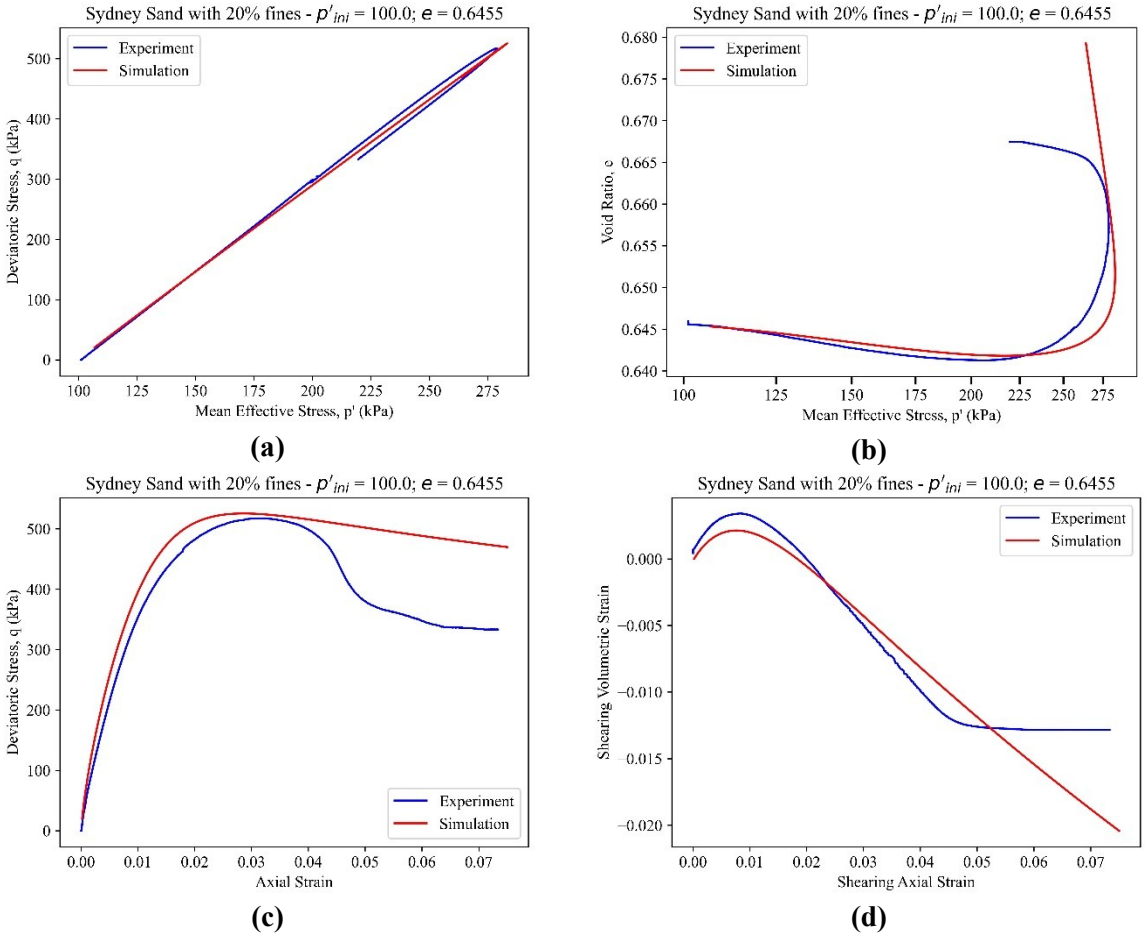

Figure 6.38: Simulation of Monotonic unsaturated – Constant suction test: Sydney sand with 20% Fines, p'_{ini} = 100 kPa; p_{suc}=10; e = 0.6455;

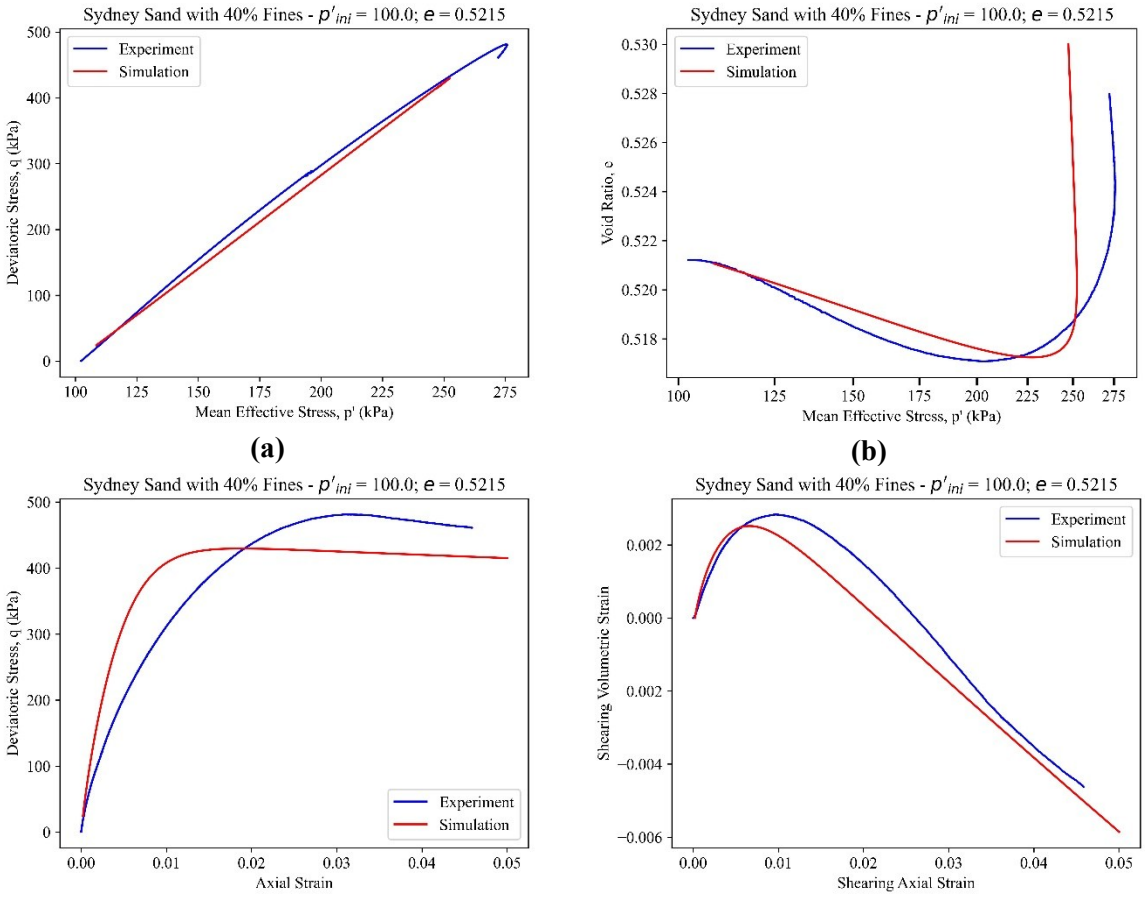

Figure 6.39: Simulation of Monotonic unsaturated – Constant suction test: Sydney sand with 40% Fines, p'_{ini} = 100 kPa; p_{suc}=10; e = 0.5215;

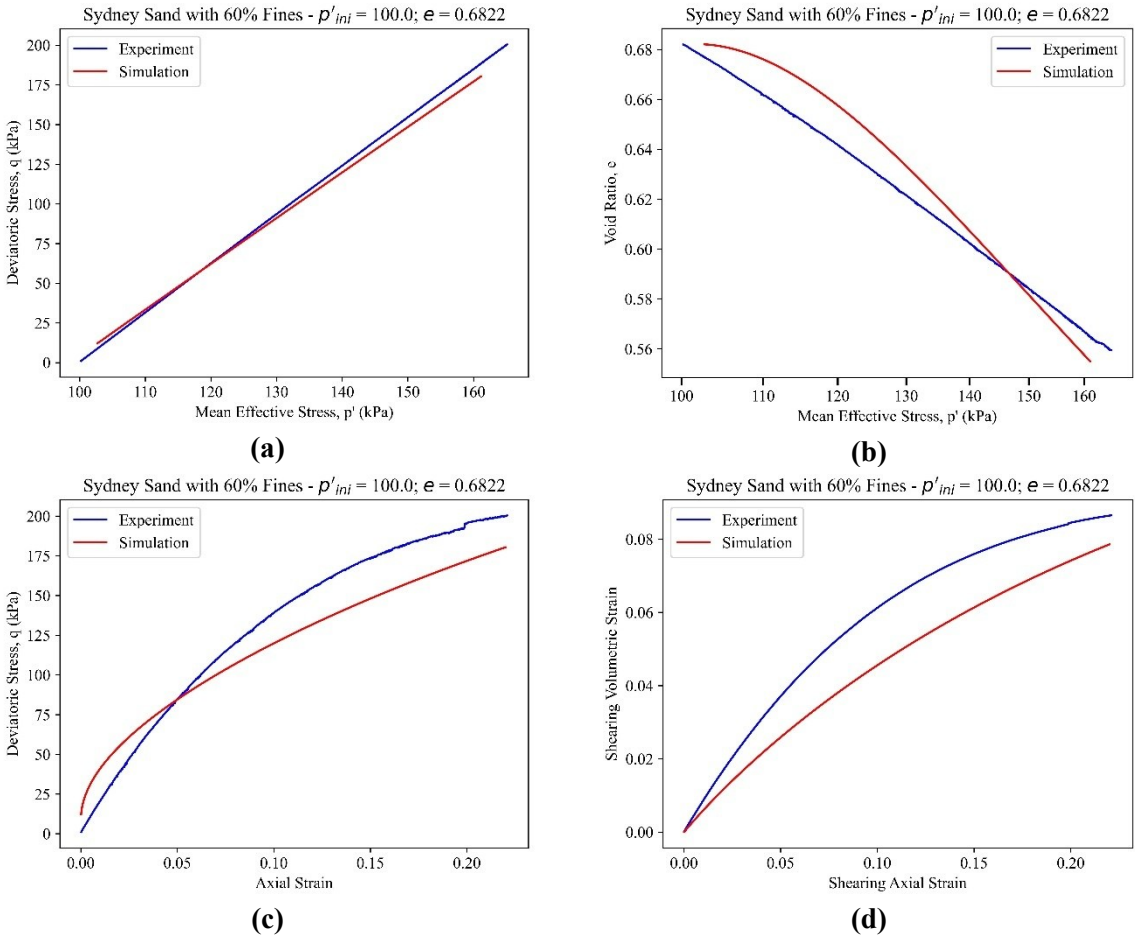

Figure 6.40: Simulation of Monotonic unsaturated – Constant suction test: Sydney sand with 60% Fines, p'_{ini} = 100 kPa; p_{suc}=10; e = 0.6822;

6.4.7 Simulation of Cyclic tests

As discussed in the calibration section, the accurate simulation of cyclic loading requires the proper calibration of memory surface (MS) parameters and semi-fluidised state (Sf) parameters, particularly when using the enhanced constitutive model developed by Chen (2024). These parameters are essential in capturing the irreversible strain accumulation and stress path-dependent behaviour under cyclic loading conditions. However, due to experimental limitations in this study, including the unavailability of a sufficient number of high-fidelity cyclic tests on partially saturated samples, the model calibration could not be fully completed. Although reference tests from prior studies, such as Mohammadi (2020) and Kwa

(2019), were considered, the data extracted from those experiments were either incomplete or not fully compatible with the required input format for parameter calibration. Consequently, a complete calibration of MS and Sf parameters specific to the current sand mixtures tested in this study was not feasible.

To address this limitation, the MS and Sf parameters for Karlsruhe's sand, which were previously calibrated in the literature and validated in other numerical studies, were adopted. Meanwhile, other material parameters such as stiffness, dilation, and peak strength parameters were taken from the saturated monotonic calibration discussed in earlier sections.

This undrained test was run with $p'_{ini} = 100$ kPa and $e_i = 0.764$, and with MS and Sf states disabled, serving as a baseline case to observe the performance of the core SANISAND formulation without enhanced cyclic features. The model reproduced key cyclic behaviours, including progressive axial strain accumulation (about 0.1–0.2 % per cycle early on), gradual pore pressure build-up, and post-cyclic stiffness response. Approximately similar number of cycles were simulated before axial strain stabilised near 8–9%, and excess pore pressure reached 80–85% of the initial effective stress. Post-cyclic monotonic loading confirmed that the model correctly represented the reduction in stiffness and strength recovery following cyclic degradation, indicating that even without the cyclic enhancements, the base model provides a reliable framework for simulating undrained cyclic mobility and effective stress evolution.

The original model proposed by Ghorbani and Airey (2021) is inherently capable of simulating undrained cyclic behaviour under saturated conditions, and this has been validated through the current study. A representative simulation of an undrained cyclic triaxial test is shown in Figure 6.41. The model exhibits a reasonably good fit with experimental data, capturing the cyclic mobility, the rate of strain accumulation per cycle, and the post-cyclic stress-strain behaviour.

Importantly, both the stress path and the development of excess pore pressure were in reasonable agreement with observed trends in the laboratory test.

However, when the same model setup was applied to simulate a drained cyclic test using the Karlsruhe-derived MS and Sf parameters and material properties from the monotonic calibration the simulation results diverged significantly from the experimental behaviour. The predicted response showed an unrealistic accumulation of strain, poor replication of stress reversal points, and lacked the hysteretic loops typically observed in drained cyclic tests. In particular, the model showed reasonable strain increments for the first few dozen cycles (0.05–0.1 % per cycle) but strain accumulation then accelerated unrealistically, indicating deficiencies in the imported MS calibration for drained conditions. This discrepancy suggested a misrepresentation of the plastic flow direction and a potential error in memory surface evolution.

To better understand the model's sensitivity to the memory surface parameters, a parametric analysis was conducted by varying the parameter a_1 within the memory surface formulation, while keeping other parameters fixed. As illustrated in Figure 6.42 (a) and (b), even a slight change in a_1 resulted in a significant alteration of the simulated cyclic stress–strain response. Specifically, Figure 6.42(a) shows the response using the baseline values from Chen (2024): a_0=2×10^{14}, a_1=4.2, and a_2=5.5. In contrast, Figure 6.42 (b) presents simulations where only a_1 is incrementally increased to 4.5, keeping a_0 and a_2 unchanged.

Both simulations were performed under identical external loading and boundary conditions, with the same q_{max} and q_{min}, number of cycles, and incremental step size. Importantly, the elastic stiffness, isotropic hardening, and critical state parameters were all carried over unchanged from the previously calibrated monotonic simulations. This controlled setup ensured that the only variable affecting the cyclic response was the memory surface parameters.

The results show that this isolated change in a_1 produced substantial differences in the rate and magnitude of strain accumulation per cycle. In simulations with a lower a_1, the model predicted faster ratcheting and larger permanent strains within fewer cycles. Increasing a_1 led to a more constrained strain development, with reduced plastic strain accumulation and tighter hysteresis loops. This striking sensitivity underscores the dominant role of the memory surface in controlling energy dissipation, stiffness degradation, and cyclic mobility characteristics in the constitutive model.

It should be noted that during early calibration trials, particularly when MS and Sf parameters were only approximately assigned, the numerical solver occasionally failed to converge. In some cases, the program entered non-terminating loops without producing results. To mitigate this, tighter convergence criteria were applied, smaller load increments were used, and parameter ranges were refined iteratively to ensure numerical stability during cyclic simulations.

These findings clearly reveal that the model is highly sensitive to memory surface (MS)-related parameters, particularly under drained conditions, where volumetric strain and stiffness evolution are significant. This behaviour is strongly influenced by the presence of suction and partial saturation, which affect yield surface hardening and dilatancy mechanisms. Accurate, soil-specific calibration of MS and semi-fluidised (Sf) parameters is thus essential to ensure reliable simulations. A purely trial-and-error calibration strategy is inadequate and may result in non-unique, unstable, or physically unrealistic outcomes.

While the model has shown strong performance in replicating saturated undrained cyclic responses, its application to drained cyclic loading in unsaturated soils necessitates a rigorous and informed calibration approach. This should be supported by systematic parametric studies and informed by high-resolution experimental datasets capturing pore pressure, suction, volumetric strain, and small-strain stiffness evolution. Future work should focus on developing

or acquiring such datasets to fully exploit the enhanced predictive capabilities of the model and to improve its robustness in unsaturated cyclic loading scenarios.

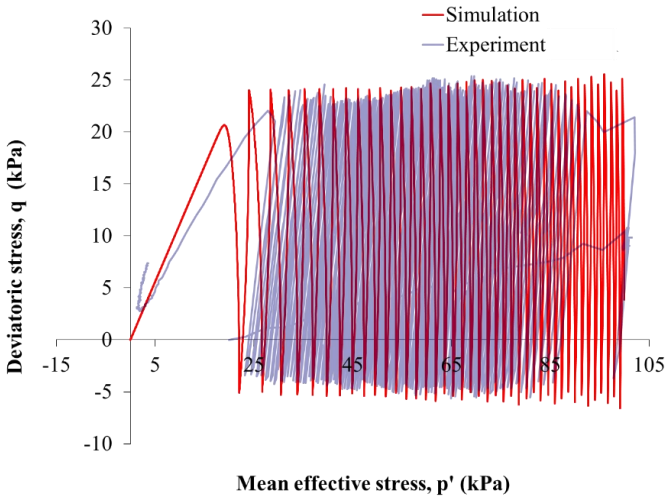

(a)

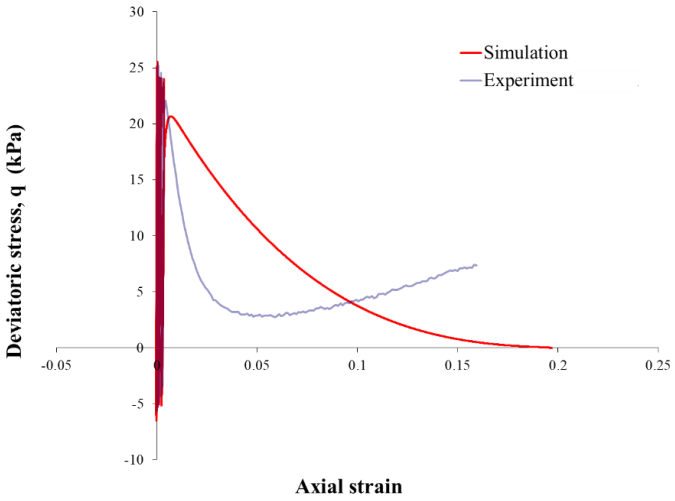

(b)

Figure 6.41: Simulation of Saturated Undrained Cyclic Test: p'_{ini} = 100 kPa; e_i = 0.764

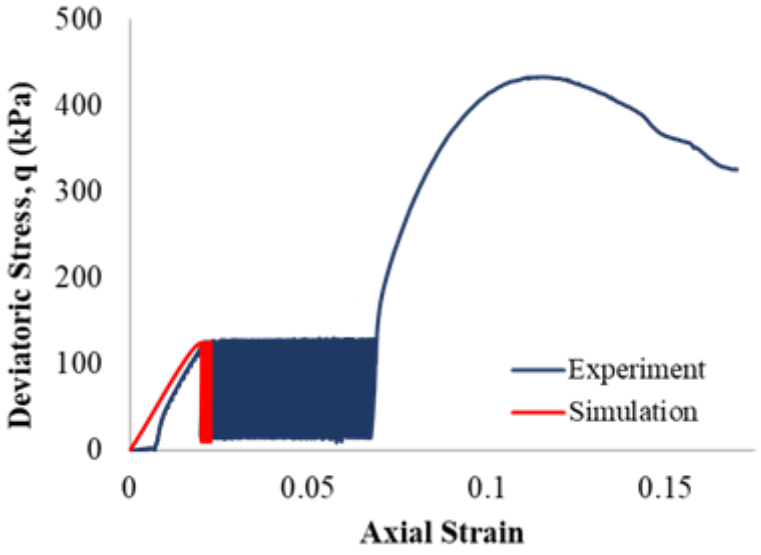

(a)

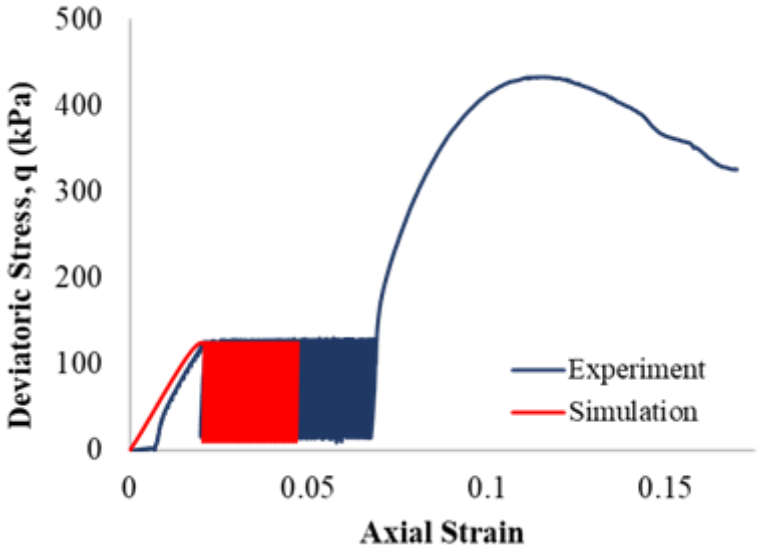

(b)

Figure 6.42: Simulation of Saturated Undrained Cyclic Test (SS60F): p'_{ini} = 100 kPa; e_i = 0.5592; (a) a_0=2×10^{14}, a_1=4.2; (b) a_0=2×10^{14}, a_1=4.5;

6.4.8 Summary of Simulations

The simulations of saturated and unsaturated soils under monotonic loading demonstrated the model's ability to capture key soil behaviour trends, including stress-strain response, volumetric change, and the approach to the critical state. The model effectively simulated both contractive and dilative responses, with better agreement observed for clean sands and samples with lower fines content. Discrepancies increased with higher fines content and elevated

suction levels, consistent with previous findings (Been & Jefferies, 1985; Lu & Likos, 2004). Saturated simulations closely matched experimental behaviour, particularly for dense specimens, although contraction was overestimated in loose samples with high fines content (Thevanayagam et al., 2002; Santamarina & Cho, 2004).

In the unsaturated regime, the integration of Bishop's effective stress principle and the Fredlund & Xing (1994) SWCC model enabled the simulation of suction-dependent strength gain and stiffness evolution (Fredlund & Rahardjo, 1993; Wheeler et al., 2003). However, limitations were observed in the accurate capture of post-peak softening, strain localization, and shear band development, particularly under high-stress conditions (Tarantino & Tombolato, 2005; Gens & Alonso, 1992). The use of constant suction during testing constrained the ability to fully explore suction-dependent behaviour, but general trends in stress paths and volumetric response were reproduced with reasonable fidelity (Ng & Pang, 2000; Rahardjo et al., 2004).

With regard to cyclic behaviour, the original model by Ghorbani and Airey (2021) successfully simulated saturated undrained cyclic tests, capturing strain accumulation, cyclic mobility, and post-cyclic responses. The simulations provided a clear picture of how axial strain accumulated cycle by cycle, how peak deviatoric stress reduced progressively over time, and how stiffness softened incrementally before stabilising. However, drained cyclic simulations revealed significant limitations. The adoption of memory surface and semi-fluidised state parameters from Karlsruhe's sand led to poor agreement with experimental results, suggesting a strong dependency on soil-specific calibration. Parametric sensitivity analysis indicated that small changes in memory surface parameters, particularly a_m, caused large variations in the predicted cyclic response. This highlights the model's high sensitivity and the critical importance of accurate calibration for drained cyclic loading simulations. Without dedicated experiments that

measure volumetric strain, pore pressure, and suction evolution under cyclic loading, predictive accuracy remains limited.

Engineering implications of these findings extend beyond academic modelling. The demonstrated ability to simulate suction-enhanced cyclic resistance suggests that shallow foundations and embankment fills in partially saturated conditions may benefit from progressive densification rather than abrupt cyclic failure, while liquefaction assessments for fine-containing sands could incorporate gradual ratcheting behaviour rather than relying solely on traditional "trigger" thresholds. Likewise, pavements and subgrades subjected to millions of low-amplitude cycles could use these insights to better predict stiffness loss and long-term performance.

Furthermore, while the model generally captured essential aspects of stress-dilatancy behaviour, accurately predicting the onset of dilation and evolution of the dilation angle remained a challenge, especially at higher fines content and under unsaturated conditions (Bolton, 1986; Lade & Pradel, 1990). Given that traditional numerical error metrics fail to quantify complex behavioural patterns, model evaluation was primarily qualitative focused on stress paths, state parameter evolution, and volumetric strain behaviour (Sheng et al., 2008; Jefferies & Been, 2015).

Future improvements should focus on incorporating state-dependent fabric evolution, suction-induced hardening, and more realistic pore pressure evolution mechanisms for undrained and partially saturated conditions (Thevanayagam, 1998; Mitchell & Soga, 2005). Specific strategies could include bounding surface plasticity with ratcheting mechanisms and the use of suction-controlled cyclic systems to provide richer calibration data. Despite current limitations, the model demonstrated the ability to simulate effective-stress soil behaviour across a wide range of densities, fines contents, and saturation levels. With further refinement,

it remains a viable framework for advanced geotechnical analysis and design (Ishihara, 1993; Vanapalli et al., 1996).

A clear pattern emerged across both the experimental program and model calibration regarding the influence of fines content on soil behaviour and model parameters. Experimentally, increasing fines led to higher stiffness, improved suction retention, and a delayed transition from dilative to contractive behaviour, with the SS40F and SS60F mixtures showing the strongest effects. Fines-rich samples displayed less dilatancy and steadier post-yield stiffness, while cleaner sands (SS0F, SS20F) maintained a more pronounced dilative response.

These patterns were mirrored in the model calibration results. Parameters such as the dilatancy constant (h_0), state parameter at critical state (ψ), and the hardening modulus (H) shifted systematically with fines content. For instance, h_0 decreased as fines increased, reflecting the reduction in dilative tendency, while the critical state line parameters (M and λ) adjusted to capture changes in compressibility and strength for fines-rich soils.

These consistent parameter trends suggest that fines content could eventually be treated as a continuous variable within SANISAND rather than requiring separate calibration for every gradation. This would align with prior approaches by Rahman & Lo (2008, 2009) and Ghafarian et al. (2020), who embedded fines effects into evolving model parameters. In summary, the simulations confirm that fines content exerts a predictable influence on soil behaviour and SANISAND parameters, supporting future work to formalise fines-dependent parameterisation and improve model efficiency and predictive power.

Chapter 7
Final Conclusions

7.1 Outline

This study adopts a coupled experimental and numerical modelling approach to understand the behaviour of sandy soils subjected to variations in fines content and degree of saturation. The experimental program was designed not only to explore key behavioural mechanisms in soils but also to generate high-quality data for calibrating and validating a constitutive model.

Two soil types were selected to widen the scope of investigation: Sydney sand, a uniformly graded sand that forms gap-graded mixtures when blended with non-plastic feldspar fines and a well-graded sand (WGS) comprising basalt aggregates of varying sizes mixed with fines. The study further integrates triaxial test data from previous work by Kwa (2019) and Mohammadi (2020) on WGS and Sydney sand, respectively, enabling validation of the model across a wide range of particle size distributions and enhancing the assessment of the model's versatility with respect to grading effects.

Using the Critical State Soil Mechanics (CSSM) framework, triaxial tests were conducted under drained and undrained conditions to define the Critical State Line (CSL) and evaluate stress-strain and volumetric responses. Tests were also performed under unsaturated conditions to investigate suction effects and saturation-dependent behaviour. The experimental program encompassed eight soil gradations, providing detailed insights into the mechanical transitions from sand-like to fines-dominated behaviour.

For the modelling component, a SANISAND-based constitutive model originally developed by Ghorbani and Airey (2021) was adopted due to its proven ability to simulate a wide variety of boundary value problems in soil mechanics. The model's recent enhancement by Chen et al. (2024) further incorporated features to represent cyclic behaviour. The experimental results were used to calibrate the model parameters, and simulations were performed for monotonic triaxial tests under both saturated and unsaturated, drained and undrained conditions. While model performance for monotonic responses was found to be satisfactory, only preliminary

attempts were made to validate its behaviour under cyclic loading due to limitations in the available test data.

These findings form the foundation for evaluating the behavioural patterns of soils with varying fines content and degrees of saturation under different loading conditions. The following section presents a structured summary of the main conclusions drawn from this research, beginning with experimental observations on monotonic and cyclic behaviour, followed by insights into unsaturated soil response and the critical state framework. The performance of the selected constitutive model is then assessed through its simulation of monotonic and cyclic triaxial tests, providing a comprehensive understanding of both the experimental and modelling outcomes.

7.2 Experimental Investigation

This experimental study aimed to characterise the monotonic and cyclic behaviour of Sydney Sand and Well-Graded Sand (WGS) mixtures with varying fines contents. Through a combination of compression tests, saturated and unsaturated triaxial tests under drained and undrained conditions, the study explored the influence of fines, density, sample preparation, and loading path on the critical state response of granular soils. The experimental data were collected with the dual purpose of understanding fundamental soil behaviour and calibrating critical state-based constitutive models.

7.2.1 Monotonic Triaxial Behaviour

Monotonic triaxial tests revealed behaviour consistent with the critical state framework. Loose samples showed strain-hardening and contractive behaviour, while dense samples displayed peak strength followed by softening and dilation. As fines content increased, dilative tendencies were progressively suppressed, and the soils exhibited more contractive responses. For example, at 60% fines, even medium-dense specimens showed strain-hardening and

compressive behaviour. These trends were evident in both stress–strain and volumetric responses, highlighting the importance of fines in modifying soil structure, stiffness, and peak strength.

7.2.2 Critical State Line (CSL) and Parameter Trends

Critical State Lines (CSLs) were clearly established for all soil mixtures in both q–p′ and e–log p′ spaces. The critical state parameters derived from the test data, namely the stress ratio at critical state (M), the slope of the CSL in log e–log p′ space (λ), and the critical state friction angle (ϕ_{cs}) showed systematic variation with fines content. For Sand-fine mixtures both M and λ increased with fines up to 40%, indicating enhanced compressibility and stress ratio due to fines-facilitated particle rearrangement. However, a slight reduction in both parameters was noted at 60% fines, likely due to the dominance of fines in the soil matrix, leading to a more compressible yet less dilative structure with fewer interlocking coarse particles. On the other hand, for Well-Graded Sand (WGS) mixtures, the behaviour followed a different trend. WGS18F, which was already well graded, exhibited a relatively high CSL due to its dense interlocking structure and high angularity. However, as fines were incrementally added (up to 60%), the CSL shifted downward progressively in both q–p′ and log e–log p′ spaces. This downward shift suggests that the addition of fines into an already well-graded soil disrupts the interparticle contact network, reduces dilative potential, and increases compressibility—leading to a lower critical stress ratio and flatter CSL. This effect was consistent across all WGS mixtures and further supports the observation that increasing fines transforms the fabric from a coarse grain-dominated skeleton to a fines-controlled structure

Notably, comparisons with previous studies such as Kwa (2019) reveal a consistent trend: soils with transitional fines contents (e.g., SS40F, SS60F, WGS28F, WGS40F, and WGS60F) are particularly susceptible to non-unique CSL behaviour.

In contrast, even medium dense samples with transitional fines contents tended to converge toward the loose-state CSL, effectively avoiding the dual CSL phenomenon. This was a deliberate choice to support model calibration, as the presence of dual CSLs introduces ambiguity in defining post-yield behaviour and complicates constitutive model validation.

In this study, cyclic triaxial tests further confirmed the influence of preparation method on CSL convergence. Samples subjected to more than 100 cycles exhibited clear cyclic densification, transitioning to denser states. However, upon subsequent monotonic shearing, the stress paths of these specimens still converged to the loose-state CSL, rather than a distinct dense CSL. Hence there was no evidence of the non-unique CSLs were observed in this study as reported by Kwa (2019).

Overall, the findings highlight that the manifestation of dual CSLs is not merely a function of fines content or initial density but is highly sensitive to the fabric imparted by sample preparation method. Controlling and documenting compaction techniques especially in soils with transitional fines content is therefore essential for generating reliable experimental data and ensuring meaningful calibration of constitutive models that rely on critical state theory.

7.2.3 Cyclic Behaviour and Densification Effects

Cyclic triaxial tests revealed important aspects of strain accumulation, cyclic densification, and pore pressure response in both soil families. Drained cyclic loading led to significant densification in all mixtures of Sydney Sand and WGS, especially those with initially loose states. Upon post-cyclic monotonic shearing, these samples displayed behaviour characteristic of denser specimens, such as dilation and strain-softening.

In undrained cyclic tests, both soils showed progressive pore pressure buildup and effective stress reduction, typical of cyclic mobility. The effect was more pronounced in fines-rich mixtures, especially SS60F and WGS60F, indicating their increased susceptibility to instability and liquefaction.

Importantly, post-cyclic shearing paths in both soil types converged toward the same CSLs defined in monotonic tests, reaffirming the applicability of CSSM under cyclic loading. Even after cyclic densification, the samples converged to the loose-state CSL, indicating that fabric evolution through cyclic loading does not replicate the structure of statically compacted dense soils. Due to apparatus limitations, WGS cyclic test data were not extensively analysed. However, initial trends aligned with the Sydney Sand results, and no contradictory behaviour was observed.

7.3 Constitutive Model Calibration and Simulation

7.3.1 Calibration

The model parameters used for calibration and simulation can be broadly categorised into the following groups: Elasticity, Critical State, Kinematic Hardening, Dilatancy, Memory Surface, Semifluidised State, Stress Integration, and Unsaturated Soil parameters. Among these, the Memory Surface and Semifluidised State parameters are specifically relevant to simulating cyclic loading behaviour. The remaining parameters were calibrated directly from experimental data or through curve fitting techniques, as detailed in Chapter 6. However, due to limitations in available experimental data, the parameters related to the memory surface and semifluidised state were adopted from existing literature on soils with similar characteristics.

7.3.2 Simulations of Saturated Monotonic Tests

Most of the parameters required for monotonic simulations were calibrated systematically, and the model has previously been validated for capturing the monotonic behaviour of uniformly graded soils such as Sydney Sand. As expected, the model successfully reproduced the stress–strain response of clean Sydney Sand under both saturated and unsaturated conditions, showing satisfactory agreement with experimental results. However, the performance of the model exhibited a non-linear trend with the addition of fines. In the case of Sydney Sand mixtures,

the accuracy of the simulations declined with increasing fines content. This may be attributed to the complex interaction between sand and fines, which modifies the soil fabric and dilatancy behaviour in a way that the current model does not fully capture. Conversely, for the well-graded sand (WGS) mixtures, model performance improved with increasing fines. As the fines content increased, the behaviour of the soil matrix became more homogeneous and fines-dominated, leading to better agreement between simulated and experimental responses. This suggests that the model is better suited to capturing the behaviour of soils with more uniform fabric and dominant fines-controlled response. This is a surprising result as model developed and shown to work for clean sands.

7.3.3 Simulations of Unsaturated Monotonic Tests

To simulate the behaviour of unsaturated soils under monotonic loading, the model was extended by incorporating an additional bonding variable to account for suction-induced apparent cohesion. This was implemented by introducing an intercept to the saturated Critical State Line (CSL), effectively shifting it to represent the enhanced strength characteristics of unsaturated soil. The estimated unsaturated CSL, based on experimental data, provided a reasonable basis for determining the key unsaturated parameters b_1 and b_2, which govern the influence of suction on the yield surface and hardening behaviour.

The effect of matric suction was captured through the Soil-Water Characteristic Curve (SWCC), using parameters calibrated from laboratory measurements and best-fit procedures. This allowed for a realistic representation of the suction-dependent mechanical response of the soil. With the majority of parameters already calibrated from saturated tests and only a few additional parameters introduced for unsaturated behaviour, the model was able to simulate the unsaturated monotonic test results with satisfactory accuracy. The simulations reproduced the increased stiffness and strength observed in unsaturated specimens, consistent with the experimental trends. Overall, the model demonstrated reasonable predictive capability in

capturing the mechanical response of unsaturated soils under monotonic loading conditions, especially for clean and low-fines Sydney Sand.

7.3.4 Simulations of Cyclic Tests

Cyclic simulations were conducted at a preliminary stage to evaluate the model's capability under both saturated and unsaturated conditions. The original model by Ghorbani and Airey (2021) could simulate undrained saturated cyclic behaviour with reasonable accuracy using primarily experimentally derived parameters and minimal curve fitting.

The enhanced version by Chen (2024) extends the model to simulate saturated drained and undrained, as well as unsaturated cyclic loading under both constant suction and constant moisture content. However, this version introduces additional parameters related to the Memory Surface and Semifluidised State, which require extensive cyclic test data and sensitivity analysis for accurate calibration. Due to limited data, these parameters were adopted from literature on Karlsruhe Sand, which shares similar grading with Sydney Sand. Initial results suggest that these parameters are highly sensitive and must be carefully calibrated. While early simulations show promising trends, further refinement and validation are necessary for more reliable predictions under cyclic loading.

7.4 Future Research

This study provides a foundation for understanding and simulating the monotonic and cyclic behaviour of saturated and unsaturated sands using an advanced constitutive model. However, several areas remain open for further research and development to enhance the model's accuracy, simplify its calibration, and expand its practical application.

- **Small-Strain Behaviour**: This study initially aimed to assess small-strain stiffness using bender element tests during unsaturated cyclic loading. Due to time constraints, this was

not completed. Future work should continue this to better capture stiffness degradation and refine elastic parameters.

- **Extended Cyclic Testing**: Additional cyclic triaxial tests under varied suctions, loading paths, and moisture conditions—are needed to properly calibrate the memory surface and semifluidised state parameters, which are highly sensitive and crucial for simulating cyclic response.
- **Model Simplification and Sensitivity**: A detailed sensitivity analysis should be performed to identify and remove less influential parameters, streamlining the model for practical use.
- **Improved Unsaturated Behaviour Modelling**: Incorporating SWCC hysteresis and small-strain stiffness variation would enhance the model's realism under drying–wetting cycles and low-strain cyclic loading.
- **Microstructural Insights**: Techniques like SEM or CT scanning can help link fabric changes to model behaviour, particularly for high-fines or well-graded soils.
- **Broader Validation**: The model should be tested on a wider range of soil types and conditions, including plastic soils and gap-graded mixtures, to assess generalisability.
- **Field and Numerical Applications**: Implementing the model in finite element software and validating it against field-scale problems (e.g., slopes, embankments) will demonstrate its practical value.
- **Collaborative Tools and AI**: Sharing model code, developing shared databases, and using machine learning could accelerate calibration, improve predictions, and support broader adoption.

References

1. Airey, D. W., & Ghorbani, J. (2021). Analysis of unsaturated soil columns with application to bulk cargo liquefaction in ships. Computers and Geotechnics, 140.

2. Alonso, E. E., Gens, A., & Josa, A. (1990). A constitutive model for partially saturated soils. Géotechnique, 40(3), 405-430.

3. Alonso, E. E., Pereira, J. M., Vaunat, J., & Olivella, S. (2010). A microstructurally based effective stress for unsaturated soils. Géotechnique, 60(12), 913-925.

4. ASTM International. (2011). ASTM D5311-11: Standard Test Method for Load Controlled Cyclic Triaxial Strength of Soil. ASTM International.

5. ASTM International. (2020). ASTM D2435/D2435M-11(2020): Standard Test Methods for One-Dimensional Consolidation Properties of Soils Using Incremental Loading. ASTM International.

6. ASTM International. (2020). ASTM D4767-11(2020): Standard Test Method for Consolidated Undrained Triaxial Compression Test for Cohesive Soils. ASTM International.

7. ASTM International. (2020). ASTM D7382-20: Standard Test Methods for Determination of Maximum Dry Unit Weight of Granular Soils Using a Vibrating Hammer. ASTM International.

8. ASTM International. (2021). ASTM D1557-12(2021): Standard Test Methods for Laboratory Compaction Characteristics of Soil Using Modified Effort (56,000 ft-lbf/ft³ (2,700 kN-m/m³)). ASTM International.

9. ASTM International. (2021). ASTM D698-12(2021): Standard Test Methods for Laboratory Compaction Characteristics of Soil Using Standard Effort (12,400 ft-lbf/ft³ (600 kN-m/m³)). ASTM International.

10. B. Jaksa, C. J. Leo, & A. K. Shahu (Eds.), Challenges and Innovations in Geomechanics (pp. 71–78). Springer.

11. Barrero, A. R., Dafalias, Y. F., & Taiebat, M. (2020). Modeling cyclic shearing of sands in the semifluidized state. International Journal for Numerical and Analytical Methods in Geomechanics, 44(3), 371–388. https://doi.org/10.1002/nag.3007.

12. Been, K., & Jefferies, M. G. (1985). A state parameter for sands. Géotechnique, 35(2), 99–112.

13. Bian, H., & Shahrour, I. (2009). Numerical model for unsaturated sandy soils under cyclic loading: Application to liquefaction. Soil Dynamics and Earthquake Engineering, 29(2), 237–244.

14. Bian, H., Shahrour, I., & Jia, Y. (2017). Influence of soil saturation on the free field response of liquefiable soils. Underground Space, 2(1), 1–7.

15. Bishop, A. W. (1959). The principle of effective stress. Teknisk Ukeblad, 106(39), 859–863.

16. Bishop, A. W., & Blight, G. E. (1963). Some aspects of effective stress in saturated and partly saturated soils. Géotechnique, 13(3), 177–197.

17. Bishop, A. W., & Donald, I. B. (1961). The experimental study of partly saturated soil in the triaxial apparatus. Proceedings of the 5th International Conference on Soil Mechanics and Foundation Engineering, 1, 13–21

18. Bishop, A. W., & Henkel, D. J. (1962). The measurement of soil properties in the triaxial test.

19. Bolton, M. D. (1986). The strength and dilatancy of sands. Géotechnique, 36(1), 65–78.

20. Bray, J. D., & Sancio, R. B. (2006). Assessment of the liquefaction susceptibility of fine-grained soils. Journal of geotechnical and geoenvironmental engineering, 132(9), 1165-1177.

21. Bulut, R., & Leong, E. C. (2008). Indirect measurement of suction. Geotechnical and Geological Engineering, 26(6), 633–644.

22. Burland, J. B. (1990). On the compressibility and shear strength of natural clays. Géotechnique, 40(3), 329-378.

23. Byrne, P. M. (1991). A cyclic shear-volume coupling and pore-pressure model for sand. In Proceedings of the 2nd International Conference on Recent Advances in Geotechnical Earthquake Engineering and Soil Dynamics. St. Louis, MO.

24. Cameron, D. A., & Carter, J. P. (2009). A constitutive model for sand based on non-linear elasticity and the state parameter. Computers and Geotechnics, 36(7), 1219–1228.

25. Carraro, J. A. H., Prezzi, M., & Salgado, R. (2009). Shear strength and stiffness of sands containing plastic or nonplastic fines. Journal of Geotechnical and Geoenvironmental Engineering, 135(9), 1167–1178.

26. Chaney, R. C. (1978, June). Saturation effects on the cyclic strength of sands. In From Volume I of Earthquake Engineering and Soil Dynamics--Proceedings of the ASCE Geotechnical Engineering Division Specialty Conference, June 19-21, 1978, Pasadena, California.

27. Chen, L., Ghorbani, J., & Kodikara, J. (2024b). Modelling of shakedown, ratcheting and liquefaction of saturated granular soils using kinematic hardening with memory surface. Computers and Geotechnics, 165, 105830. https://doi.org/10.1016/j.compgeo.2023.105830.

28. Chen, L., Ghorbani, J., Dutta, T. T., Zhou, A., McCartney, J. S., & Kodikara, J. (2024a). A new multi-surface plasticity model for cyclic hardening of unsaturated granular soils. Computers and Geotechnics, 173, Article 106500.

29. Chen, L., Ghorbani, J., Dutta, T. T., Zhou, A., McCartney, J. S., & Kodikara, J. (2024c). A new multi-surface plasticity model for cyclic hardening of unsaturated granular soils. Computers and Geotechnics, 173, 106500. https://doi.org/10.1016/j.compgeo.2024.106500

30. Chen, L., Ghorbani, J., Zhang, C., & Kodikara, J. (2022a). A robust solution to address overshooting in bounding surface plasticity models.

31. Chen, L., Ghorbani, J., Zhang, C., & Kodikara, J. (2022b). Stress overshooting solution for soil plasticity models. Computers and Geotechnics, 149, 104829.

32. Chen, L., Ghorbani, J., Zhang, C., Dutta, T. T., & Kodikara, J. (2021). A novel unified model for volumetric hardening and water retention in unsaturated soils. Computers and Geotechnics, 140, 104446.

33. Chin, K.-B., Leong, E.-C., & Rahardjo, H. (2010). A simplified method to estimate the soil-water characteristic curve. Canadian Geotechnical Journal, 47(12), 1382–1400.

34. Chu, J., & Lo, S. C. R. (1991). On the implementation of strain path testing. In Deformation of Soils and Displacements of Structures X ECSMFE (Vol. 1, pp. 53–56). Publ by A.A. Balkema.

35. Coop, M. R., & Atkinson, J. H. (1993). The mechanics of cemented carbonate sands. Géotechnique, 43(1), 53–67.

36. Corti, R., Diambra, A., Muir Wood, D., & Ibraim, E. (2016). Memory surface hardening model for granular soils under repeated loading conditions. Acta Geotechnica, 11(5), 1103–1119.

37. Cubrinovski, M., & Ishihara, K. (1999). Empirical correlation between SPT N-value and relative density for sandy soils. Soils and Foundations, 39(5), 61–71.

38. Cubrinovski, M., Bradley, B., Wotherspoon, L., Green, R., Bray, J., Wood, C., ... & Wells, D. (2011). Geotechnical aspects of the 22 February 2011 Christchurch earthquake. Bulletin of the New Zealand Society for Earthquake Engineering, 44(4), 205-226.

39. Cui, Y. J., & Delage, P. (1996). Yielding and plastic behaviour of an unsaturated compacted silt. Géotechnique, 46(2), 291–311

40. Cui, Y. J., & Delage, P. (1996). Yielding and plastic behaviour of an unsaturated compacted silt. Géotechnique, 46(2), 291–311. https://doi.org/10.1680/geot.1996.46.2.291.

41. Dafalias, Y. F., & Manzari, M. T. (2004). Simple plasticity sand model accounting for fabric change effects. Journal of Engineering Mechanics, 130(6), 622–634.

42. Dafalias, Y. F., & Taiebat, M. (2016). SANISAND-Z: Zero elastic range sand plasticity model. Géotechnique, 66(12), 999–1013.

43. Das, B. M. (2013). Advanced Soil Mechanics (4th ed.). CRC Press.

44. Dayal, C. (2017). The modified Proctor & Fagerberg test. Seaways, (April), 14–16.

45. Di Benedetto, H., Blanc, M., & Tiouajni, S. (2014). Elastoplastic model with loading memory surfaces (LMS) for monotonic and cyclic behaviour of geomaterials. International Journal for Numerical and Analytical Methods in Geomechanics, 38(14), 1477–1502. https://doi.org/10.1002/nag.2265.

46. Dixon, N., Jones, D. R. V., & Fowmes, G. J. (2006). Interface shear strength variability and its use in reliability-based landfill stability analysis. Geosynthetics International, 13(1), 1-14.

47. Duraisamy, Y. (2016). Strength and stiffness improvement of bio-cemented Sydney sand (Doctoral dissertation, The University of Sydney). The University of Sydney Repository. https://ses.library.usyd.edu.au/handle/2123/15533.

48. Escribano, D. E., Nash, D. F. T., & Diambra, A. (2019). Local and global volumetric strain comparison in sand specimens subjected to drained cyclic and monotonic triaxial compression loading. Geotechnical Testing Journal, 42(4), Article 54.

49. Federal Highway Administration. (2016). Periodic evaluation of facilities repeatedly requiring repair and reconstruction due to emergency events. Federal Register, 81(205), 73196–73222.

50. Fisher, R. A. (1926). On the capillary forces in an ideal soil; correction of formulae given by WB Haines. The Journal of Agricultural Science, 16(3), 492-505.

51. Fredlund, D. G., & Rahardjo, H. (1993). Soil mechanics for unsaturated soils. John Wiley & Sons.

52. Fredlund, D. G., & Xing, A. (1994). Equations for the soil-water characteristic curve. Canadian Geotechnical Journal, 31(4), 521–532.

53. Fredlund, D. G., Rahardjo, H., & Fredlund, M. D. (2012). Unsaturated Soil Mechanics in Engineering Practice. Wiley.

54. Gallipoli, D., Gens, A., Sharma, R., & Vaunat, J. (2003). An elasto-plastic model for unsaturated soil incorporating the effects of suction and degree of saturation on mechanical behaviour. Géotechnique, 53(1), 123–135. https://doi.org/10.1680/geot.2003.53.1.123.

55. Gens, A., & Alonso, E. E. (1992). A framework for the behaviour of unsaturated expansive clays. Canadian Geotechnical Journal, 29(6), 1013–1032

56. Gens, A., & Potts, D. M. (1988). Critical state models in computational geomechanics. Engineering Computations, 5(3), 178–197.

57. Ghafarian, D., Imam, S. R., & Zarei, M. (2020). Modeling the behavior of sand-fines mixtures by improving an existing critical state constitutive model. Soil Dynamics and Earthquake Engineering, 139, Article 106271.

58. Ghayoomi, M., & McCartney, J. S. (2011). Measurement of small-strain shear moduli of partially saturated sand during infiltration in a geotechnical centrifuge. Geotechnical Testing Journal, 34(5), 503–513.technical Journal, 39(6), 1313–1332.

59. Ghayoomi, M., McCartney, J. S., & Ko, H.-Y. (2013). Empirical methodology to estimate seismically induced settlement of partially saturated sand. Journal of Geotechnical and Geoenvironmental Engineering, 139(3), 367–376.

60. Ghorbani, J., & Airey, D. (2019). Mechanism of dissipation of excess flow pressures in unsaturated granular soils subjected to seismic excitations. Japanese Geotechnical Society Special Publication, 7(2), 595-600.

61. Ghorbani, J., & Airey, D. W. (2021). Modelling stress-induced anisotropy in multi-phase granular soils. Computational Mechanics, 67(2), 497-521.

62. Ghorbani, J., Airey, D. W., & El-Zein, A. (2018). Numerical framework for considering the dependency of SWCCs on volume changes and their hysteretic responses in modelling elasto-plastic response of unsaturated soils. Computer Methods in Applied Mechanics and Engineering, 336, 80–110.

63. Ghorbani, J., Nazem, M., & Carter, J. P. (2016). Dynamic analysis of unsaturated soils subjected to large deformations. Applied Mechanics and Materials, 846, 354–359.

64. Guerra, N., Matos Fernandes, M., Ferreira, C., Gomes Correia, A., Pinto, A., & Sêco Pinto, P. (Eds.). (2024). Geotechnical Engineering Challenges to Meet Current and Emerging Needs of Society (1st ed.). CRC Press. https://doi.org/10.1201/9781003431749.

65. Head, K. H. (1980). Manual of Soil Laboratory Testing: Volume 2 – Permeability, Shear Strength and Compressibility Tests. Pentech Press.

66. HYPROP User Manual. (2011). Munich, Germany: UMS GmbH.

67. Ishihara, K. (1993). Liquefaction and flow failure during earthquakes. Geotechnique, 43(3), 351-451.

68. Ishihara, K., & Tsukamoto, Y. (2004). Cyclic strength of imperfectly saturated sands and analysis of liquefaction. Proceedings of the Japan Academy, Series B: Physical and Biological Sciences, 80(8), 372–391

69. Ishihara, K., Tsukamoto, Y., & Sawada, S. (2004). Settlement of silty sand deposits following liquefaction during earthquakes. Soils and Foundations, 44(5), 135–148.

70. Ishikawa T, Zhang Y, Tokoro T and Miura S (2014) Medium-sized triaxial apparatus for unsaturated granular subbase course materials, Soils and Foundations, 54, 1, 67-80.

71. Jefferies, M., & Been, K. (2006). Soil Liquefaction: A Critical State Approach (1st ed.). CRC Press.

72. Jefferies, M., & Been, K. (2015). Soil Liquefaction: A Critical State Approach, Second Edition (2nd ed.). CRC Press. https://doi.org/10.1201/b19114.

73. Jibson, R. W. (2005). Landslide hazards at La Conchita, California (Open-File Report 2005-1067). U.S. Geological Survey.

74. Juneja, A., & Mohammed-Aslam, A. K. (2017). A comparative study on some cyclic models in sands and silts subjected to dynamic loading. Proceedings of the 19th International Conference on Soil Mechanics and Geotechnical Engineering, 3143-3146.

75. Khalili, N., Habte, M. A., & Zargarbashi, S. (2008). A fully coupled flow deformation model for cyclic analysis of unsaturated soils including hydraulic and mechanical hystereses. Computers and Geotechnics, 35(6), 872–889.

76. Khoei, A. R., & Mohammadnejad, T. (2011). Numerical modeling of multiphase fluid flow in deforming porous media: A comparison between two- and three-phase models for seismic analysis of earth and rockfill dams. Computers and Geotechnics, 38(2), 142–166.

77. Kim, J., Kazama, M., & Kawai, T. (2019). Evaluation of post-liquefaction volumetric strain of silty sand based on a new density index. Proceedings of the 7th International Conference on Earthquake Geotechnical Engineering.

78. Kimoto, S., Oka, F., Tsai, P. S. Y., & Kato, R. (2011). Damage patterns of river embankments due to the 2011 off the Pacific Coast of Tohoku Earthquake and a numerical modeling of the deformation of river embankments with a clayey subsoil layer. Soils and Foundations, 52(5), 843–860.

79. Kwa, K. A. (2019). Liquefaction behaviour of shipped metallic ores from a soil mechanics perspective (Doctoral dissertation, University of Sydney).

80. Kwa, K. A., & Airey, D. W. (2016). Critical state interpretation of effects of fines in silty sands. Géotechnique Letters, 6(1), 100-105.

81. Lade, P. V. (1993). Initiation of static instability in the submarine Nerlerk berm. Canadian Geotechnical Journal, 30(6), 895-904.

82. Lade, P. V. (2016). Triaxial testing of soils. John Wiley & Sons.

83. Lade, P. V., & Pradel, D. (1990). Instability and plastic flow of soils. I: Experimental observations. Journal of engineering mechanics, 116(11), 2532-2550.

84. Lade, P. V., Liggio, C. D., Jr., & Yamamuro, J. A. (1998). Effects of nonplastic fines on minimum and maximum void ratios of sand. Geotechnical Testing Journal, 21(4), 336–347.

85. Lewis, R. and Schrefler, B. (1982). "A finite element simulation of the subsidence of gas reservoirs undergoing a water drive." Finite elements in fluids 4: 179-199.

86. Li, X. S., & Wang, Y. (1998). Linear representation of steady-state line for sand. Journal of geotechnical and geoenvironmental engineering, 124(12), 1215-1217.

87. Liu, C., & Muraleetharan, K. K. (2012). Coupled hydro-mechanical elastoplastic constitutive model for unsaturated sands and silts. I: Formulation. International Journal of Geomechanics, 12(3), 239–247.

88. Liu, J., & Xiao, Y. (2021). Frost Resistance of Desert Sand Concrete. Advances in Materials Science and Engineering, 2021, Article ID 6620058.

89. Liu, M. D., & Carter, J. P. (2002). A structured Cam Clay model. Canadian Geo.

90. Lu, N., & Likos, W. J. (2004). Unsaturated Soil Mechanics. John Wiley & Sons.

91. Main Roads Western Australia. (2015). WA seasonal soil movements. Main Roads Western Australia.

92. Manzanal, D., Pastor, M., & Fernández-Merodo, J. A. (2011). Generalized plasticity state parameter-based model for saturated and unsaturated soils. Part I: Saturated state. International Journal for Numerical and Analytical Methods in Geomechanics, 35(18), 1899–1917.

93. Mitchell, J. K., & Soga, K. (2005). Fundamentals of Soil Behavior (3rd ed.). John Wiley & Sons.

94. Mohammadi, A. (2021). The effects of initial state on the cyclic response of Sydney sand (Doctoral dissertation, University of Sydney).

95. Mohammadi, A., & Airey, D. (2019). Undrained response of Sydney sand under non-reversal cyclic loading. E3S Web of Conferences, 92, 08005.

96. Monkul, M. M., & Ozden, G. (2007). Compressional behavior of clayey sand and transition fines content. Engineering Geology, 89(3-4), 195-205.

97. Murray, E. J., & Sivakumar, V. (2010). Unsaturated Soils: A Fundamental Interpretation of Soil Behaviour. Wiley-Blackwell.

98. National Disaster Management Authority. (2014). Annual Report 2013-14. Government of India.

99. Ng, C. W. W., & Menzies, B. (2007). Advanced Unsaturated Soil Mechanics and Engineering. Taylor & Francis.

100. Ng, C. W. W., & Menzies, B. (2014). Advanced unsaturated soil mechanics and engineering. CRC Press.

101. Ohiduzzaman, M., Subramaniam, K. V. L., & Ahmad, F. (2014). Influence of fines content on unbound granular base materials under cyclic axial and radial stress. Transportation Geotechnics, 1(3), 129–136.

102. Oka, F., Yashima, A., & Tateishi, A. (1999). A cyclic elasto-plastic constitutive model for sand considering a plastic-strain dependence of the shear modulus. Geotechnique, 49(5), 661–680. https://doi.org/10.1680/geot.1999.49.5.661.

103. Pedrotti, M., Tarantino, A., & Ridley, A. (2019). Desiccation behaviour of colloidal silica grouted sand. Engineering Geology, 260, 105236.

104. Pedrotti, M., Wong, C., El Mountassir, G., Renshaw, J. C., & Lunn, R. J. (2020). Desiccation behaviour of colloidal silica grouted sand: A new material for the creation of near surface hydraulic barriers. Engineering Geology, 270, 105579.

105. Peters, A., & Durner, W. (2006). Improved estimation of soil water retention characteristics from hydrostatic column experiments. Water Resources Research, 42(11), W11401.

106. Peters, A., & Durner, W. (2008). A simple model for describing hydraulic conductivity in unsaturated porous media accounting for film and capillary flow. Water Resources Research, 44(11), W11417.

107. Pham, H. Q., Fredlund, D. G., & Barbour, S. L. (2005). A study of hysteresis models for soil-water characteristic curves. Canadian Geotechnical Journal, 42(6), 1548–1568.

108. Polito, C. P., & Martin II, J. R. (2001). Effects of nonplastic fines on the liquefaction resistance of sands. Journal of geotechnical and geoenvironmental engineering, 127(5), 408-415.

109. Potts, D. M., & Zdravković, L. (1999). Finite Element Analysis in Geotechnical Engineering: Theory (Vol. 1). Thomas Telford Publishing.

110. Queensland Reconstruction Authority. (2012). Annual Report 2011–2012. Queensland Government.

111. Rahardjo, H., Satyanaga, A., D'Amore, G. A., & Leong, E. C. (2012). Soil–water characteristic curves of gap-graded soils. Engineering Geology, 125, 102-107.

112. Rahman, M. M., & Lo, S. R. (2007). Equivalent granular void ratio and state parameters for loose clean sand with small amount of fines. In Proceedings of the 10th Australia New Zealand Conference on Geomechanics (pp. 674–679).

113. Rahman, M. M., & Lo, S. R. (2008). The prediction of equivalent granular steady state line of loose sand with fines. Geomechanics and Geoengineering, 3(3), 179–190.

114. Rahman, M. M., Lo, S. R., & Gnanendran, C. T. (2009). Reply to the discussion by Wanatowski and Chu on 'On equivalent granular void ratio and steady state behaviour of loose sand with fines'. Canadian Geotechnical Journal, 46(4), 483–486.

115. Rahman, M. M., Lo, S. R., & Gnanendran, C. T. (2011). Equivalent granular state parameter and undrained behaviour of sand–fines mixtures. Acta Geotechnica, 6(4), 183–194. https://doi.org/10.1007/s11440-011-0145-4

116. Romero, E., Della Vecchia, G., & Jommi, C. (2000). An insight into the water retention properties of compacted clayey soils. Géotechnique, 59(4), 313–322.

117. Romero, E., Gens, A., & Lloret, A. (1999). Water permeability, water retention and microstructure of unsaturated compacted Boom clay. Engineering Geology, 54(1–2), 117–127. https://doi.org/10.1016/S0013-7952(99)00067-3.

118. Roscoe, K. H., & Burland, J. B. (1968). On the generalised stress-strain behaviour of 'wet clay'. In Engineering plasticity. Cambridge University Press.

119. Santamarina, J. C., & Cho, G. C. (2004). Soil behaviour: The role of particle shape. In R. J. Jardine, D. M. Potts, & K. G. Higgins (Eds.), Advances in Geotechnical Engineering: The Skempton Conference (pp. 604–617). Thomas Telford.

120. Santamarina, J. C., Klein, A., & Fam, M. A. (2001). Soils and waves: Particulate materials behavior, characterization and process monitoring. Journal of Soils and Sediments, 1(2), 130-130.

121. Schindler, U., Durner, W., von Unold, G., & Müller, L. (2010). The evaporation method: Extending the measurement range of soil hydraulic properties using the air-entry pressure of the ceramic cup. Journal of Plant Nutrition and Soil Science, 173(4), 563–572.

122. Schindler, U., Durner, W., von Unold, G., & Müller, L. (2010b). Evaporation method for measuring unsaturated hydraulic properties of soils: Extending the measurement range. Soil Science Society of America Journal, 74(5), 1568–1571. https://doi.org/10.2136/sssaj2008.0358.

123. Schindler, U., & Müller, L. (2006). Simplifying the evaporation method for quantifying soil hydraulic properties. Journal of Plant Nutrition and Soil Science, 169(5), 623–629.

124. Schofield, A. N., & Wroth, P. (1968). Critical State Soil Mechanics. McGraw-Hill.

125. Seed, H. B., & Idriss, I. M. (1971). Simplified procedure for evaluating soil liquefaction potential. Journal of the Soil Mechanics and Foundations Division, 97(9), 1249–1273.

126. Shahbodagh-Khan, B., Khalili, N., & Alipour Esgandani, G. (2015). A numerical model for nonlinear large deformation dynamic analysis of unsaturated porous media including hydraulic hysteresis. Computers and Geotechnics, 69, 411–423.

127. Sheng, D., Fredlund, D. G., & Gens, A. (2008). A new modelling approach for unsaturated soils using independent stress variables. Canadian Geotechnical Journal, 45(4), 511–534.

128. Shipton, B., & Coop, M. R. (2012). On the compression behaviour of reconstituted soils. Soils and Foundations, 52(4), 668-681.

129. Shire, T., & O'Sullivan, C. (2013). Micromechanical assessment of an internal stability criterion. Acta Geotechnica, 8(1), 81–90.

130. Skempton, A. W. (1954). The pore-pressure coefficients A and B. Géotechnique, 4(4), 143–147.

131. Standards Australia. (2004). AS 1289.5.3.1—2004: Methods of testing soils for engineering purposes – Method 5.3.1: Soils compaction and density tests – Determination of the field density of a soil – Sand replacement method using a sand-cone pouring apparatus. Sydney, Australia: Standards Australia.

132. Taiebat, M., & Dafalias, Y. F. (2008). SANISAND: Simple anisotropic sand plasticity model. International Journal for Numerical and Analytical Methods in Geomechanics, 32(8), 915-948.

133. Tang, Y., Taiebat, H. A., & Russell, A. R. (2018). Numerical Modeling of Consolidation of Unsaturated Soils Considering Hydraulic Hysteresis. International Journal of Geomechanics, 18(2), 04017136.

134. Tarantino, A. (2009). A water retention model for deformable soils. Géotechnique, 59(9), 751–762.

135. Tarantino, A., & De Col, E. (2008). Compaction behaviour of clay. Géotechnique, 58(3), 199–213.

136. Tarantino, A., & Tombolato, S. (2005). Coupling of hydraulic and mechanical behaviour in unsaturated compacted clay. Géotechnique, 55(4), 307–317.

137. Teague, B., McLeod, R., & Pascoe, S. (2010). 2009 Victorian Bushfires Royal Commission Final Report. Parliament of Victoria.

138. Terzaghi, K. (1943). Theoretical Soil Mechanics. John Wiley & Sons.

139. Thevanayagam, S. (1998). Effect of fines and confining stress on undrained shear strength of silty sands. Journal of geotechnical and geoenvironmental engineering, 124(6), 479-491.

140. Thevanayagam, S. (2007). Intergrain contact density indices for granular mixes—I: Framework. Earthquake Engineering and Engineering Vibration, 6(2), 123–134

141. Thevanayagam, S., & Martin, G. R. (2002). Liquefaction in silty soils—screening and remediation issues. Soil Dynamics and Earthquake Engineering, 22(9–12), 1035–1042.

142. Thevanayagam, S., Shenthan, T., Mohan, S., & Liang, J. (2002). Undrained fragility of clean sands, silty sands, and sandy silts. Journal of Geotechnical and Geoenvironmental Engineering, 128(10), 849–859.

143. Toll, D. G. (1990). A framework for unsaturated soil behaviour. Géotechnique, 40(1), 31–44.

144. Tsukamoto, Y., & Ishihara, K. (2022). Advances in soil liquefaction engineering. Singapore: Springer.

145. Tsukamoto, Y., Kawabe, S., Matsumoto, J., & Hagiwara, S. (2014). Cyclic resistance of two unsaturated silty sands against soil liquefaction. Soils and Foundations, 54(6), 1094–1103.

146. Unno, T., Kazama, M., Sento, N., & Uzuoka, R. (2008). Liquefaction of unsaturated sand considering the pore air pressure. In Proceedings of the 14th World Conference on Earthquake Engineering (Paper No. 04-02-0083).

147. Vaid, Y. P., & Sivathayalan, S. (1996). Static and cyclic liquefaction potential of Fraser Delta sand in simple shear and triaxial tests. Canadian Geotechnical Journal, 33(2), 281–289.

148. Vallejo, L. E., & Mawby, R. (2000). Porosity influence on the shear strength of granular material–clay mixtures. Engineering Geology, 58(2), 125–136.

149. Van Genuchten, M. T. (1980). A closed-form equation for predicting the hydraulic conductivity of unsaturated soils. Soil Science Society of America Journal, 44(5), 892–898.

150. Vanapalli, S. K., Fredlund, D. G., & Pufahl, D. E. (1999). The influence of soil structure and stress history on the soil–water characteristics of a compacted till. Géotechnique, 49(2), 143–159. https://doi.org/10.1680/geot.1999.49.2.143.

151. Vanapalli, S. K., Fredlund, D. G., Pufahl, D. E., & Clifton, A. W. (1996). Model for the prediction of shear strength with respect to soil suction. Canadian Geotechnical Journal, 33(3), 379–392
s

152. Vivoda Prodan, Martina & Peranić, Josip & Jagodnik, Vedran & Marusic, Davor & Štiberc, D. & Kamenar, Nika & Arbanas, Zeljko. (2024). Shear strength of sand under different range of confining stresses using various shearing devices. 10.1201/9781003431749-252.

153. Wang, W., Xie, L., & Shen, J. (2011). One year later: Mental health problems among survivors in hard-hit areas of the Wenchuan earthquake. Public Health, 125(5), 293–300. https://doi.org/10.1016/j.puhe.2010.12.008.

154. Whang, D. H., Stewart, J. P., & Bray, J. D. (2004). Effect of compaction conditions on the seismic compression of compacted fill soils. Geotechnical Testing Journal, 27(4), 356–364.

155. Wheeler, S. J., Sharma, R. S., & Buisson, M. S. R. (2003). Coupling of hydraulic hysteresis and stress–strain behaviour in unsaturated soils. Géotechnique, 53(1), 41–54.

156. Wichmann, V., & Becht, M. (2005). Modeling of geomorphic processes in an alpine catchment. In P. M. Atkinson, G. M. Foody, S. E. Darby, & F. Wu (Eds.), GeoDynamics (pp. 61–87). CRC Press.

157. Wichtmann, T., & Triantafyllidis, T. (2016). An experimental data base for the development, calibration and verification of constitutive models for sand with focus to cyclic loading. Part I: Tests with monotonic loading and stress cycles. Acta Geotechnica, 11(4), 739–761.

158. Wood, D. M. (1990). Soil Behaviour and Critical State Soil Mechanics. Cambridge University Press.

159. World Bank. (2023). Earthquake Damage in Türkiye Estimated to Exceed $34 billion: World Bank Disaster Assessment Report. Retrieved from https://www.worldbank.org/en/news/press-release/2023/02/27/earthquake-damage-in-turkiye-estimated-to-exceed-34-billion-world-bank-disaster-assessment-report.

160. Xiao, Yang, et al. "Transitional behaviors in well-graded coarse granular soils." Journal of Geotechnical and Geoenvironmental Engineering 142.12 (2016): 06016018.

161. Yamagishi, H., & Yamazaki, F. (2018). Landslides by the 2018 hokkaido iburi-tobu earthquake on september 6. Landslides, 15(12), 2521-2524.

162. Yang, M., Taiebat, M., & Dafalias, Y. F. (2022). SANISAND-MSf: A sand plasticity model with memory surface and semifluidized state. Géotechnique, 72(3), 227–246.

163. Yin, Z. Y., & Chang, C. S. (2009). Microstructural modelling of stress-dependent behaviour of clay. International Journal of Solids and Structures, 46(6), 1373-1388.

164. Yu, H.-S. (2006). Plasticity and Geotechnics. Springer.

165. Zhang, L., Jiang, X., Sun, R., Gu, H., & Qiu, Y. (2024). Stability analysis of unsaturated soil slopes with cracks under rainfall infiltration conditions. Computers and Geotechnics, 165, 105907.

166. Zhang, X., & Lytton, R. L. (2009). Modified state-surface approach to the study of unsaturated soil behaviour. Part I: Basic concept. Canadian Geotechnical Journal, 46(5), 536–552.

167. Zienkiewicz, O. C., Chan, A. H. C., Pastor, M., Schrefler, B. A., & Shiomi, T. (1999). Computational Geomechanics with Special Reference to Earthquake Engineering. John Wiley & Sons.

168. Zlatović, S., & Ishihara, K. (1995). On the influence of nonplastic fines on residual strength. In K. Ishihara (Ed.), Proceedings of the First International Conference on Earthquake Geotechnical Engineering (Vol. 1, pp. 239–244). A.A. Balkema.

Appendix

A.1 Pore Pressure Measurements in Unsaturated Cyclic Tests

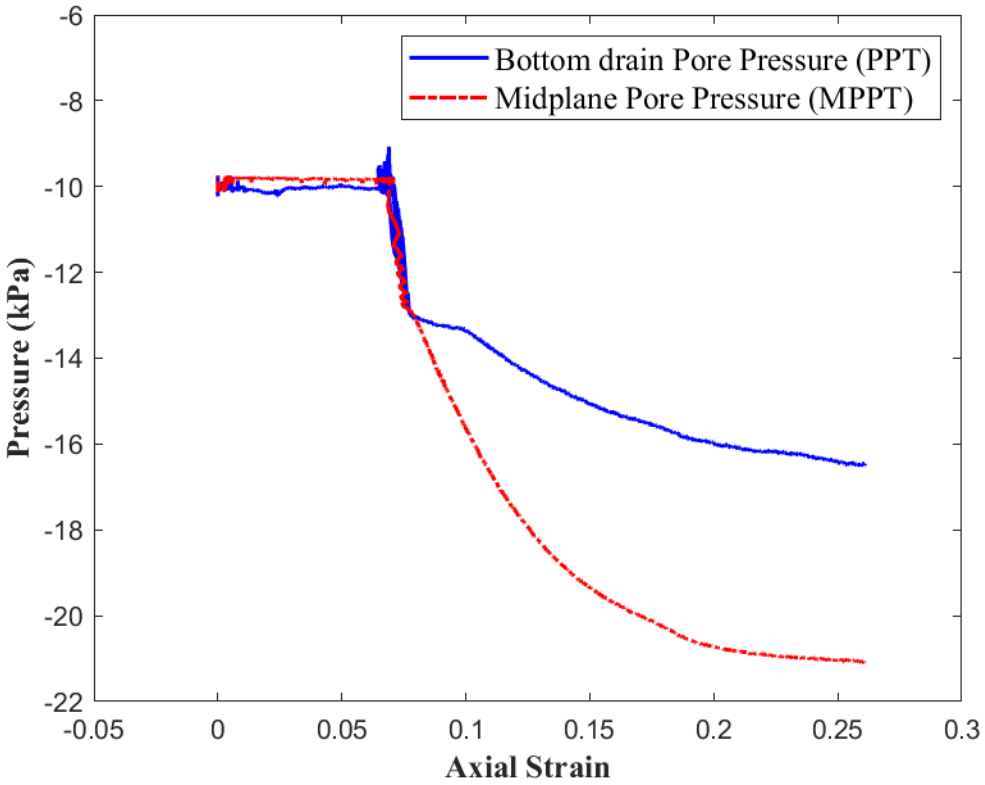

Figure A.1: Comparison of Pore pressure measurement.

The figure above compares pore pressure measurements obtained from two different transducers during a Cyclic triaxial test on an unsaturated soil sample. The bottom Drain Pore Pressure Transducer (PPT) is connected at the bottom drainage line, while the Mid-Plane Pore Pressure Transducer (MPPT) is embedded at the mid-height of the sample. The comparison of their readings across axial strain provides important insights into pore pressure development and measurement reliability in unsaturated conditions.

In unsaturated soils, the presence of air voids within the pore structure can affect the transmission of pore pressure signals, potentially leading to measurement lag or attenuation especially when the pressure is sensed externally through the drainage line. This phenomenon is evident in the monotonic shearing stage of the test, where the bottom drain PPT exhibits a noticeable lag compared to the mid-plane readings. During loading, the MPPT consistently

detects a more rapid and larger reduction in pore pressure than the drain-based PPT. This discrepancy becomes more pronounced at larger strains, where the stress state and pore pressure response evolve quickly.

The mid-plane transducer, being located within the soil specimen and in closer proximity to the pore space, responds more promptly and accurately to changes in suction and pore pressure. It is especially effective in capturing local changes without the delay introduced by fluid transmission through drainage lines. Moreover, the measurement range of the mid-plane transducer (-20 kPa to 480 kPa) is narrower than that of the bottom drain PPT (-20 kPa to 1950 kPa), which contributes to its higher sensitivity and lower signal noise. This enhanced resolution is particularly beneficial in unsaturated soil testing where pressure changes are often subtle and localized.

However, due to the limited experimental evidence and the lack of established criteria to determine which transducer consistently provides the most accurate representation of pore pressure in unsaturated samples, this study adopts the conventional bottom drain PPT readings for all calculation purposes. The discrepancies observed, particularly during monotonic loading, suggest that this is an important area for further investigation.

Therefore, while the mid-plane transducer data provides valuable insights, the conservative approach of using bottom drain measurements is retained in this research for consistency and comparability with established methods. A detailed evaluation of the reliability and suitability of mid-plane versus drainage-line pore pressure measurements in unsaturated soils is recommended as future research.

A.2 Setup with Bender Elements and Mid-plane Pressure Transducer

A limited number of triaxial tests were conducted using an apparatus equipped with bender elements and a mid-plane pore pressure transducer to investigate the uniformity of the suction and the variation in shear modulus and pore pressure during consolidation and shearing. The bender elements also allow for the measurement of small strain stiffness during cyclic loading in the triaxial tests. Therefore, the existing setup was modified with the necessary adjustments to incorporate both the bender elements and the pore pressure transducer.

Since the unsaturated triaxial tests are performed with a HAEPD at the bottom, the conventional axial arrangement of bender elements is not feasible. Also, the mid-plane pore pressure transducer must be held at the middle of the sample, while keeping the sample free from wiring. So, a special sample former and latex membrane as shown in Figure A2. and Figure A.3 are manufactured to accommodate the bender elements and pore pressure transducer. An additional triaxial ring is fitted on the triaxial base to provide room for the wirings from the instruments to data acquisition system.

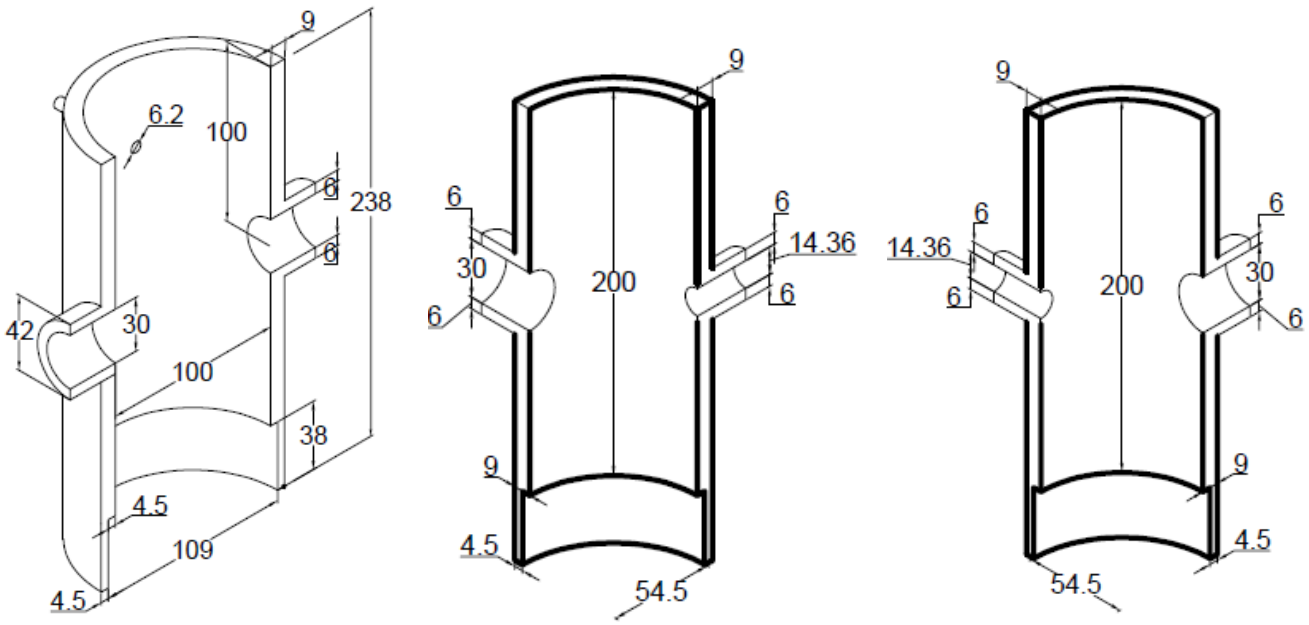

Part - A Part - B Part - C

Figure A.2: Scheme of Sample Former

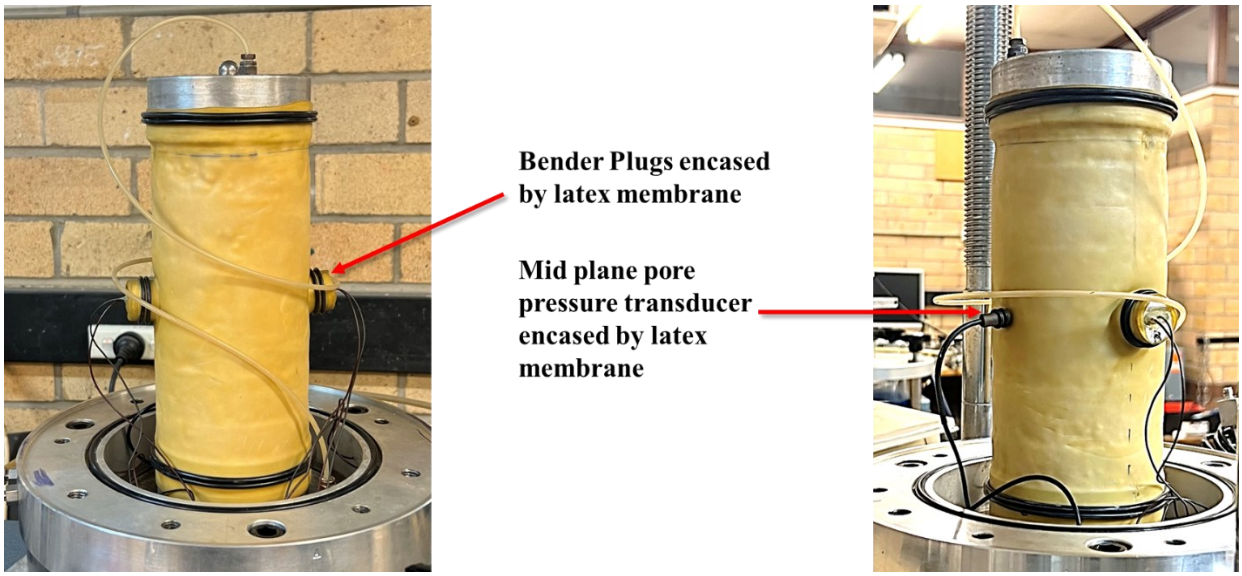

Figure A.3: Manufactured Latex membrane to accommodate instrumentation

First, the elements were encased in epoxy resin using a purpose-built mold for waterproofing. They were then mounted in slots within the bender plugs, with gaps filled using silicone sealant. The plug with bender element is then inserted into the latex membrane which is placed on bottom platen similar to the previous setup. The positioning is crucial, with one-third of the element lying in the platen slot, and two-third protruding into the specimen. This careful mounting process ensured optimal wave transmission and reception through the soil sample. Then the latex membrane and bender plugs are secured with two O-rings. In a similar procedure, the mid-plane pore pressure transducer is also inserted into the latex membrane in its slot and secured with two O-rings of suitable size. The pore pressure transducer was calibrated with reference to pressure controller.

The bender elements are mounted on a cylindrical plug with suitable cuttings. Bender elements, used for generating and receiving shear waves, are electro-mechanical transducers made from piezoelectric ceramics. These elements consist of two longitudinally expanding piezoelectric plates separated by an insulating layer. Constructed from lead zirconate and lead titanate (PZT), they were supplied as large sheets of bonded PZT strips, known as bimorphs. For this research,

the bimorphs were cut into 13 mm × 10 mm × 0.5 mm pieces. Two types of bender elements were used: series-connected elements, which are more effective as receivers, and parallel-connected elements, which perform better as transmitters.

Hewlett Packard HP33120A 15 MHz Function Generator/Arbitrary Waveform Generator is used to pulse the bender elements. This device employs direct digital-synthesis techniques to produce stable and accurate output signals. It offers four built-in waveforms (sine, square, triangle, and ramp) and allows for the creation of custom waveforms. With a frequency range of 100 μHz to 15 MHz for sine and square waves, it provides flexibility for various testing needs. The function generator was connected via a GPIB (General Purpose Interface Bus) interface and controlled by custom software, enabling seamless integration with the overall testing system.

A Yokogawa DL1520L two-channel Digital Oscilloscope was employed to monitor and record the waveform. This high-performance instrument boasts a maximum sampling rate of 200 Ms/s, a record length of 1 M words, and a frequency bandwidth of 150 MHz. It offers full voltage ranges from 1 mV/div to 10 V/div across all channels. The oscilloscope was operated in 'AVERAGE' mode with an averaging count of 256 to reduce noise and enhance signal clarity. Like the function generator, it was connected to the system via a GPIB interface, allowing for computerized control and data acquisition.

The function generator and oscilloscope were checked for linearity using sine waveforms at different voltages. This calibration process ensured the reliability of measurements across all instruments. The data acquisition system comprised several integrated components. It included a 12-bit A/D converter (CIO-DAS 1600/12) board with 8 channels, an 8-bit GPIB board (ISAGPIB/LC), an amplifier, and a desktop computer. This setup allowed for automatic logging of converted data, continuous monitoring and display of test progress, and full control

of the GDS controllers and Tritech compression machine. The system's design enabled precise measurements and real-time data analysis throughout the testing process.

A.3 Shear Modulus from Bender Elements

A series of triaxial tests were conducted on clean Sydney sand using an apparatus equipped with bender elements to evaluate the evolution of small-strain stiffness (G_{max}) during shearing under both monotonic and cyclic loading conditions. Among these, two representative tests are presented in Figures A.4 and A.5 to illustrate the relationship between deviatoric stress–strain behaviour and shear modulus variation with strain. The selected tests correspond to medium dense samples with void ratios of 0.7931 and 0.7765, respectively, providing comparable density conditions for interpreting stiffness evolution.

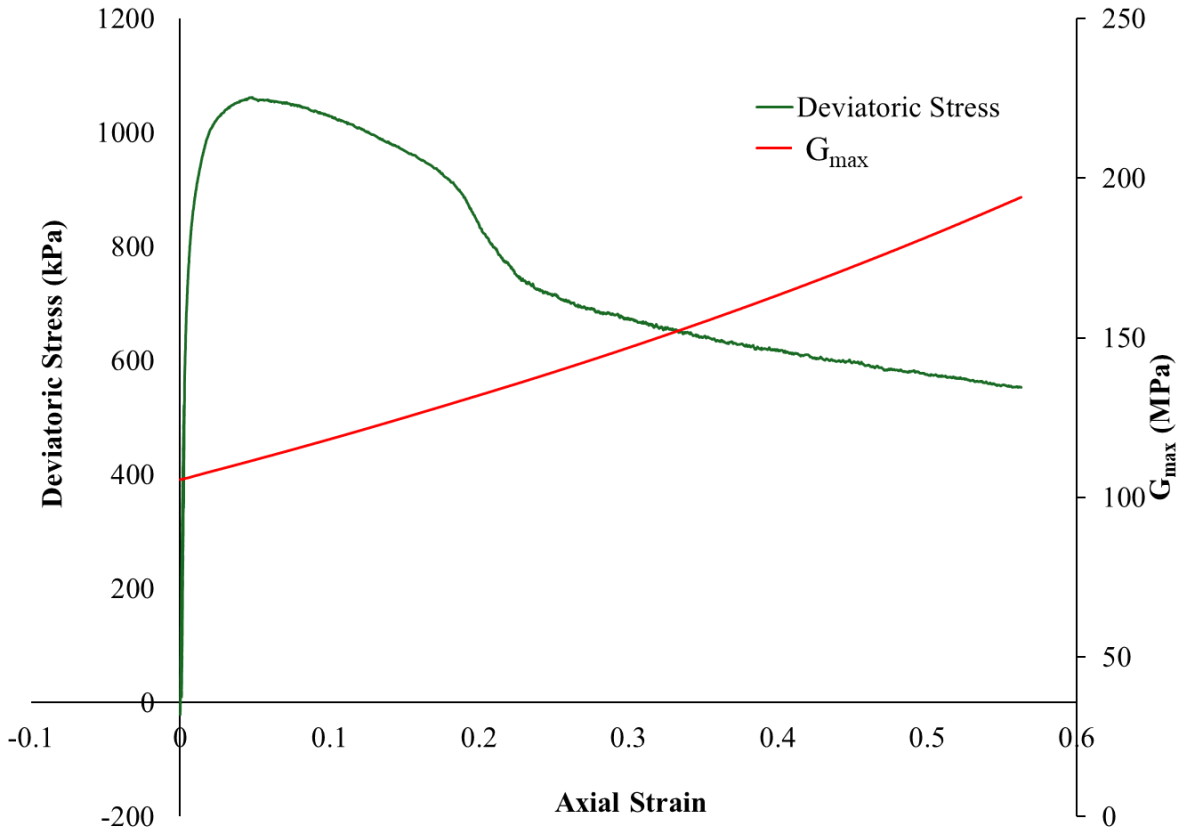

Figure A.4: Deviatoric stress and G_{max} variation with axial strain for clean Sydney Sand under monotonic loading (e = 0.7931).

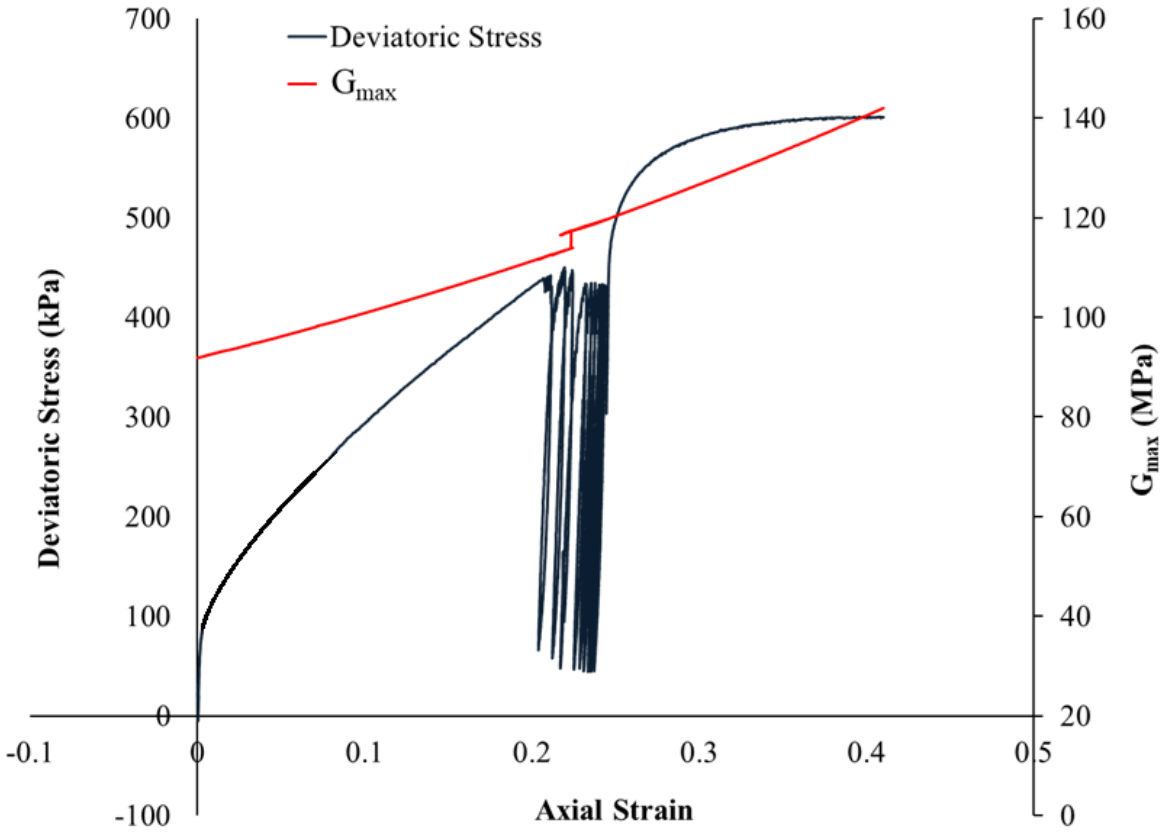

Figure A.5: Deviatoric stress and G_{max} variation with axial strain for clean Sydney Sand under cyclic loading (e = 0.7765).